

**Technische Universität München**

Fakultät für Physik

**Max-Planck-Institut für Physik**

(Werner-Heisenberg-Institut)

**TeV  $\gamma$ -Flux and Spectrum of Markarian 421  
in  
1999/2000 with Hegera CT1 using refined  
Analysis Methods**

Martin Kestel

Vollständiger Abdruck der von der Fakultät für Physik der Technischen Universität München zur Erlangung des akademischen Grades eines Doktors der Naturwissenschaften genehmigten Dissertation.

Vorsitzender: Univ.-Prof. Dr. M. Lindner

Prüfer der Dissertation:

1. Hon.-Prof. Dr. N. Schmitz
2. Univ.-Prof. Dr. F. von Feilitzsch

Die Dissertation wurde am 03. 04. 2003 bei der Technischen Universität München eingereicht und durch die Fakultät für Physik am 23. 06. 2003 angenommen.



# Contents

<b>1</b>	<b>Introduction</b>	<b>1</b>
<b>2</b>	<b>Physics background</b>	<b>5</b>
2.1	A generalised picture of AGN . . . . .	5
2.2	Possible spectral distortions caused by interactions of TeV $\gamma$ -rays with the cosmological background of infrared photons . . . . .	5
2.2.1	Cosmic Microwave Background . . . . .	5
2.2.2	Cosmological background of infrared photons . . . . .	7
<b>3</b>	<b>The AGN Markarian 421</b>	<b>13</b>
3.1	Morphology of the AGN Markarian 421 . . . . .	13
3.2	Broadband energy spectrum of Markarian 421 . . . . .	14
3.2.1	The radio range . . . . .	14
3.2.2	The optical range . . . . .	14
3.2.3	The UV to X-ray range . . . . .	16
3.2.4	MeV observations with COMPTEL and GeV observations with EGRET . . . . .	17
3.2.5	TeV $\gamma$ -ray observations . . . . .	18
3.2.6	Contemporaneous X-ray and TeV $\gamma$ -ray observations . . . . .	19
<b>4</b>	<b>CT1 telescope hardware and relevant features of the data acquisition system</b>	<b>25</b>
4.1	The tracking system . . . . .	26
4.2	The main reflector . . . . .	26
4.3	The CT1 photomultiplier camera . . . . .	27
4.4	The current CT1 electronics setup . . . . .	31
4.5	Data recording sequence . . . . .	34
4.6	The pedestal run . . . . .	34
4.7	The calibration run . . . . .	35
4.8	The data run . . . . .	37
<b>5</b>	<b>The conversion of raw data to photoelectron images and the determination of image parameters</b>	<b>39</b>
5.1	General quality requirements, detection of hardware defects . . . . .	39
5.1.1	Noise removal from the data . . . . .	39
5.1.2	Pedestal and real event analysis used to find certain hardware defects . . . . .	41
5.2	Pixel currents as starlight indicators . . . . .	42
5.3	Pointing accuracy and tracking correction . . . . .	44
5.4	Determination of ADC pedestal level and RMS . . . . .	48
5.4.1	Influence of starlight on the width of ADC pedestal spectra . . . . .	48
5.4.2	Excluding cosmic ray events from the pedestal sample . . . . .	49
5.4.3	Removing electromagnetic pickup from pedestal events . . . . .	50
5.5	Relative PM gain calibration (Flatfielding) . . . . .	52

5.6	Conversion of ADC counts to photoelectron content . . . . .	53
5.6.1	The conversion of ADC counts to photoelectrons . . . . .	53
5.6.2	Correcting individual events for coherent electromagnetic pickup . . . . .	54
5.7	Image parameter determination and image cleaning . . . . .	57
5.7.1	Image cleaning . . . . .	58
5.7.2	Image parameter definitions . . . . .	59
5.8	Image parameters under variable night sky background light . . . . .	64
5.8.1	Simulated influence of different NSB light levels on Monte Carlo $\gamma$ -event samples . . . . .	64
5.8.2	A crosscheck of image parameters from Monte Carlo protons and real data at different NSB levels . . . . .	66
5.8.3	Variations of the <i>Width</i> and <i>Length</i> of Monte Carlo generated $\gamma$ - and proton events as a function of the NSB level . . . . .	67
5.8.4	Investigation of the effect of NSB on the Crab data set from 2000-2001 . . . . .	69
5.8.5	Investigating real data which spans a large range of different NSB levels . . . . .	69
5.8.6	Proposal of the ' <i>Zonk</i> ' method to reduce the NSB influence on <i>Width</i> and <i>Length</i> . . . . .	71
<b>6</b>	<b>Ways to enhance the signal-to-noise ratio in raw data</b>	<b>77</b>
6.1	General motivation for and possible implementation methods of a cut procedure . . . . .	77
6.2	The method used to optimise the $\gamma$ -hadron separation cuts . . . . .	79
6.3	Determination of the significance of signals . . . . .	80
6.4	Improvements through the <i>Zonk</i> method . . . . .	82
6.4.1	The $\gamma$ -rate of the 2001 Crab data . . . . .	82
6.4.2	Background rates for Crab and Mkn 421 . . . . .	83
6.4.3	<i>Alpha</i> plots for Crab and Mkn 421 data . . . . .	83
<b>7</b>	<b>Energy calibration and flux determination</b>	<b>87</b>
7.1	Setup of the Monte Carlo simulation and the analysis presented in this thesis . . . . .	88
7.2	Impact parameter estimation . . . . .	89
7.2.1	Procedure used in the present analysis . . . . .	89
7.2.2	Quality of the impact parameter reconstruction . . . . .	91
7.3	Energy estimation of the primary particle . . . . .	93
7.3.1	Procedure used in this analysis . . . . .	93
7.3.2	Quality of the energy reconstruction . . . . .	95
7.4	Trigger and cut efficiencies . . . . .	95
7.4.1	Trigger efficiency . . . . .	95
7.4.2	Cut efficiency . . . . .	98
7.5	Effective trigger areas . . . . .	99
7.6	Energy threshold estimation for CT1 . . . . .	100
7.7	Effective areas after software cuts . . . . .	101
7.8	Formalism for spectrum and flux determination in this analysis . . . . .	103

7.8.1	Determination of energy spectra from CT1 data . . . . .	104
7.8.2	Determination of powerlaw index and cutoff energy . . . . .	105
7.8.3	Flux determination for CT1 . . . . .	105
<b>8</b>	<b>Mkn 421 light curve and spectrum in 1999-2000</b>	<b>109</b>
8.1	Verification of the analysis methods using Crab data . . . . .	109
8.1.1	Spectral analysis of Crab data from 1999-2000 and from 2000-2001 . . .	110
8.1.2	Crab flux as a function of the zenith angle . . . . .	112
8.2	The HEGRA CT1 data set of Mkn 421 in 1999-2000 . . . . .	112
8.3	Flux curve of Mkn 421 in 1999-2000 with HEGRA CT1 . . . . .	112
8.4	TeV spectrum of Mkn 421 in 1999-2000 with HEGRA CT1 . . . . .	118
8.4.1	Time averaged energy spectrum . . . . .	118
8.4.2	Time averaged energy spectrum from 2000-2001 . . . . .	118
8.4.3	Shape investigation of the Mkn 421 spectra . . . . .	119
8.4.4	Flux-dependent analysis of the spectral shape . . . . .	121
8.4.5	Unfolding to source-intrinsic spectra at different flux levels . . . . .	123
<b>9</b>	<b>Summary and outlook</b>	<b>129</b>
9.1	Monte Carlo simulation and analysis . . . . .	129
9.2	Data quality . . . . .	129
9.3	Analysis improvements . . . . .	129
9.4	Results . . . . .	130
9.5	Outlook . . . . .	131
<b>10</b>	<b>Acknowledgements / Danksagung</b>	<b>133</b>
<b>11</b>	<b>Appendix: Definitions of flux and related quantities</b>	<b>137</b>
11.1	Definitions of some basic physical quantities relevant to spectral analyses . . .	137
11.2	Example: flux, luminosity and intensity of the sun . . . . .	140
<b>12</b>	<b>Appendix: Viewing effects</b>	<b>142</b>
12.1	Superluminal motion . . . . .	142
12.2	Relativistic bulk motion . . . . .	142
<b>13</b>	<b>Appendix: Relevant radiation processes</b>	<b>145</b>
13.1	Thermal processes . . . . .	145
13.2	High energy processes . . . . .	147
<b>14</b>	<b>Appendix: Ordering schemes for AGN related objects</b>	<b>152</b>
<b>15</b>	<b>Appendix: Image parameter distributions</b>	<b>154</b>

<b>16 Appendix: Monte Carlo simulation of CT1 hardware and trigger</b>	<b>157</b>
16.1 Simulation of the shower development in the atmosphere . . . . .	157
16.2 Tracking CHERENKOV light through the atmosphere to the telescope and the photomultiplier windows . . . . .	162
16.3 Simulation of the electrical pulse production of photomultipliers . . . . .	165
16.4 Simulation of the trigger decision . . . . .	168
16.5 Simulation of the influence of NSB light and of the <i>Zonk</i> correction . . . . .	169
16.5.1 Modeling the NSB level for a given observation . . . . .	169
16.5.2 Deriving the <i>Zonk</i> correction to be used for Monte Carlo events from real data . . . . .	170
16.6 Number of simulated Monte Carlo events . . . . .	170
16.6.1 Simulation statistics of Monte Carlo $\gamma$ -events . . . . .	171
16.6.2 Simulation statistics of Monte Carlo proton events . . . . .	171
<b>17 Appendix: Supplemental information for data quality requirements</b>	<b>175</b>
17.1 High voltage adjustments for CT1 . . . . .	175
17.2 Quality cuts regarding the starlight contribution . . . . .	176





## Abstract

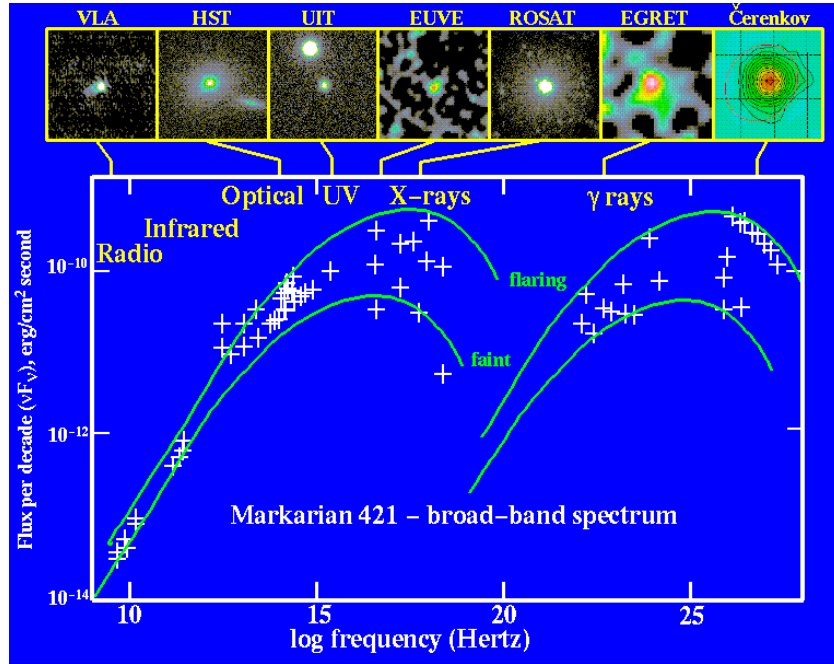
Between November 1999 and June 2000 the nearby AGN Markarian 421, abbreviated Mkn 421, located at a redshift of  $z = 0.031$ , was observed with the CHERENKOV telescope 'CT1' of the HEGRA collaboration. During this period Mkn 421 showed several prominent flares and was in general more active in the TeV region than it had been during the years before.

The HEGRA CT1 instrument was equipped with a new mirror of twice the original size in autumn 1998. A new, sophisticated Monte Carlo simulation has since been carried out for CT1 with this larger mirror, using time resolved photoelectron response simulation for an optimal simulation of the trigger decision.

This thesis describes the analysis of the new Monte Carlo data and the extraction of the energy spectrum and light curve of Mkn 421 in 1999-2000 for energies above around 750 GeV as well as the improvement of the data analysis with respect to quality criteria, treatment of night sky background noise and the estimation of impact parameters and energies.

Fitting a pure powerlaw spectrum, Mkn 421 showed a time-averaged power law spectral index of  $2.90 \pm 0.08^{\text{stat}} \pm 0.16^{\text{syst}}$  in 1999-2000. The maximum flux above energies of 1 TeV was  $(6.42 \pm 0.89^{\text{stat}} \pm 0.35^{\text{syst}}) \cdot 10^{-11} \text{ cm}^{-2}\text{s}^{-1}$ , which corresponds to more than four times the flux of the Crab nebula. This maximum was observed on MJD 51662.9 (April 29, 2000).

In contrast to the preliminary results for 2001, which have so far displayed even higher flux levels and an energy spectrum with a cutoff energy of  $2.3 \pm 0.9 \text{ TeV}$ , the 1999-2000 spectrum does not contain enough events to distinguish between a pure power law and a cutoff spectrum.



Mkn 421 has become a very popular object in  $\gamma$ -astronomy due to its brightness from radio to TeV energies.

The top row shows false colour source maps ranging from the lowest energies on the left to the highest energies on the right. The respective energy is indicated by the connecting lines joining the individual pictures with the appropriate values according to the frequency scale in the lower plot. The fact that it has been detected over almost the entire energy range is one of the outstanding and remarkable features of Mkn 421.

The main graph shows the relative flux levels in the broadband energy spectrum. The symbols denote measured values while the two curves represent model fits according to the synchrotron-self-COMPTON model, the lower and the upper curves indicating the low-flux and the high-flux states of the source, respectively.

This thesis covers TeV  $\gamma$ -observations located at the upper energy end, consisting of both low-flux and high-flux observations.

Source: (Keel, 2001)

# 1 Introduction

The TeV<sup>1</sup> region was the most recent energy window to be opened for astrophysical observations. It is also one of the highest energy windows accessible by the use of photons as messengers from distant objects. Unlike charged particles of lower energies, which are isotropised in interstellar magnetic fields, the photons point back to their origin, thus permitting the identification of their sources.

The highest energy observations allow one to address acceleration and emission processes in the sources, for which no complete theory has yet been established. Furthermore pair production reactions of TeV photons with the photons of the infrared background decrease the TeV  $\gamma$ -radiation on the photons' way to Earth. This in turn allows one to deduce the density of this background, which is very difficult to measure directly and which plays an important role in the discussion of cosmological star and galaxy formation.

The first Cherenkov telescope of the HEGRA collaboration, named 'CT1', has been used to carry out TeV  $\gamma$ -ray observations since around 1992. The hardware of CT1 was upgraded several times during this time period. A new Monte Carlo simulation has been carried out for the present configuration. The analysis using this Monte Carlo simulation is presented in this thesis.

Data analysis has been improved with respect to the treatment of night sky background (NSB) noise. A correction software has been developed to correct for the bias introduced by NSB noise and the image cleaning procedure of CT1 data.

---

Three years after the first significant observation of TeV  $\gamma$ -emission from Crab, a galactic source, in 1989 (Weekes et al., 1989), the discovery of Mkn 421 as a  $\gamma$ -source was announced in 1992 (Punch et al., 1992a). Thereafter, in 1995, Mkn 501 was another Markarian type galaxy to be found to emit TeV  $\gamma$ -rays, see e.g. (Quinn et al., 1996; Bradbury et al., 1997) or (Protheroe et al., 1998).

Since 1989 the Crab Nebula has served as TeV standard candle in the northern hemisphere. Its flux level is constant within present measuring precision and the fluxes measured from other objects are often expressed in units of 'Crab'.

**Active Galactic Nuclei (AGN) are far more luminous objects than the TeV standard candle, the Crab Nebula.**

It is instructive to compare the numbers of observed TeV photons emitted from some AGNi and from Crab respectively and to relate these numbers to the distances of the objects.

---

<sup>1</sup>Tera electron-volt: 1 TeV = 10<sup>12</sup> eV.

In the TeV region fluxes of up to ten times that of Crab have been observed for both Mkn 421 and Mkn 501. The distance to Crab is roughly 2 kpc and that to Mkn 421 and Mkn 501 is roughly 130 Mpc. Under the assumption of isotropic emission the observation of similar numbers of  $\gamma$ -rays on Earth means that these AGN have a luminosity roughly  $4 \cdot 10^9$  times higher than that of Crab.

On the other hand it is believed that the TeV emission of Mkn 421 and Mkn 501 is highly collimated in two narrow, opposing jets, one of them pointing approximately towards the Earth. Assuming a jet opening angle of  $5^\circ$  between the mantle of the jet cone and the jet axis, the two jets correspond to a solid angle of roughly 24 msr each.

If Crab emits isotropically into  $4\pi$  sr, this implies that per unit time both Mkn 421 and Mkn 501 emit with both jets roughly  $1.5 \cdot 10^7$  times more energy in the TeV range than Crab.

**With only few examples of TeV emitters available for study, the emission mechanisms are still mostly enigmatic.**

One possible explanation for TeV  $\gamma$ -ray emission from AGNi is that the TeV photons have been upscattered from lower energies, i.e. the X-ray region, to TeV energies by inverse-COMPTON processes<sup>2</sup>. The models differ in what they suggest to be the source of the photons. Most of the models assume electron acceleration inside the relativistic jet, which needs to point closely to the line of sight for TeV  $\gamma$ -radiation to become observable.

A different origin of TeV  $\gamma$ -rays is seen in highly relativistic proton interactions. In hadronic interactions involving other particles in the jet or in nearby gas clouds, they produce secondary particles, from which the neutral pions decay into two high-energy  $\gamma$ s, which become observable as TeV  $\gamma$ -rays through relativistic beaming effects in the jet.

TeV flux doubling times of around one hour have been reported for Mkn 501 (Quinn et al., 1999) and even shorter ones of around 15 minutes for Mkn 421 (Gaidos et al., 1996). This suggests that the size of the acceleration region for the parent particles of TeV  $\gamma$ -rays seen from our rest frame is  $\mathcal{O}(1 \text{ lighthouse})$ , a size of the order of our solar system. All observations at other wavelengths with higher spatial resolution strongly suggest that the TeV emission region is located close to the very center of these galaxies.

**Around 1992 the first Cherenkov telescope of the HEGRA collaboration, named CT1, began its observations.**

The telescope hardware has been upgraded several times since then. In the configuration which has been used since autumn 1998, CT1 has a main reflector dish of  $10 \text{ m}^2$  area and a camera made up of 127 pixels, with a total field of view of roughly  $3^\circ$ .

This configuration has been modeled in a new Monte Carlo study. The analysis and interpretation of data based on this Monte Carlo study form a substantial part of this thesis. As no testbeam is available for CHERENKOV telescopes, the energy and flux calibration relies entirely on Monte Carlo simulations.

---

<sup>2</sup>See Appendix 13.2 for a brief review of the emission and interaction processes mentioned here and in the following.

The CT1 data of Mkn 421 is the most complete dataset recorded with TeV instruments. The observations started around 1995-1996 — when the mirror area was  $5\text{ m}^2$  — and still continue.

The flux curve, shown and discussed in Chapter 8, displays modest activity up to the period 1998-1999. From 1999-2000 onwards intense episodic flaring has been observed. The flaring reached its highest level so far in 2000-2001, the study of which is outside the scope of this thesis. The outbursts of both years were observed simultaneously with other TeV CHERENKOV telescopes and many other instruments at all wavelengths. Various multi-wavelength campaigns have been carried out.

One of the best models of the cosmological background of infrared photons known today was used to de-convolve the TeV  $\gamma$ -ray data at different flux levels to yield intrinsic spectra of Mkn 421. The intention is to compare the source-intrinsic dynamical behaviour in the TeV region to that in the X-ray region.

**This thesis is structured as follows:**

### **1. A general AGN paradigm and the object Mkn 421**

Chapter 2 begins with the current paradigm of AGN research, i.e. a generalised picture of AGNi. Next, a short overview of the impact of the cosmological background of infrared photons on TeV  $\gamma$ -spectra observed on Earth is given.

In Chapter 3 selected morphological and spectral features of Mkn 421 are reviewed briefly.

### **2. Description of CT1 hardware elements and the data acquisition system**

Chapter 4 covers the hardware and the data acquisition system of HEGRA CT1 as far as is relevant.

### **3. Analysis steps leading from raw and Monte Carlo data to the spectrum and the light curve**

Chapter 5 explains the analysis steps that lead from the raw data to the image parameters. This chapter goes into some detail and also describes new ideas which have led to improvements.

Chapter 6 outlines the method used to discriminate signal events from the cosmic ray background.

The analysis presented in this thesis is based on a new Monte Carlo study. The procedure used to extract the light curve and the spectrum is given in Chapter 7. The general idea of this Monte Carlo study and the most important improvements as compared to earlier simulations have been added as an appendix to this thesis (Appendix 16).

### **4. Results and their discussion.**

Chapter 8 presents the light curve and the spectrum of the Mkn 421 dataset of 1999-2000. The thesis concludes with a discussion of the results in Chapter 9.



## 2 Physics background

This chapter briefly introduces a generalised picture of active galaxies, the current paradigm of AGN research. Thereafter one of the most important aspects of AGN research is addressed, which is the possibility to address the density of the cosmological background of infrared photons through their influence on the TeV region of AGN energy spectra.

---

### 2.1 A generalised picture of AGN

It has been tried to order the big variety of astronomical objects, which are related to AGN phenomena, into several, partly overlapping, object classes. One such ordering scheme for AGNi and related objects is presented in Appendix 14.

Figure 2.1 visualises the generalised picture that emerged from the study of the observations of AGNi that have been carried out at all accessible wavelengths. The objects' appearance vary depending on the angle under which the observer on Earth sees the object, and the various classes listed in Appendix 14 seem to be present.

In all radio quiet quasars and AGNi the regions close to the nucleus emit broad lines and a featureless continuum. The core is surrounded by an opaque torus that lies in the plane of the galaxy around the axis of rotation, which in the drawing in Figure 2.1 connects the two radio lobes through the central part. Strong radio emitting jets are present in 10% of the AGN, faint, non-thermal radio emission seems to be ubiquitous.

The jets consist of relativistic particles which produce powerful radio emission through the synchrotron process, with relativistic bulk motion<sup>3</sup> close to the nucleus.

Clouds, which emit narrow lines and which may be directly visible, are present outside the torus. When very luminous cores are obscured from direct viewing by the torus, they may still be seen indirectly through reflections and therefore at an increased level of polarisation.

When viewing the object with the line of sight close to the jet axis, the observer sees a continuum, with superposed broad and narrow lines, and a single sided jet, perhaps showing superluminal motion. Viewed from a position forming a very small angle with the jet axis the object appears like a blazar, as beamed emission in the jet may produce the spectral properties of blazars.

### 2.2 Possible spectral distortions caused by interactions of TeV $\gamma$ -rays with the cosmological background of infrared photons

#### 2.2.1 Cosmic Microwave Background

In 1965 the cosmic microwave background (CMB) was discovered by PENZIAS and WILSON (Penzias and Wilson, 1965). This background was found to almost perfectly follow a PLANCK

---

<sup>3</sup>C.f. Appendix 12 for a short discussion of superluminal and relativistic bulk motion.

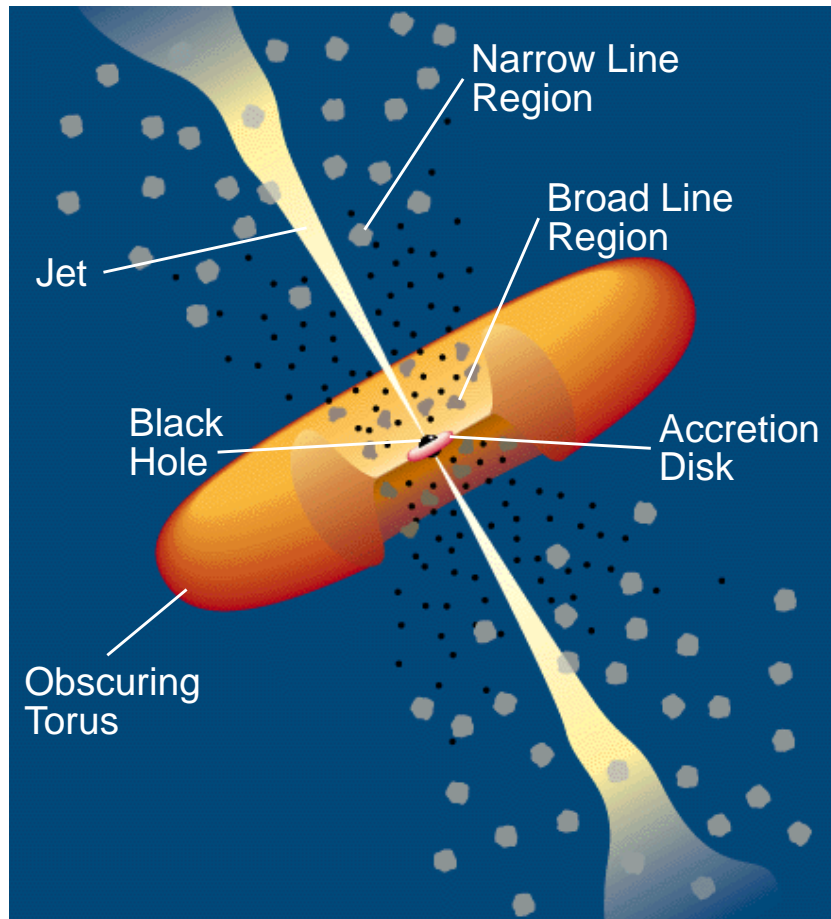


Figure 2.1: Generalised picture of AGNi showing the black hole at the center strongly exaggerated in size, the accretion disk and the torus in the plane of the galaxy. Also depicted are the regions where the broad line and the narrow line emitting clouds are thought to be located. Depending on the angle of the direction to the observer different classes of objects seem to be observed: for instance the broad line region may be obscured by the torus, so that only narrow lines and maybe scattered, polarised light from the central region is observable. Source: (Urry and Padovani, 1995)

blackbody spectrum, characterised by a temperature of  $2.725 \pm 0.001$  K, (Mather et al., 1999; Particle Data Group, 2000).

Particles created after the Big Bang were in close interaction with an ubiquitous and strong radiation field. Any atom that formed got immediately ionised. In the tail of a PLANCKian distribution with a characteristic temperature of  $T_0 = 4000$  K enough photons are present to ionise hydrogen. At a certain stage of the expansion of the universe the temperature dropped below this level, allowing the formation of atomic hydrogen. The corresponding epoch is referred to as the epoch of recombination. In an even earlier epoch helium was fully ionised.

A non-interacting PLANCKian distribution of (initial) temperature  $T_i$  at redshift  $z_i$  transforms with the universal expansion to another PLANCKian distribution at redshift  $z_f$ , characterised by the (final) temperature  $T_f$  for which  $T_f/(1+z_f) = T_i/(1+z_i)$  (Particle Data Group, 2000, p. 145). For  $z_f = 0$ , i.e. the present time, the so-called 'surface of last scatter' has a redshift of  $z \approx 1500$ . Therefore the microwave background may be interpreted as a signal from redshift  $z \approx 1500$ . The most remote quasar to date, SDSSp J104433.04-012502.2, has a redshift of  $z = 5.80$  (Fan et al., 2000). Up to now, no signal could be measured and assigned a redshift between these limits.

### 2.2.2 Cosmological background of infrared photons

Any structure observable today, e.g. stars or galaxies, started to form between redshifts  $z$  of roughly 1500 and 6. A graphical representation of the measurements of the star formation rate, reaching to redshifts of around four, is given in Figure 2.2 (Kneiske et al., 2002a). This figure shows that star formation displays maximum activity at a redshift of around one. An upper limit for the star formation rate at larger redshifts can be derived from the interpretation of observed TeV  $\gamma$ -spectra from Mkn 421 and Mkn 501 (Kneiske et al., 2002a).

As (Bond et al., 1986) point out, the energy range of the radiation emitted by protogalaxies, pregalactic stars, quasars, black hole surroundings and decaying relict particles is presumably shifted mostly to the far infrared range of around 100 to 1000  $\mu\text{m}$  wavelength by absorption and reradiation from dust.

A direct measurement of the infrared background radiation with satellite borne instruments is very difficult to obtain and not free of systematic errors. The difficulties are not only due to the very low temperatures the spacecraft needs to maintain, but also and predominantly due to the fact that it is very difficult to model the (foreground) infrared emission of the solar system and of our own Galaxy as a whole in order to correct for it. In Figure 2.3 a selection of measurements (see (Kneiske et al., 2002b) for references) is shown along with a model for the extragalactic background light (EBL). This model spectrum has uncertainties reflected in a lower and an upper estimate of the EBL level.

The TeV  $\gamma$ -rays interact in the intergalactic space with infrared photons in a  $\gamma\gamma \longrightarrow e^+e^-$  pair creation reaction. The cross section peaks at a pairing of low ( $E_{max, IR}$ ) and high energy ( $E_\gamma$ ) photons whose energies (see Equation (13.3) in Appendix 13.2) are approximately related as

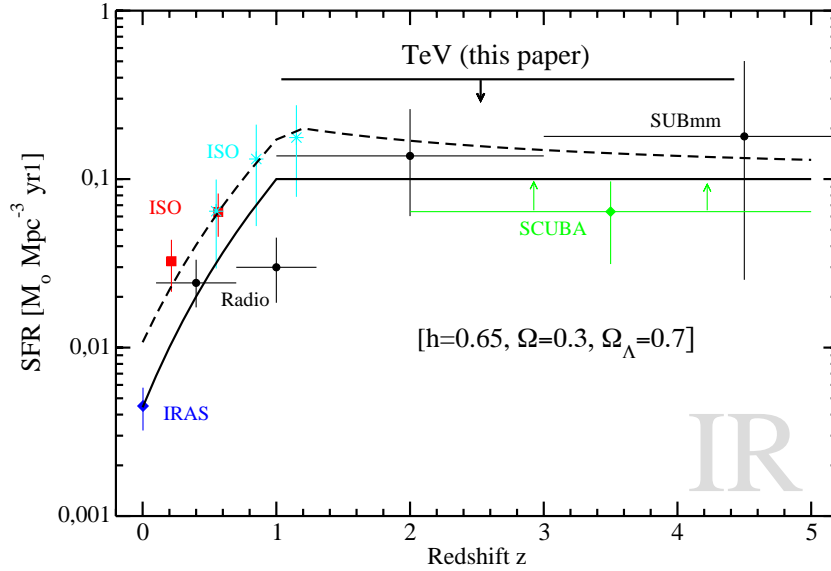


Figure 2.2: The infrared star formation rate (solid line) and the total star formation rate (dashed line) as a function of the redshift. An upper limit of the star formation rate has been derived using TeV data of Mkn 421 and Mkn 501 from several CHERENKOV telescopes. Source: (Kneiske et al., 2002a)

$$\frac{E_\gamma}{\text{TeV}} \approx 0.5 \cdot \frac{\text{eV}}{E_{max, IR}} . \quad (2.1)$$

This connects the energy sensitivity range of the current CHERENKOV telescopes to the yet unexplored infrared energy range. This corresponds to a certain attenuation length for the TeV photons traveling in the background of infrared photons. Figure 2.5 reproduces the calculations by (Coppi and Aharonian, 1997). The figure relates the energy of high energy photons, as indicated on the  $x$ -axis, to the attenuation length for these photons. The CT1 energy range has been superimposed on the original diagram. The partner energies for the CT1 energy range correspond to photons from the infrared background. The distance to Mkn 421 is also indicated in the graph. Its distance makes the spectrum of Mkn 421 sensitive to test different infrared background models, e.g. the ones labeled  $a$ ,  $b$  and  $c$ .

This sensitivity to the density of the infrared background is also shown in Figure 2.4. This figure shows the influence of the background model of Figure 2.3 on powerlaw spectra of several sources at different redshifts, drawn with a powerlaw index inferred from EGRET measurements in the energy range from 10 GeV to 100 TeV . As expected, the influence on the energy spectrum of Mkn 421 is smallest, as its redshift is the smallest in the sample shown here.

The cosmological background of infrared photons could in principle be addressed in two different, yet opposing ways:

- Based on a large set of TeV spectra from sources located at different redshifts, the brightness of the infrared background could be determined. This option requires knowledge of the spectral shape of the cosmic infrared background and a very good understanding of source-intrinsic energy spectra (see e.g. (Hauser and Dwek, 2001) and references therein).

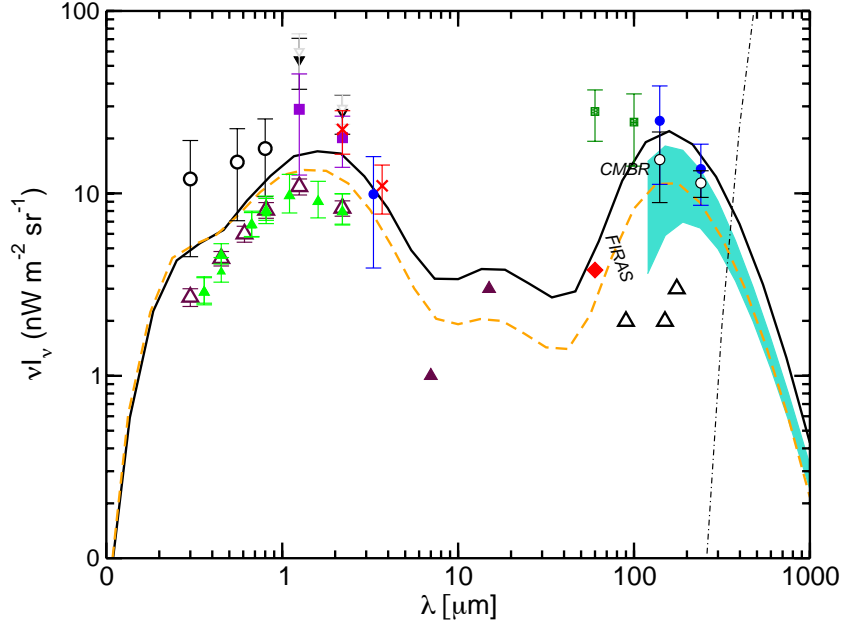


Figure 2.3: The extragalactic background light computed with the model as discussed in (Kneiske et al., 2002b) (for the data points see the references therein). Due to uncertainties a lower (dashed line) and an upper estimate (solid line) mark the range of validity of this model. Both model curves have been used to de-convolve the spectra of Mkn 421, as is discussed in Section 9. The dot-dashed line represents the microwave background density. Source: (Kneiske et al., 2002b)

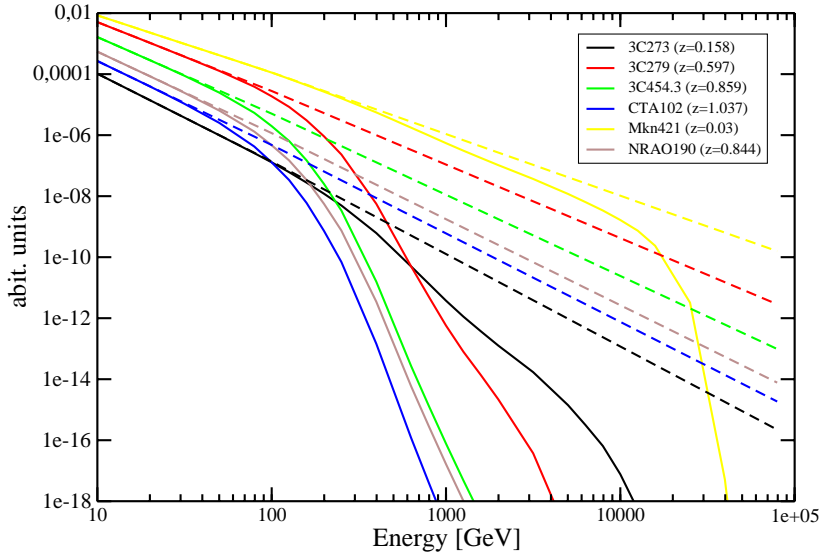


Figure 2.4: Powerlaw spectra with indices as inferred from EGRET measurements of several sources at different redshifts (dashed lines) and after convolution with the infrared background model as shown in Figure 2.3 (solid lines). From top to bottom: Mkn 421, 3C 279, 3C 454.3, NRAO 190, CTA 102 and 3C 273. Source: (Kneiske et al., 2001)

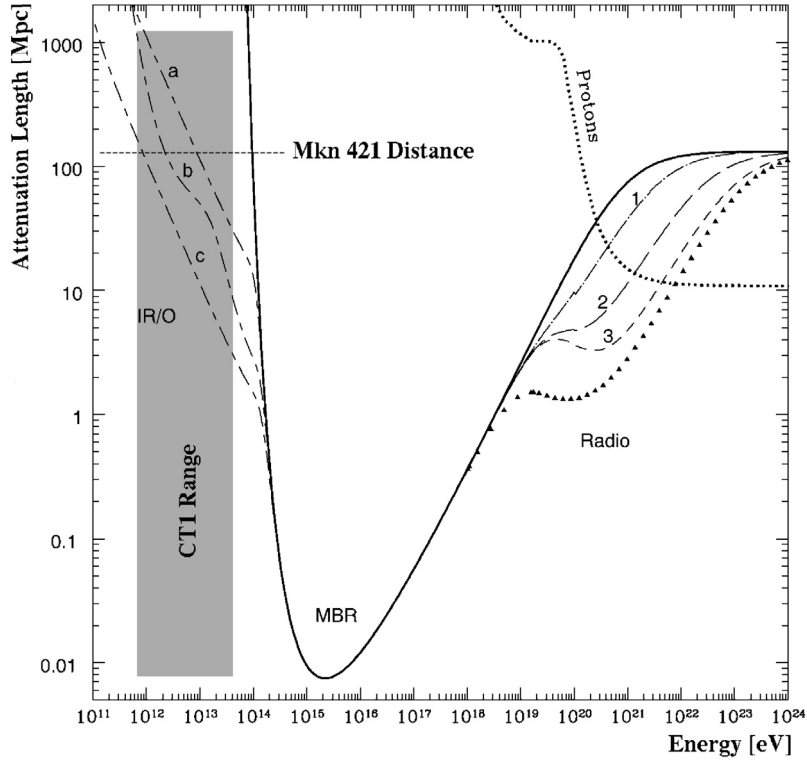


Figure 2.5: Attenuation length for pair production of high energy photons as a function of energy ( $x$ -axis). The energy range accessible with HEGRA CT1 is superimposed on the graph. The distance to Mkn 421 is also indicated. The dashed lines  $a$ ,  $b$ , and  $c$  correspond to different models of the infrared background, lines 1 through 3 correspond to different models of the radio background radiation.

Source: (Coppi and Aharonian, 1997)

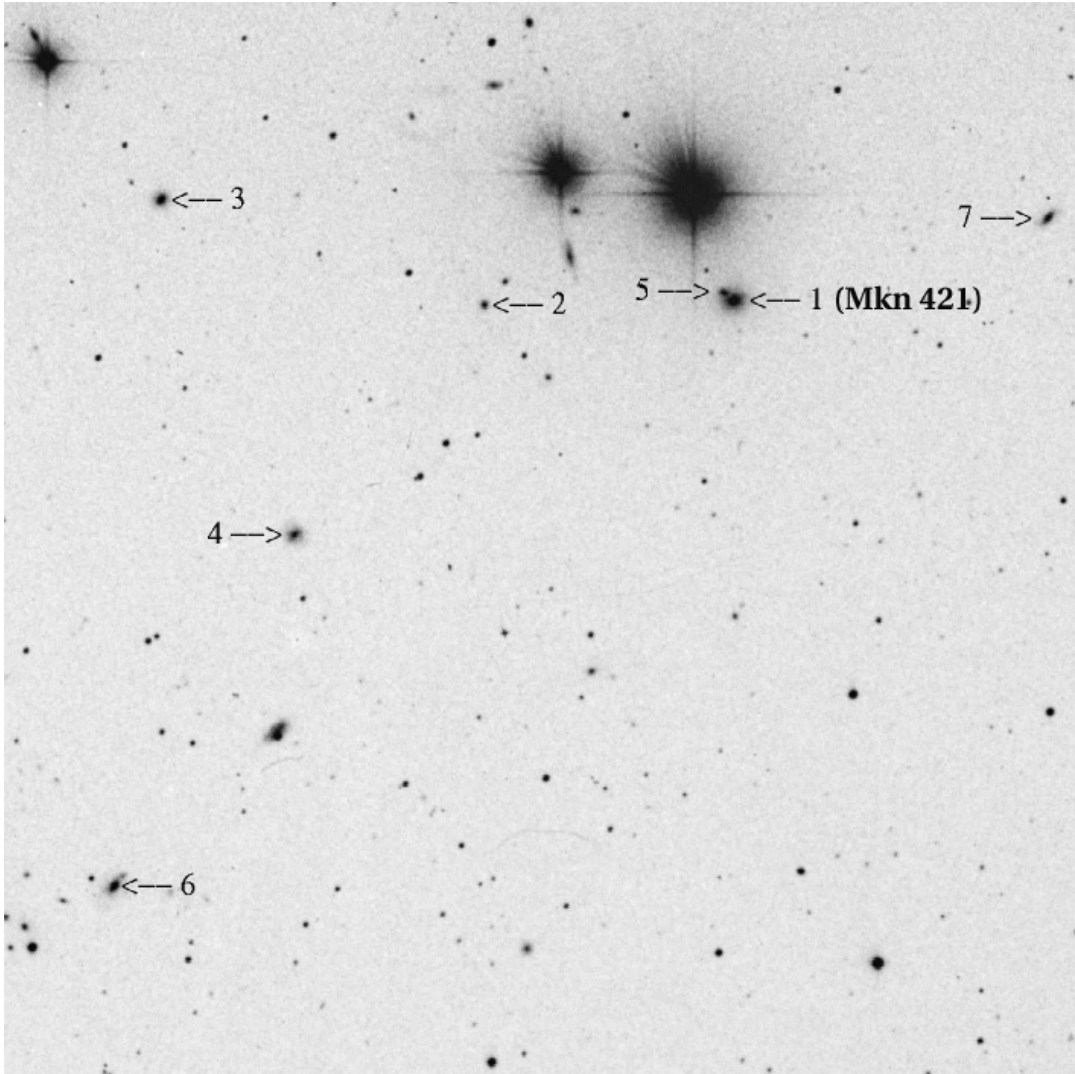
- Using a model of the infrared background like the one shown in Figure 2.3, source-intrinsic energy spectra can be determined, allowing one to study AGN physics.

The first option has been followed in the past for several times (see e.g. (Stecker and de Jager, 1993; de Jager et al., 1994; Dwek and Slavin, 1994)). (Biller et al., 1995) pointed out the difficulties of this approach, which were only partly overcome later ((Stanev and Franceschini, 1998; Funk et al., 1998; Mannheim, 1998)) due to high-quality and high-flux TeV data of Mkn 501 from 1997.

For this thesis it has been chosen to follow the second option, as the background model (Figure 2.3) represents the measurements sufficiently well, allowing one to tackle source physics and because the TeV emitters found until now are not understood to a degree that would be necessary for option one.

In Chapter 8 the spectra as measured with HEGRA CT1 in 1999-2000 combined with the high-flux data from 2001 are de-convolved using the two curves of the model shown in Figure 2.3.





Finding chart ( $20' \times 20'$ ) from the STScI all sky digitised sky survey (DSS1). A cluster of galaxies (numbered 1 (Mkn 421) to 7) with similar redshifts is located within a radius of 15 arcminutes around Mkn 421.

Source: (Space Telescope Science Institute, 2001), after (Ulrich, 1978)

### 3 The AGN Markarian 421

Markarian 421 (Mkn 421) is one of the best studied active galactic nuclei. Mkn 421 has been observed in all accessible energy regions, i.e. from  $10^{-4}$  eV to  $10^{12}$  eV, in a part of which it shows an extensive dynamic range of fluxes. This chapter presents the general appearance of one of only four established northern hemisphere extragalactic TeV  $\gamma$ -sources<sup>4</sup> and a selection of optical, UV, X-ray and TeV studies.

---

#### 3.1 Morphology of the AGN Markarian 421

Mkn 421 is a giant elliptical galaxy and the brightest member of a group of galaxies at similar redshifts (Ulrich, 1978). The redshift value of  $z = 0.0308$  was determined by investigating the weak absorption lines of Mkn 421 (Ulrich et al., 1975). This value was later refined, confirming the first finding of  $z = 0.031$  (Laurent-Muehleisen et al., 1999).

Figure 2.2.2 on the preceding page shows a finding chart based on data from the STScI digitised all sky survey (DSS1). In this finding chart, the numbering scheme by (Ulrich, 1978) was used for the other members of the cluster, which were all found at a similar redshift within a radius of roughly 15 arcmin around Mkn 421.

The close neighbour of Mkn 421 was named Mkn 421-5 by (Ulrich, 1978). This close pair was investigated in detail by (Gorham et al., 2000). The authors base their interpretation on the argument that the presence of the group suggests that Mkn 421-5 is in physical interaction with Mkn 421 and does not just appear to be close to it according to the line of sight. As (Shlosman et al., 1990) and (Walker et al., 1996) point out, AGN phenomena seem to be connected to galaxy mergers or close encounters. BL Lacs have, in general, been found to be associated with close companions or groups of nearby galaxies. (Gorham et al., 2000) studied this particular close pair using archival HST imagery and the Mount Palomar 5 m dish equipped with a double spectrometer, whose slit was oriented in such a way that it covered both objects. Mkn 421-5 has a bright nucleus which is too compact to be a typical star forming region. It is more likely to be a compact nuclear star cluster or more probably an active nucleus. The companion is likely to be in tidal interaction with Mkn 421 as they are in very close proximity both spatially and in velocity space. Mkn 421-5 shows an unusual stellar population that might be due to significant tidal interactions in the past. This is interpreted as an indication of a scenario where Mkn 421 and Mkn 421-5 have already undergone a close encounter, so that the current observations of this pair are made after this encounter / these encounters. Under these assumptions, a lower mass limit of between  $5.9 \cdot 10^{11}$  and  $10^{13} M_{\odot}$  was derived for the whole galaxy Mkn 421 (Gorham et al., 2000). Even with a mass at the lower end of this range, the galaxy Mkn 421 is still at the upper end of the mass scale for giant elliptical galaxies. The

---

<sup>4</sup>Two fellow AGNi to Mkn 421 and Mkn 501, 1ES 2344 (Catanese et al., 1998) and 1ES 1959 (Nishiyama et al., 1999), have been observed from installations on the northern hemisphere. At present these sources are only identified by one instrument and the  $\gamma$ -statistics are low.

mass-to-light ratio  $M/L$  of Mkn 421 has been found to be  $M/L \gtrsim 17$ , indicating a substantial dark matter contribution to the total mass of Mkn 421. (Gorham et al., 2000) also quote a range for the putative central black hole mass  $M_{BH}$  of  $1.8 \cdot 10^8 M_{\odot} \leq M_{BH} \leq 3.6 \cdot 10^9 M_{\odot}$ .

From these findings the authors conclude that the center of mass of the system Mkn 421 and Mkn 421-5 should be displaced by some hundred parsec or more from the location of the central black hole of Mkn 421. They suggest that careful measurements of the movement of stars close to the center of Mkn 421 could prove or disprove the proximity of Mkn 421-5.

It is not yet clear whether or not Mkn 421 shows superluminal motion. The strong cm-wavelength radio source Mkn 421 has been reported to show superluminal motion according to (Zhang and Baath, 1990), while a more recent study (Piner et al., 1999) arrives at the opposite conclusion.

## 3.2 Broadband energy spectrum of Markarian 421

In this section a small selection of measurements (see Figures 3.1 through 3.3) and conclusions is presented, which, far from being complete, aims to give an overview of the object's properties.

### 3.2.1 The radio range

This range is specified by the limits  $\nu \lesssim 10^{12}$  Hz,  $\lambda \gtrsim 10^{5.5}$  nm,  $E \lesssim 10^{-2.5}$  eV.

As indicated in Figure 3.2 on page 17<sup>5</sup> Mkn 421 shows a featureless and flat, non-thermal continuum flux spectrum in the radio range.

Some authors argue that the lack of a sharp synchrotron selfabsorption cutoff in the radio range — in contrast to the textbook cutoff shown in Figure 13.1 in Appendix 13.2 — suggests that the non-thermal continuum originates in an inhomogeneous emission region (Zhang and Baath, 1990). That is, the observed spectrum does not stem from a single source but from several such sources located in the relativistic jet that originates in the active nucleus of the host galaxy (Marscher, 1980; Königl, 1981).

It has also been suggested that the flatness of the radio spectrum is due to a complex overlay of individually selfabsorbed radio sources (Kellermann and Pauliny-Toth, 1968).

The variability has been found to be much less pronounced in the radio band than at higher energies (Purton et al., 1977), c.f. also Figure 3.2, which is further described and discussed below.

### 3.2.2 The optical range

This range is specified by the limits  $4 \cdot 10^{14}$  Hz  $\lesssim \nu \lesssim 8.3 \cdot 10^{14}$  Hz,  $360$  nm  $\lesssim \lambda \lesssim 750$  nm,  $1.7$  eV  $\lesssim E \lesssim 3.5$  eV.

Figure 3.1(a) shows the spectrum in the visible wavelength range of the Mkn 421 core by (Gorham et al., 2000), which, as opposed to earlier spectra, includes newly discovered emission lines. The emission lines of  $H_{\alpha}$  and NII seem to be associated solely with the nucleus and not

---

<sup>5</sup>This figure is discussed in more detail in Section 3.2.3.

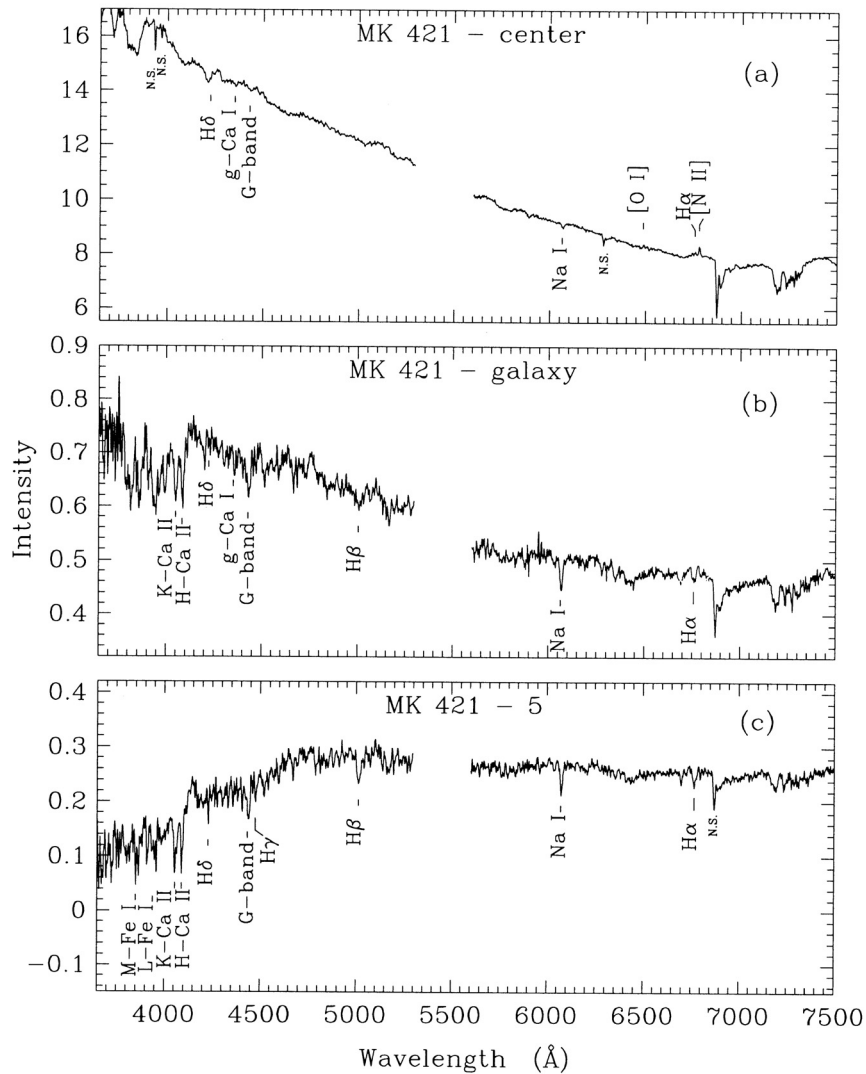


Figure 3.1: The optical spectra of Mkn 421 recorded with the Palomar double spectrograph. Subfigure (a) shows the spectrum of Mkn 421’s core, Subfigure (b) that of the Mkn 421 galaxy without the core, and Subfigure (c) that of the companion Mkn 421-5 as a whole. Units are  $\text{erg cm}^{-2} \text{s}^{-1} \text{\AA}^{-1}$  ( $1 \text{\AA} = 0.1 \text{ nm}$ ) with an overall flux calibration uncertainty of 20%. This is the first report of emission lines for this object at  $\text{H}\alpha$  and  $\text{N II}$ . Both galaxies (excluding the core of Mkn 421) show a number of well-defined absorption lines, whereas no line emission is present.

Source: (Gorham et al., 2000)

with the galaxy itself, as can be seen from Figure 3.1(b). The authors attribute the small, underlying increase in the emission wavelength range around the lines to the emission of the core of Mkn 421, which outshines the rest of the galaxy by far, a fact that is easily seen from the scales of plots (a) and (b).

Earlier spectra taken from Mkn 421 did not show emission lines. The appearance of emission lines in hitherto featureless BL Lac-spectra has previously been reported for the objects BL Lac, OJ 287 or PKS 0521-365, as pointed out by (Gorham et al., 2000) (see references therein). The authors suggest a special monitoring program dedicated to these emission features as a means to determine whether their (dis-)appearance is correlated with other processes.

### Periodicity investigations in the B band<sup>6</sup>

An extensive set of optical B band data recorded since 1900 was compiled and tested for periodicities using JURKEVICH's  $V_m^2$  test by (Liu et al., 1997). The data showed a significant period of around 23.1 years, which is covered only four times by the observation time window. Two prominent optical outbursts occurred around 1934 and 1982 respectively, while an intermediate putative peak-window around 1957 was less prominent due to sparse observations. Assuming the 23 year periodicity, the next peak in the optical B band is to be expected around the years 2003 to 2007. Another period of around 15 years indicated by the data was less significant. Assuming the periodicity of 23 years the mass of the putative black hole at the center of Mkn 421 was estimated to be  $2 \cdot 10^6 M_\odot$ , contrary to the value quoted by (Gorham et al., 2000).

### 3.2.3 The UV to X-ray range

This range is defined by the limits  $10^{15} \text{ Hz} \lesssim \nu \lesssim 10^{19.5} \text{ Hz}$ ,  $10^{-2} \text{ nm} \lesssim \lambda \lesssim 10^{2.5} \text{ nm}$ ,  $10^{0.5} \text{ eV} \lesssim E \lesssim 10^5 \text{ eV}$ .

Mkn 421 was the first X-ray source of BL Lac type to be established (Ricketts et al., 1976; Cooke et al., 1978). Its X-ray spectrum has a soft power law form (Mushotzky et al., 1978; Hall et al., 1981) which shows significant variability (Mushotzky et al., 1979).

During 1984 and 1985 joint observations of Mkn 421 were made with the IUE and the EXOSAT satellites (see e.g. (NASA, 2001; ESA, 2001) or (George et al., 1988) and the references therein). The observations covered wavelength intervals of 1230 to 1900 Å and 2100 to 3200 Å on the IUE instruments SWP and LWP respectively. In the X-ray domain the energies range from 0.03 to 2.0 keV on the LE instrument and from 1 to 10 keV on the ME instrument.

Despite the sparse data sampling an outburst was recorded in early December 1984, which had decayed by the time of the next observation in January 1985.

More interesting than the variability timescale — the authors give an  $e$ -folding time scale of  $5 \cdot 10^4 \text{ s}$  for the steep decline in flux — is the fact that the flux in the X-ray domain changed dramatically over time, and also showed a change in the spectral shape and slope, while the flux in contemporary UV data showed patterns consistent with no change. Figure 3.2 shows

---

<sup>6</sup>The sensitivity of photographic plates peaks in the blue (hence the letter 'B') part of the optical spectrum and corresponds to an effective wavelength of 440 nm (Harwit, 1998, p. 586).

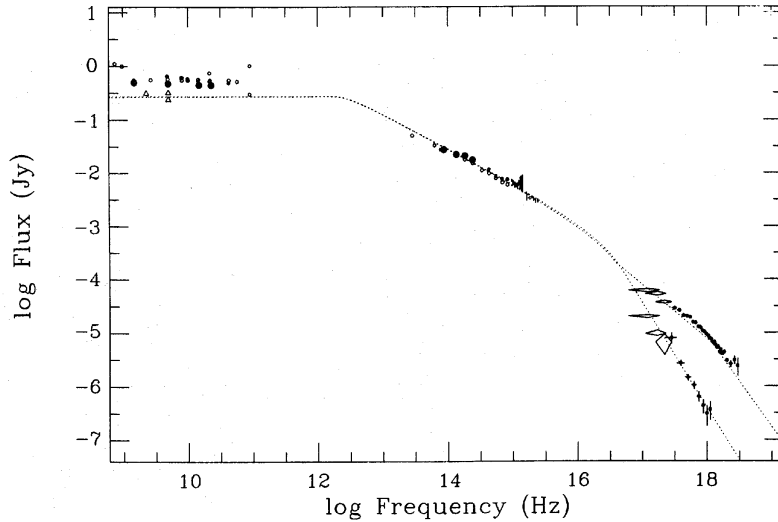


Figure 3.2: Flux from Mkn 421 as a function of energy, ranging from the radio band to X-ray energies. The radio region looks flat in this plot of the flux (usually the intensity is plotted). In the X-ray region an outburst was recorded in early December 1984 (upper points between  $10^{17}$  Hz and  $10^{18}$  Hz), opposed to the low flux level of the X-rays. While the low, soft X-ray emission changed over time to a high, hard emission, the contemporary UV flux did not change its level and characteristics.

Source: (George et al., 1988)

the flux as a function of energy ranging from the radio band to the X-ray energies of EXOSAT. This figure is taken from (George et al., 1988), where references for the other data points in the optical and radio range can be found.

Various authors point out the fact that considerable spectral hardening in conjunction with increases in the flux has been observed for SEYFERT galaxies in the UV-range (e.g. (Bromage et al., 1982; Perola et al., 1982; Ulrich and Boisson, 1983)).

### 3.2.4 MeV observations with COMPTEL and GeV observations with EGRET

The COMPTEL experiment aboard the CGRO observed Mkn 421 and Mkn 501 at a large number of occasions between April 1991 and December 1998. (Collmar et al., 1999) report on the analysis of all data in the range of 10 to 30 MeV, which yields an overall signal at the  $3.5\sigma$  level at a position that is consistent with Mkn 421. Below 3 MeV the data are consistent with noise; in the range of 2 to 10 MeV and that at 10 to 30 MeV, significance values of  $2\sigma$  and  $3\sigma$  are recorded, respectively. The authors point out that part of the MeV observations were carried out while Mkn 421 was not observable with TeV instruments.

Mkn 501 was not detected at all by COMPTEL; it was, however, detected during its strong TeV outburst in 1997 by EGRET. Above energies of 500 MeV a signal with a significance of  $5.2\sigma$  (Kataoka et al., 1999) was measured. Mkn 421 was one of the weakest and the first blazar to be detected by EGRET (Lin et al., 1992). A pointed observation between June 27 and July 11 1991 resulted in a spectrum with a power law index of  $1.96 \pm 0.16$  measured between 50 MeV and just above 1 GeV.

### 3.2.5 TeV $\gamma$ -ray observations

#### Detection of TeV $\gamma$ -rays from Mkn 421

Between March 24 and June 2 1992 Mkn 421 was observed with the WHIPPLE CHERENKOV telescope ((Punch et al., 1992b); see (Cawley et al., 1990) for a description of the telescope). In 7.5 hours observation time a flux of photons with energies above 0.3 TeV of 0.3 times the Crab flux level was observed for Mkn 421, corresponding to a significance of  $6\sigma$ .

#### Confirmation with the Hegera telescopes CT1 and CT2

In the observation period between December 1994 and May 1995 26 hours worth of data were collected with HEGRA CT1 and 41 hours worth with CT2. This data yielded a significance of  $4.0\sigma$  from CT1 and  $4.2\sigma$  from CT2, which give a combined significance of approximately  $5.8\sigma$ .

The data not only confirmed the presence of the source, but also yielded a powerlaw spectral index of  $3.6 \pm 1.0$ , measured when the flux level was estimated to be roughly half the Crab flux.

#### Very rapid bursts from Mkn 421

In the night of May 7 1996 the WHIPPLE telescope recorded an extremely intense and rapid flare from Mkn 421 (Gaidos et al., 1996). The flux level reached around ten times that of Crab. The threshold of the telescope was around 350 GeV at the time. The doubling time of the flare was found to be 1 hour. For this flare event a powerlaw spectral index of  $2.56 \pm 0.07^{\text{stat}} \pm 0.1^{\text{sys}}$  was found, with no hint of a spectral cutoff (Zweerink et al., 1997).

In the night of May 15 1996 another flare was recorded, which showed a doubling time for the rise and the decay of around 15 minutes only. The spectral properties were investigated using hardness ratios and were found to remain more or less unchanged during the flare. The most important constraint one can deduce from this observation is posed on the size of the emission site of the TeV  $\gamma$ -rays. The authors conclude that the DOPPLER factors  $\mathcal{D}$  (c.f. Equation (12.4) in Appendix 12.2) are restricted to values of  $\mathcal{D} \geq 9$ , which, together with the variability timescale  $\Delta t$ , leads to estimates of the size of the emission region  $R$  of

$$R < c \cdot \Delta t \cdot \mathcal{D} / (1 + z) \quad (3.1)$$

where

$z$  is the cosmological redshift.

With  $\Delta t \approx 1$  hour and  $\mathcal{D} \approx 10$ , the spatial extension is constrained to lie within the limits (Gaidos et al., 1996)

$$1 < R < 10 \text{ light hours} \quad . \quad (3.2)$$

#### TeV spectrum of Mkn 421 recorded with the Cat telescope

In the night of March 24/25 1998 the CAT CHERENKOV telescope ((Barrau et al., 1998; Le Bohec et al., 1998)) recorded an intense flare from Mkn 421. The spectrum was evaluated for

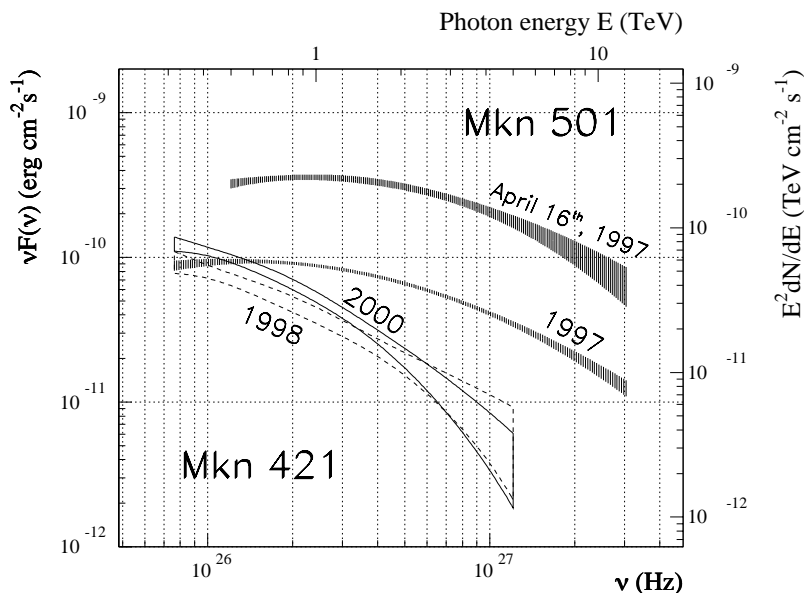


Figure 3.3: Mkn 421 and Mkn 501 TeV energy spectra recorded by the CAT telescope. The graphs show a low-flux and a high-flux spectrum.

Source: (Piron et al., 2001)

zenith angles below  $16^\circ$  and energies  $E$  in the range  $330 \text{ GeV} < E < 5.2 \text{ TeV}$ . A differential powerlaw index  $\alpha$  of  $\alpha = 2.96 \pm 0.13^{\text{stat}} \pm 0.05^{\text{sys-MC}}$ , and a flux constant  $\phi_0$  of  $\phi_0 = (1.96 \pm 0.20^{\text{stat}} \pm 0.12^{\text{sys-MC}} \pm 1.07^{\text{sys-atm}}) \cdot 10^{-11} \text{ cm}^{-2} \text{ s}^{-1} \text{ TeV}^{-1}$  were found, with no hint of any curvature like the one present for instance in the Mkn 501 spectrum at around 6 TeV.

### A study of the spectral properties of Mkn 421 comparing several instruments

Very recently the  $\gamma$ -ray properties in the TeV domain were studied by (Piron et al., 2001). The time averaged spectrum between 0.3 and 5.0 TeV was fitted by a powerlaw with an index of  $2.88 \pm 0.12^{\text{stat}} \pm 0.06^{\text{sys}}$ . An overlay of low-flux and high-flux TeV spectra of both Mkn 421 and Mkn 501 is shown in Figure 3.3.

### 3.2.6 Contemporaneous X-ray and TeV $\gamma$ -ray observations

#### RXTE and ASCA satellite observations in the X-ray domain and TeV observations by Whipple

(Kataoka et al., 2001) analysed five years of archival data of pointed observations of Mkn 421 and Mkn 501 from the ASCA (recorded between 1993 and 1998) and RXTE (recorded between 1996 and 1998) satellites. They combined this X-ray data with truly simultaneous TeV observations carried out with the WHIPPLE CHERENKOV telescope (for references see (Kataoka et al., 2001)) and reported three main findings:

- A double peak structure is present in the  $\nu \cdot I_\nu$  plot, as well in the X-ray domain and in the TeV domain.

- In the X-ray band the peak energy is a function of the flux level. While Mkn 421 showed peak energies  $E_p$  in the range of 0.5 to 2 keV, the range of 1 to 100 keV which is spanned by Mkn 501 is much larger. The functional behaviour of the peak luminosity  $L_p$  is  $E_p \propto L_p^{0.4}$  for Mkn 421 and  $E_p \propto L_p^{1.6}$  for Mkn 501.
- The connection between X-ray flux levels ([X – ray flux]) and TeV flux levels ([TeV  $\gamma$  – ray flux]) also differs between the two objects: while

$$[\text{TeV } \gamma - \text{ray flux}]_{\text{Mkn 421}} \propto [\text{X} - \text{ray flux}]_{\text{Mkn 421}}^{0.92 \pm 0.12} \quad (3.3)$$

holds for Mkn 421, the relation for Mkn 501 is

$$[\text{TeV } \gamma - \text{ray flux}]_{\text{Mkn 501}} \propto [\text{X} - \text{ray flux}]_{\text{Mkn 501}}^{1.96 \pm 0.07} \quad (3.4)$$

These results indicate that the relationship between the fluxes in the X-ray and the TeV domain may be highly complicated. Usually the X-ray peak is associated with synchrotron emission by highly relativistic electrons in the jet (c.f. Appendix 13.2). The nature of the second, high energy peak is still the subject of a major debate. The multi-frequency spectra of Mkn 421 and Mkn 501 are reproduced in Figures 3.4(a) and (b).

### **Joint Beppo-Sax (X-Rays) and Whipple (TeV) observations in April 1998**

During April 1998 a multi-wavelength observation of the BEPPO-SAX satellite (Boella et al., 1997) and the WHIPPLE TeV CHERENKOV telescope (Cawley et al., 1990; Buckley, 1999) observed a huge flare of Mkn 421. It was recorded on all instruments of the satellite. In their analysis of this multi-wavelength data (Maraschi et al., 1999) stress the lag of the hard photons with respect to the soft ones, i.e. the X-rays in the LECS (0.1 to 0.5 keV) lag the photons recorded in the MECS (4.0 to 6.0 keV) by 2 to 3 ks. The flare shows an asymmetric rise and decay especially at the higher X-ray energies, while at energies corresponding to the synchrotron peak the flare seems to develop more symmetrically. Figure 3.5 shows the development of the flare on the different instruments. Especially noteworthy is the fact that the decay times of the flare in different energy ranges are different. An explanation for this behaviour within the framework of SSC models seems to be difficult.

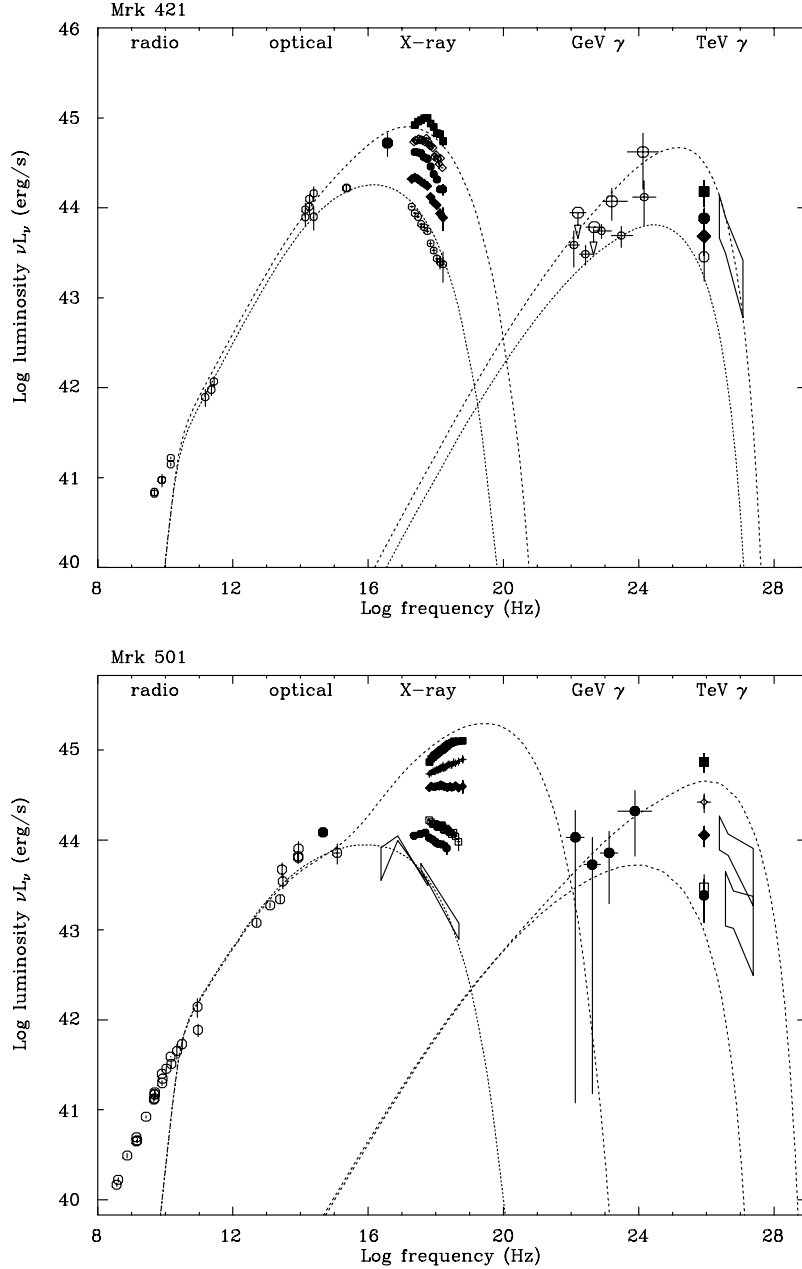


Figure 3.4: Multi-frequency spectra of Mkn 421 (top) and Mkn 501 (bottom), containing simultaneously recorded data. The dotted lines correspond to SSC-model fits for quiescent and for flaring states. The multiwavelength spectrum of Mkn 421 (top) shows that the X-ray and the TeV fluxes are correlated, displaying a similar slope in the X-ray and in the TeV domain. While the fluxes in the X-ray domain changed dramatically with time, the position of the peak remained almost the same. The multiwavelength spectrum of Mkn 501 (bottom) shows that changes in the X-ray flux are accompanied by large shifts in the position of the synchrotron peak. While the slope varies over a wide range in the X-ray spectrum, it stays almost constant in the TeV range. Further the flux variation is much larger in the TeV band than in the X-ray band.

Source: (Kataoka et al., 2001)

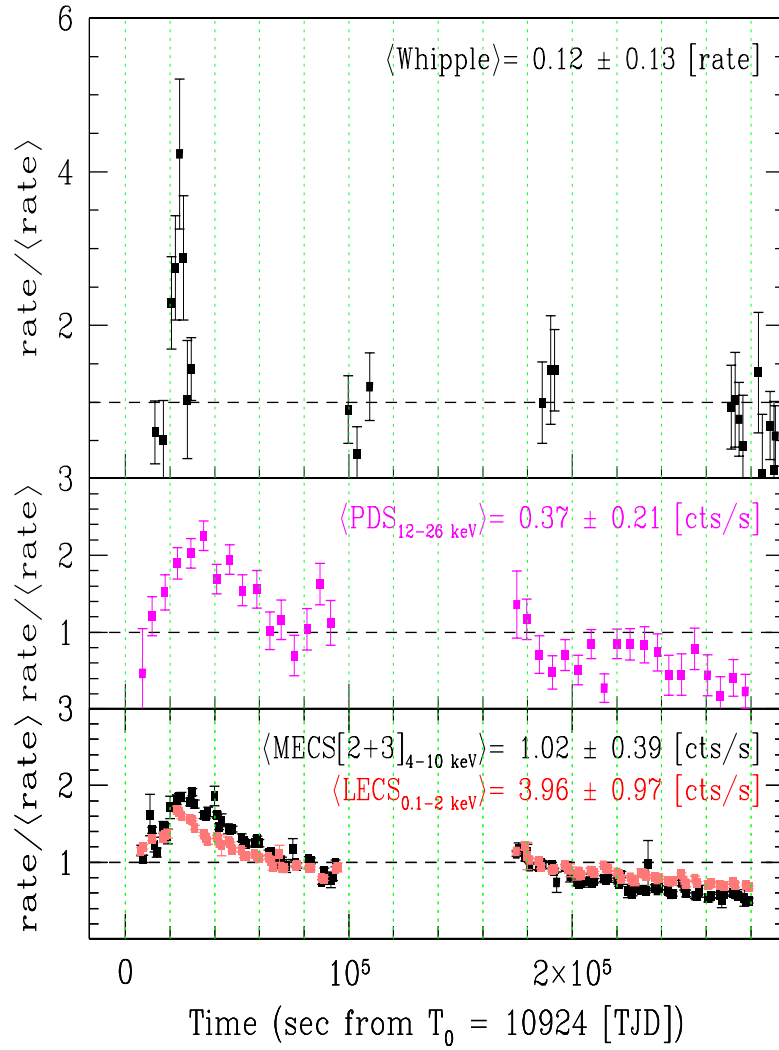


Figure 3.5: The multi-wavelength evolution of a huge flare that was recorded both by the Beppo-SAX satellite and the WHIPPLe CHERENKOV telescope during a multi-wavelength campaign. Source: (Maraschi et al., 1999)





The focusing of CT1 is demonstrated here in a night with a humidity close to 100%. A lamp, shown on the left-hand side of the picture, is placed at a distance of slightly more than twice the focal length from the main reflector. The light is then concentrated below the CT1 camera, as is made visible through the scattering of the water drops in the air.  
Photo: M. Kestel



Figure 4.1: CT1 was built in 1991 as the first CHERENKOV telescope of the HEGRA collaboration.

Photo: M. Kestel

## 4 CT1 telescope hardware and relevant features of the data acquisition system

**This chapter presents a description of those key elements of both the telescope hardware and the data acquisition system (abbreviated as 'DAQ' in the following) that appear in the description of the analysis steps in Chapter 5. Additional details can be found in (Mirzoyan et al., 1994; Cortina et al., 1999).**

---

HEGRA CT1 is located on Roque de los Muchachos on the Canary Islands, Spain, at the terrestrial coordinates  $28^{\circ} : 45' : 30''$  N,  $17^{\circ} : 52' : 48''$  W. The telescope was built in 1991 at a height a.s.l. of 2200 m and was fitted with an equatorial mount. Initially it was equipped with a 37 pixel camera at a distance of 4.90 m from the  $5 \text{ m}^2$  main reflector composed of spherical glass mirrors. In 1994 the camera was exchanged for the current 127 pixel camera with much smaller pixels. In autumn 1998 the glass mirrors were replaced by 33 light weight hexagonal mirror tiles with a diamond-milled aluminium surface. Roughly at the same time the trigger logic was changed. Now only events in which two neighbouring out of 127 available pixel signals exceed the trigger threshold of around 13 photoelectrons trigger event readout. This leads to a dramatic reduction of background noise, which in turn allows one to raise the high voltage setting of the photomultipliers, leading to a lower telescope threshold<sup>7</sup> of around 700 GeV as opposed to the previous threshold of 1.2 TeV close to zenith.

---

<sup>7</sup>See Section 7.6 for the definition of the telescope threshold quoted here.

Motor Steps	Shaft Encoder Steps	Axis Rotation [°]
487600	16384	360
1354.4	45.5	1
1	0.03	$7.38 \cdot 10^{-4}$
29.76	1	$2.20 \cdot 10^{-2}$

Table 4.1: Correspondence of motor steps, shaft encoder steps and the rotation of the telescope axis. The parameters are the same for both axes of CT1.

In the following the most important hardware elements and part of the data acquisition electronics are described in some detail.

#### 4.1 The tracking system

One of the two axes of CT1 is parallel to the Earth's axis of rotation. It is called hour axis as it counteracts the rotation of the Earth,  $360^\circ$  during one sidereal day, corresponding to  $23^{\text{h}} 56^{\text{m}} 04.09053^{\text{s}}$  (Epoch 2001.0, (Particle Data Group, 2000)). During tracking the angular velocity of this axis is constant, as regular as a clock, hence the name. The second axis, the declination axis, is used to adjust the declination of the tracked object. It is connected perpendicularly to the hour axis. During tracking the declination axis, with the mirrors and camera attached to it, rotates around the hour axis. The image in the focal plane does not rotate with this type of mount, a fact which, together with the simplicity of tracking, represented an argument for its use with photographic plates on hand-steered telescopes in the past.

CT1 carries roughly six tons of lead counterweight. The axes are driven by two powerful stepping motors, controlled via two shaft encoders which are used for the position readout. The stepping motors require 200 steps per  $360^\circ$  revolution of their axes.

A technical drawing of the declination axis, which has been modified for display purposes, is reproduced in Figure 4.2. The drawing shows the stepping motor on the right, as well as the reduction gear (46 : 1) attached to this and the worm drive (53 : 1, self-blocking) which is mounted on the axes. These ratios are the same on both axes and are much finer than the position readout can resolve. The shaft encoders are of absolute type and have a resolution of 14 bit for  $360^\circ$ . Table 4.1 gives the correspondence between motor steps, shaft encoder steps and the angle by which the axis has rotated. The parameters are equal for both axes. Despite the fine resolution of the shaft encoders, the overall tracking accuracy is only of order  $0.1^\circ$ . The reasons for this and a method of correction are described in detail in Section 5.3.

#### 4.2 The main reflector

The main reflector of CT1 is designed to collect as much CHERENKOV light as possible, to keep the spread between photon arrival times small and to give an undistorted projection of the shower over the whole field of view of the camera. In consequence the requirements for mirrors are not as demanding for CHERENKOV telescopes as for optical telescopes. The goal is not to record images of a pointlike object at infinity but to focus CHERENKOV photons from extended showers into a rather roughly pixelated photomultiplier camera. For cost reasons the telescope

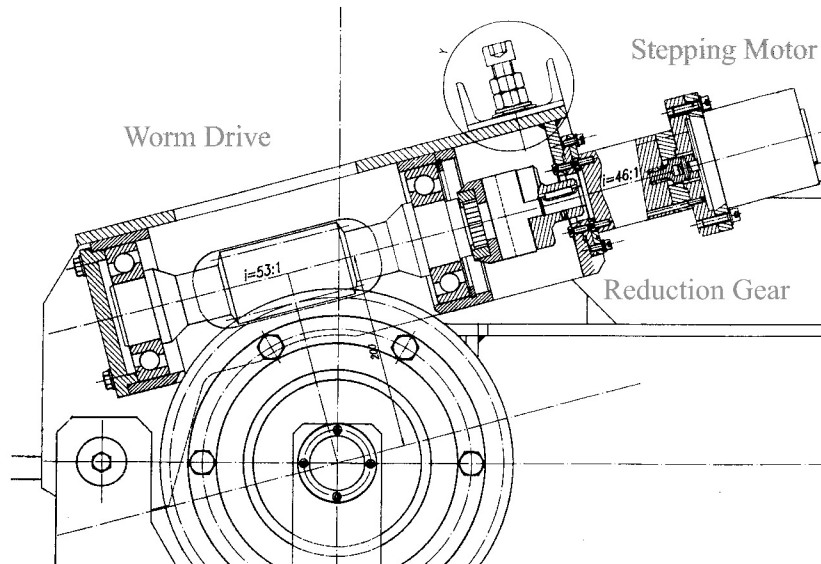


Figure 4.2: Modified technical drawing of the declination drive unit of CT1. The drawing shows the stepping motor on the right, the reduction gear attached to this and the worm drive. Both axes of the telescope are constructed in the same way. Source: MPI Munich, Construction Office.

has no protective dome, i.e. the mirrors are exposed to sunlight and heat as well as rain, dust, fog and ice. In order to avoid ice deposition on their surfaces that might damage the telescope and to permit observations in cold nights an integrated heating system is used to de-fog and de-ice the reflective surfaces.

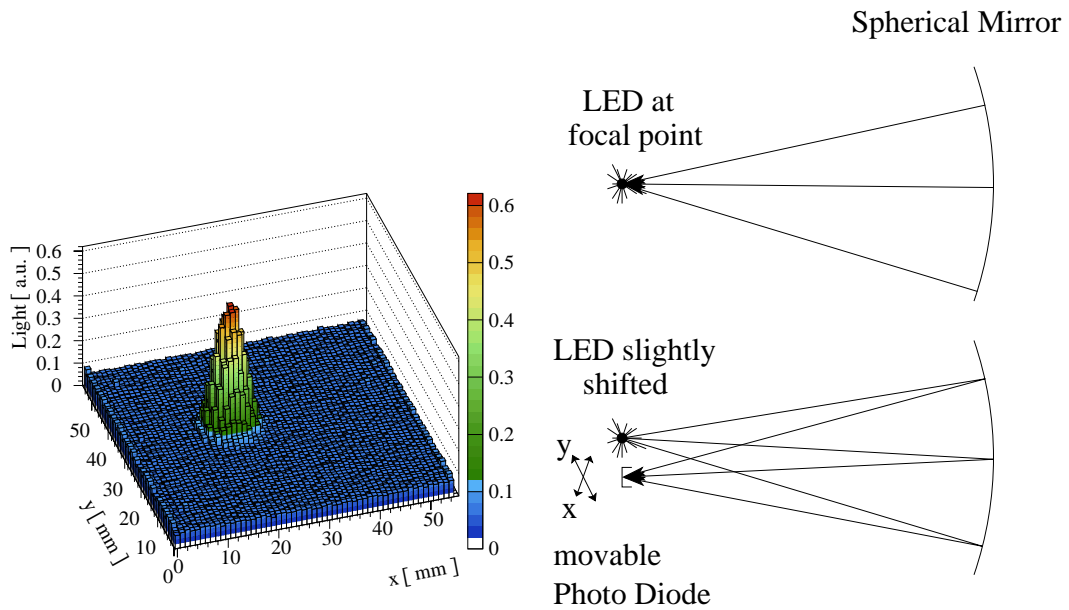
Figure 4.1 shows a photograph of the CHERENKOV telescope CT1 in the present configuration. The hexagon-shaped main reflector is made up of 33 hexagonal mirror units. The individual mirror units are of spherical shape with a radius of 980 cm, combined to an overall spherical shape. Each of the mirrors is mounted onto the support dish of the telescope with three support joints. Two movable joints permit their adjustment by hand. The mirror technology was developed at the MPI Munich for use on the MAGIC telescope. Hexagonally shaped prototypes were mounted onto CT1.

The point spread function, which is defined as the RMS width of the image of a point source, is used to qualify mirror quality. Figure 4.3 shows a scan of such a light spot measured for one of the MAGIC prototype mirrors. It is the image of a 5 mm  $\emptyset$  LED located at a distance of twice the focal length. The illuminated area corresponds to a point spread function with  $0.02^\circ$  RMS, which exceeds the requirements, as the pixels have a diameter of  $0.25^\circ$  each.

Use of this new mirror fabrication technology permitted an increase of the mirror area to twice its original size, with the weight of all new mirrors only slightly exceeding that of the glass mirrors used before.

### 4.3 The CT1 photomultiplier camera

The camera of CT1 consists of

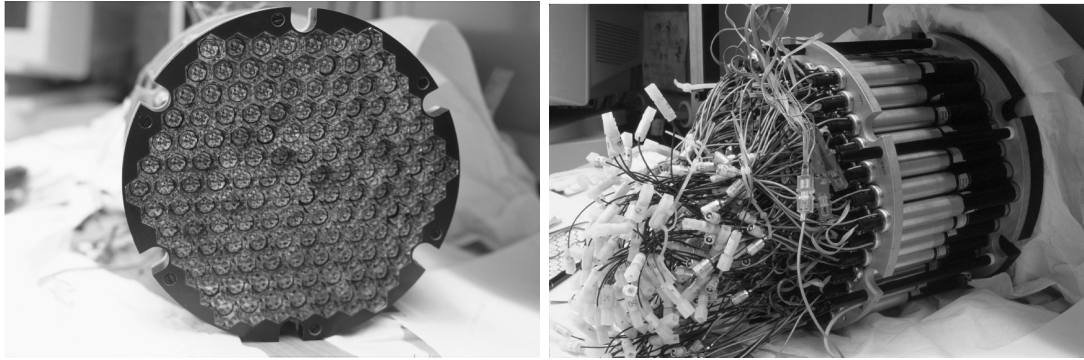


(a) Scan of the light reflection from a Magic aluminium mirror. The scan was made according to the sketch on the right.

(b) The spherical mirrors were illuminated by an LED close to their focal point in the focal plane. The light distribution of the reflected light was then recorded in steps of 1 mm in two directions.

Figure 4.3: The focusing properties of the CT1 mirrors are similar to the properties of the mirrors to be used on the MAGIC telescope. The image of a 5 mm  $\emptyset$  LED has an RMS of roughly 2.3 mm in either dimension, i.e. equivalent to about  $0.02^\circ$ . 99% of the light is contained within a 10.8 mm  $\emptyset$  spot.

Scan courtesy of M. Laatiaoui



(a) The front of the camera is formed by a grid of 127 tiny Winston cones. Here the PMTs are still in place before being removed and cleaned for maintenance purposes.

(b) The interior of the CT1 camera. Three cables connect the individual pixels, which are held in place by a supporting frame.

Figure 4.4: Front view and interior of the CT1 camera when it was opened for inspection and repair.

Photos: J. A. Coarasa, MPI Munich

- 127 photomultipliers with divider bases and pre-amplifiers,
- a WINSTON cone plate,
- a front window,
- the camera casing, housing the necessary cables and connectors.

During daytime the camera's front cover is closed and the high voltage (HV) for the photomultiplier tubes is switched off. The front cover is held closed by a spring, against the force of which a pneumatic cylinder opens the camera lid for observations. This construction guarantees that the camera does not stay open in the event of a drop in air pressure.

- The 1 mm UV transmitting foil window

This foil is a protection against water and dirt that might otherwise enter the camera casing through the front opening.

- The WINSTON cone plate

In order to collect as much light as possible from the fraction that hits the inevitable gaps between the round photo-multiplier tubes, an entrance light guide plate was added that carries hex to round reduction cones (so-called WINSTON cones) with highly reflective surfaces. This WINSTON cone plate together with the photomultipliers is shown in Figure 4.4(a) in a front view. The WINSTON cones increase the light collection efficiency by a factor of two compared to the plain photomultiplier matrix.

- The photomultiplier tubes, their bases with signal preamplifiers and connections

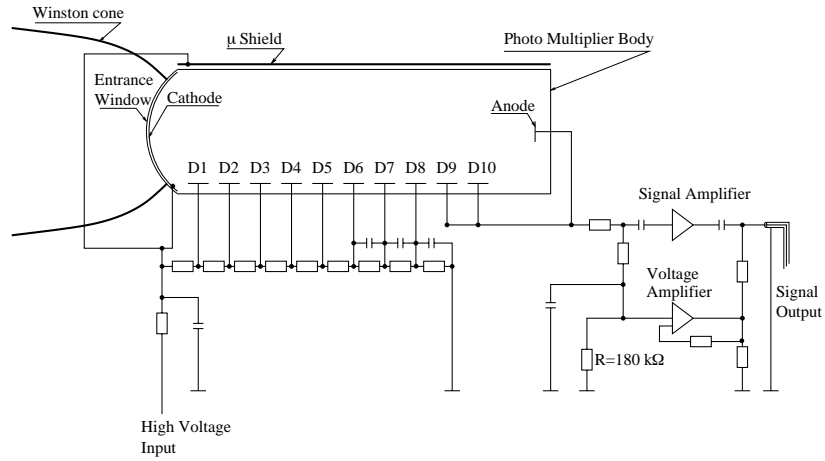


Figure 4.5: Circuit diagram of the high voltage divider chain, signal preamplifier and anode current measurement circuit that are located on the pixels' boards, located inside the shielding tubes. The high voltage input, applied to the cathode, is split by a voltage divider chain to the respective value for each of the dynodes (labels 'D1' through 'D10'). Dynodes D9, D10, and the anode are gauged together in order to operate the photomultiplier tube at a lower gain. The anode current is measured as the voltage drop at the  $180\text{ k}\Omega$  resistor indicated in the sketch. See text.

Details supplied by H.G. Börst, Univ. of Kiel

Inside the camera casing a frame holds the photo-multiplier tubes and their bases, packed into electromagnetic shielding tubes, in place. This is shown in Figure 4.4(b), a rear view of the interior of the CT1 camera. Inside these tubes the pre-amplifier cards for the photo-multipliers are located.

In order not to damage the photomultipliers by prolonged observations in the presence of the night sky background light, the gain has been reduced by using only eight of the ten available PM dynodes. In order to compensate for the low gain, the signals are fed into pre-amplifiers. Figure 4.5 shows a sketch of the circuits which are installed on the pixels' boards.

The HV is adjusted to the appropriate value for the respective pixel via computer control with a set of optocoupler cards. Two power supply units provide high voltage at different levels in order to apply well-matched voltages and to account for the limited range of the optocoupler cards.

The  $\mu$ -metal shield is connected to the photocathode, i.e. also to the high voltage level. The signal is extracted from the (gauged together) dynodes number 9 and 10 and the anode through a capacitor and preamplified on the board. Via a second capacitor the preamplified signal is then sent to the main electronics (c.f. Figure 4.5) by a coax cable.

The anode current is measured via the voltage drop across the  $R = 180\text{ k}\Omega$  resistor indicated in the circuit diagram. In order to avoid measuring this voltage from a high-resistance 'supply', a further amplifier with gain 'one' is implemented. Then the output voltage is fed into the coax signal cable and can be measured at the other end. In the telescope main electronics, sketched in Figure 4.6, the DC voltage is branched off and measured (see below).

The anode currents are of order  $\mu\text{A}$ . For an anode current  $I_{anode}$  of  $I_{anode} = 1\mu\text{A}$  the DC-voltage  $U_{bias}$  added to the signal is

$$\begin{aligned} U_{bias}(I_{anode} = 1\mu\text{A}) &= R \cdot I_{anode} \\ &= 180\text{k}\Omega \cdot 1\mu\text{A} \\ &= 0.18\text{V} \quad , \end{aligned} \tag{4.1}$$

which is a reasonably large voltage and can be measured with high precision. The value of  $180\text{k}\Omega$  was selected to match the dynamic range of this measurement to useful limits of the digital voltmeter.

The further processing of the analog, pre-amplified photomultiplier output signals is described in the following section.

#### 4.4 The current CT1 electronics setup

The initial electronics setup of CT1, shown in Figure 4.6, is described in detail by (Mirzoyan et al., 1994). The basic concept has been maintained whereas the hardware and software have since been updated several times. The new readout concept was finalised during the first weeks of data recording on Mkn 421 in 1999-2000. This section describes the current status; further details of the DAQ concept can be found in (Cortina et al., 1999).

##### ■ pixel readout

Instead of the original 37 pixels 127 pixels now feed their pre-amplified signals into the custom made factor-10 amplifier with dual output. One set of output signals is digitised with LE CROY 2249A charge sensitive 12 bit Q-ADC<sup>8</sup> units after an appropriate delay of 85 ns. It is the task of the data analysis to relate the resulting number of ADC channels to the number of incident photoelectrons in each pixel.

The ADC units are gated by external signals which open ('open' or 'start' signal) and close ('close' or 'stop' signal) the so-called 'gate': during the gate time the charge arriving at the input is integrated, digitised and then stored in the ADC unit. Together with the gate 'stop' a so-called 'inhibit' signal is sent out by the DAQ program, preventing any further integration on top of the value stored in the ADC-internal memory. Next the ADC counts for all pixels are read out from the units' memory chips by the DAQ computer. Thereafter the ADC memory is cleared (using a 'clear' signal) and the 'inhibit' signal is cancelled; the signals from the next neighbour trigger logic are accepted again, the cycle may continue.

##### ■ trigger logic

The start signal for the charge integration of photo-multiplier pulses, i.e. the gate 'open' signal for the Q-ADCs which is also called trigger signal, is generated by the next-neighbour-trigger

---

<sup>8</sup>Q-ADC is the abbreviation for charge sensitive (hence 'Q') analog to digital converters. They integrate over pulse shapes over a certain time, the gate time, and convert the charge under the pulse into one number, their output.

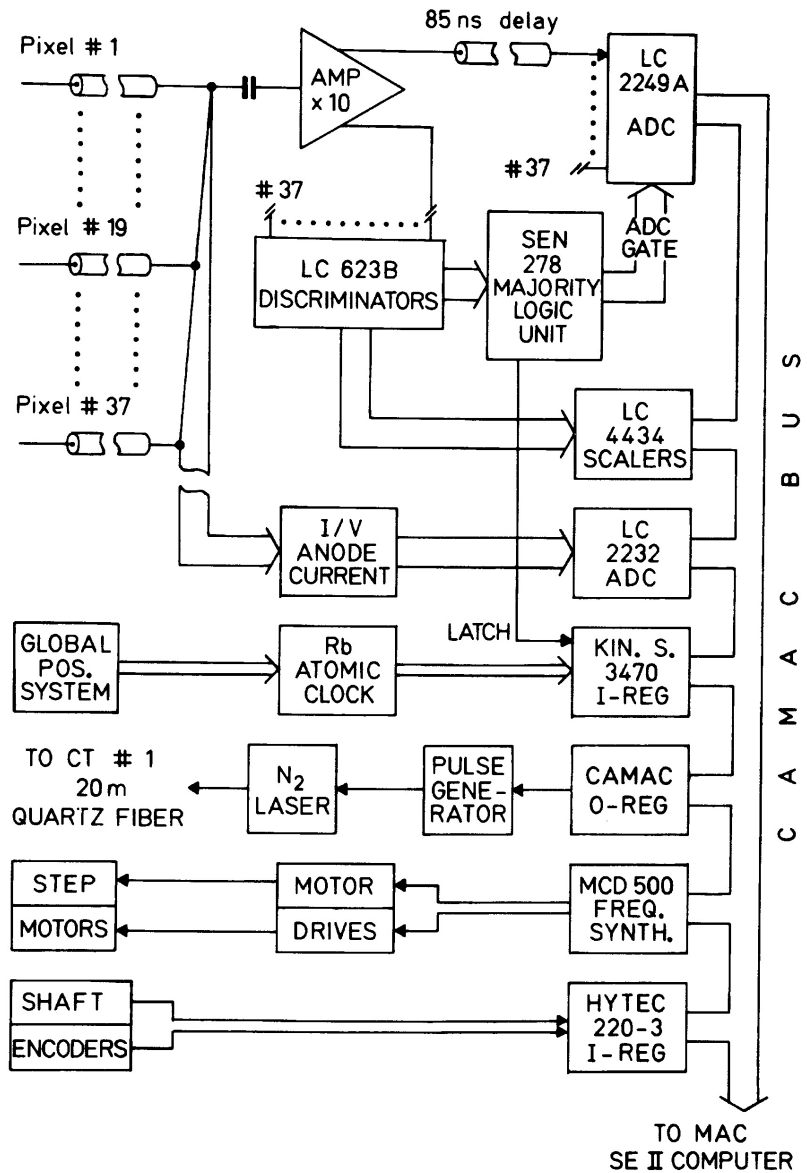


Figure 4.6: Sketch of the initial setup of the electronics system of CT1. The hardware and the software have since been updated several times. The most important improvements in the setup and the working principle are described in the text. Reproduced from [Mirzoyan et al., 1994].

unit<sup>9</sup>: whenever two neighbouring pixels out of the 127 available pixels, both within an effective time window of 6 ns width<sup>10</sup>, show peaks in their analog pulses that exceed the hardware threshold of an equivalent of 12 to 13 times the average level of a single photoelectron pulse, the corresponding event is digitised by the Q-ADCs and read out by the DAQ. This trigger scheme significantly reduces the number of night sky noise induced accidental coincidences as compared to the number of noise events that would trigger the telescope if a simple logic according to 'any two out of 127 pixels' were implemented. With LE CROY 4434 scalers the number of triggering events per pixel is counted and recorded in two minute intervals. This information is currently not put to further use except for monitoring of the camera performance.

■ high voltage and anode current measurement

Currently, the anode currents are no longer measured with the LE CROY 2232 ADC units but with two new, custom made 64 channel ADC units. Furthermore, two additional ADC units have been installed to measure the high voltage delivered by the two power supplies for the photo-multiplier tubes.

■ event time information

Time information (universal time) is read in from the GPS satellite receiver synchronised Rb atomic clock through a KINETICS SYSTEMS 3470 input register.

■ external trigger for the calibration laser

By use of a CAMAC output register a nitrogen calibration laser for flatfielding the camera pixels can be triggered externally (c.f. Section 4.7).

■ CT1 positioning

The telescope axis positions, which are read out from the shaft encoders via a HYTEC 220-3 register, are compared to the predicted source positions calculated by the DAQ computer. The tracking algorithm steers the MCD 500 frequency generation units for the two stepping motors driving the axes of CT1 (c.f. Section 4.1).

■ computer interface

The original CAMAC crate controllers used to access the electronics from a MAC II computer were replaced by two WIENER CC 16 crate controllers interfaced to a 300 MHz PENTIUM II processor with two PC16-TURBO ISA cards. The computer is running a LINUX 2.0.36 kernel. It hosts a fast event builder, slow control and user interface.

With the custom developed driver very fast access to the interrupt driven readout is possible, with a very low dead time of 0.5%. Tests have shown the DAQ system to run stable up to trigger rates of  $\mathcal{O}(70 \text{ Hz})$ . This rate is well above the highest regular raw trigger rates of around 7 Hz to 9 Hz (including noise triggers) close to zenith.

---

<sup>9</sup>In the original electronics (Figure 4.6) a simple majority logic was used. This unit generated a trigger signal whenever  $\geq 2$  out of 37 available pixel signals exceeded the level of around 20 photo electrons.

<sup>10</sup>The discriminator output pulses have a width of 8 ns. The logic requires a minimum overlap time of 2 ns, which results in the effective trigger time window of 6 ns quoted here.

## 4.5 Data recording sequence

During data recording the sequence

1. pedestal run (ca. 30 s duration),
2. laser pulser calibration run (ca. 30 s duration),
3. data run (regularly 20 min duration)

is recorded.

Whenever a trigger signal is generated when the ADC units do not have their 'inhibit' flags set, the digitisation of photo-multiplier pulses described above sets in. The string of ADC values, which are read out from the ADC units is called 'event' in the following.

## 4.6 The pedestal run

Pedestal runs consist of events recorded using an artificially produced trigger signal. Thus the ADC units integrate over 'everything except a CHERENKOV shower'. The resulting ADC signal is made up of three components:

1. a charge injected from an adjustable steady current source.  
This injected charge allows one to offset the zero-point of the ADC to a few channels. Thus it is possible to verify very small signals as well as electromagnetic pickup, resulting in 'negative' signals (see below).
2. fluctuations of night sky light; depending on the starfield, occasionally even direct starlight.
3. electronic noise stemming from within the ADC units.

The pedestal events serve to determine:

1. the zero level of the ADC channel, expressed in ADC counts, the so-called ADC pedestal level and
2. the width of the fluctuation of this zero level, the so-called pedestal RMS.

The ADC pedestals differ from pixel to pixel and are subtracted from ADC signals recorded in real events. The width of the fluctuation of the pedestal level is a measure of the amount of background light shining into the respective pixel. A strong illumination, e.g. due to an image of a bright star in the field of view, corresponds to a large value of the pedestal RMS.

In total 500 pedestal events are recorded. Examples of ADC spectra are displayed in Figure 5.2. Their general appearance allows one to identify certain hardware defects, as is described in Section 5.1.

Similar to the case of calibration events (see following section), a few cosmic ray events are collected within the pedestal data set. The process by which they are recognised and excluded by the analysis software is described in Section 5.4.

## 4.7 The calibration run

**A nitrogen UV laser 'shooting' onto a scintillator plate provides homogenous, short light flashes for a relative calibration of the photomultiplier tubes.**

Although the light flux in the individual pixels is equal, the response of different pixels varies due to component variations in

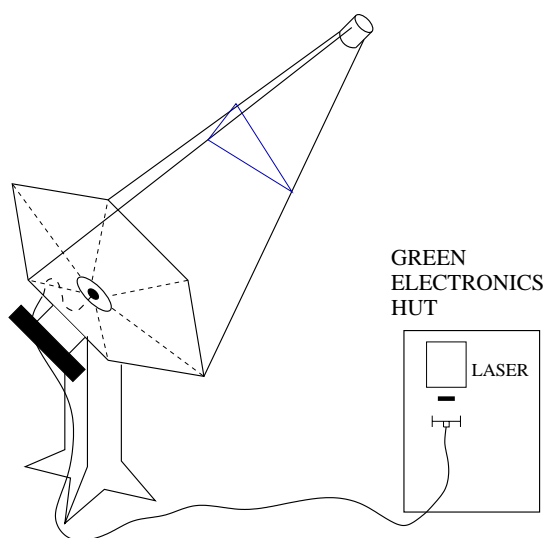
- the geometry of the WINSTON cones,
- their reflectivity,
- the photomultipliers' quantum efficiency,
- the photomultipliers' photo-electron collection efficiency and
- their gain.

The relative light response from pixel to pixel is determined and used to gauge the pixels relative to each other.

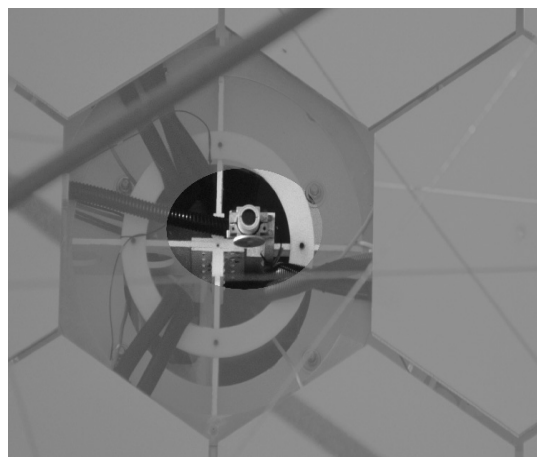
Figures 4.7(a) and (b) show the laser calibration system. A nitrogen laser in a separate casing is triggered by the DAQ system and produces UV laser pulses of roughly 15 ns duration at a wavelength of 337 nm. A quartz fibre transports the UV photons onto a scintillator plate located at the center of the mirror dish, where the central mirror is left out, as the camera would anyway cast a shadow on it (c.f. Figure 4.7(b)). The scintillator is a slab of NE 102A material with a thickness of 6 mm. The reemitted pulse spreads from 380 to 480 nm (FWHM) with a peak emission around 410 nm. A covering blue filter protects the scintillator and reduces scintillator degradation caused by intense sunlight. Figures 4.7(b) and (c) show a photograph and a sketch of the setup respectively. Typically 100 photoelectrons are generated in each pixel per laser pulse.

Calibration runs consist of 100 calibration events: the laser is triggered 100 times and the resulting images are recorded similarly to 'normal' events. Before the laser is triggered, the DAQ clears the ADC memory and cancels the inhibit signal of the ADC units. The next neighbour trigger unit is used to trigger digitisation and event readout like in the case of cosmic ray events. This complicated setup — opposed to the coupling of laser trigger and a properly delayed gate signal — is necessary, as the laser shows large fluctuations in the time between the trigger and the actual light flash.

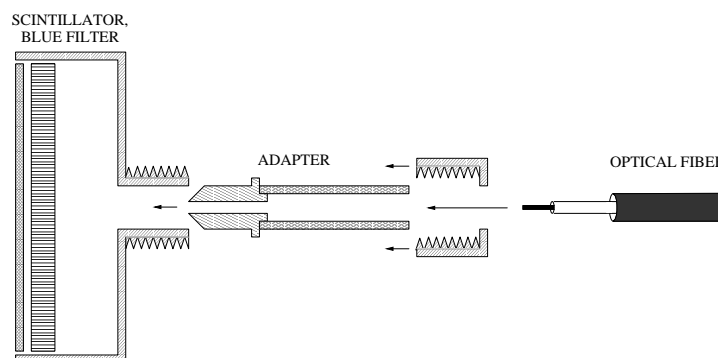
During a short time — between the cancellation of the ADC-inhibit and the actual laser flash — cosmic ray events may occur and be recorded instead of the laser pulses. Such false events occur at a rate of roughly one percent. A procedure to find and exclude them in pedestal and calibration data sets is described in Section 5.5.



(a) General sketch of the setup: the nitrogen UV-laser, triggered externally by the DAQ, is kept in a separate casing, the light is fed to the scintillator with a quartz fibre..



(b) Photograph of the calibration device, the small circular device near the center of the mirror dish.



(c) Exploded view of the installation at the center of the mirror dish: the laser light is guided to a scintillator plate and a blue filter.

Figure 4.7: The setup of the calibration system. The laser light flashes with a wavelength of 337 nm are directed onto a scintillator plate, a slab of NE 102A of 6 mm thickness. A uniform pulse is released by the scintillator with an average wavelength of around 390 nm and a duration of around 20 ns, slightly longer than the laser pulse duration of roughly 15 ns.

Source: (a) and (c): 'CT1 little online helper', Instruction manual for CT1, drawings by M. Mathys; (b): Photo: M. Kestel

## 4.8 The data run

During a data run the DAQ system carries out the following jobs:

- The telescope is steered to follow the object in the sky. The PC system time is used to calculate the respective shaft encoder positions. It is perpetually adjusted using external resources like time servers on the internet and signals from the global positioning system.
- The trigger system is initialised and thereafter runs freely, recording events as they occur, provided their trigger signals do not coincide with the time period required to readout the previous event. The readout time is, at  $\mathcal{O}(\mu s)$ , much longer than the gate time of the Q-ADCs at 30 ns. Each event carries an individual event number, a time stamp with a resolution of 200 ns according to the frequency of the Rb clock signals, further source coordinates and tracking information.

After 20 minutes data recording is stopped and a further sequence of pedestal, calibration and the next data run is initialised.

Each sequence of pedestal, calibration and data run is assigned a so-called run-number. A naming scheme is implemented that includes source names, high voltage information and the date of the recording.



## 5 The conversion of raw data to photoelectron images and the determination of image parameters

Raw data consists of a string of ADC counts per pixel, some of them containing information on a shower. This chapter describes the conversion of ADC information to photoelectron images. Before this conversion can be carried out, however, it is necessary to perform some quality checks and to correct e.g. for the limited tracking accuracy.

---

### 5.1 General quality requirements, detection of hardware defects

The conversion from ADC counts to photoelectrons is performed for each individual event and includes the following steps:

- The pedestal value of each of the ADC channels is determined.
- The NSB noise contribution, which is reflected in the RMS variation of the pedestal values of each channel, is determined.
- Electromagnetic pickup is quantified and corrected for in all steps, if possible.
- Relative calibration constants are determined for each pixel. These are used for the relative calibration of the photo-multipliers in the camera.
- The pixel signals, which are given in ADC counts, are, after pedestal subtraction, converted to photoelectrons. This yields the number of photoelectrons recorded in each pixel.
- The images are 'cleaned' by removing entries that most likely stem from NSB noise. This is done via the so-called tailcut image cleaning process.
- The image parameters of the resulting images are calculated. These so-called HILLAS parameters represent the information about showers concerning their extension in the camera and their location and orientation with respect to the telescope.

The usual data recording policy is to record data even under sub-optimal conditions. This requires mechanisms to exclude problematic data caused by bad weather, hardware problems or other incidents.

#### 5.1.1 Noise removal from the data

Hardware malfunctions relevant for data quality as well as weather reports are recorded in run books by the observers in La Palma. Data which is affected by such incidents is removed from the sample to be analysed.

In the following analysis the so-called 'filter cut' is applied at first, which is used to remove events from the data set that most likely stem from NSB noise.

The requirements that the **noise filter** must meet includes the following restrictions:

1. **Minimum Size:** The sum of all photoelectrons in the image must be larger than 60 photoelectrons. This cut selects events which are most probably real events and de-selects most of the random coincidences of two neighbouring noisy pixels.
2. **Triggering pixels in the inner camera:** At least two next neighbours out of the inner 92 pixels are required to exceed the software trigger threshold of 13 ph. el., i.e. the outermost ring of pixels is excluded from the (hardware) trigger decision. Other images are most likely truncated by the camera border and therefore rejected.
3. **Minimum number of core pixels:** At least four pixels are required to have signals which are at least three times higher than the respective pedestal RMS value. Such pixels are called 'core pixels'. Images with less than four core pixels tend to have poorly defined image parameters.
4. **Maximum number of core pixels:** Events that have more than 92 core pixels cover almost the whole camera. These events are most likely only recorded in parts and cannot be reconstructed reliably.
5. **Tracking condition:** Events, where the actual shaft encoder positions are farther than  $0.1^\circ$  away from their calculated correct values, are also excluded. Such instances have not yet been observed with the new DAQ scheme. These glitches stem from communication problems between the formerly used MAC computer and the stepping motors. This quality cut, however, is still being applied.

Figure 5.1 shows the raw trigger rates of CT1 during Mkn 421 data recording and the rates after the application of a noise filter. The data runs shown here were recorded with 'nominal' HV settings<sup>11</sup>.

The HV was increased in regular intervals in order to correct for photomultiplier tubes ageing. A stable trigger rate of around 2.5 Hz close to zenith was used as reference, calculated after the application of the filter cut. In cases where the moon was shining but the currents in the pixels allowed one to keep the HV at the nominal level, the data are said to be recorded under 'HV00'<sup>12</sup>.

The trigger rates form two bands around 3.5 Hz and around 4.5 Hz, which correspond to autumn and winter/spring, respectively. The different night sky background (NSB) noise conditions do not affect the datarates after the application of the noise filter cut. To assure good data quality, the ADC spectra of a large fraction of the pedestal, laser and run data were in addition examined for unusual shapes, which would indicate hardware defects. Data recorded at

---

<sup>11</sup>Such data is labelled 'nom' when shown in this thesis.

<sup>12</sup>Such data is labelled 'HV00', whenever it appears in this thesis.

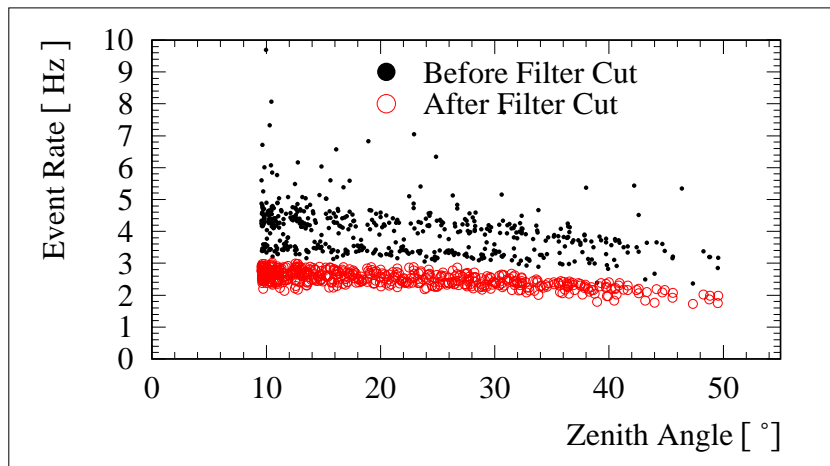


Figure 5.1: Rate before (solid markers) and after the application of the filter cut (open symbols) of the Mkn 421 data set, recorded with nominal high voltage settings. The two bands 'before filter' correspond to data taken at generally differing weather conditions in autumn (lower band) and winter, spring (upper band) respectively. Source: CT1 observations of Mkn 421 in 1999-2000 with nominal HV settings

the end of the year 1999 was particularly likely to be excluded because of spurious double-peak structures in the ADC spectra of the run data.

The data rate decreases with an increasing zenith angle as only the higher energy events then produce enough light to trigger the telescope. As the cosmic ray spectrum — which accounts for the raw trigger rate — decreases with increasing energy, fewer trigger events occur under larger zenith angles. On the other hand the trigger rate does not drop as fast as predicted from the increased threshold. Part of the losses are compensated by the increase of collection area with increased zenith angles.

### 5.1.2 Pedestal and real event analysis used to find certain hardware defects

As a prerequisite for the study and correct subtraction of the NSB light from the data, 500 pedestal events are recorded before each data run. These events also serve as testcases for channel control.

In order to find **hardware faults** in the data, several tests are performed on the raw pedestal level and RMS<sup>13</sup>:

- **Maximum average pedestal level:** The pedestal level of an individual pixel, averaged over all pedestal events in the pedestal run, is required to be lower than 50 ADC counts.
- **Limited range for the pedestal RMS:** The pedestal RMS is required to lie between 0.5 and 15 ADC counts. The lower limit is sensitive to faults such as missing connections to the pixel's signal cable, resulting in a very narrow ADC spectrum and consequently an RMS value close to zero. The upper limit is sensitive to incidents like bit errors in

<sup>13</sup>Section 5.4.3 gives the calculation scheme for the pedestal level and RMS. The quality cut described here is actually carried out by the software routine that calculates the pedestal level and RMS.

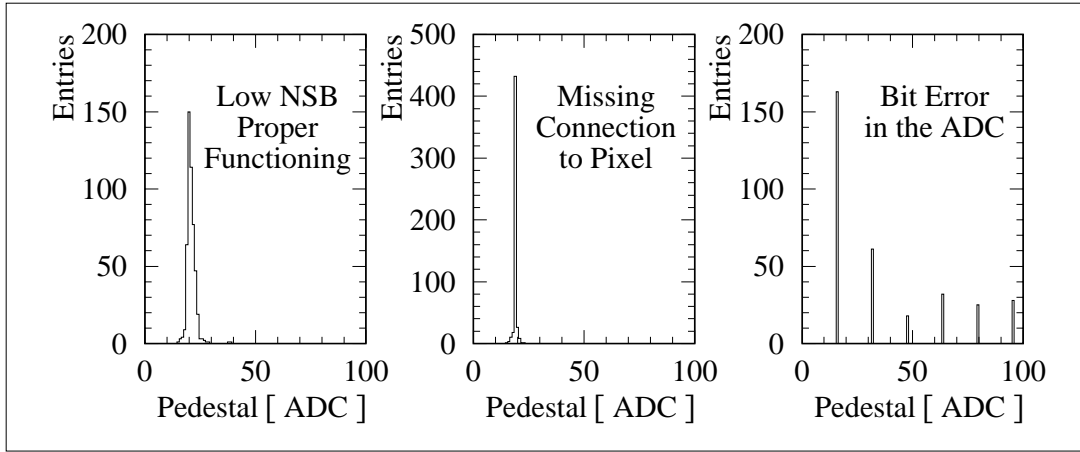


Figure 5.2: Examples of pedestal measurements of a correctly functioning pixel and two problem pixels: one of them was temporarily not connected to the ADC, the other showed a bit error in the ADC unit. These faults were detected examining the pedestal RMS values. (See text) Source: CT1 data, pedestal run 9529, pixels 54, 93, 61.

the digitisation unit of the ADC module, for instance when a certain bit is more or less always present. Examples for a correctly functioning pixel and two problematic cases are shown in Figure 5.2.

- **Similar tests on real events:** A further quality test is based on the events in data runs: the mean and the RMS of the ADC spectrum is evaluated, using the softer limits of 0.5 to 170 ADC counts for the RMS; the limit for the mean is kept the same like in the pedestal evaluation. This additional check is sensitive to several faults which do not show up in the pedestal runs. It has turned out that this second check is very valuable in terms of data quality<sup>14</sup>.

The pixels that are affected by these errors, are not considered for the calculation of image parameters in the following data run. Thus a tiny uncertainty is introduced into the calculation of image parameters. When up to five single pixels are affected, only these pixels are excluded from further analysis, while data runs with more than five problematic pixels are disregarded entirely.

## 5.2 Pixel currents as starlight indicators

Changes of atmospheric properties are a major problem for the analysis of CHERENKOV telescope data. Using the current measurement of the photomultiplier pixels, a scheme has been developed to identify data runs with lower than average and with very high currents.

The currents in individual pixels are measured like is described in Section 4.3 on page 27. Every two minutes the currents are written to a log-file, from where they are read and averaged over the duration of the data run. For all pixels, which are found to operate normally (c.f. the description of quality criteria individual pixels have to pass below), a histogram with a

<sup>14</sup>The hardware checks described here are done on a daily basis, so that any faults detected can be repaired as soon as possible. The hardware of CT1 was very reliable during the Mkn 421 observations.

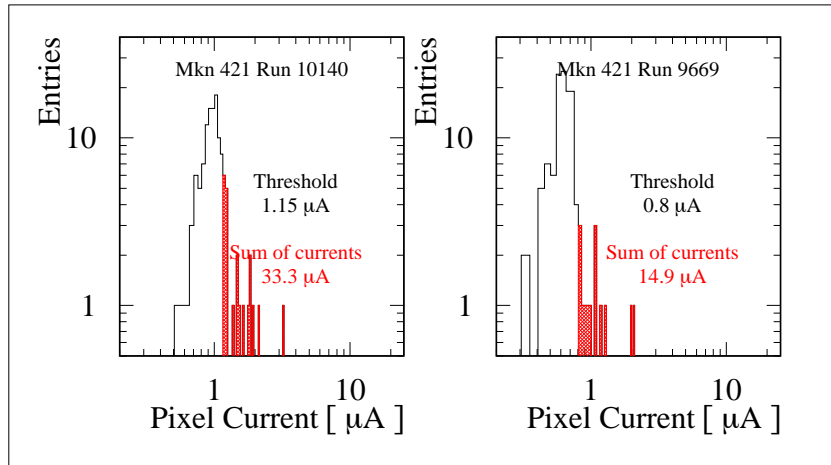


Figure 5.3: Current histograms for all pixels for two data runs. On the left-hand side the star contribution represents an average data run, whereas the data run on the right-hand side displays a generally lower current in the pixels. See text for the definition of the threshold indicated in the graphs.

Source: Mkn 421 observations CT1 1999-2000, data runs 10140 and 9669

binwidth of  $0.05 \mu\text{A}$  is filled with the pixel currents of this data run. This histogram serves to determine the threshold current, above which most probably the images of bright stars are selected in order to serve as indicators for atmospheric transmission properties. This threshold is found in a four-step procedure:

1. The gain-corrected currents of all well-operating pixels is filled in a histogram. The gain of individual pixels is determined as described in Section 5.5.
2. The peak of this histogram is searched for. If there are any two peaks of equal height, the one corresponding to the higher current is selected.
3. The average peak height from the maximum and the three neighbours to the left and to the right of the peak is calculated.
4. That current-bin above the peak is searched for, where for the first time the number of pixels with this current crosses  $1/3$  of the maximum as calculated in step 3. This pixel current is used as threshold value for the definition of the current induced by stars in the field of view (c.f. Figure 5.3).

All pixel currents above this threshold value are summed up and stored along with the run-number and other characteristics of the data run in a database.

The current histogram of the arbitrarily selected run number 10140 from Mkn 421 data from 1999-2000 is shown on the left-hand side of Figure 5.3, the hatched area indicating the starlight induced currents as determined with the procedure described above. The right-hand side of Figure 5.3 shows the same type of histogram for run number 9669. Along with the other pixels, the star-containing pixels show lower currents.

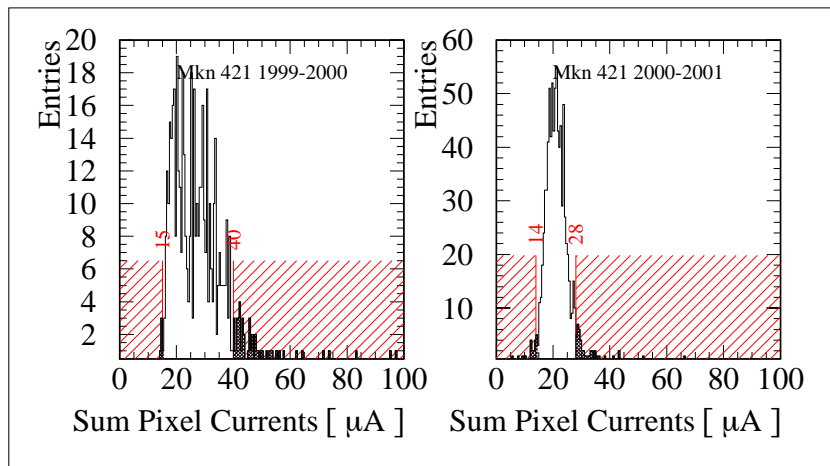


Figure 5.4: Current values from star-containing pixels for all data runs on Mkn 421 from 1999-2000 (left-hand side) and 2000-2001 (right-hand side). Data runs under the hatched areas are excluded from the analysis.

Source: Mkn 421 observations CT1 1999-2000 and 2000-2001 before the star current quality cut was carried out

The values measured with this scheme are different for different portions of the sky and therefore any cut must be defined separately for each source, data set and high voltage setting. In order to do so, the sums of star-induced pixel currents are filled into a histogram for each data set<sup>15</sup>. In a selection by hand, the lower limits for the acceptable currents are determined, de-selecting the other data runs, which are not furtherly used. As atmospheric properties are extremely important for reliable analysis results, the limits have been chosen quite 'strict'. The starlight current histograms and the limits for the Mkn 421 data sets from 1999-2000 and 2000-2001 are shown in Figure 5.4. It is to note that the high current sums in the 1999-2000 data stem from extensions of the observations into the fading dusk and the upcoming dawn. In order to maximise the amount of available data, most of these runs have been kept for the analysis, as the goal of this quality cut is mostly the identification of poor atmospheric transmission. The influence of straylight is discussed in Section 5.8.

This cut has been applied after the rate-cut described in Section 5.1.1. Runs located under the shaded areas of the histograms in Figure 5.4 have been excluded from this analysis.

### 5.3 Pointing accuracy and tracking correction

The pointing accuracy during data recording is of order  $\mathcal{O}(0.1^\circ)$ . The uncertainty stems from camera mast bending, mirror misalignments and other imperfections. The tracking algorithm basically relates the universal time (UT) and the geographical coordinates of the telescope to the celestial coordinates of a given object and determines the shaft encoder positions at each instant. Then the motors are controlled in such a way that the actual shaft encoder positions

<sup>15</sup>For Crab data from 2000-2001 the data set was split in two, as in December 2000 the camera had to be repaired and afterwards the high voltage was slightly changed. Clearly high voltage changes affect the result of the current measurements, which must be accounted for properly when carrying out such a quality cut. The histograms for Crab data from 1999-2000 and from 2000-2001 are shown in Appendix 17.2.

are as close to the correct ones as possible. The local time information is received from the global positioning system satellites and from time servers on the worldwide web. If neither of them is available, a local atomic clock time is used. A deviation of 24 sidereal seconds corresponds to a mispointing of  $0.1^\circ$ .

As both the atomic clock time and the time that is used by the tracking algorithm are recorded in two-minute intervals, the data is examined for any offset between the two. Due to the equatorial mount type of CT1 only the hour angle, corresponding to the camera's  $x$ -coordinate, is affected by timing problems. The hour angle on the sky that corresponds to the time offset is multiplied with the cosine of the source's declination. This value is then used to correct the pointing in the  $x$ -coordinate of the camera.

The main cause for mispointing is, however, usually not timing inaccuracy but the fact that the masts bend under the weight of the camera, thus permitting the camera — even though stabilised with steel ropes — to rotate<sup>16</sup> slightly about the optical axis of CT1. Camera rotation is, however, not a major problem in the observation of point sources like Mkn 421, and is therefore neglected in this analysis.

Further the hour axis of the telescope does not point exactly to the celestial pole. A correction mechanism has been developed that is based on earlier work on the pointing measurement (Petry, 1997). The following paragraphs describe the pointing measurement and the correction method.

**Using bright stars as guides, the positioning can be corrected offline to an accuracy of order  $\mathcal{O}(0.02^\circ)$ .**

The positions of stars are known very accurately and are used as a reference system. When tracking a bright star, the light collected with the big reflector leads to an enhanced current in the pixel onto which most of the starlight is reflected. As the main reflector is focussed at a distance of roughly 8 km, i.e. to the height of the maximum light production of CHERENKOV showers, the star light may be distributed over a larger area, i.e. it does not necessarily correspond to a point image. In general the pixel size is larger than the light spot of a star. The best measuring precision of the star location is achieved when the star image passes from one pixel to the next. For the determination of the mispointing the telescope is steered in a zig-zag pattern covering roughly  $0.4^\circ$  in camera coordinates to either side and the currents are recorded and evaluated.

In order to measure the pointing deviation, images of stars at several declinations and hour angles are moved over the pixels. The resulting current maps are then used to deduce the correction parameters in declination bands for each hour angle.

A sketch of the procedure and an example of a current map are shown in Figure 5.5. The red points in the left-hand plot show the image points of the star Her- $\zeta$  in camera coordinates which were tracked consecutively. At each of these points the currents of all pixels were recorded as an indication of the amount of light falling into them. The central point ( $x = 0, y = 0$ ) corresponds to the star's coordinates. The right-hand side of Figure 5.5 shows the currents

---

<sup>16</sup>The rotation angles are very small with an estimated order of  $\mathcal{O}(0.1^\circ)$ .

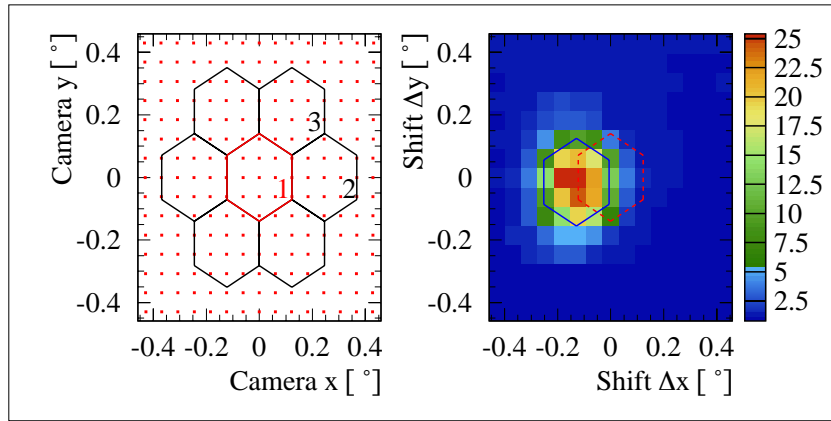


Figure 5.5: Scan points (red dots) of a pointrun on the sky, the star’s image points in camera coordinates (left-hand side) and the currents that are measured in the central pixel at these positions (right-hand side). Also indicated are the contours of the seven central pixels. The numbers 1, 2, 3 correspond to the first three pixels in the so-called ‘spiral’ numbering scheme, indicating the definitions of the camera  $x$ - and  $y$ -axis. In the right-hand plot the  $\Delta x$ - and  $\Delta y$ -axes correspond to the pointing correction shifts, which, when subtracted from the pixel coordinates in the course of the analysis, result in pointing-corrected data. The dashed, red contour corresponds to the location of the central pixel for perfect tracking. This example has been chosen to present extreme mispointing.

Source: CT1 pointrun 9963 on Her- $\zeta$

in the central pixel that were measured at these positions according to the color code (with arbitrary units) depicted on the right-hand side of the plot.

The barycenter of the current distribution is marked with a blue hexagon, indicating the central pixel’s shape. It is apparent that in this example the center of the camera, indicated by the red, dashed hexagon at  $\Delta x = 0$ ,  $\Delta y = 0$ , does not coincide with the star’s image.

Along the path of Mkn 421, i.e. in a declination band of  $30$  to  $40^\circ$ , several stars have been used to extract the mispointing characteristics of CT1 in the  $x$ - (corresponding to the right ascension, respectively to the hour angle) and the  $y$ -direction (corresponding to the declination) of the camera coordinate system. The necessary shifts for the pointing correction according to Figure 5.5 have been plotted in Figure 5.6 as a function of the hour angle<sup>17</sup>.

Ideal tracking corresponds to zero correction values  $\Delta x$  and  $\Delta y$  in both panels.

A second order polynomial has been fitted to the data points and has been added in the plots. The deviations of the measured points from the fitted polynomial are indicated by the red boxes along the ideal-tracking line at  $\Delta x = 0$  and  $\Delta y = 0$ , respectively.

Before the image parameters are calculated (c.f. Section 5.7) the geometrical center of the camera is shifted using the average hour angle per data run and the parametrisation as of Figure 5.6.

A conservative estimate of the pointing accuracy after correction is that it is better than  $0.01^\circ$  in both the camera  $x$ - and the camera  $y$ -axis separately. The value of  $0.01^\circ$  corresponds to the pointing accuracy on the sky for the declination axis, while the pointing accuracy in the

<sup>17</sup>The pointruns used were taken after Nov. 1st; data recording on Mkn 421 started on Nov. 4. 1999.

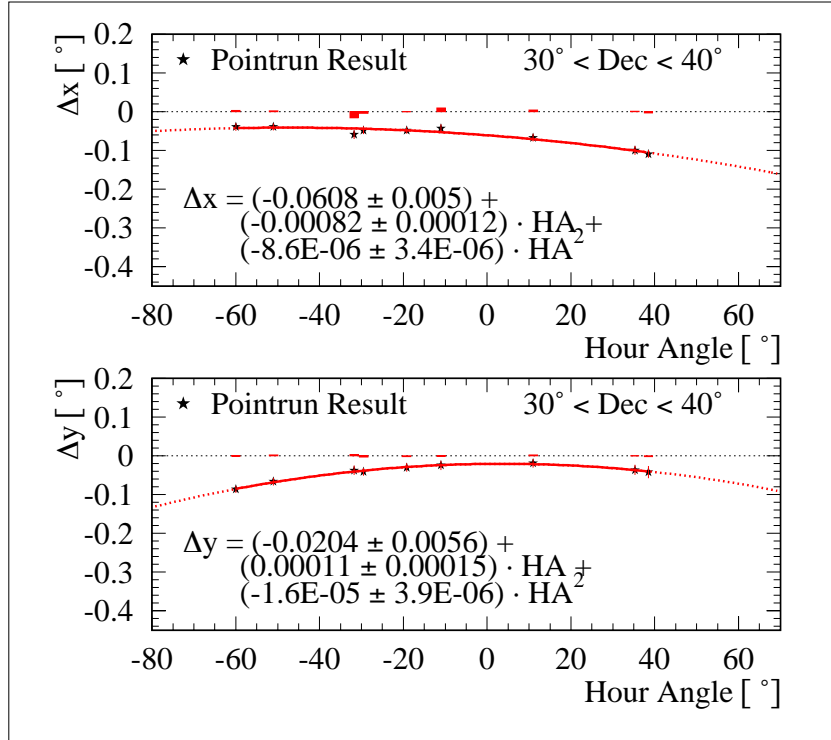


Figure 5.6: Pointing Correction Shifts in the camera- $x$  and the camera- $y$  axis for declinations between 30 and 40° (red curves); Mkn 421 has a declination of 38° : 12' : 36" (J2000). The differences after correction between the fitted polynomial ('HA' denotes hour angle) and the single pointrun results is indicated by the red boxes along the zero lines. The global offset of the pointing to the ideal lines at  $\Delta x = 0$  and  $\Delta y = 0$  could be corrected by a change of the zero positions of the shaft encoders, c.f. Section 4.1 on page 26.

Source: CT1 Pointruns with Declinations of 30 to 40° recorded after Nov. 1 1999.

hour axis is  $0.01^\circ / \cos(DEC)$  for a source with a declination value  $DEC$ . This corresponds to a combined pointing accuracy  $\Delta_{pointing}$  for sources with a declination similar to that of Mkn 421 ( $DEC \approx 38.2^\circ$ ) of

$$\Delta_{pointing}(DEC = 38.2^\circ, \text{Sky}) = \sqrt{(0.01^\circ)^2 + (0.01^\circ / \cos(38.2^\circ))^2} = 0.016^\circ \quad (5.1)$$

on the sky and

$$\Delta_{pointing}(30^\circ < DEC < 40^\circ, \text{Camera}) = 0.014^\circ \quad (5.2)$$

in the camera. After the pointing correction the uncertainty introduced by the pixelation of the CT1 camera is much larger than that of pointing uncertainties.

## 5.4 Determination of ADC pedestal level and RMS

The ADC units of the CT1 telescope measure the charge that is collected in the photomultiplier pixels during a gate time of 30 ns. The pedestal level in each individual channel fluctuates from event to event. Reasons for the fluctuations are:

- **Electronic noise**, which has a width of typically one ADC channel.
- **Fluctuations of the night sky background** (see below). The dark night sky areas show fluctuations of around two to three ADC channels with POISSONIAN characteristics. In cases where a bright star is projected onto a pixel or measurements are carried out in the presence of (weak) straylight, the background light level can be quite high, resulting in a wide distribution of pedestal values (c.f. Figures 5.7 and 5.8).
- **Pickup of external electronic sources**, in our case mostly of the switching of the stepping motors or of radio transmitters close to the observation site. Most of these signals have been strongly suppressed, but some pickup is present in data presented here. Pickup is rare, unpredictable, in first order symmetric around the baseline and almost equal in all channels. The pickup distribution is normally non-GAUSSIAN. The values of the pickup can be high and, if not corrected for, result in completely wrong or strongly biased image parameters.

The actual pedestal distribution is a mixture of the contributing distributions listed above. It should be noted that in the case of a dominant POISSONIAN contribution the mean pedestal values are not equal to the peaks of the distributions.

### 5.4.1 Influence of starlight on the width of ADC pedestal spectra

The influence of starlight on the width of ADC spectra recorded in pedestal runs is demonstrated in Figures 5.7 and 5.8 for pixel 1 and the arbitrarily selected pixel number 14 (spiral numbering). 500 events were recorded with closed camera (Figure 5.7) and during tracking of

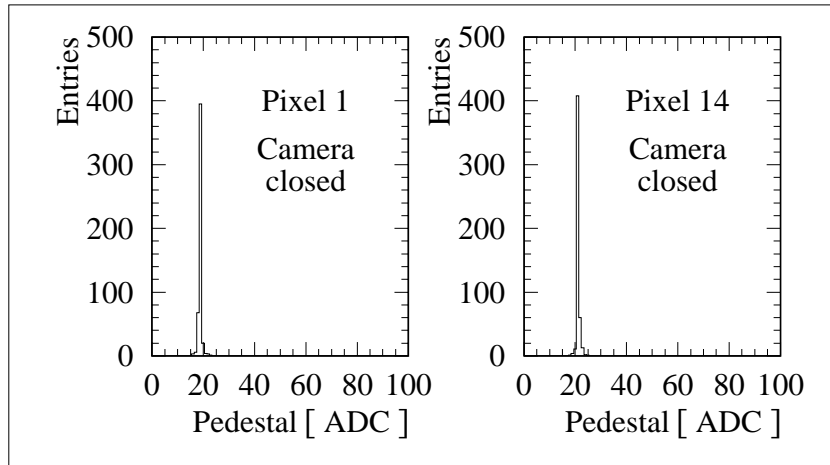


Figure 5.7: ADC pedestal spectra of pixels 1 and 14 (spiral numbering), recorded with closed camera. No pickup correction was applied to the data displayed in this plot. 500 events were recorded, with triggering produced artificially by the DAQ system.

Source: CT1 data, pedestal run 8181, pixels 1, 14.

Mkn 421. While pixel 14 corresponds to a rather dark sky region, pixel 1 collects the light from the bright foreground stars close to the Mkn 421 position, c.f. Figure 2.2.2 on page 12. The fluctuations of the ADC pedestal values increase with an increase of the light level collected in a given pixel. The RMS information is used to help determine which pixels' signals are to be combined to images of extended air showers. This procedure is described in Section 5.7.

#### 5.4.2 Excluding cosmic ray events from the pedestal sample

Some CHERENKOV showers trigger readout during the pedestal runs and may prevent the correct determination of pedestal level and RMS. Therefore the pedestal runs are examined for such events and any such events found are excluded. The check that is performed on each pixel in order to discover such spurious events, consists of the following steps:

1. Find the pedestal value  $ADC_{max}$  with most entries (e.g.  $ADC_{max} = 22$  for pixel 14 in Figure 5.8).
2. Pixels are allowed to have pedestal values in the range  $[ADC_{max} - 15; ADC_{max} + 15]$ .
3. For each event, the number of pixels that fulfill requirement (2) is determined.

Whenever more than five pixels show values outside the allowed range, the event is considered of cosmic origin and is not used for the pedestal calculation. Roughly 2% of the pedestal events are disregarded. It is required that at least 100 genuine pedestal events are contained in the pedestal file (with 500 recorded events), else a different input file is used. During the first two weeks of data recording with the new DAQ system only few real pedestal events were recorded per pedestal run. In order to nevertheless permit the data to be used, several pedestal runs of Mkn 421 were merged until around 250 useful, genuine pedestal events were available. This seems an appropriate solution, which has since also been used on calibration files suffering from the same problem.

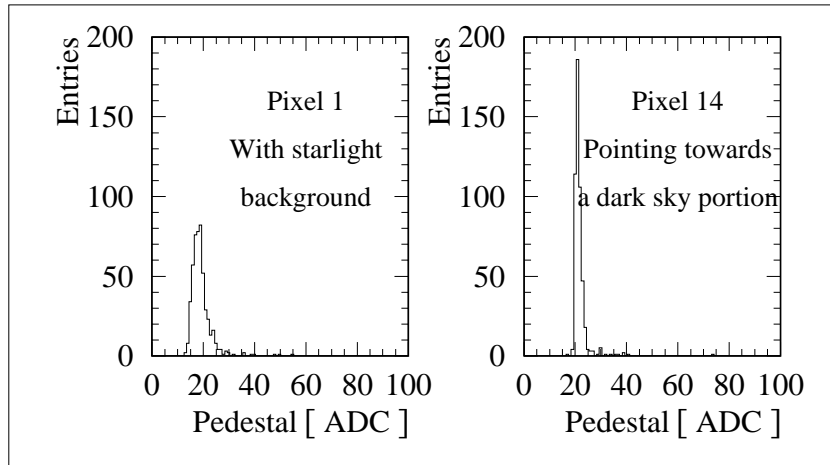


Figure 5.8: ADC pedestal spectra of pixels 1 and 14 (spiral numbering), recorded with open camera while tracking Mkn 421. No pickup correction was applied for this plot. The spectra were recorded immediately before the ones shown in Figure 5.7. A tiny fraction of the 500 events shown here was triggered by real events. These events appear as higher ADC values in this plot. The treatment of this cosmic ray event pollution is described in the text. Source: CT1 data, pedestal run 8180, pixels 1, 14.

### 5.4.3 Removing electromagnetic pickup from pedestal events

High frequency electromagnetic signals, mostly originating from the stepping motors, are picked up by all pixels simultaneously at almost the same level<sup>18</sup>. This pickup can be quite high for individual images and can, if not corrected for, make the correct determination of pedestal level and RMS, as well as that of calibration constants and the image parameters impossible. Simple and effective correction methods have been introduced for the different event types. A method for pedestal correction is described in the following.

The pedestal level and RMS of each individual pixel are determined after standardising the data with respect to a global mean over all pixels and all genuine pedestal events. In other words, the average pedestal level per image is the reference value in relation to which the pedestal mean level and the width of the pedestal distribution of each individual pixel is determined.

The following definitions are used in the following:

- $i$ : index letter, numbering the pixels from 1 to the number of active pixels in the camera  $N_{pix}$ , currently 127.
- $j$ : index letter, numbering the events from 1 to the number of available pedestal events  $N_{ev}$  in the file.
- $p_i^j$ : a pedestal signal recorded from pixel number  $i$  during event number  $j$ .

The procedure which is carried out before the relative calibration includes the following steps:

<sup>18</sup>Coherent pickup was especially strong during the 1997 flare of Mkn 501. The correction methods explained here have been applied to this data and have proven to be very useful. At present coherent pickup effects are hardly recognisable, the correction method, however, is still applied.

1. For each pedestal event the arithmetic mean  $\overline{p^j}$  over all available pixels is calculated:

$$\overline{p^j} := \frac{\sum_i p_i^j}{N_{pix}} \quad (5.3)$$

2. The global ADC pedestal mean  $\overline{P}$  is calculated over all  $N_{ev}$  non-cosmic events and all  $N_{pix}$  pixels that were not excluded due to missed quality criteria:

$$\overline{P} = \frac{\sum_j \overline{p^j}}{N_{ev}} = \frac{\sum_{ij} p_i^j}{N_{ev} \cdot N_{pix}} \quad (5.4)$$

3. For each event and for each pixel the difference  $d_i^j$  between the active pixel's ADC value  $p_i^j$  and the event mean  $\overline{p^j}$  is calculated:

$$d_i^j := p_i^j - \overline{p^j} \quad (5.5)$$

4. For each pixel  $i$  the mean difference  $\overline{d_i}$  between the pixel's ADC values and the different events' mean values is calculated:

$$\overline{d_i} = \frac{\sum_j d_i^j}{N_{ev}} \quad (5.6)$$

5. For each pixel the RMS of the deviation of the pixel's signal from the event mean is then calculated relative to this particular pixel's mean value ( $\overline{d_i}$ , as calculated in step 4):

$$\sigma_i^2 = \sqrt{\frac{\sum_j (d_i^j - \overline{d_i})^2}{N_{ev}}} \quad (5.7)$$

This corresponds to the pickup-corrected pedestal RMS value.

6. Finally, the pedestal level per pixel is calculated by adding the mean difference  $\overline{d_i}$  of step 4 to the overall mean over all pixels and all events as calculated in step 2:

$$\overline{p_i} = \overline{P} + \overline{d_i} = \frac{1}{N_{ev}} \cdot \sum_j p_i^j \quad (5.8)$$

This is equal to the simple average over all signals from available events in pixel number  $i$ .

The determination of pickup corrected values needed for the relative calibration (see the following section) proceeds along the same lines.

As mentioned above (c.f. Section 5.1.2, Figure 5.2), a given pixel is excluded from further analysis, i.e. its content is no longer taken into account, in the following instances:

- The mean pedestal level exceeds 50 ADC counts.
- The pedestal RMS does not lie within the limits of 0.5 to 15 ADC counts.

The upper limit on the mean pedestal level is sensitive to the type of error shown on the right-hand side of Figure 5.2: the bit error in the ADC channel fakes a huge average value. Secondly, the limitation placed on the pedestal RMS values is sensitive to hardware faults like a missing connection between the pixel and the ADC unit, an error which results in a very narrow ADC spectrum.

The mean pedestal levels for the individual pixels, their average over the whole camera, and the pickup-corrected RMS values are used in the subsequent analysis.

## 5.5 Relative PM gain calibration (Flatfielding)

The pixels are operated at individually adjusted high voltage levels to account for the different gains of the individual photo-multiplier tubes (c.f. Section 4.3). It is necessary to measure the response of the individual photo-multiplier tubes to a preset light flux in order to adjust the gains such that the overall pixel response is close to 'flat'. From time to time the individual pixels' high voltage values are adjusted close to a 'flat' response across the camera. As short- and long-term drifts of the gains occur, the individual photo-multiplier gains are measured in the data taking cycle (c.f. Section 4.7): the camera is illuminated uniformly by a light flash and the resulting photo-multiplier signals are measured. The images collected in this way are cleaned from cosmic ray triggers and corrected for pickup. The result serves to apply a software correction such that for uniform light flux the corrected ADC contents are equal and to calculate a gain-corrected pixel current for the data quality cut described in Section 5.2. An absolute calibration is not possible, as the total light output from the laser is not measured.

### **Accidental cosmic ray events are detected in a way similar to the pedestal case.**

The images in the camera are examined to determine whether they are triggered by laser pulser light flashes rather than from cosmic ray events.

- The most probable ADC value is calculated for each pixel for all events in the calibration run.
- The recorded values of up to ten pixels per event are allowed to lie outside a range of  $\pm 200$  ADC counts below or above the most probable value of the respective pixel. Else this particular event is not considered further.

These limits are relaxed compared to the pedestal case, for in a standard cosmic ray event only few pixels display non-pedestal signals, while in any calibration event the correctly functioning pixels have entries well above the pedestal level. Moreover the light pulser has some intrinsic amplitude jitter over a typical calibration run. In order for a calibration run to be accepted for the analysis, a minimum of 50 out of the available 100 calibration events are required.

As with the pedestal runs, cases in which too few useful events have been recorded in the first few calibration files with the new DAQ program were corrected for by merging several calibration files for the same source within one or two consecutive observation nights.

In order to remove the influence of electromagnetic pickup from the calibration events, the mean over all pixel signals from all events serves as a reference value for the determination of pickup-corrected values. The mean of the laser response and the RMS estimates are determined with respect to this reference value. This does not change the mean and the relative gains, but does influence the determination of the RMS scatter of the laser response in the individual pixels, which is used to determine the adjusted conversion factors from ADC counts to photoelectrons, as is described in Section 5.6.1.

## 5.6 Conversion of ADC counts to photoelectron content

As a result of the analysis steps performed so far, the images are represented in ADC units. This section first describes the conversion of ADC counts to photoelectrons and then goes on to describe a correction mechanism, which removes coherent electromagnetic pickup. This correction method is similar to the pickup correction procedure applied to the pedestal and calibration data.

### 5.6.1 The conversion of ADC counts to photoelectrons

The average conversion factor  $\langle\chi\rangle$  between the number of photoelectrons (abbreviated 'ph. el.')

 and ADC counts (abbreviated 'ADC ct' in the following) for the CT1 camera was measured in 1995 (Mirzoyan et al., 1995). The result for the averaged conversion factor was:

$$\langle\chi\rangle = 0.72_{-0.07}^{+0.08} \frac{\text{ph. el.}}{\text{ADC ct}} \quad . \quad (5.9)$$

This number was measured directly by inserting a gain 10 amplifier in individual channels and then triggering on single photoelectron 'events' induced by a very low light level LED pulser.

The photo-multiplier tubes have been exposed to light for years, partly under full moon, resulting in gain reduction (called 'ageing'). The HV level has been increased in regular intervals in order to compensate for this ageing effect. For this reason it is to be expected that the conversion factors have changed.

In an attempt to deduce the conversion factors for later data sets (i.e. after 1995), one can exploit a relation between the so-called excess noise factor  $F$ , the average signal heights  $\langle Q_i \rangle$  and the RMS scatter  $\sigma^2(Q_i)$  recorded in calibration runs to estimate individual conversion factors  $\chi_i$  (pixel number  $i$ ) as (Mirzoyan and Lorenz, 1998):

$$\chi_i = \frac{m_i}{\langle Q_i \rangle} = \frac{F_i^2 \cdot \langle Q_i \rangle}{\sigma^2(Q_i)} \quad , \quad (5.10)$$

where

- $i$  is an index to identify quantities related to pixel number  $i$ ,
- $Q_i$  is the charge corresponding to  $m_i$  photoelectrons with an average value of  $\langle Q_i \rangle$  and a variance of  $\sigma^2(Q_i)$ .

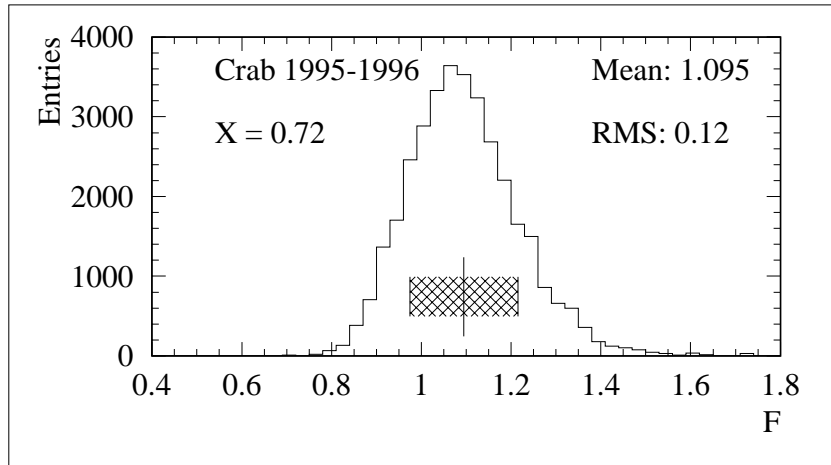


Figure 5.9: Excess noise factor  $F$  calculated according to Equation (5.10) for the 1995 data set of Crab. As input the directly measured average conversion factor of  $\langle\chi\rangle = 0.72$  ph.el./ADC ct was used. The resulting excess noise factor of  $\langle F\rangle = 1.095$  was used to determine the conversion factors for other data sets.

Source: CT1 Crab observations 1995-1996, nominal HV, approx. 100 h

$F_i$  is called the excess noise factor<sup>19</sup> and is a measure of the quality of the PM.

Typical values are  $F \approx 1.15$ , while better tubes have smaller values.  $F$  does not change with time.

Using Equation (5.10) it is possible to relate the measured values of  $\langle\chi\rangle$  from 1995 to the most probable values of  $\langle\chi\rangle$  to be used in the present analysis.

In a first step an average excess noise factor  $\langle F\rangle$  is determined, which in a second step serves to determine an average conversion factor for the present recording sequence, again using Equation (5.10).

In order to determine an average excess noise factor  $\langle F\rangle$  from the direct measurement (Mirzoyan et al., 1995) of the conversion factor  $\langle\chi\rangle$ , Equation (5.10) has been resolved for  $F$  and plotted for laser runs taken during Crab observations in period 1995-1996, using as input an average value of the conversion factor of  $\langle\chi\rangle = 0.72$  ph.el./ADC ct. The resulting average excess noise factor of  $\langle F\rangle = 1.095$  has been used to estimate the conversion factor  $\langle\chi\rangle$  for the analysis of datasets recorded in different years. Figures 5.9 and 5.10 represent the conversion factors to be used for the data recorded in 1999-2000, i.e the Mkn 421 data in question here, as well as for data recorded in 2000-2001.

A short systematic study, which is presented in Chapter 8, has been performed on Crab data from 1999-2000 in order to estimate the influence of the conversion factor uncertainty on the flux and spectrum determination.

### 5.6.2 Correcting individual events for coherent electromagnetic pickup

In  $\gamma$ -like images, only few pixels record the signals from an extended air shower. The spectrum of photoelectron contents drawn from all pixels should be dominated by pedestal-like data and

<sup>19</sup> $F$  denotes the increase of the statistical fluctuation of  $n$  photo electrons compared to  $\sqrt{n}$ .

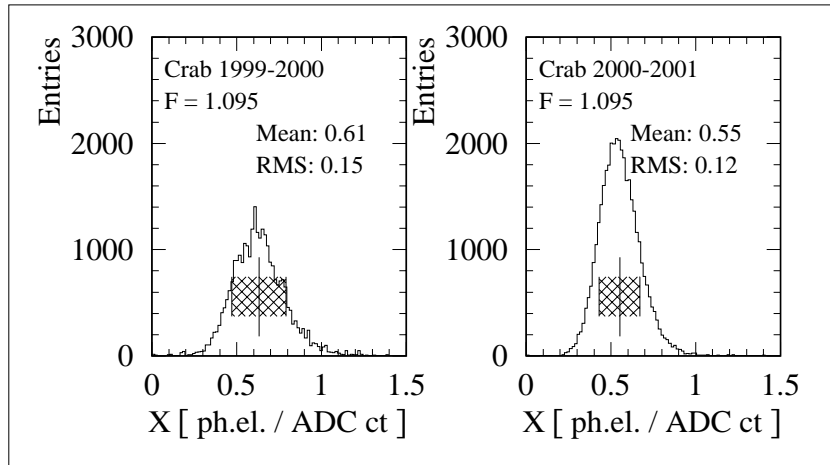


Figure 5.10: Distribution of conversion factors calculated with the method according to Equation (5.10) for the 1999-2000 and 2000-2001 data sets of Crab. As input the average excess noise factor of  $\langle F \rangle = 1.095$  was used (see Figure 5.9).

Source: CT1 Crab observations 1999-2000, nominal HV, approx. 72 h, CT1 Crab observations 2000-2001, nominal HV, approx. 100 h

should peak close to zero. In the event of coherent pickup the whole signal distribution is shifted, including the zero-peak.

An example of such an event with negative electromagnetic pickup contribution is shown in Figure 5.11. The left-hand plot shows the image in the camera, the color scale to the right indicates the number of photoelectrons that were recorded. The right-hand plot shows the photoelectron spectrum of this image. If no pickup were present, the peak of this (photoelectron) distribution should be located at zero, corresponding to the fact that no CHERENKOV light falls into most of the pixels (and the pedestal has already been subtracted)<sup>20</sup>. The signals in most of the pixels should then lie around zero, with small fluctuations due to the stochastic nature of the NSB light and electronic noise.

In Figure 5.12 the same event is shown after the application of a correction: all pixel signals have been changed such that the peak in the photoelectron spectrum now occurs at zero ph.el. .

In the case of events that involve many pixels, i.e. events where the spectrum peak no longer coincides with the zero light level, a shift according to the method described above must not be carried out, as it would involve the unjustified neglect of small pixel contents, thereby shifting the light content of the whole event to unreasonably small values. Therefore the pickup correction is only applied to events where the total number of recorded photoelectrons does not exceed 100. Individual events with more than 100 photo electrons may still be affected by coherent pickup, but this effect is unquantifiable and cannot be corrected for.

Figure 5.13 shows the distribution of corrections that were applied to a data run (left-hand plot) and the distribution of FWHM values of the zero peaks of the pickup corrected images (right-hand plot). The gap in the left-hand plot, corresponding to small corrections, is due to the fact that shifts smaller than 0.8 times the average pedestal RMS value are not carried out.

<sup>20</sup>In the case of a POISSONIAN background light distribution the peak is slightly below zero, but for our procedure we will neglect this effect.

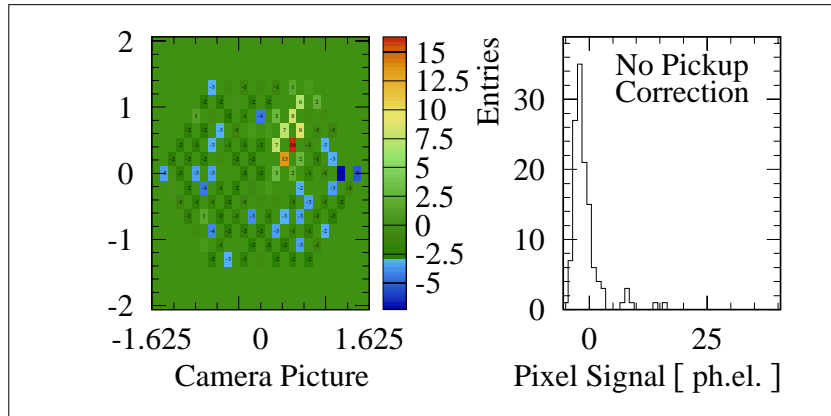


Figure 5.11: photoelectron image of an event showing electromagnetic pickup. The ph.el. spectrum should peak close to zero, corresponding to the fact that the image is small and most of the camera does not record any light from the event. Pixel 62, displaying the lowest entry, suffers from a hardware problem and is ignored in the calculation of the pickup correction. Source: CT1 data run 7472 (Mkn 421), Event 5 (after Filter)

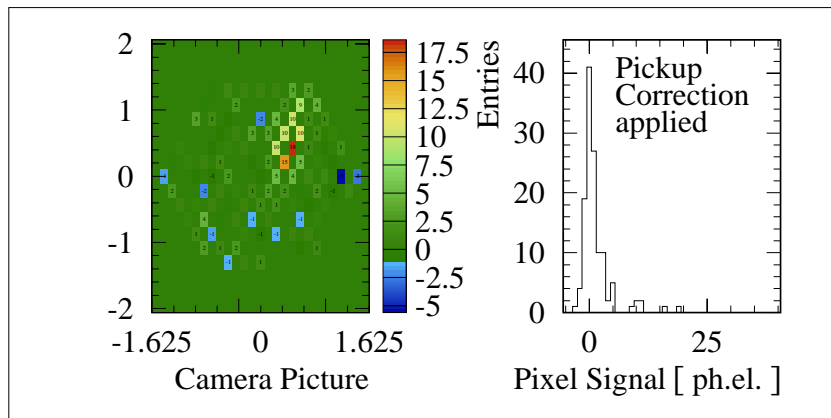


Figure 5.12: photoelectron image of the same event as shown in Figure 5.11 after electromagnetic pickup correction. The correction is achieved by shifting all signals until the maximum of the spectrum is located at zero. Source: CT1 data run 7472 (Mkn 421), Event 5 (after Filter)

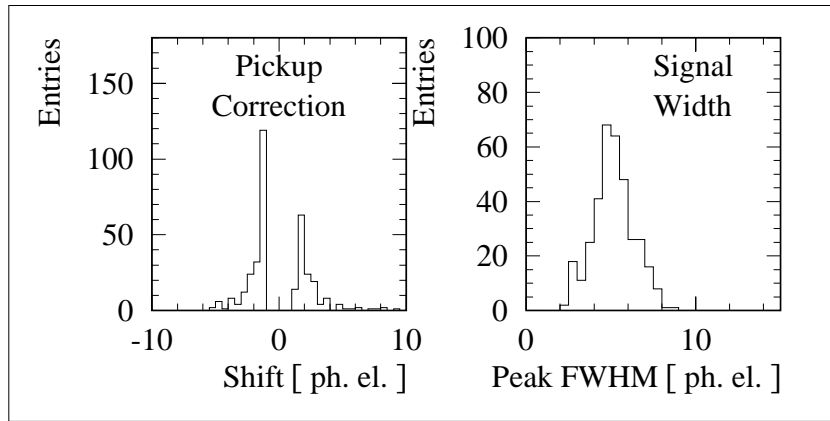


Figure 5.13: Pickup correction shifts for a data run and the corresponding distribution of FWHM of the signal peaks in the images. Shifts below 0.8 times the average pedestal RMS, i.e. here around 1 ph.el. were not applied.

Source: CT1 data run 7472 (Mkn 421)

The number of pickup corrected events and the size of the required shifts represent the typical values found in data sets recorded in the same period as the Mkn 421 dataset of 1999-2000<sup>21</sup>.

## 5.7 Image parameter determination and image cleaning

In the case of CT1 a total of 127 channels are recorded per event, some of them carrying information on the shower and most of them displaying fluctuations around their pedestal that are ruled by the nightsky noise.

Because  $\gamma$ -rays are extremely rare compared to the charged cosmic ray flux in the CT1 energy range, only few recorded events stem from  $\gamma$ s, as the trigger does not distinguish significantly between  $\gamma$  and hadron showers of equal light intensity. It is therefore necessary to implement an algorithm that allows one to efficiently separate the two fractions, i.e. that rejects the hadron candidates and at the same time retains as many as possible of the  $\gamma$ -candidates.

The most successful approach that has so far been developed classifies the images according to their shape, their location in the camera, their orientation and the amount of light they contain. The overall appearance of  $\gamma$ -showers and hadron showers is different; Monte Carlo studies have shown that the  $\gamma$ -images tend to be concentrated in few pixels, c.f. the following section and Appendix 16. Further the telescope geometry means that images of events stemming from a source at the center of the camera are oriented with their main axes located radially about the camera center. These general differences are exploited for  $\gamma$ -hadron separation, as described in Chapter 6. The following section introduces the ideas of image cleaning before the image parameter definitions are briefly reviewed.

<sup>21</sup>The largest correction shifts have been necessary for the analysis of Mkn 501 data from 1997.

### 5.7.1 Image cleaning

It was mentioned above (see Section 5.4) that the nightsky noise level varies from pixel to pixel. For a given pixel, the level around which a signal entry can be significantly distinguished from fluctuation is determined by the noise level.

In the CT1 analysis pixel signals are used if they exceed 2.5 times respectively three times the pedestal RMS level. The pixels that are used to determine the image parameters for a given image are selected in a three step procedure:

1. Find all pixels that have a signal exceeding three times the pedestal RMS that is measured in this pixel. Such pixels are called 'core pixels'.
2. Find all next neighbours of the core pixels that have a signal exceeding 2.5 times the corresponding pedestal RMS of this pixel.
3. Set all the other pixel signals to zero.

If less than four neighbouring core pixels are found, the event is discerned<sup>22</sup>.

The steps one through three make up the so-called 'dynamic tail-cut image cleaning', as the lower limit for pixel entries varies with the noise level in this pixel. This cleaning procedure is applied in the analysis of all CT1 data shown in this thesis.

In approaches other than the CT1 analysis, images are cleaned from NSB noise by discarding signals below a certain, constant level, e.g. signals below 6 photoelectrons or signals below 4 photoelectrons in the presence of a neighbouring pixel with a signal of 6 or more photoelectrons (see e.g. (Daum et al., 1997)) in the case of the HEGRA CT SYSTEM analysis. The major drawback of such a static cleaning process is the fact that useful information may be neglected: in dark sky regions the noise level in pixels is so low that signals below 6 (or 4) photoelectrons can be clearly distinguished from noise and can therefore be used in the analysis. A larger difficulty obviously arises when high noise is present in a given pixel but the static limits are used; then the noise may not be filtered correctly.

Another approach would be to determine the image characteristics by fitting the image to the shape of the light distribution. Then the pedestal RMS could serve as a measure of the error in a pixel signal and a suitable fitting algorithm would account for the noise without the need to disregard any information. Such fitting routines are used in the analysis of data from the CAT telescope after application of a constant tail cleaning cut (Le Bohec et al., 1998). For CT1, however, all such attempts have failed so far, as the coarse pixelation of the CT1 camera as well as the limited camera size, which leads to frequent truncation of images, pose major problems for any fit.

---

<sup>22</sup>The requirement of a minimum number of core pixels is part of the noise filter cut (c.f. Section 5.1.1 on page 39), which is applied before any physics investigation is carried out.

In the unlikely event that two separate cores are found in one image, the subsequent image parameter determination may fail, i.e. it may determine wrong values.

## 5.7.2 Image parameter definitions

The image parameter approach was introduced by HILLAS (Hillas, 1985), in honour of whom these parameters are called 'HILLAS parameters'. Detailed description of these parameters are to be found in the literature; a recent detailed review is given in (Kranich, 2001). For this reason this section will only give a brief description of their definitions — except for the newly defined '*Leakage*' and '*Asymmetry*' parameter — and of their use in the current CT1 data analysis. Raw distributions for hadrons from off-data and from simulated  $\gamma$ -rays for the 'classical' image parameters are shown in Appendix 15.

- ***Dist***: The distance between the barycenter of the image and the image point of the source in the camera is called '*Dist*' and is measured in units of degrees in camera coordinates. Depending on the height of the shower maximum in the atmosphere and on the distance between the impact point of the primary on the ground and the telescope, the barycenter of the image shall be more or less close to the center of the camera.

The largest recorded distance is close to the radius of the camera, i.e. close to  $1.5^\circ$  in the case of CT1.

The distance distribution shows an increase up to roughly  $1.0^\circ$  and a fast decline at larger values. Because of the limited camera diameter it is likely that large *Dist* values correspond to a truncation of images<sup>23</sup>.

- ***Size***: The total amount of light that is measured in the camera is called '*Size*' of the image and is expressed in photoelectrons. It is closely related to the energy of the primary (c.f. Figure 16.6 on page 165).

In general the *Size* of a given event is smaller at larger zenith angles (due to the larger airmass that needs to be traversed) and when the atmospheric transmission is worse.

The primary's impact parameter also influences the event's *Size*: at a given energy level the events with larger impact parameters usually have smaller *Size* values.

- ***Conc***: It has been found that the extension of  $\gamma$ -images in the camera is generally smaller than that of hadronic images. Therefore a valuable quantity is the parameter called '*Conc*', defined as the ratio of the sum of the two highest pixel signals to the *Size* of the image, quantifying the 'concentration' of the image.

For  $\gamma$ s the *Conc* value is weakly dependent on the event's energy respectively *Size*.

- ***Width, Length***: '*Width*' and '*Length*' reflect the shape of shower images. They are defined as the RMS of the light distribution along the major image axis (*Length*) and orthogonal to it (*Width*). *Width* and *Length* are powerful quantities to separate  $\gamma$ s and hadrons. This fact can be seen e.g. in Figures 5.21 and 5.22 in Section 5.8.3.

- ***Alpha***: The image parameter with the highest separation power for point sources is the orientation angle '*Alpha*'. Showers, whose axes are co-planar with the the telescope's

---

<sup>23</sup>Truncated images can be partly 'repaired' using the *Leakage* parameter as is discussed below and e.g. in Sections 7.2 or 7.3, where the *Leakage* parameter is used in a corrective manner.

optical axis, produce an image that points towards the center of the camera, which is the image point of the source. Any shower with a main shower axis that is warped with respect to the telescope's optical axis will have a significant *Alpha* value.

See Figures 5.14 and 5.15 for the geometrical meaning of the image parameters *Width*, *Length*, *Dist* and *Alpha*.

- **Leakage**<sup>24</sup>: It was noted above that the small size of the CT1 camera frequently results in truncation of shower images at the camera border. The fraction of the image content that is likely to be truncated (i.e. not recorded) is estimated as the ratio of the sum of pixel values next to the camera border divided by the Size of the image in question.

The values of the dimensionless parameter *Leakage* are thus defined to lie between zero (when the complete image of the shower is contained within the camera) and one (the image consists of pixels from the outermost ring only); the latter is more or less hypothetical, as such images, even if triggering the telescope, shall be cut by the noise filter cut (c.f. Section 5.1.1).

The distributions of the *Leakage* parameter for off-data and Monte Carlo  $\gamma$ -events are shown in Figure 5.16. The histograms clearly show that the maximum *Leakage* values observed lie around 0.8. The use of the *Leakage* parameter for impact parameter and energy estimation yielded an improvement in energy resolution.

- **Asymmetry**: The *Asymmetry* parameter has been redefined (Schweizer, 2002) with respect to the earlier definition as of (Petry, 1997). The earlier definition used the vector pointing from the pixel with the highest signal towards the barycenter of the image, thus suffering from the pixelation of the camera. The new definition uses a vector pointing between barycenters of the image under investigation when firstly calculated using the squares of the signal heights in the individual pixels and the barycenter calculated secondly with the signals as recorded. For this analysis the length of the projection of this vector onto the line connecting the barycenter and the camera center was used. Note the difference in *Asymmetry* for offdata and for Monte Carlo  $\gamma$ -events shown in Figure 5.17: while the offdata display a symmetric distribution of *Asymmetry* values, the Monte Carlo  $\gamma$ -events show mostly positive values of *Asymmetry*. Use of this quantity has proven very useful, leading to an enhancement of the signal-to-noise ratio in Mkn 421 data from 2000-2001<sup>25</sup>.

The formulae and the procedure to calculate the image parameters that are not explained here, were given in (Petry, 1997).

Table 5.1 summarises the meaning and definition of the image parameters which are used for this analysis.

---

<sup>24</sup>This parameter and the *Asymmetry* parameter were only recently defined by T. Schweizer (Schweizer, 2002).

<sup>25</sup>This data set has been used to optimise the cuts applied to the data set of Mkn 421 from 1999-2000, as described in Section 6.2.

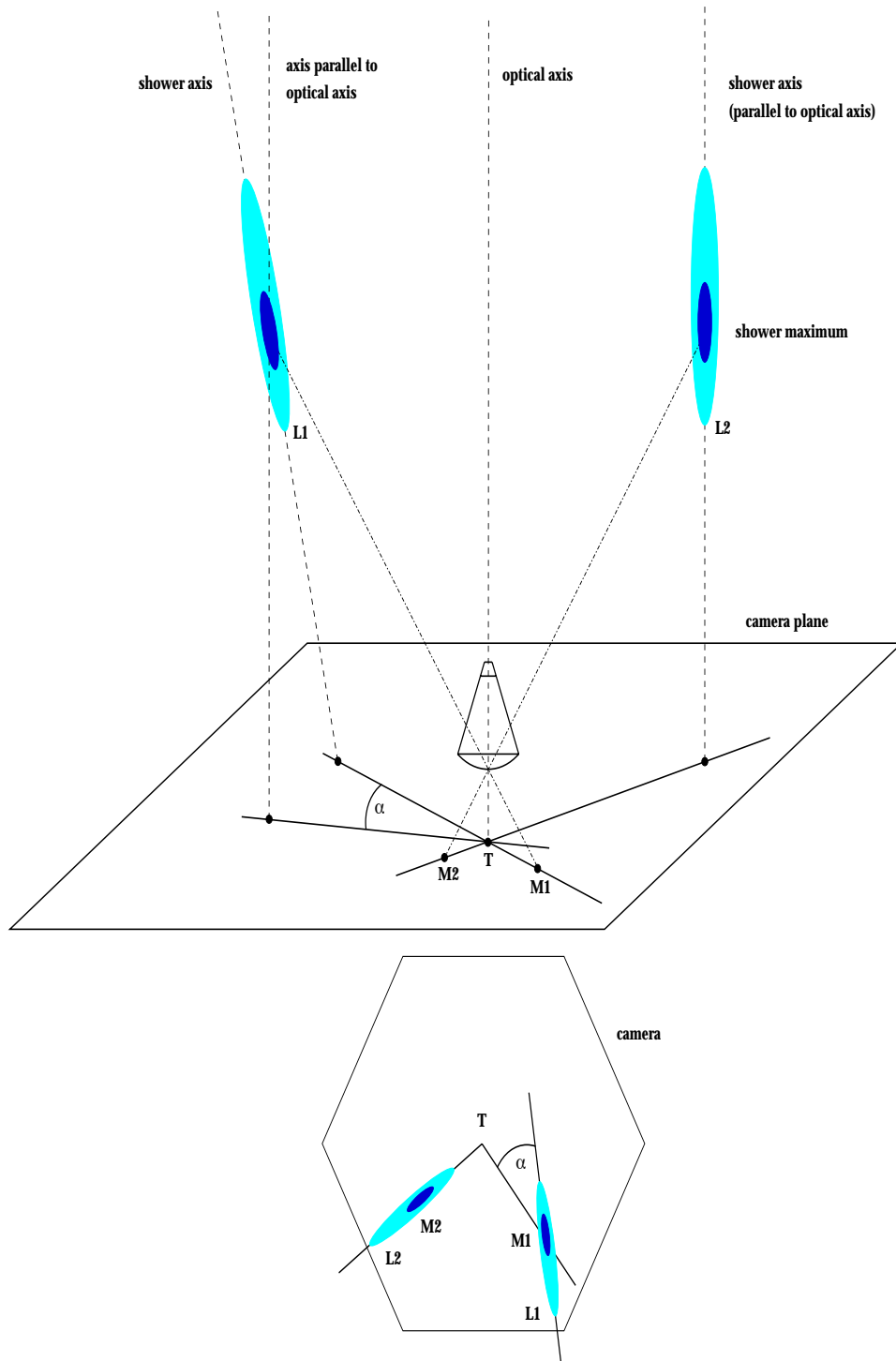


Figure 5.14: Visualisation of the definition of the orientation angle *Alpha*. Showers which are not warped with respect to the telescope's optical axis, e.g. showers that originate from the tracked object, have small values of *Alpha*.

The labels M1 and M2 refer to the shower maxima and their image points. Similarly, the points L1 and L2 are indicated at the shower location and at their image points in the camera.

Source: (Kranich, 2001), after (Deckers, 1997)

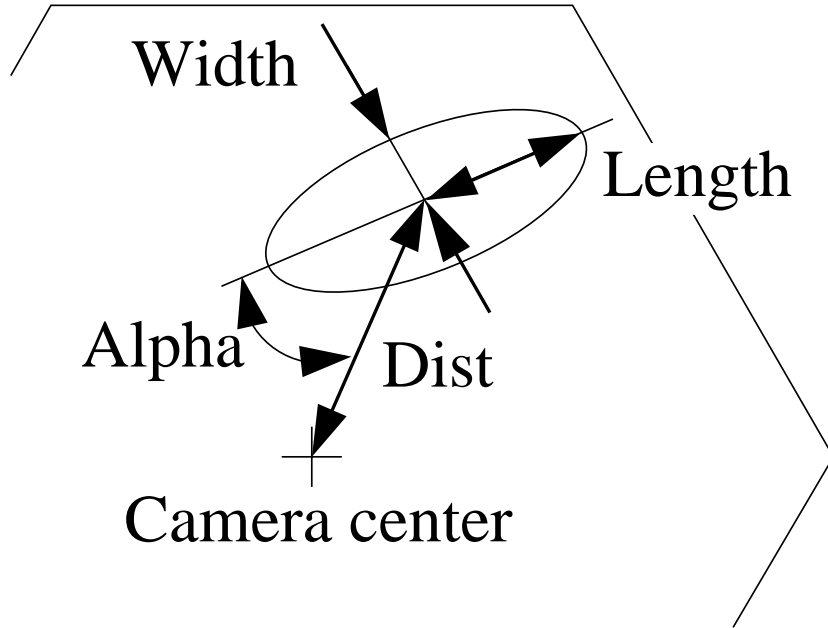


Figure 5.15: Sketch to illustrate the image parameter definitions as they are used in this thesis. *Width* and *Length* are defined as the RMS of the signal distribution along the major axes of the image, depicted here as idealised one-sigma contour ellipse. See text.

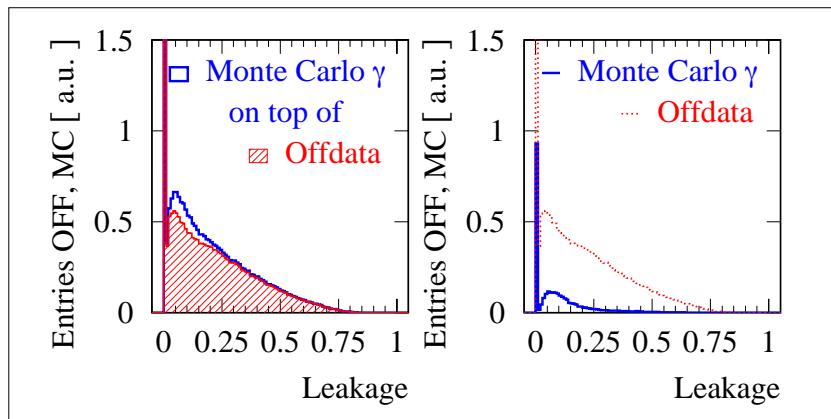


Figure 5.16: Distribution of the *Leakage* parameter for off-data, i.e. hadrons, (shaded histogram), with the corresponding distribution for Monte Carlo generated  $\gamma$ -images superimposed as the blank histogram.

On the right-hand side the same off-data is shown, here with the distribution for the Monte Carlo generated  $\gamma$ s superimposed as the blue histogram with highly exaggerated statistics.

The peak at zero is due to images that are fully contained in the camera.

Source: CT1 offdata and Monte Carlo simulations after noise filter, zenith angle between  $10^\circ$  and  $30^\circ$ .

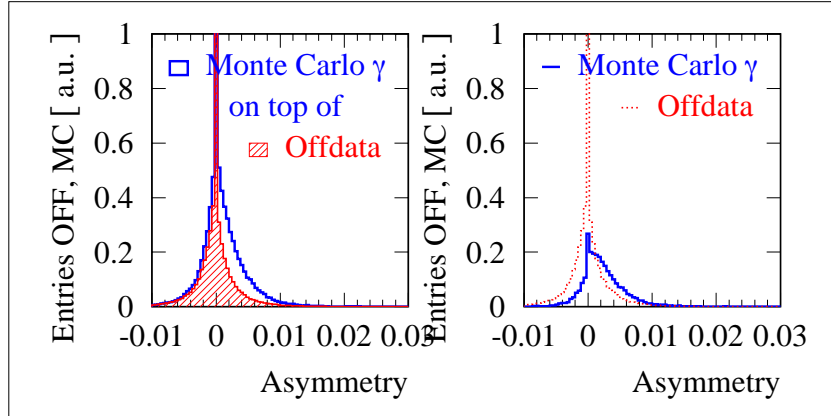


Figure 5.17: Distribution of the *Asymmetry* parameter for off-data, i.e. hadrons, (shaded histogram), with the corresponding distribution for Monte Carlo generated  $\gamma$ -images superimposed as the blank histogram.

On the right-hand side the same off-data is shown, here with the distribution for the Monte Carlo generated  $\gamma$ s superimposed as the blue histogram with highly exaggerated statistics.

Source: CT1 offdata and Monte Carlo simulations after noise filter, zenith angle between  $10^\circ$  and  $30^\circ$ .

Name	Unit	Meaning
<i>Size</i>	[ph.el.]	Total number of photo electrons after image cleaning
<i>Dist</i>	[ $^\circ$ ]	The distance of the image's barycenter to the camera center
<i>Conc</i>		The sum of the two highest pixel values divided by the <i>Size</i>
<i>Width</i>	[ $^\circ$ ]	RMS of the ph.el. distribution along the image's short axis
<i>Length</i>	[ $^\circ$ ]	RMS of the ph.el. distribution along the image's long axis
<i>Alpha</i>	[ $^\circ$ ]	Tilt angle of the image against the radial direction
<i>Leakage</i>		Estimated ratio of missing light to contained light in the camera
<i>Asymmetry</i>	[ $^\circ$ ]	Difference between image centers using different weights

Table 5.1: Image parameters and their meaning as used for the analysis. The parameters are calculated after the pointing correction, relative and absolute calibration, pickup correction and image cleaning have been performed.

## 5.8 Image parameters under variable night sky background light

While the dynamic nature of the image cleaning process is advantageous in terms of small signals, it also introduces a dependence of the image parameters on the NSB light level during data taking.

With increasing NSB level larger values of the pedestal RMS are measured in the pixels. As a consequence, for the same shower<sup>26</sup> fewer pixels contain significant signals in terms of pedestal RMS, as an increasing noise level makes it ever more difficult to distinguish small entries from noise. Therefore fewer pixels will be used to calculate the image parameters for events that are recorded under higher NSB levels. The influence of NSB noise onto the determination of image parameters is investigated in the following section, before a correction mechanism is suggested that permits one to retain the advantages of dynamic image cleaning, while at the same time removing the dependence of image parameters on the NSB level.

### 5.8.1 Simulated influence of different NSB light levels on Monte Carlo $\gamma$ -event samples

In order to explore the dependencies of *Width* and *Length* on zenith angle and nightsky background level, the complete Monte Carlo dataset of  $\gamma$ -events was simulated at different noise levels and then subjected to the image cleaning procedure explained in Section 5.7.1<sup>27</sup>. Around 1000 simulated events were grouped together in each run, of which on average 250 events triggered the telescope. They were simulated at a set of fixed zenith angles. The average *Width* and *Length* for each run was calculated from a subset of the data which fulfilled the requirements

1. *Size*  $\geq 60$  ph.el.,
  2. *Dist*  $\leq 1.0^\circ$  and
  3. *Alpha*  $\leq 60^\circ$ .
- (3)

**These limits are referred to in the following as 'condition (3)'**<sup>28</sup>.

The resulting medians of the *Width* and *Length* distribution are shown in Figure 5.18: on the left-hand side the average values of *Width* and *Length* per Monte Carlo run are displayed for different zenith angles and for average pedestal RMS values of 0.8 ph. el. and 1.7 ph. el. . The average values of *Width* and *Length* for the ZA of  $15^\circ$  and for the ZA of  $45^\circ$  are plotted on the right-hand side for three different simulated pedestal RMS levels. The Monte Carlo  $\gamma$ s shown here were simulated with a powerlaw spectral index of 1.5.

It becomes apparent that

---

<sup>26</sup>Of course it is purely hypothetical to record the same shower twice.

<sup>27</sup>It is important to note that the behaviour shown here appears due to the particular combination of different levels of NSB and the dynamic image cleaning that is employed in the CT1 analysis.

<sup>28</sup>All plots that are shown in this section (Section 5.8) were made after applying this set of restrictions.

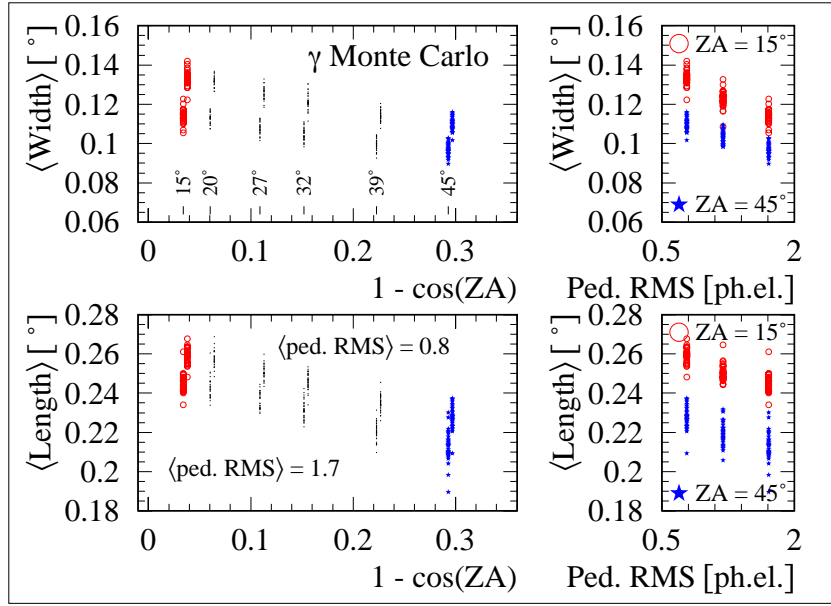


Figure 5.18: Average *Width* and *Length* of Monte Carlo generated  $\gamma$ -images, simulated with different zenith angles and noise levels. On the left-hand side the average *Width* and *Length* values are drawn as a function of the zenith angle at two different levels of NSB noise. For zenith angles of  $15^\circ$  and  $45^\circ$  the average *Width* and *Length* are plotted as a function of the simulated average pedestal RMS level as a measure of the NSB noise level on the right-hand side.

Error bars have been omitted for clarity.

Source: CT1 Monte Carlo simulation of  $\gamma$ -events

- higher NSB fluctuations result in smaller values of *Width* and *Length* (using the image cleaning scheme of the CT1 analysis).

In addition it is apparent that

- the images' *Width* and *Length* in the camera decrease with increasing zenith angles<sup>29</sup>.

This zenith angle dependence is found at different levels for different background noise levels: a higher noise level leads to smaller reconstructed images. This proves that this effect is an add-on to the ZA dependence of image parameters. The current findings can be summarised:

- a low tail cut leaves the difference between  $\gamma$ - and hadron images more pronounced (c.f. Figures 5.21 and 5.22).

As a consequence the image cuts must be dynamic in terms of the NSB level or the data have to be calibrated.

<sup>29</sup>This can be deduced from Figure 5.18, as for each of the two bands of different NSB levels the average values of *Width* and *Length* decrease with increasing zenith angle. No other parameter was varied and the distribution of available energies at the different zenith angles is roughly equal, see e.g. Figure 16.13.

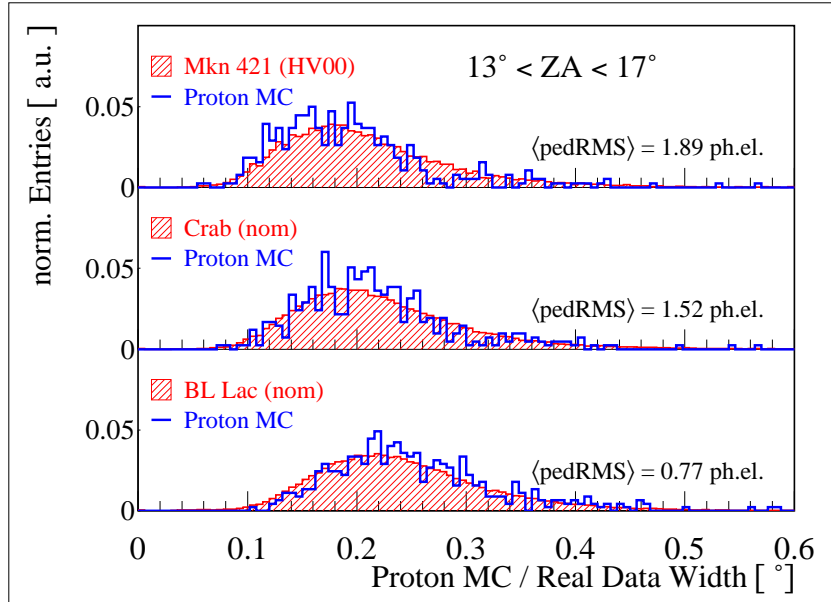


Figure 5.19: *Width* distributions of real data and of proton Monte Carlo data, simulated at several different NSB noise levels, indicated by the average pedestal RMS measured in the camera. A differential power law spectral index of 1.7 was used here. Source: CT1 Monte Carlo simulation of proton events; Observations of Mkn 421 1999-2000 'HV00', Crab 1999-2000 'nom', BL Lac 1999-00 'nom'

### 5.8.2 A crosscheck of image parameters from Monte Carlo protons and real data at different NSB levels

As a next step it is necessary to verify that the image parameters of Monte Carlo simulated events coincide with the image parameters from real data.

One important test for any Monte Carlo simulation of hadronic events (for this thesis only protons were available) is, to test whether their image parameter distributions compare to those of real data, i.e. raw data, which is mostly made up of shower images from protons and Helium nuclei.

A further question is whether the image parameter distributions of Monte Carlo protons and raw data (all of them subjected to condition (3)) compare even under different NSB conditions.

Only rather limited statistics are available for the Monte Carlo generated proton data, which was furthermore generated only for a zenith angle of  $15^\circ$  (c.f. Section 16.6). The proton data was simulated according to the descriptions given in Appendix 16 at different NSB levels, taken from BL Lac (1997, HV 'nom'), Crab (1999-2000, HV 'nom') and Mkn 421 (1999-2000, HV 'HV00') observations. A corresponding zenith angle range ( $13^\circ$  to  $17^\circ$ ) was selected from the real data. Normalised *Width* and *Length* distributions were superimposed on top of each other for the same NSB level and stacked into the same graph, the NSB level rising from the bottom to the top panel. They are displayed in Figures 5.19 and 5.20.

The conclusions to be drawn from these Figures are:

1. Given the limited statistics of the proton Monte Carlo data set, the *Width* and *Length* distributions of (predominantly hadronic) real data and proton Monte Carlo data agree

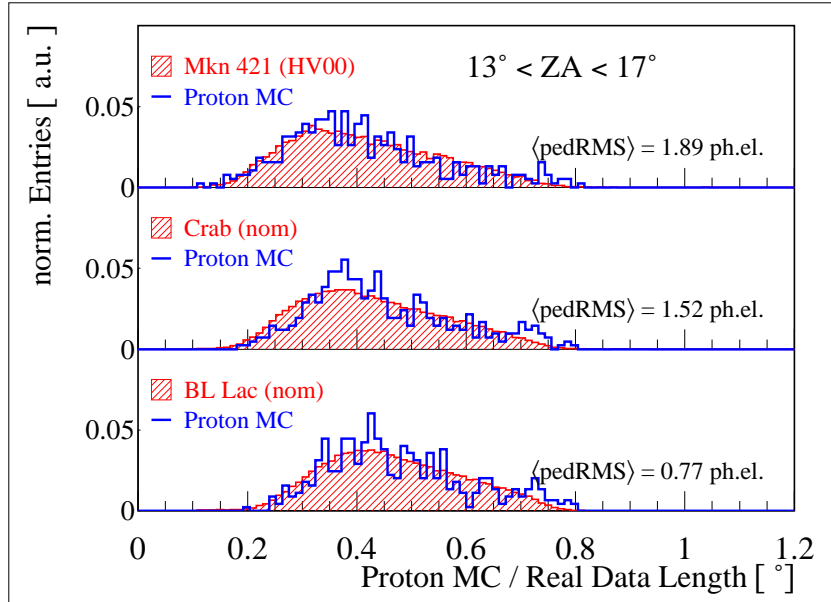


Figure 5.20: *Length* distributions of real data and of proton Monte Carlo data, simulated at several different NSB noise levels, indicated by the average pedestal RMS measured in the camera. A differential power law spectral index of 1.7 was used here. Source: CT1 Monte Carlo simulation of proton events; Observations of Mkn 421 1999-2000 'HV00', Crab 1999-2000 'nom', BL Lac 1999-00 'nom'

within statistics.

2. The distributions track each other under the different NSB conditions that were recorded in the real data and simulated in the Monte Carlo data.

Therefore we conclude that the effect that was shown for Monte Carlo proton events describes reality quite well. Before carrying out more refined studies, however, it is interesting to compare the changes in proton Monte Carlo image parameters with changing NSB levels to the changes that are observed in Monte Carlo generated  $\gamma$ -events.

### 5.8.3 Variations of the *Width* and *Length* of Monte Carlo generated $\gamma$ - and proton events as a function of the NSB level

The changes of the *Width* and *Length* distributions with the NSB level have been shown for a set of Monte Carlo  $\gamma$ -data (Figure 5.18) and for Monte Carlo proton showers, which were moreover compared to real data (Figures 5.19 and 5.20).

In this section the *Width* and *Length* distributions of  $\gamma$ -events and proton events are compared. Figures 5.21 and 5.22 show these distributions for different levels of NSB light. The distributions have been normalised arbitrarily for the display.

The following conclusions can be drawn from Figures 5.21 and 5.22:

1. Both  $\gamma$ - and proton distributions show a shift of the *Width* and *Length* distributions towards lower values with increasing simulated NSB level.

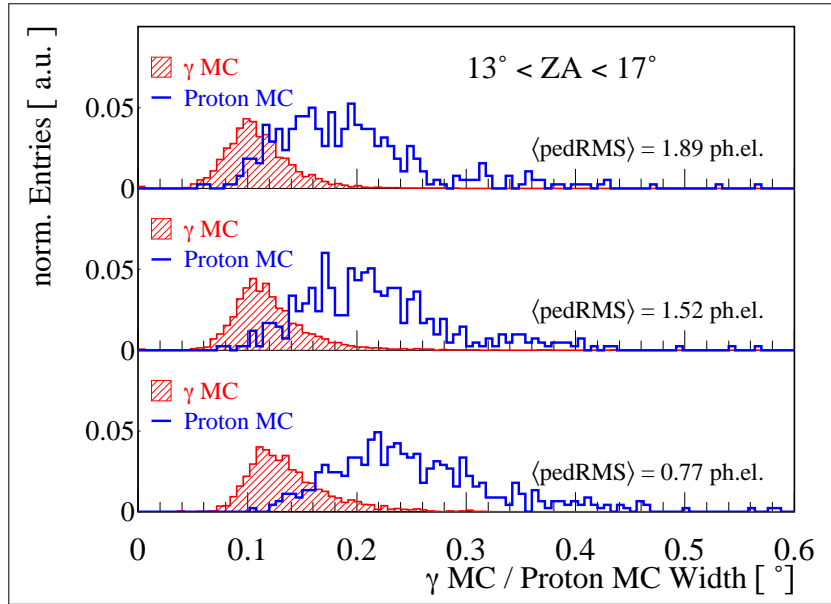


Figure 5.21: *Width* distributions for  $\gamma$ - and proton Monte Carlo events, simulated at several different NSB noise levels (indicated by the average pedestal RMS).

The  $\gamma$ -events were weighted according to their simulated energy such that an overall powerlaw energy spectrum with a differential index of 2.7 was achieved. The proton simulation followed the powerlaw energy spectrum of hadronic background data, i.e. it was simulated with a differential spectral index of 1.7.

Source: CT1 Monte Carlo simulation of  $\gamma$ - and proton events

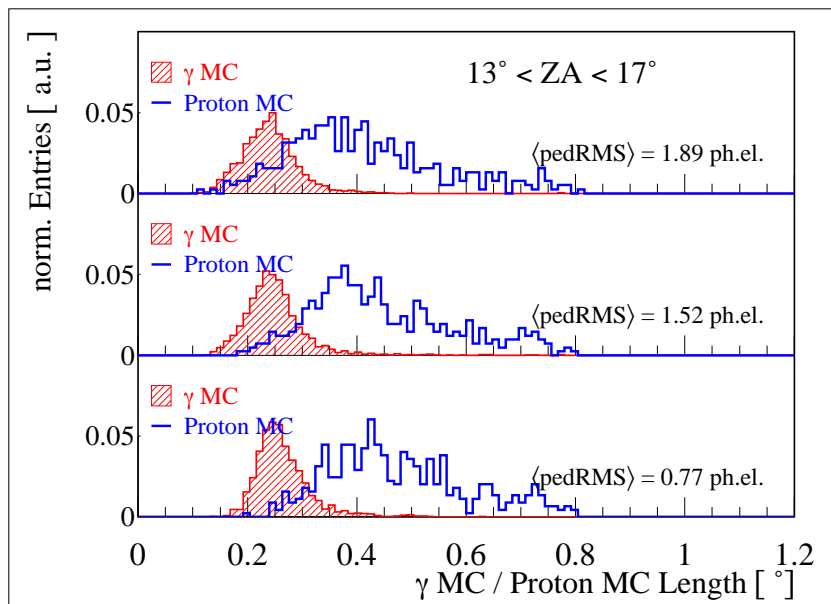


Figure 5.22: Like Figure 5.21; *Length* distributions for  $\gamma$ - and proton Monte Carlo events, simulated at several different NSB noise levels (indicated by the average pedestal RMS).

Source: CT1 Monte Carlo simulation of  $\gamma$ - and proton events

2. The limited statistics of simulated proton events do not allow one to draw any conclusions regarding the slope of the changes with the NSB level. This topic must be addressed using real data, which is done in the following section.
3. The distributions show significant differences for  $\gamma$ s and protons. The  $\gamma$ -hadron separation is based on such differences and is dealt with in Chapter 6.
4. A discrimination which is independent of the varying NSB levels, however, is only possible if the dependence of the *Width* and *Length* distributions on the NSB level is well understood and corrected for. Otherwise the calculation of effective areas and impact parameter as well as energy estimation shall be NSB dependent.

It must be noted at this point that it does not seem appropriate to deduce the parameters of the shift of the *Width* and *Length* distributions with NSB level from Figures 5.21 and 5.22. It is left as an axiom for the correction method suggested below that  $\gamma$ -images and proton images are, on average, affected by the same shift as a function of the NSB level.

#### 5.8.4 Investigation of the effect of NSB on the Crab data set from 2000-2001

As mentioned above, the limited statistics of proton Monte Carlo events do not allow one to deduce the functional dependence of the average *Width* and *Length* on the NSB level for Monte Carlo data. Therefore the Crab dataset recorded between January and March 2001 was chosen to serve as reference data set for this purpose. The average *Width* and *Length* were calculated in accordance with condition (3) and have been plotted in Figure 5.23 as a function of the zenith angle of the observation shown in Figure 5.18. The RMS scatter of *Width* and *Length* within each data run is drawn as errorbars to the data points. The distributions of the smallest zenith angle data (zenith angles below  $10^\circ$ ) and the largest zenith angle data (zenith angles above  $30^\circ$ ) are marked in colour and repeated on the right-hand side, plotted now as a function of the average level of the pedestal RMS scatter<sup>30</sup>.

Two main features are apparent in Figure 5.23:

1. Comparing the scale of the vertical axis of Figure 5.23 to the values of *Width* and *Length* shown in Figures 5.21 and 5.22, reveals that the average *Width* and *Length* values of real data are close to those of simulated hadronic events, which are larger than those of the  $\gamma$ -events.
2. The average *Width* and *Length* values are scattered around a certain function and decrease with increasing zenith angles, as generally expected.

#### 5.8.5 Investigating real data which spans a large range of different NSB levels

It was claimed in the preceding paragraph that the spread of the average *Width* and *Length* values can be attributed to different NSB levels during data recording. It is demonstrated here

---

<sup>30</sup>Only the correctly functioning pixels are used to calculate this average value over the camera. The procedure is described in detail in Section 5.4.

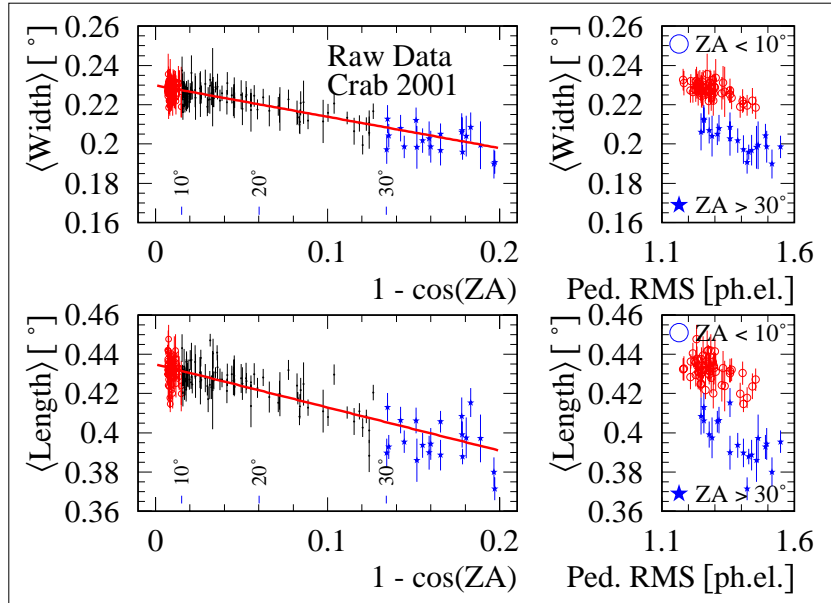


Figure 5.23: Average *Width* and *Length* of Crab data recorded in 2001, which has been chosen to serve as reference data set. The data set and the meaning of the red lines is explained in Section 5.8.6.

On the left-hand side the average values for *Width* and *Length* are drawn as a function of the zenith angle.

For zenith angles below  $10^\circ$  and above  $30^\circ$  the average *Width* and *Length* are plotted as a function of the pedestal RMS level on the right-hand side.

The error bars represent the RMS of the distributions within a data run of usually 20 minutes duration.

Source: CT1 observations of Crab January to March 2001, nominal HV, no moonshine.

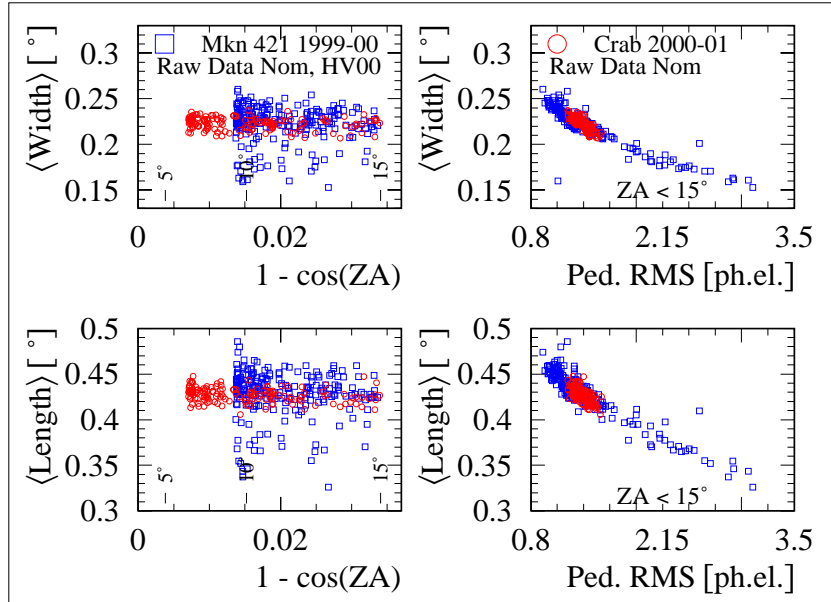


Figure 5.24: Raw data with a limited zenith angle range (below  $15^\circ$ ) but a wide range of NSB levels is combined here: Mkn 421 1999-2000 observations, recorded with nominal HV with ('HV00') and without moonshine ('Nom'), and Crab 2000-2001 observations, with nominal HV without moonshine. *Width* and *Length* were averaged over all data which fulfill condition (3) on page 64. The average values are plotted as a function of the zenith angle on the left-hand side and as a function of the pedestal RMS on the right-hand side.

Error bars have been left out for clarity.

Source: CT1 observations of Mkn 421 1999-2000 nominal HV with and without moonshine and of Crab 2000-2001, nominal HV without moonshine.

that a combined set of Crab data (2000-2001, 'nom') and Mkn 421 data (1999-2000, both 'nom' and 'HV00') with zenith angles limited to values below  $15^\circ$  is well suited to prove this claim.

The resulting graphs, shown in Figure 5.24, allow one to draw two main conclusions:

1. Most of the Mkn 421 hadronic background data (blue, empty squares) is found to have larger average *Width* and *Length* values than the corresponding Crab data (red, empty circles), see left-hand side of Figure 5.24.
2. This discrepancy disappears when the average values of *Width* and *Length* are plotted versus the average pedestal RMS of the data run: the trend of smaller image parameters with higher noise is confirmed to be valid over the entire range of noise levels for both sources.

### 5.8.6 Proposal of the 'Zonk' method to reduce the NSB influence on *Width* and *Length*

Any correction mechanism for the bias of NSB noise on the determination of image parameters should fulfill the following requirements:

- **Image Cleaning:** We want to stick to the dynamic tail-cut image cleaning, i.e. the

aim is to retain as much information as possible from images that were recorded under different conditions.

- **Only one set of Monte Carlo events** is to be used for the whole study rather than a separate set for each source and NSB condition.
- **$\gamma$ -Hadron Separation:** Only one set of  $\gamma$ -hadron separating cuts is to be used; the optimisation of cuts on one dataset should not bias the results obtained from data recorded under different NSB conditions.
- **Off data:** If an ON-OFF approach is used, one should keep only one OFF-dataset that compares well to any kind of ON-data<sup>31</sup>.

Earlier approaches that intended to solve the difficulties induced by varying NSB levels included the following:

- **Use of a constant cut level for image cleaning.** The level of the cut is chosen conservatively, i.e. rather high, so that the most noisy data is still treated correctly. In the HEGRA CT SYSTEM analysis a constant cut of 6 photoelectrons is used as the lower limit on pixel entries.  
**Drawback:** True small signals contained in low-noise pixels are disregarded and the separation of the *Width* and *Length* of  $\gamma$ s from those of hadrons is not optimal.
- **Variation of the dynamic tail-cut level until the image parameter distributions of different datasets coincide.** In order to do so, one dataset needs to be selected as reference data set. In practice the level of the tail-cut cleaning is chosen in terms of multiples of the noise level in the pixels, once per dataset.  
**Drawbacks:**
  - (a) The selection of the reference dataset rules the quality of the result: choosing low noise data as reference data leads to improper image cleaning in any dataset with a higher general noise level. Therefore the correct dataset to be chosen as reference dataset is the one with the highest noise.
  - (b) For practical reasons the cleaning level is usually chosen once per dataset. Any variation of the NSB level from night to night or as a result of for instance zodiacal light or by the rise or set of the Milky Way during one night is still present in the data.
  - (c) In essence this method is a copy of the above option.
  - (d) This approach is extremely difficult to model correctly in a Monte Carlo simulation.
- **Use of '*Padding*'.** Noise is added artificially to each pixel content separately, either by installing tiny lamps at the PM windows at the time of data recording or offline in the analysis software, such that the noise level is equally high in all pixels. The noise level per pixel is selected separately for each source.  
**Drawback:** The highest noise in a pixel rules the noise level of the whole observation.

---

<sup>31</sup>In ON-OFF approaches the background under a measured *Alpha* distribution is estimated using off-data that has been normalised to the ON-data set. For a more detailed description see e.g. (Petry, 1997).

Bright stars like Tauri- $\zeta$  in the vicinity of Crab may ruin the signals in darker sky regions. Here, too, the modeling in Monte Carlo simulations is difficult if a different general noise level is chosen from source to source.

**We therefore introduce a new method called<sup>32</sup> 'zeroth order night sky korrection', 'Zonk'.**

**The *Zonk* method dynamically corrects for noisy data in a way that fulfills almost all the requirements listed above simultaneously.**

The *Zonk* method has been developed for the analysis presented in this thesis and is based on the following set of assumptions:

- The hadronic background arriving on top of the atmosphere is identical whatever direction the telescope is pointing to. Therefore the hadronic events may serve as 'calibrator' that should essentially show equal image parameter distributions<sup>33</sup>.
- The zenith angle dependence of *Width* and *Length* is ruled partly by geometry and partly by NSB influences onto the image cleaning algorithms.
- Both  $\gamma$ - and hadron events are affected in the same proportion by the NSB. Therefore the  $\gamma$ -events undergo the same correction shifts as the hadron events in the correction process. Even in data sets with strongly varying NSB conditions the  $\gamma$ -events are then found in the same region of the image parameter space in the corrected versions of the data sets.

The specifications of the correction method include a set of rules and definitions:

- **Rules to calculate average values of *Width* and *Length* per data run:** A well defined subset of the hadronic data which is not affected by the limited camera size and threshold effects is used to extract the average *Width* and *Length* values from each data run. The rule that is chosen is identical to condition (3).
- **Definition of a reference dataset:** The dependence of the medians of *Width* and *Length* distributions as a function of the zenith angle is evaluated. Crab data recorded between January and March 2001 is selected to represent reference behaviour. The straight line fits through the plots in Figure 5.23, marked by red lines, represent the reference values:

$$\langle Width(\theta) \rangle = 0.238^\circ - 0.160^\circ \cdot (1 - \cos(\theta)) \quad , \quad (5.11)$$

$$\langle Length(\theta) \rangle = 0.441^\circ - 0.206^\circ \cdot (1 - \cos(\theta)) \quad . \quad (5.12)$$

where

---

<sup>32</sup>The correction was developed by the author of this thesis and tried with a toy program first. Its dummy name 'zonk' was kept in the end.

<sup>33</sup>Although it is anticipated that all image parameters are affected, the correction is, in a first step, applied only to *Width* and *Length*. Other image parameters, such as *Size* and *Conc* may be considered in a second development step of *Zonk*.

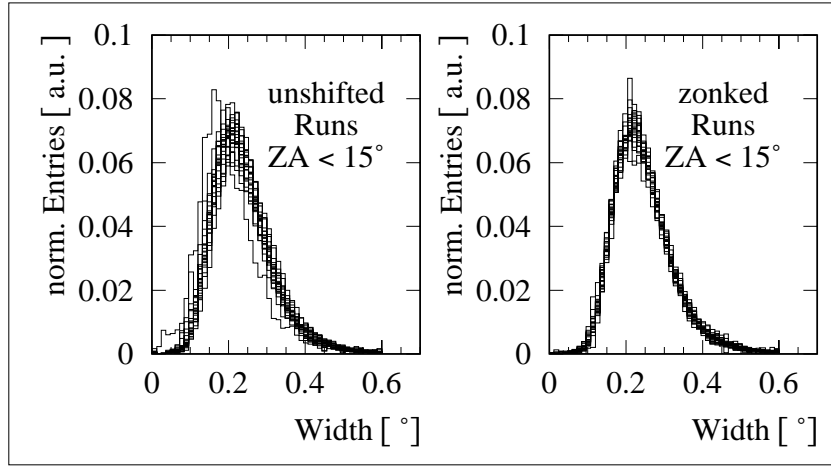


Figure 5.25: Several *Width* distributions of Mkn 421 raw data with a ZA below  $15^\circ$ , normalised to an area of 1 and superimposed on top of each other: The left-hand plot shows the uncorrected raw data, the right-hand plot shows the same data after application of the *Zonk* method. Especially that distribution containing the high number of events at very small values of *Width* can be seen to be shifted nicely into the combined data set. Errorbars have been omitted for clarity.

Source: CT1 observations of Mkn 421, 1999-2000, zenith angle below  $15^\circ$ , uncorrected and corrected.

$\theta$  is the zenith angle of the observation.

For this data set the image parameter cuts were optimised, see Section 6.2.

- **Rules how to find correction values for all other datasets:** It is possible to find the median of the *Width* and *Length* distribution in any data run of any other data set, using the subset of hadronic events selected according to condition (3). The reference value of *Width* and *Length* for the zenith angle of the observation in question can then be calculated using Equations (5.11) and (5.12).
- **Rules for the application of the correction:** Applying the correction means that the individual events' values of *Width* and *Length* are multiplied with correction factors such that the medians of the resulting distributions match the reference values.
- **Rules for the  $\gamma$ -hadron separation:** Any  $\gamma$ -hadron separating cut is performed after the *Zonk* correction has been applied.

The NSB influence and the correction steps must be modelled correctly in the Monte Carlo simulation. In the analysis presented here the average NSB noise during data recording is simulated for a given dataset. Then the average *Zonk* shifts that were applied to the real data are applied to the Monte Carlo dataset, too. A detailed description of these steps can be found in Section 16.5.

As an example of how the procedure performs on *Width* distributions of real data, a sub-sample of Crab data from 1999-2000 with zenith angles below  $15^\circ$  was selected. Figure 5.25 shows these normalised *Width* distributions, superimposed on top of each other. The left-hand

side shows them as they were recorded, the right-hand side shows them after application of the correction method. A clear improvement in the spread is evident.

For an assessment of the changes brought about by *Zonk*, the excess rate in Crab observations, the background rate in Crab and in Mkn 421 observations and the change in the final result, i.e. the *Alpha* plots, are collected in Section 6.4.



## 6 Ways to enhance the signal-to-noise ratio in raw data

It is difficult to develop a trigger logic for Cherenkov telescopes that suppresses most of the hadronic background already at the trigger level. Therefore data recorded by CT1 is, as is the case with other Cherenkov telescopes, dominated by background.

The Hillas parameters describe the shower images in terms of geometry and intensity related quantities. Their distributions differ for  $\gamma$ -ray induced showers on the one hand and hadron induced showers on the other hand. Cuts may thus be used to separate those groups in order to increase the  $\gamma$ -hadron ratio.

---

### 6.1 General motivation for and possible implementation methods of a cut procedure

Satellite borne  $\gamma$ -detectors, like e.g. EGRET, use(d) anti-coincidence shields to efficiently block hadrons from being recorded. Raw data from CHERENKOV telescopes, however, is mostly made up of hadronic events, the  $\gamma$ -signals from sources are buried under a mass of cosmic ray background events.

Crab is the strongest known galactic TeV source in the northern hemisphere. During observations of Crab at small zenith angles only around 47 photons per hour trigger CT1 after filter cuts (c.f. Section 5.1.1) according to Monte Carlo simulations. During the same time order  $\mathcal{O}(10^4)$  hadrons are collected. At small zenith angles the present CT1 analysis finds roughly 20 to 25 (depending on the cut performed) excess events per hour from Crab after all cuts have been performed. These excess events are accompanied by a somewhat lower number of background hadrons that are accepted by the cut procedure.

In order to achieve this background suppression factor of around 400, several cuts were performed on the image parameter distributions. Most effective in this respect is the cut requiring small values of the orientation angle *Alpha*: this cut selects or de-selects events depending on whether or not their primaries arrived in a plane that also contains the telescope's optical axis.

Several other properties, which are not related to the orientation of the shower with respect to the telescope and which are different for hadrons and  $\gamma$ s, may be used in principle to separate the two kinds:

1.  $\gamma$ -images are more concentrated, they have an elliptical shape with a narrow range of the ratio *Width* over *Length*.
2. It is known from Monte Carlo simulations that the arrival times of CHERENKOV photons from hadron images show a larger spread than those of  $\gamma$ -showers, i.e. fewer photoelectrons are superimposed at any time.

3. In the energy range accessible with CT1,  $\gamma$ -showers produce roughly two times more CHERENKOV light in the atmosphere compared to hadrons of the same energy (c.f. Section 16.1).
4. For  $\gamma$ -events the geometrical center of the outline of the shower image in the camera does usually not coincide with the brightest spot.

Exploitation of arrival time differences is impossible in the CT1 analysis, as no timing information is available but is already inherent on the trigger level on events with small values of *Size*. Therefore only cuts that are based on image shapes and image location in the camera and on the orientation angle *Alpha* are used.

The cuts performed on the multidimensional image parameter space are expected to select  $\gamma$ -candidates in preference of hadronic showers. The image parameters *Width* and *Length*<sup>34</sup> describe the shape of shower images. The *Dist* parameter describes the shower location with respect to the telescope. To a certain extent is the *Dist* together with *Size* a measure of the impact parameter and the height of the shower maximum above the ground. The orientation angle *Alpha* describes the tilt angle of the shower's main axis against the line connecting the source's image point in the camera and the image's barycenter.

This angle is small for showers originating from the tracked object and is larger for any initial direction that does not lie in a plane with the optical axis of the telescope. Therefore any  $\gamma$ -signal that comes from the source should display small values of *Alpha*.

Off-source events which have a shower axis in the same plane as the telescope's axis also have small values of *Alpha* although they do not originate from the source in question. If they are in addition similar to  $\gamma$ -images<sup>35</sup> and fulfill the cut restrictions posed on the other image parameters, they form a background that can no longer be distinguished from true source photons.

In principle the hadronic background has a flat *Alpha* distribution, as any arrival direction is equally likely for the background of isotropically arriving cosmic ray events. The small size of the CT1 camera, however, leads to a truncation of images that are close to the camera border. This truncation in turn leads to a bias in the *Alpha* estimates, predominantly for events with larger *Dist* values. The *Alpha* plots for data restricted to a set of *Dist* ranges are displayed in Figure 6.1. Note that these distributions are shown for raw data, only the noise filter cut has been applied. Above a certain value of *Dist* the maximum of the recorded light distribution is located very close to the camera border. The parallelism of the pixel rows to the camera border (c.f. Figure 4.4(a)) leads to estimates of *Alpha* with values close to  $90^\circ$ . This increase in the value of the *Alpha* estimates with increasing *Dist* values can be seen in Figure 6.1.

In addition to the fact that energy estimates become very difficult for partly truncated events, this is another reason why all events with a *Dist* value above  $1.05^\circ$  are rejected by the cuts.

---

<sup>34</sup>C.f. Figures 5.14 and 5.15 for sketches of the image parameter definitions mentioned here.

<sup>35</sup>Hadronic events appear more similar to  $\gamma$ -events, if in the first interaction most energy is transferred to  $\pi^0$  (i.e. into the electromagnetic channel) or if the transverse projection happens to be very narrow.

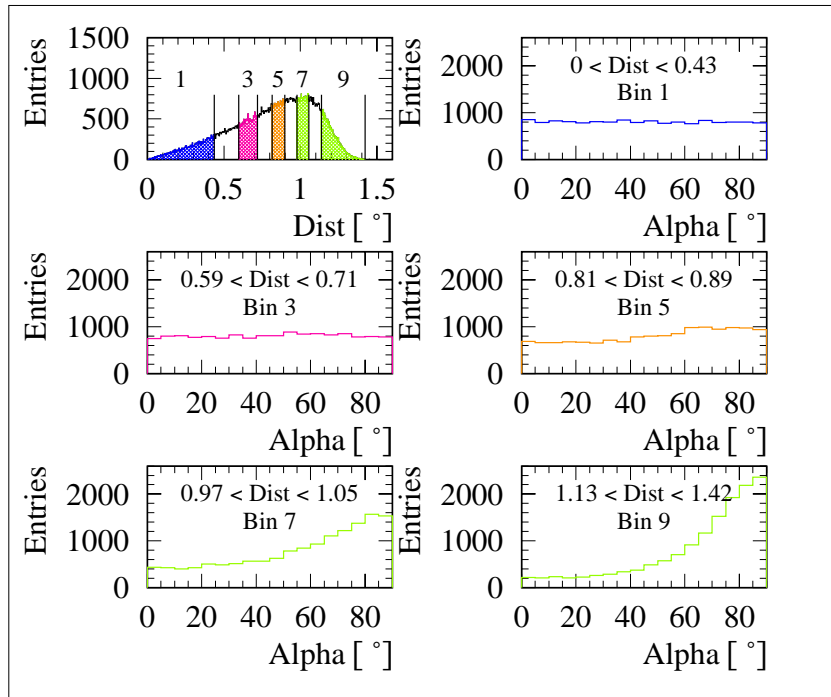


Figure 6.1: The  $Alpha$  distributions for the  $Dist$  bins indicated in the uppermost plot on the left-hand side. Above a certain  $Dist$  value (around  $1.05^\circ$ ), mis-assignments of  $Alpha$  dominate and the events are therefore no longer used.

Source: CT1 Monte Carlo simulation

A signal from a  $\gamma$ -source as well as background hadrons that arrive coplanar with the telescope's optical axis will be visible at small  $Alpha$  values. A  $\gamma$ -signal shall be seen at small values of  $Alpha$  on top of the flat background in the variable  $Alpha$ .

## 6.2 The method used to optimise the $\gamma$ -hadron separation cuts

The  $\gamma$ -hadron separation is one of the most important analysis steps and has been the subject of extensive earlier work on the CT1 analysis. (Kranich, 1997) describes the basic ideas and the current status. The programs to optimise the separation cuts have been applied to Mkn 421 data recorded in the year 2001. Before the optimisation was carried out, however, the data were NSB corrected using the *Zonk* method. The starting values for the cut optimisation were varied over a wide range in order to determine whether a stable optimum could be found. Indeed, a very consistent set of optimal cuts was found. We attribute this fact to the application of the *Zonk* method.

Whenever a data set is used for the optimisation of cuts, it is in principle no longer permissible to use this set of cuts to derive physics results from the same data set. The result may be over-optimised in the sense that the optimisation routine 'learns' the characteristics of this particular data set. Therefore only one half of the  $\gamma$ -events, selected at random from the complete data set, have been used for the optimisation. It has been shown (c.f. (Kranich, 1997)) that the cuts are very similar when different subsets are used in several optimisation runs. Therefore it seems appropriate to use the resulting cut (in our case the  $m_{421\_01\_z}$  cut)

Parameter	a [°]	b [°]	c [°]	d [°]	e [°]	f [°]	g [°]	h [°]
$Length_{up}$	0.3085	-0.0018	0.1621	-0.0027	0.0073	0.0172	0.0037	-0.0057
$Length_{low}$	0.3049	-0.2453	7.898	0.0591	0.0380	16.04	0.0559	0.0307
$Width_{up}$	0.1534	-0.0196	0.0813	0.0262	-0.0156	0.0270	0.0160	-0.0131
$Width_{low}$	0.0681	0.0022	0.0475	0.0049	0.0110	0.0348	0.0061	-0.0453
$Dist_{up}$	4.519	—	28.25	801.2	—	5.533	1.367	—
$Dist_{low}$	0.6599	—	-0.0425	0.0304	—	1.243	-0.0452	—
$Asym_{up}$	0.1008	0.0218	0.0145	0.0194	0.0234	0.0207	0.0171	0.0144
$Asym_{low}$	0.0014	-0.0041	0.0049	0.0002	0.0000	-0.0009	0.0002	-0.0005
$Alpha_{up}$	13.32	—	—	—	—	—	—	—

Table 6.1: Cut parameters of the ‘ $m421_{01_z}$ ’ cut, which had been optimised on the Mkn 421 data set recorded in 2001.

on the complete data from Mkn 421 from the year 2001, as it is done in Chapter 8.

The cut which was eventually used for the Mkn 421 data in this analysis, was named after the optimisation data set, followed by the letter ‘z’, which indicates that the data set was *zonked*<sup>36</sup> before optimisation. The resulting name is ‘ $m421_{01_z}$ ’. The properties of this cut are given below.

The parameters describing the lower and upper cuts  $Cut_{lo/up}$  as a function of the zenith angle  $\theta$ ,  $Size$  and  $Dist$ , are summarised in Table 6.1. The formula is basically a polynomial Ansatz but makes use of some empirical observations.

$$\begin{aligned}
Cut_{lo/up} = & a + b \cdot (Dist [^\circ])^2 + c \cdot (\cos(\theta) - 1) + \\
& (\ln(Size [ph. el.]) - 4.1) \cdot (d + e \cdot (Dist [^\circ])^2 + f \cdot (\cos(\theta) - 1)) + \\
& (\ln(Size [ph. el.]) - 4.1)^2 \cdot (g + h \cdot (Dist [^\circ])^2)
\end{aligned} \tag{6.1}$$

The parameters  $a$  through  $h$  carry units of degrees. For the image parameter  $Dist$  a global cut value of

$$0.5^\circ \leq Dist \leq 1.05^\circ \tag{6.2}$$

is introduced which overrides any other calculated allowed lower or upper value for  $Dist$ . Both these limits take care of some physical effects. For  $Dist$  values below  $0.5^\circ$  one ‘sees’ only light from the shower tail which is very similar in structure for both the  $\gamma$ - and hadron showers. Events with  $Dist$  values larger than  $1.05^\circ$  are only made up of light from the shower halo and the events are in addition very likely truncated.

### 6.3 Determination of the significance of signals

The significance is a measure of the probability that a given signal is ‘real’ and not merely caused by a fluctuation of the background. It is interpreted as a measure of the probability that the signal in an  $Alpha$  plot is due to a genuine source. The excess observed from a source is expressed in multiples of the estimator of the standard deviation of the fluctuation level of

<sup>36</sup>‘zonked’ is used here as a synonym for ‘analysis making use of the *zonk* method’, as such a phrase enhances the readability of the text.

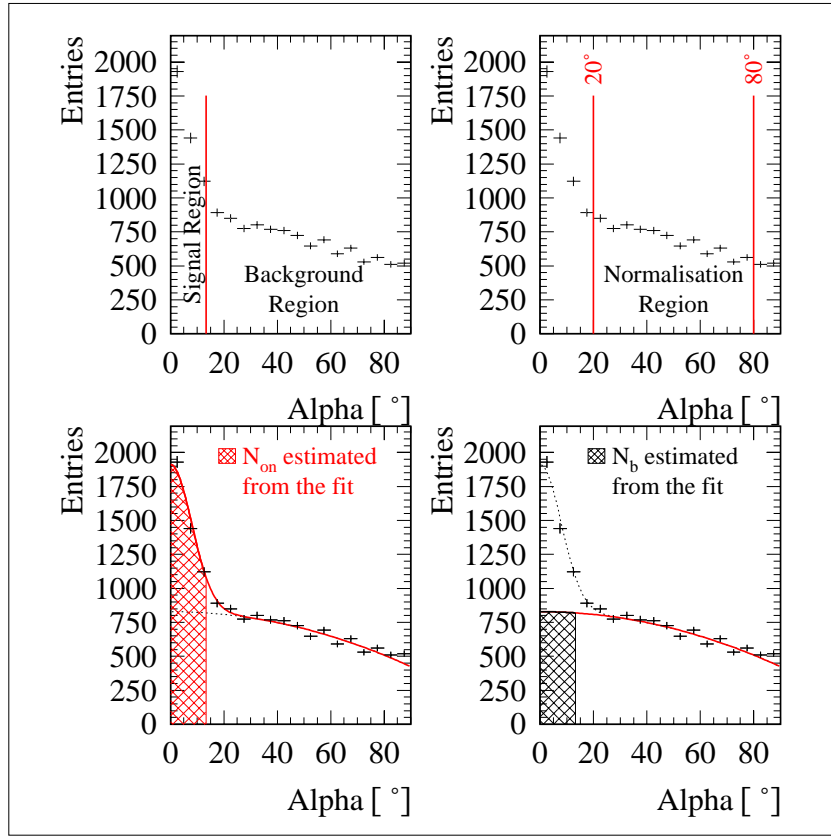


Figure 6.2: Sketches to illustrate the quantities involved in the determination of significance values.

Source: CT1 data from Mkn 421, recorded in 1999-2000

the background. This so-called discovery significance must not be mixed up with an error on the flux determination (see Section 7.8.3).

The method used here is described in (Kranich, 2001). The procedure consists of two steps:

1. A model is set up for the distribution of  $Alpha$ , and is fitted to the actually observed distribution. The Ansatz is a smooth background distribution in  $Alpha$  and a possible contribution from a pointsource aligned with the telescope's optical axis. The number of signal events, background events and finally excess events is calculated from the fit parameters.
2. The significance of an excess is judged by a hypothesis testing: the quantile for the probability for an excess to stem from fluctuation is a measure of the significance.

The significance is usually expressed in multiples of the standard deviations  $\sigma$ . The quantities involved in the determination of significances and which appear in the further discussion are sketched in Figure 6.2.

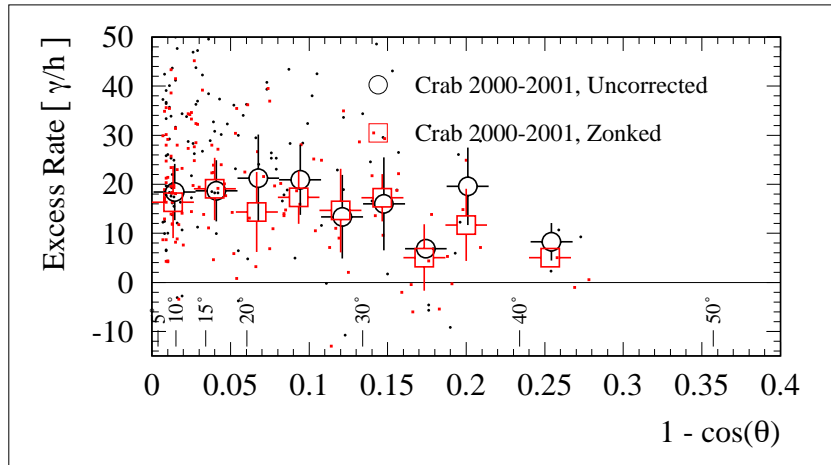


Figure 6.3: Excess rate measured from Crab between January and March 2001 as a function of the zenith angle of the observation. The plot shows the excess rates before and after the *Zonk* correction: the small symbols indicate the excess rate for small time units in the range of 0.3 to 0.75 hours, while the larger symbols mark the averaged excess rate for the zenith angle range defined by the horizontal error bars, given that the total observation time in this bin is longer than two hours.

Source: CT1 observations of Crab, recorded between January and March 2001.

## 6.4 Improvements through the *Zonk* method

The excess rate in Crab observations and the background rate in Crab and in Mkn 421 observations are collected here. They allow one, together with the final results, i.e. the *Alpha* plots, to judge the improvements that were achieved by the use of the *Zonk* method.

### 6.4.1 The $\gamma$ -rate of the 2001 Crab data

Crab is a steady source of  $\gamma$ -rays and data from January to March 2001 was selected as reference data set for the *Zonk* method. Therefore the excess rates of the reference dataset should be similar before and after the correction. A comparison is shown in Figure 6.3: data points corresponding to observations with a duration between 0.2 and 0.75 hours are shown as dots. For clarity their errorbars are omitted in the graphs; the errors were, however, used in the calculation of the average excess rates over bins in the quantity  $1 - \cos(\theta)$ , shown in Figures 6.3 through 6.5. The average excess rates are plotted as large symbols. The horizontal errorbars mark the zenith angle range of a given bin, while the vertical errorbars give the spread of the averaged single data points that fall into this zenith angle bin. The uncorrected distributions (circles) are plotted horizontally slightly offset against the corrected ones (squares).

The overall acceptance of  $\gamma$ -events shows a marginal change with the *Zonk* correction. It was anticipated that the change was small, as the correction is set up such that the corrected dataset matches the reference dataset itself as well as possible.

Besides the level of the excess — roughly 20 events per hour in the lowest zenith angle bin — the decrease in the acceptance rate with an increasing zenith angle is evident. This is in part due to the increasing threshold at larger zenith angles.

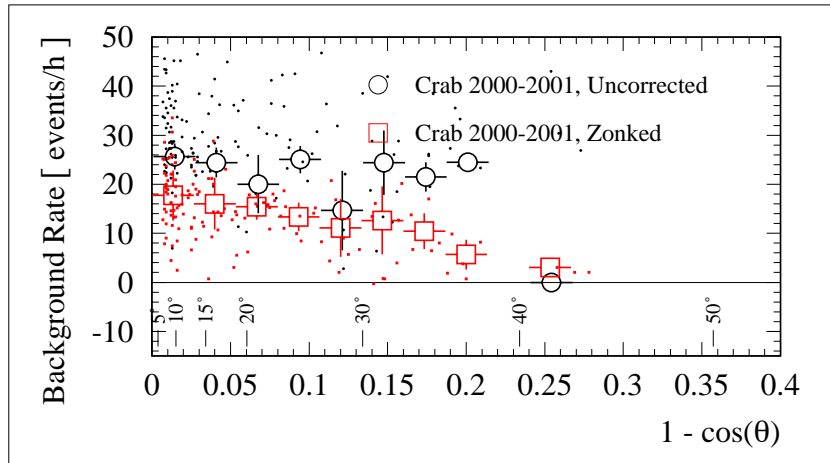


Figure 6.4: The background rate measured from Crab between January and March 2001 as a function of the zenith angle of the observation. The plotting method is equivalent to that used in Figure 6.3. See text.

Source: CT1 observations of Crab, recorded between January and March 2001

#### 6.4.2 Background rates for Crab and Mkn 421

As mentioned in the previous section, there is a background of hadronic events that cannot be distinguished from  $\gamma$ -events. The background events have small  $Alpha$  values and fulfill the other image parameter cut restrictions. Their number is estimated from the integral over the fit function in the range  $0^\circ < Alpha < 13.32^\circ$  (c.f. Table 6.1), corresponding to the signal region as sketched in Figure 6.2.

The impact of the *Zonk* correction is demonstrated through the comparison of background collection rates, both of Crab and of Mkn 421. They are shown in Figures 6.4 and 6.5.

The most important improvements that are visible in these plots are:

- The background rate is significantly lower and, seen as a function of the zenith angle, appears to be smoother for the *zonked* data in both sets.
- The background rate of Mkn 421 and that of Crab agree well when the correction method is applied, whereas the uncorrected background rates are not equal.

#### 6.4.3 $Alpha$ plots for Crab and Mkn 421 data

The final  $Alpha$  plots for the Crab dataset of 1999-2000 and for the Mkn 421 data set are shown in Figures 6.6 and 6.7.

The similarity of the results before and after correction for the Crab analysis was anticipated, as this dataset was selected as the reference dataset for the *Zonk* method. The higher significance from Mkn 421 is brought about by the *Zonk* method: although the number of excess candidates is reduced in the corrected case, the significance of the Mkn 421 signal is larger than that of the uncorrected data, because the reduction of background events is also stronger. For the comparison shown here the same set of image parameter cuts was applied to all datasets.

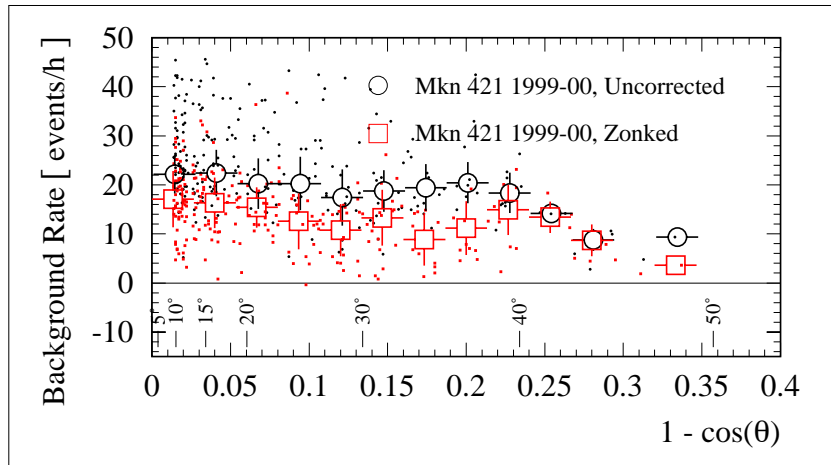


Figure 6.5: The background rate measured from the 1999-2000 dataset of Mkn 421 as a function of the zenith angle of the observation. The plotting method is equivalent to that used in Figures 6.3 and 6.4. See text.

Source: CT1 observations of Mkn 421 recorded in 1999-2000

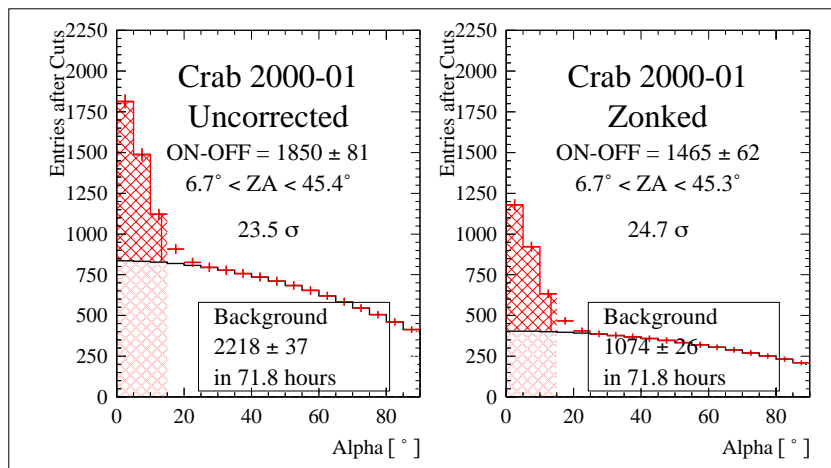


Figure 6.6: *Alpha* plot of the Crab reference data from January through March 2001; uncorrected data in the left-hand plot and data treated with the *Zonk* method in the right-hand plot.

Source: CT1 observations of Crab, recorded between January and March 2001

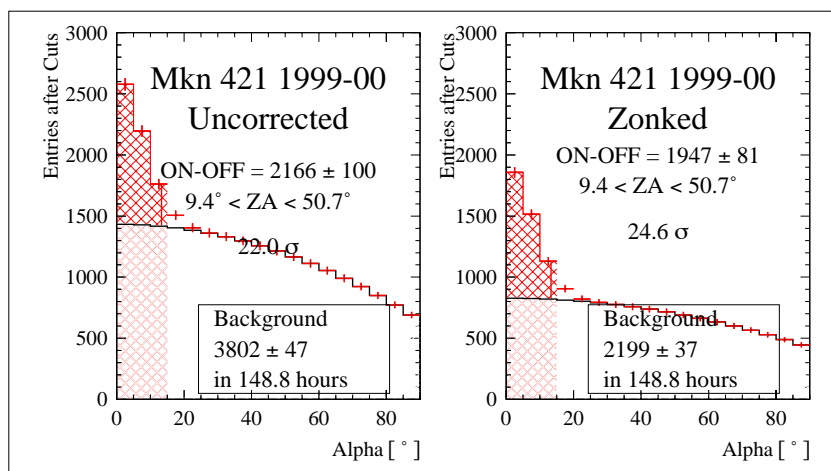


Figure 6.7: *Alpha* plot of the Mkn 421 dataset from 1999-2000; uncorrected data in the left-hand plot and data treated with the *Zonk* method in the right-hand plot.

Source: CT1 observations of Mkn 421 recorded in 1999-2000



## 7 Energy calibration and flux determination

In autumn 1998 the main reflector area was doubled to  $10.3\text{ m}^2$ . A new Monte Carlo simulation has since been developed to account for this change. Among other improvements this new simulation includes a trigger simulation that is based on a time resolved pulse shape simulation from single photoelectrons in the photomultipliers of CT1. As this simulation has been carried out by D. Sobczynska on the one hand and is on the other hand not described in full detail in the literature yet<sup>37</sup>, an appendix (Appendix 16) has been added which contains such a description<sup>38</sup>.

As noted earlier in this thesis no testbeam facility is available for carrying out an energy and flux calibration of Cherenkov telescopes.

While the initial impact parameter and energy are known for simulated  $\gamma$ -events, this information is missing in real data and must be calculated from measured quantities like image parameters and from external information like the zenith angle of the observation.

This chapter describes the estimation of initial energies for  $\gamma$ -candidate events and the derivation of effective areas, which are necessary to determine energy spectra and fluxes.

---

The energy range of CHERENKOV telescopes is of the order  $\mathcal{O}(\text{TeV})$ , i.e. so high that it is impossible to calibrate them with test beams, like calorimeters are calibrated in collider experiments. Therefore the interpretation of data collected with CHERENKOV telescopes relies on estimates from Monte Carlo simulations.

The characterisation of the telescope hardware elements for simulation purposes represents at best a time averaged definition. A major uncertainty stems from the lack of precise knowledge of the conversion factors from ADC counts to photoelectrons (c.f. Section 5.6), followed by uncertainties concerning mirror reflectivities and adjustment, which may vary with time and weather conditions. Long-term gain drifts in the electronics and the effects of the regular HV increases at the percent level intended to counterbalance photo-multiplier ageing are difficult to model. The noise level in photo-multipliers varies depending on whether or not a moon-observation was made earlier the same night. At best, a Monte Carlo simulation is a snapshot of an average system.

The approach chosen for the *Zonk* method (see Section 5.8 on page 64) attempts to account for most of these changes. The distributions of the hadrons are shifted to reference distributions before the analysis is continued. Along with the hadron distributions the image parameters of

---

<sup>37</sup>(Sobczynska and Lorenz, 2002) contains a description of the new trigger simulation approach.

<sup>38</sup>The description of the simulation process is not essential for the understanding of the CT1 data analysis, the extraction of calibration constants is. Therefore the analysis of the Monte Carlo data is described in the main body of the thesis.

the  $\gamma$ -images are also shifted. Therefore it is necessary to apply correction shifts also to the simulated  $\gamma$ -ray image parameters. The difficulty here is to find the correct shift values for the  $\gamma$ -images, as these must be derived solely from the hadronic distributions. This particular difficulty is addressed in Section 16.5 in the appendix.

## 7.1 Setup of the Monte Carlo simulation and the analysis presented in this thesis

Starting with a primary  $\gamma$ -ray or charged particle of a certain energy value, flight direction and impact parameter, the simulation procedure proceeds along five steps:

1. High energy processes in the shower are simulated that lead to the production of secondary particles which emit CHERENKOV light on their way through the atmosphere.
2. The loss of CHERENKOV photons due to ozone absorption and MIE and RAYLEIGH scattering in the atmosphere and in the optical system of the telescope are simulated until the light reaches the entrance windows of the photomultipliers.
3. The detector response is simulated, taking into account the optical and photosensor parameters. If the trigger decision is positive, a photoelectron image of the shower is recorded.
4. Background light is simulated and added to the showers' photoelectron images.
5. Finally the *Zonk* correction and the  $\gamma$ -hadron separating cuts are applied to the simulated data in the same way as real data is treated.

These topics are addressed in Appendix 16.

Comparing the simulated event sample with the event samples after trigger and after cuts, one can derive several quantities which allow one to characterise the simulated hardware and to extract spectra and fluxes from real data:

- the ratio of triggered to simulated events for showers impinging on a disc of a preset radius around the telescope, i.e. the trigger efficiency,
- the trigger efficiency integrated over the impact parameter, i.e. the effective area<sup>39</sup> for the trigger,
- the ratio of the number of  $\gamma$ -events after cuts to the number of simulated events, characterising the efficiency of a particular cut,
- the detection efficiency for  $\gamma$ -events integrated over the impact parameter range, i.e. the effective area after cuts and
- the threshold energy as a function of zenith angle and primary particle type and

---

<sup>39</sup>'Effective area' and 'effective collection area' are used synonymously.

- the energy as reconstructed from image parameters and the energy resolution.

These topics are addressed in the following chapter.

The energy estimation procedure is trained using Monte Carlo events. The energy estimation proceeds along two steps:

1. First the impact parameter is estimated from the image parameters *Dist*, *Width* and the zenith angle of the observation.
2. The primary energy rules the amount of light that reaches the ground around the telescope. The event *Size*, *Width*, *Length*, zenith angle information and the estimated impact parameter are used to calculate a guess value of the initial energy.

This sequence is motivated by the fact that the energy is strongly correlated to the *Size* of the recorded image. Figure 16.6 on page 165 shows this relation and in addition the fact that the image *Size* varies with impact parameter. The impact parameter cannot be measured directly with a single telescope but can be guessed from its relation to the image parameter *Dist*. As a fraction of the event's image often leaks out of the camera, the *Leakage* parameter is used to correct in first order.

The quality of the estimates of impact parameter and energy can be judged by comparing the simulated and estimated energy values for a Monte Carlo event sample. A further test is conducted in which the impact parameters and energies estimated for individual  $\gamma$ -candidate events from Mkn 421 are compared to those that were recorded simultaneously by both HEGRA CT1 and the CT SYSTEM, when the source was highly active.

When investigating source spectra which decrease steeply with increasing energy values using a method with non-zero energy resolution, the higher energy bins shall be populated with events that were wrongly assigned to these bins (so-called overspill), an error that occurs all the more frequently, the steeper the spectrum. In the Monte Carlo simulation the initial energy is known, therefore a systematic shift due to energy misassignments in the analysis of real data can be quantified and corrected for to a certain degree. Together with efficiency studies this allows one to deduce source spectra and flux estimates.

## 7.2 Impact parameter estimation

### 7.2.1 Procedure used in the present analysis

In an approach different from that discussed in (Kranich, 2001), the scaling of the ratio *Dist* / *Width* with the impact parameter<sup>40</sup> is employed to estimate the impact parameter  $I_r$  (the index  $r$  stands for 'reconstructed') of an individual  $\gamma$ -candidate event. A first interpretation is that an event's *Dist* value is most certainly connected to the impact parameter of the primary. This connection is shown in Figure 7.1. Around the 'hump' of the light distribution (c.f.

---

<sup>40</sup>The impact parameter is the distance of the hypothetical impact point of the primary on the ground to the telescope. A set of Monte Carlo  $\gamma$  and proton events was simulated at different energies and the amount of light in the camera was investigated as a function of the impact parameter. The result is shown in Appendix 16.2 in Figure 16.6.

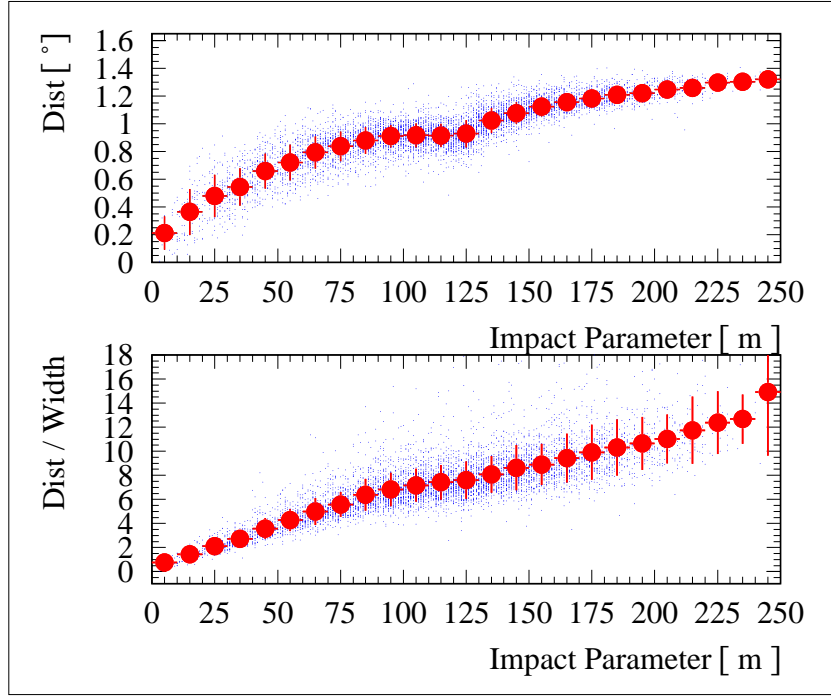


Figure 7.1: Values of  $Dist$  (upper plot) and of the ratio  $Dist/Width$  (bottom plot) drawn versus the simulated impact parameter for simulated  $\gamma$ -events of  $15^\circ$  zenith angle.  
Source: Monte Carlo simulation for CT1

Figure 16.6), a characteristic kink is visible. This kink is related to the maximum CHERENKOV angle from on-axis tracks. As shown in Figure 7.1 the ratio  $Dist / Width$  is more universally connected to the impact parameter than either image parameter alone. Therefore the impact parameter is estimated as

$$I_r = (a_i + b_i \cdot Dist/Width + c_i \cdot Leakage) \cdot \left( \frac{1}{\cos(\theta)} + \frac{d_i}{\cos^2(\theta)} \right), \quad (7.1)$$

where

$a_i$  to  $d_i$  are the parameters of this estimate, the index 'i' referring to the impact parameter,

$\theta$  is the zenith angle of the observation and

$Dist$ ,  $Width$  and  $Leakage$ <sup>41</sup> are the image parameter values of the event in question.

For each event a normalised impact parameter difference  $\Delta I$  between the simulated and the estimated impact parameter is calculated as

$$\Delta I := \frac{I_{mc} - I_r}{I_{mc}}, \quad (7.2)$$

where

<sup>41</sup>For the definition and meaning of the  $Leakage$  parameter see Section 5.7.2 on page 59.

Parameter	Value	Unit
$a_i$	$12.6 \pm 2.7$	m
$b_i$	$9.2 \pm 1.2$	m
$c_i$	$88.7 \pm 18.7$	m
$d_i$	$0.18 \pm 0.12$	—

Table 7.1: Parameters  $a_i$  through  $d_i$  and their errors. These parameters are used to estimate the impact parameter of  $\gamma$ -candidates for the cut  $m421\_01\_z$  and events from Mkn 421 (recorded in 1999-2000).

$I_{mc}$  is the initial impact parameter and

$I_r$  is the reconstructed impact parameter for the Monte Carlo event in question.

The parameters  $a_i$  to  $d_i$  are not known beforehand. They are determined with a routine from the MINUIT software package (CN/ASD Group, 1994) that minimises the value of the mean squared error  $MSE(\Delta I)$ , defined as

$$MSE(\Delta I) := \sigma^2(\Delta I) + bias^2(\Delta I) = \langle (\Delta I)^2 \rangle \quad , \quad (7.3)$$

where

$\sigma(\Delta I)$  is the width and

$bias(\Delta I)$  is the mean value of the distribution of  $\Delta I$ .

The parameters  $a_i$  to  $d_i$  are optimised for a given  $\gamma$ -hadron separation cut and for a particular data set, whose pedestal RMS distribution served to simulate the night sky noise for the Monte Carlo analysis (c.f. Appendix 16.5). As an example the parameters  $a_i$  to  $d_i$  for the  $m421\_01\_z$  cut, adjusted to Mkn 421 data recorded in 1999-2000, are given in Table 7.1.

The distribution of  $bias(\Delta I)$  is shown as a function of the simulated energy in Figure 7.2. The values for different zenith angles are plotted separately. The impact parameter is overestimated at small energies with the lowest data points containing very low statistics. The impact parameter resolution for a set of zenith angles, given here as the RMS width of the distribution of  $\Delta I$  as a function of the initial energy, is shown in Figure 7.3. The overall resolution is around 10 to 20% , with better estimates for higher energies.

## 7.2.2 Quality of the impact parameter reconstruction

In order to give an example of the performance of the reconstruction procedure, the estimated impact parameter is plotted on the left-hand side of Figure 7.4 versus the simulated impact parameter for all Monte Carlo events that passed the  $m421\_01\_z$  cut and whose *Alpha* values were below  $13.3^\circ$ . A set of Mkn 421 events, recorded simultaneously by the HEGRA CT SYSTEM and CT1, when Mkn 421 was highly active during the period January to March 2001, is used to compare the impact parameter estimates of both instruments. The plot on the right-hand side of Figure 7.4 displays the CT SYSTEM estimates on the  $x$ -axis and the CT1 results

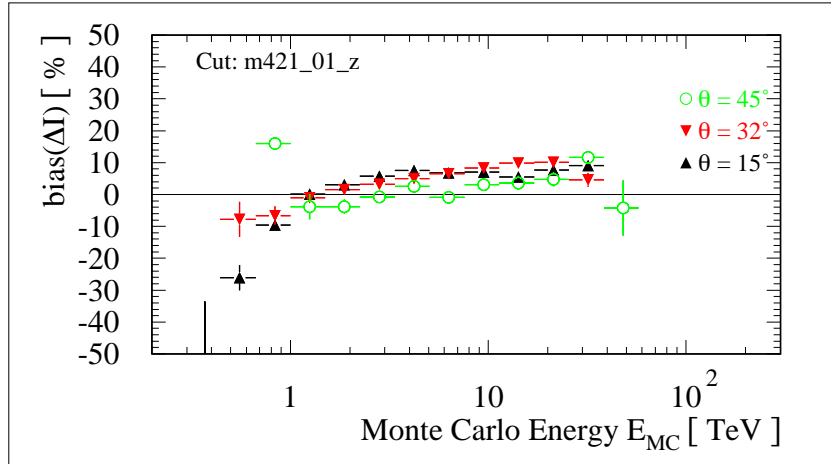


Figure 7.2: The mean values of the relative difference between estimated and actually simulated impact parameter, the quantity  $bias(\Delta I)$ , drawn versus the simulated energy for a set of different zenith angles. A certain overall bias of the estimates is accepted by the optimisation routine, as the RMS of the distribution of  $\Delta I$  is considered as well. Note that the two data points with the largest negative values of  $bias(\Delta I)$  contain very low statistics. Source: Monte Carlo simulation for CT1

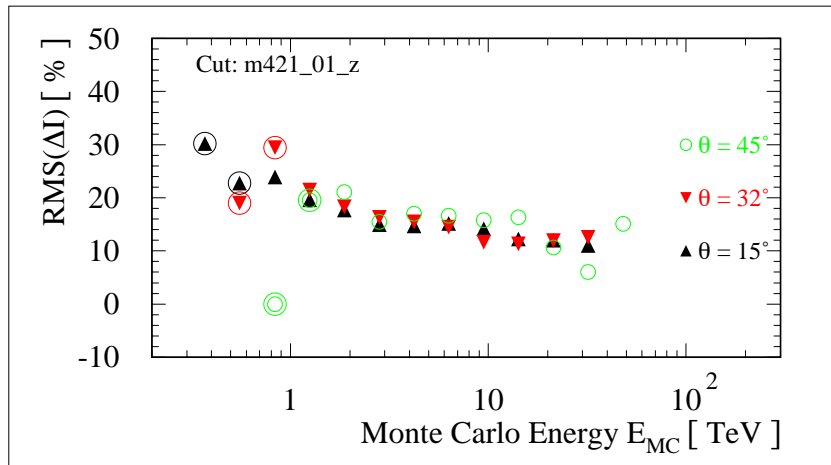


Figure 7.3: The values of  $RMS(\Delta I)$  drawn versus the simulated energy for data sets at different zenith angles. Data points in energy bins with trigger efficiencies below 5% have been marked with an additional circle. The RMS estimate at the lowest energy points is biased due to low event statistics that triggered the telescope and passed the  $\gamma$ -hadron separation. Source: Monte Carlo simulation for CT1

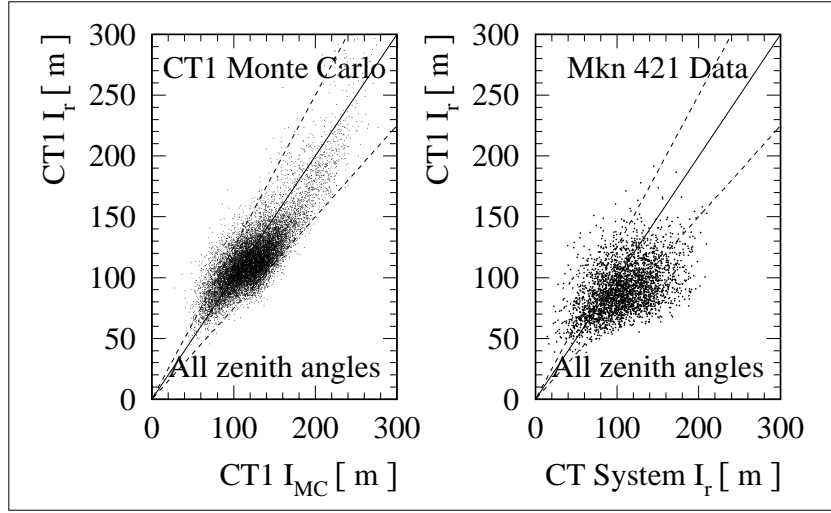


Figure 7.4: Left-hand plot: comparison of simulated and estimated impact parameters from CT1 Monte Carlo events. Right-hand plot: coincident events from a Mkn 421 highly active period recorded simultaneously with HEGRA CT1 and CT SYSTEM in January 2001. The  $\pm 25\%$  error bands around the perfect match are marked by dashed lines. The coincident events were required to occur within a time window of  $\pm 2$  ms around the CT1 event time. Source: CT1 Monte Carlo simulation, Mkn 421 data from January to March 2001, recorded with HEGRA CT1 and CT SYSTEM

on the  $y$ -axis. The  $\gamma$ -candidate events were identified by the requirement that their event time stamps from both instruments be equal within a narrow time window of  $\pm 2$  ms. A detailed description of the search method is given in (Kranich, 2001). The same data has been plotted in a normalised manner in a second plot, shown in Figure 7.5. The rather poor agreement with the CT SYSTEM is unexplainable for the time being.

### 7.3 Energy estimation of the primary particle

#### 7.3.1 Procedure used in this analysis

In a slightly different approach from that in (Kranich, 2001), the following formula is used to estimate the initial energy  $E_r$  (the index  $r$  stands for 'reconstructed') for individual events:

$$E_r = \left( a_e + b_e \cdot \frac{Size}{Width} + c_e \cdot I_r + d_e \cdot Leakage \right) \cdot \left( \frac{1}{\cos^2(\theta)} + \frac{e_e}{\cos^3(\theta)} + \frac{f_e}{\cos^4(\theta)} \right), \quad (7.4)$$

where

$a_e$  to  $f_e$  are the fitted parameters with the index 'e' referring to the energy,

$\theta$  is the zenith angle of the observation or simulation and

$Size$ ,  $Width$ ,  $Length$  and  $Leakage$ <sup>42</sup> are the image parameter values of the event being evaluated.

<sup>42</sup>For the definition and meaning of the *Leakage* parameter see Section 5.7.2.

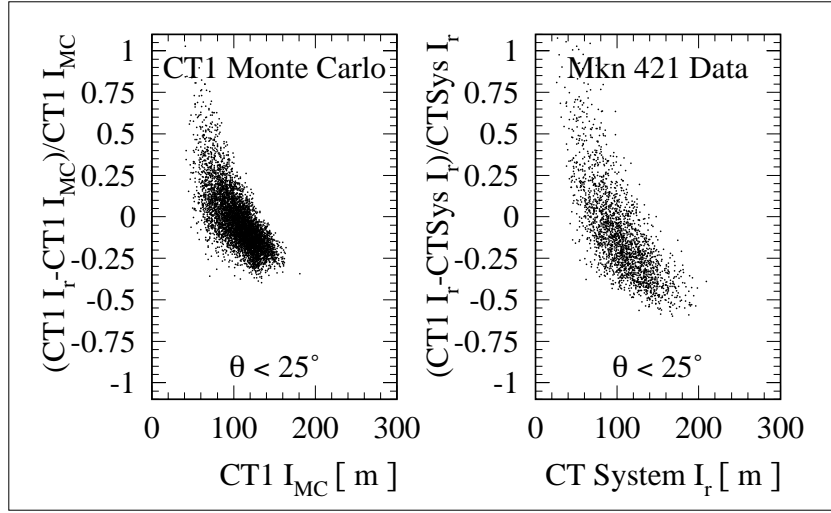


Figure 7.5: Left-hand plot: relative difference of simulated and estimated impact parameters for CT1 Monte Carlo events, plotted as a function of the simulated impact parameter. Right-hand plot: relative difference of the reconstructed impact parameter for CT1 and CT SYSTEM for coincident events from Mkn 421. For both plots the zenith angle  $\theta$  was limited to values below  $25^\circ$ .

Source: CT1 Monte Carlo simulation, Mkn 421 data from January to March 2001, recorded with HEGRA CT1 and CT SYSTEM

A normalised energy difference  $\Delta E$  is calculated as

$$\Delta E := \frac{E_{mc} - E_r}{E_{mc}} \quad , \quad (7.5)$$

where

$E_{mc}$  is the simulated energy.

$\Delta E$  is used to optimise the parameters  $a_e$  to  $f_e$  of the energy reconstruction in the same way as in the impact parameter estimation with a MINUIT routine that minimises the value of the mean squared error  $MSE(\Delta E)$ . It is defined as

$$MSE(\Delta E) := \sigma^2(\Delta E) + bias^2(\Delta E) = \langle (\Delta E)^2 \rangle \quad , \quad (7.6)$$

where

$\sigma(\Delta E)$  is the width and

$bias(\Delta E)$  is the mean value of the distribution of  $\Delta E$ .

The values of the parameters  $a_e$  to  $f_e$  used for the energy estimation are summarised in Table 7.2. For each data set, the respective set of estimation parameters  $a_i$  to  $d_i$  and  $a_e$  to  $f_e$  have been used for the calculation of the effective areas (see the following chapter).

The distribution of the mean of  $\Delta E$ , called  $bias(\Delta E)$ , is shown in Figure 7.6 for bins of simulated energy  $E_{MC}$ . Figure 7.7 shows the RMS of the distribution of the values of  $\Delta E$

Parameter	Value	Unit
$a_e$	$4.05 \pm 0.92$	TeV
$b_e$	$0.0072 \pm 0.0014$	TeV $\cdot$ ( $^\circ$ ) $\cdot$ ph. el. $^{-1}$
$c_e$	$-0.0392 \pm 0.0085$	TeV $\cdot$ m $^{-1}$
$d_e$	$31.9 \pm 6.8$	TeV
$e_e$	$-1.460 \pm 0.049$	—
$f_e$	$0.625 \pm 0.021$	—

Table 7.2: Parameters values  $a_e$  to  $f_e$  as used to estimate the energies of individual  $\gamma$ -candidates for the cut  $m421\_01\_z$  for the Mkn 421 data set of 1999-2000.

Bin Number	1	2	3	4	5	6	7	8
Upper Bound [TeV]	0.06	0.09	0.13	0.20	0.30	0.44	0.67	1.00
Lower Bound [TeV]	0.0	0.06	0.09	0.13	0.20	0.30	0.44	0.67
Bin Number	9	10	11	12	13	14	15	16
Upper Bound [TeV]	1.50	2.25	3.38	5.06	7.59	11.39	17.09	25.63
Lower Bound [TeV]	1.00	1.50	2.25	3.38	5.06	7.59	11.39	17.09
Bin Number	17	18	19	20	—	—	—	—
Upper Bound [TeV]	38.44	57.67	80.0	400.0				
Lower Bound [TeV]	25.63	38.44	57.67	80.0				

Table 7.3: Energy bounds as used in the analysis. The bin size was chosen to be roughly twice the energy resolution. Bins number 1 and number 20 are not used.

as estimator for the energy resolution of the telescope. The RMS is typically 25% with some modest improvement at higher energies. The energy bins for the spectrum determination were chosen to have a width of roughly twice the resolution. This avoids correlations from bin to bin. The bin borders are given in Table 7.3.

### 7.3.2 Quality of the energy reconstruction

The energy estimates for the set of events whose impact parameter estimates are shown in Figures 7.4 and 7.5 are displayed in Figures 7.8 and 7.9. The simulated and the reconstructed energies nicely agree with each other.

## 7.4 Trigger and cut efficiencies

### 7.4.1 Trigger efficiency

The trigger efficiency<sup>43</sup>  $\eta_{trig}(\theta, E, r)$  is defined as that fraction of events arriving on a uniformly populated disc ring with radius  $r$  and width  $dr$  that triggers the readout system of the telescope at a given zenith angle  $\theta$ , and initial energy  $E$ . The estimator for this quantity is

$$\eta_{trig}(\theta, E, r) := \frac{N_{trig}(\theta, E, r)}{N_{sim}(\theta, E, r)}, \quad (7.7)$$

<sup>43</sup>The trigger efficiency is often also called trigger probability. The emphasis in this thesis, however, is on the fact that this quantity describes a hardware property. Therefore the term ‘efficiency’ is used here.

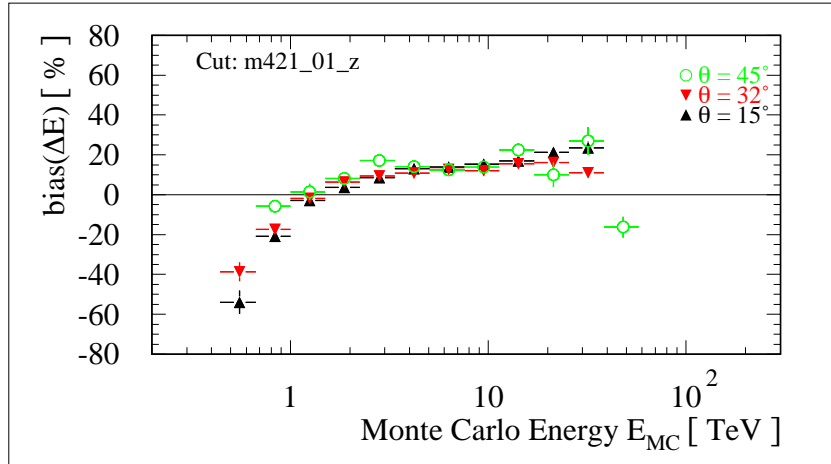


Figure 7.6: The mean normalised difference  $\Delta E$  between the simulated and the reconstructed energy values drawn as a function of the simulated energy. The plot shows  $bias(\Delta E)$  as a function of the simulated energy for a set of different zenith angles.

Source: Monte Carlo simulation for CT1

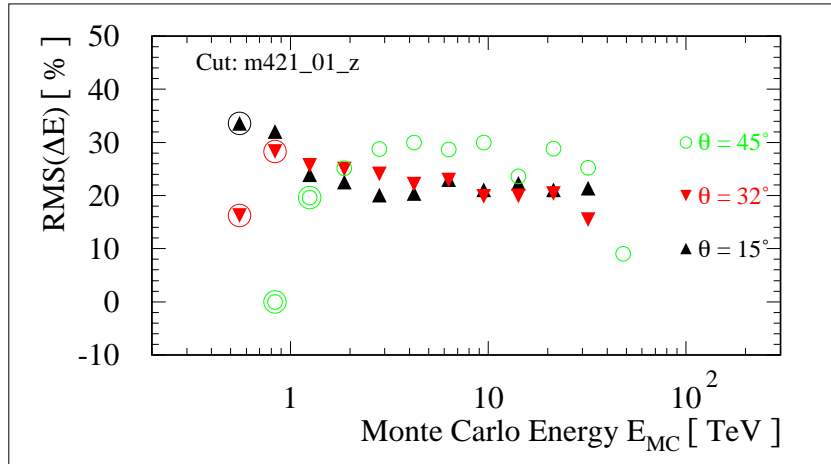


Figure 7.7: The values of  $RMS(\Delta E)$  drawn as a function of the simulated energy for four different zenith angles. Data points in energy bins with trigger efficiencies below 5% have been marked with an additional circle. The RMS estimate of the lowest energy points are biased due to low event statistics that triggered the telescope and passed the  $\gamma$ -hadron separation.

Source: Monte Carlo simulation for CT1

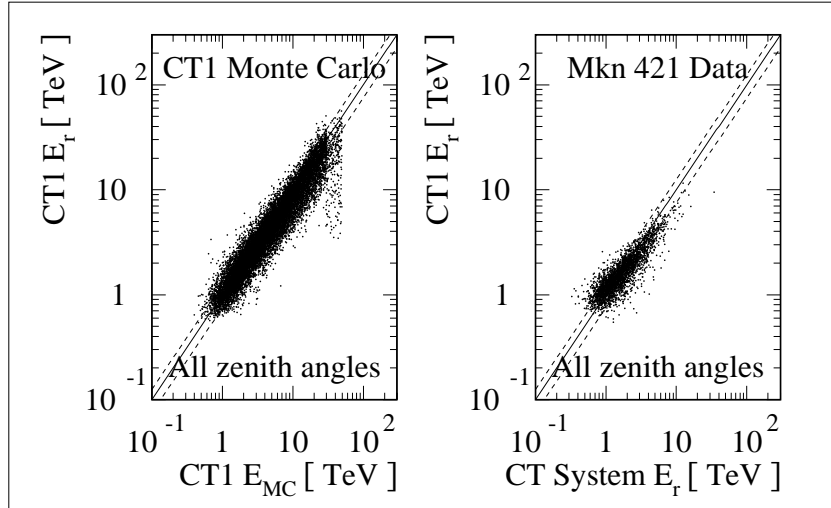


Figure 7.8: Comparison of simulated and estimated energy for CT1 Monte Carlo events (left-hand side) and for coincident events from a Mkn 421 highly active period recorded simultaneously with HEGRA CT1 and CT SYSTEM (right hand side). The  $\pm 25\%$  regions around the perfect match are marked with dashed lines. The coincident events were required to occur within a time window of  $\pm 2$ ms around the CT1 event time.

Source: CT1 Monte Carlo simulation, Mkn 421 data from January to March 2001, recorded with HEGRA CT1 and CT SYSTEM

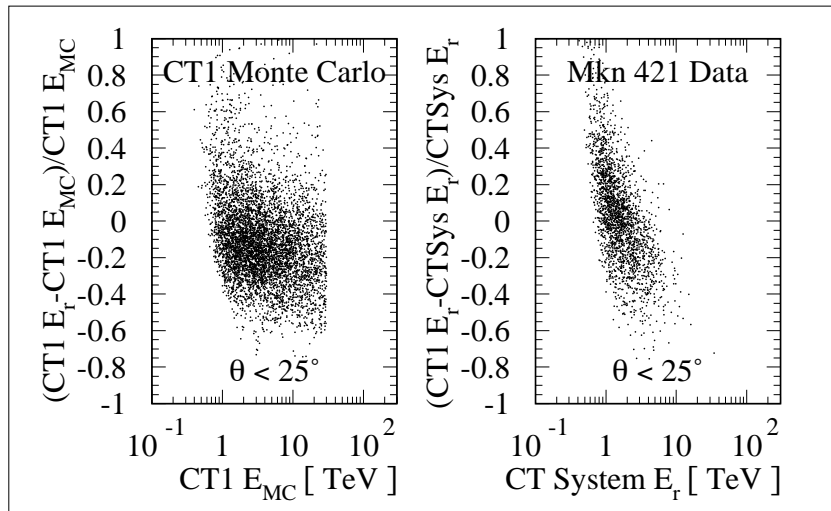


Figure 7.9: Left-hand plot: relative difference of simulated and estimated energy from CT1 Monte Carlo events as a function of the simulated energy. Right-hand plot: relative difference of the reconstructed energy for CT1 and CT SYSTEM from coincident events from Mkn 421. For both plots the zenith angle  $\theta$  was limited to values below  $25^\circ$ .

Source: CT1 Monte Carlo simulation, Mkn 421 data from January to March 2001, recorded with HEGRA CT1 and CT SYSTEM

Bin Number	1	2	3	4	5	6	7	8
Upper Bound [°]	14.07	19.95	24.50	28.36	31.79	34.92	37.81	40.54
Lower Bound [°]	0.0	14.07	19.95	24.50	28.36	31.79	34.92	37.81
Bin Number	9	10	11	12	13	14	15	16
Upper Bound [°]	43.11	45.57	47.93	50.21	52.41	54.55	56.63	58.67
Lower Bound [°]	40.54	43.11	45.57	47.93	50.21	52.41	54.55	56.63
Bin Number	17	18	19	20	—	—	—	—
Upper Bound [°]	60.66	62.61	64.53	66.42				
Lower Bound [°]	56.63	60.66	62.61	64.53				

Table 7.4: Zenith angle bounds as used in the current analysis of Monte Carlo quantities. In analyses of real data the statistics rule the chosen zenith angle intervals.

where

$N_{trig}(\theta, E, r)$  is the number of events which pass the trigger condition and passed the noise filter cut,

$N_{sim}(\theta, E, r)$  is the number of simulated events.

In general, the trigger efficiency is smaller for larger impact parameters and rises with increasing primary energy. At larger zenith angles a higher onset for the trigger efficiency in energy is observed. This is due to the geometry of the Earth's atmosphere together with the directed emission of CHERENKOV light and the stronger suppression through MIE and RAYLEIGH scattering along the longer paths in the atmosphere.

In order to calculate the trigger efficiency, the Monte Carlo events are sorted into bins in  $\theta$ ,  $E$ , and  $r$ , marked as  $\Delta\theta$ ,  $\Delta E$ ,  $\Delta r$ , respectively. Then the trigger efficiency is calculated according to the definition

$$\eta_{trig}(\Delta\theta, \Delta E, \Delta r) := \frac{N_{trig}(\Delta\theta, \Delta E, \Delta r)}{N_{sim}(\Delta\theta, \Delta E, \Delta r)} . \quad (7.8)$$

The energy bin limits are given in Table 7.3. The impact parameter was binned in intervals of 20 m, which is a rather fine binning. The zenith angle binning is given in Table 7.4. The zenith angle bins are needed in the analysis of real data and for the extraction of parameters which enter the simulation and vary depending on the zenith angle, like e.g. the pedestal RMS values for night sky noise simulation. The Monte Carlo  $\gamma$ -events were simulated at a set of fixed zenith angles, as shown in Figure 16.11 on page 171.

#### 7.4.2 Cut efficiency

The cut efficiency  $\eta_{cut}(\theta, E, r)$ , which is also called  $\gamma$ -efficiency, is defined as the fraction of triggering  $\gamma$ -events that pass the  $\gamma$ -hadron separating cuts, i.e. those  $\gamma$ -events that are in fact considered as  $\gamma$ -candidates. It is defined as:

$$\eta_{cut}(\theta, E, r) := \frac{N_{cut}(\theta, E, r)}{N_{trig}(\theta, E, r)} , \quad (7.9)$$

where

$N_{cut}(\theta, E, r)$  is the number of events that pass the image parameter cuts.

The estimator is calculated in binned form as

$$\eta_{cut}(\Delta\theta, \Delta E, \Delta r) := \frac{N_{cut}(\Delta\theta, \Delta E, \Delta r)}{N_{trig}(\Delta\theta, \Delta E, \Delta r)} . \quad (7.10)$$

Both the trigger and the cut efficiency are needed for the calculation of effective areas, as is described in the following.

## 7.5 Effective trigger areas

Folding the trigger efficiency for a given zenith angle, energy, and impact parameter with the ring area corresponding to this impact parameter yields an effective area, which is equivalent to the size of a (hypothetical) detector where the arrival of any single particle triggers readout. The effective trigger area  $A_{trig}(\theta, E)$  ('trigger area' in the following) is defined as

$$A_{trig}(\theta, E) := 2\pi \cdot \int_0^{r_{max}} \eta_{trig}(\theta, E, r) \cdot r \, dr \quad , \quad (7.11)$$

with  $r_{max}$  equal to the maximum impact parameter where no more triggers are generated.

With the usual binning in zenith angle, energy, and impact parameter, this corresponds to:

$$A_{trig}(\Delta\theta, \Delta E) := \pi \cdot \sum_{\Delta r_i = \Delta r_0}^{\Delta r_{max}} \eta_{trig}(\Delta\theta, \Delta E, \Delta r_i) \cdot (r_{i+1}^2 - r_i^2) \quad , \quad (7.12)$$

where

$\Delta\theta$  is the zenith angle bin,

$\Delta E$  is the energy bin and

$\Delta r_i$  is the  $i$ -th impact parameter bin. The first impact parameter bin  $\Delta r_0$  starts at an impact parameter of  $r_0 = 0$  m and extends to  $r_1$ , the upper bound of the first impact parameter bin, which is equivalent to the lower bound of the second bin.

The other bins are defined accordingly.

The largest simulated impact parameter values, i.e. the upper end of bin  $\Delta r_{max}$ , were chosen large enough to prevent any single event from this bin from triggering the telescope. An illustration is given in Figure 16.12 on page 172. Thus it is ensured that the entire impact parameter range accessible by the telescope is covered by the simulation. The effective trigger areas as a function of energy for different simulated zenith angles are shown in Figure 7.10. The trigger areas rise very quickly to sizes which are much larger than the geometrical size of the telescope itself, an advantage of the ground based CHERENKOV telescopes over space borne detectors. The latter have trigger areas corresponding only to their actual size while the Earth's atmosphere allows CHERENKOV telescopes to collect events which do not hit the instrument directly.

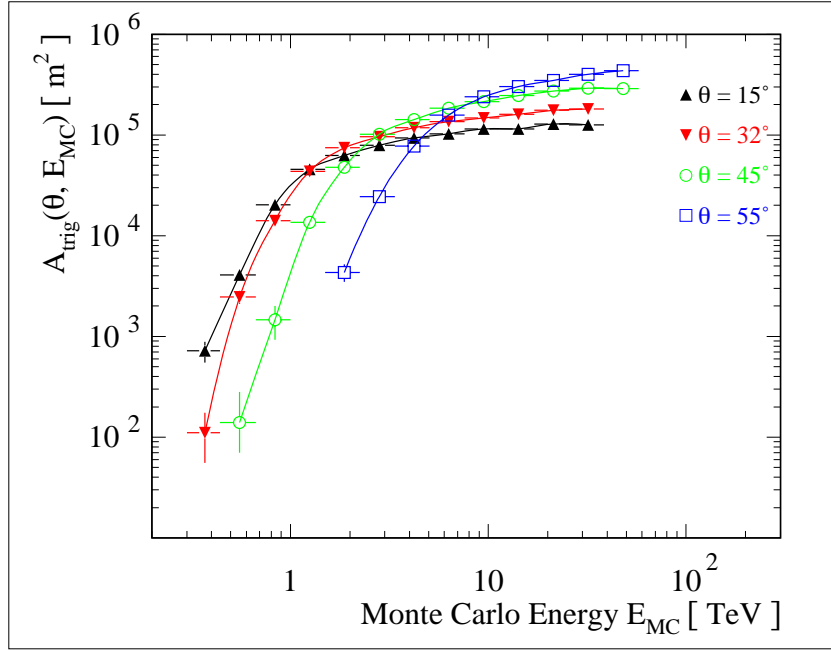


Figure 7.10: Effective trigger areas  $A_{trig}(\theta, E)$  drawn as a function of the simulated energy for four simulated zenith angles. The dependence of the trigger efficiency  $\eta_{trig}(\theta, E)$ , which rises with increasing values of zenith angle and energy, is mirrored in the shape of the corresponding effective trigger areas.

Source: Monte Carlo simulation for CT1

## 7.6 Energy threshold estimation for CT1

Two different definitions of the threshold energy are used to compare different CHERENKOV telescopes:

1. The energy where the observed differential spectrum after trigger peaks when a Crab-like energy spectrum is simulated.
2. The energy where the effective collection area crosses a value of  $10^4 \text{ m}^2$ .

The second definition is less commonly used and is not discussed any further here.

The CT1 response to a Crab-like spectrum is simulated in the following way: the effective trigger areas are multiplied bin by bin with a flux histogram. The flux histogram has been filled bin by bin with the bin-wise integrals over the differential flux function<sup>44</sup>

$$\frac{dF}{dE} = 2.7 \cdot 10^{-7} \cdot \left( \frac{E}{\text{TeV}} \right)^{-2.7} \text{ m}^{-2} \text{ s}^{-1} \text{ TeV}^{-1} \quad . \quad (7.13)$$

The resulting product represents the number of triggering events per unit time for a given energy bin. When the contents of the resulting histogram multiplied with the bin widths are summed up bin by bin, the result is equal to the estimated trigger rate for  $\gamma$ s arriving on Earth

<sup>44</sup>This function was chosen to be close to the differential energy spectrum of Crab measured with the HEGRA CT SYSTEM (Aharonian et al., 2000).

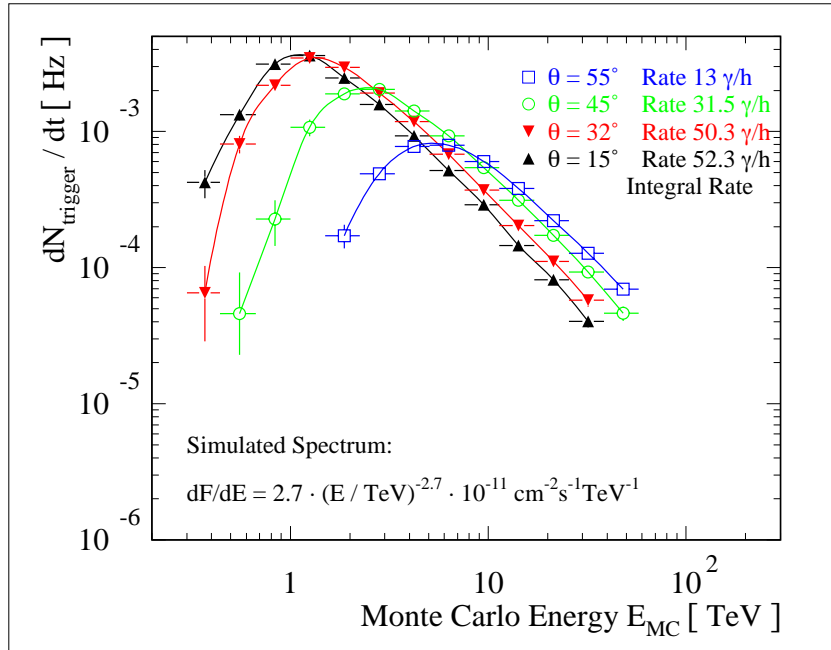


Figure 7.11: The estimated trigger rate as a function of the simulated energy is drawn for a simulated stream of  $\gamma$ s which follow the energy spectrum quoted in the figure, the simulation predicts the integral trigger rates as indicated for the different zenith angles. The peak positions of these distributions are usually referred to as the energy threshold of the telescope. The estimates of the threshold energies for the complete set of simulated zenith angles are shown in Figure 7.12.

Source: Monte Carlo simulation for CT1

from a source that emits a Crab-like spectrum. It is found that close to 52  $\gamma$ -events per hour should trigger CT1 at a zenith angle of  $15^\circ$  in the entire range of energies accessible with CT1.

The peaks of the triggered spectra were estimated from a simple spline interpolations that connect the entries in the histograms of Figure 7.11. The estimated trigger threshold as a function of the simulated zenith angle is plotted in Figure 7.12. With the definitions used above and the current understanding of the trigger process, the lowest energy threshold of CT1 is attained for the smallest zenith angles at values close to 1 TeV .

- It must be noted that the results shown here were obtained using the night sky background as measured in Crab observations and without applying any cut to the image parameter *Size*. Thus the results represent pure counting of triggering events. The aim was to obtain results which can be compared easily with other telescopes' performance characteristics.
- It should also be noted that the threshold as defined above is running with the spectral powerlaw index  $\alpha$ . For small values of  $\alpha$ , so-called 'hard' spectra, the threshold is determined higher than for 'soft' spectra with large values of  $\alpha$ .

## 7.7 Effective areas after software cuts

Similarly to the effective trigger areas, the effective cut areas correspond to the size of a hypothetical instrument that is 100% efficient in the collection of  $\gamma$ -events that the CT1

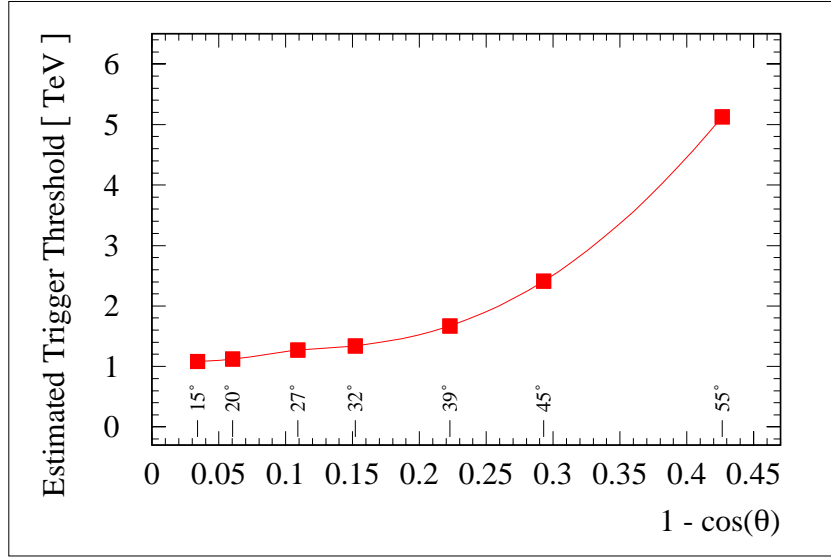


Figure 7.12: Energy threshold estimates for CT1 derived from the estimated peak positions of the triggered spectra  $dN_{trigger}/dt$  (c.f. Figure 7.11) for a simulated Crab source for the different zenith angles in the Monte Carlo simulation.

Source: Monte Carlo simulation CT1

analysis would class as  $\gamma$ -candidates of the triggering  $\gamma$ -sample. The effective area after cut  $A_{cut}(\theta, E_{MC})$  for the observation of events of initial energies  $E_{MC}$  under a zenith angle  $\theta$  is calculated according to the following definition:

$$A_{cut}(\theta, E_{MC}) := 2\pi \cdot \int_0^{r_{max}} \eta_{trig}(\theta, E_{MC}, r) \cdot \eta_{cut}(\theta, E_{MC}, r) \cdot r \, dr \quad . \quad (7.14)$$

Using the same binning as above, this becomes:

$$A_{cut}(\Delta\theta, \Delta E_{MC}) := \pi \cdot \sum_{\Delta r_i = \Delta r_0}^{\Delta r_{max}} \eta_{trig}(\Delta\theta, \Delta E_{MC}, \Delta r_i) \cdot \eta_{cut}(\Delta\theta, \Delta E_{MC}, \Delta r_i) \cdot (r_{i+1}^2 - r_i^2) \quad . \quad (7.15)$$

Note that the effective areas are determined as a function of the simulated energy  $E_{MC}$ . The analysis of real data, however, only deals with estimated energies  $E_{Est}$ . In order to avoid any bias, the effective areas are corrected using a set of correction constants  $\kappa(\Delta\theta, \Delta E)$ , which are defined as

$$\kappa(\Delta\theta, \Delta E) := \frac{N(\Delta\theta, \Delta E_{MC})}{N(\Delta\theta, \Delta E_{Est})} \quad , \quad (7.16)$$

where

$N(\Delta\theta, \Delta E_{MC})$  is the number of simulated  $\gamma$ -events in a certain zenith angle bin  $\Delta\theta$  and Monte Carlo energy bin  $\Delta E_{MC}$  and

$N(\Delta\theta, \Delta E_{Est})$  is the number of  $\gamma$ -events in a certain zenith angle bin  $\Delta\theta$  whose energies have been estimated so as to fall into the energy bin  $\Delta E_{Est}$ , using the same bin borders as for the Monte Carlo energy, see Table 7.3 on page 95.

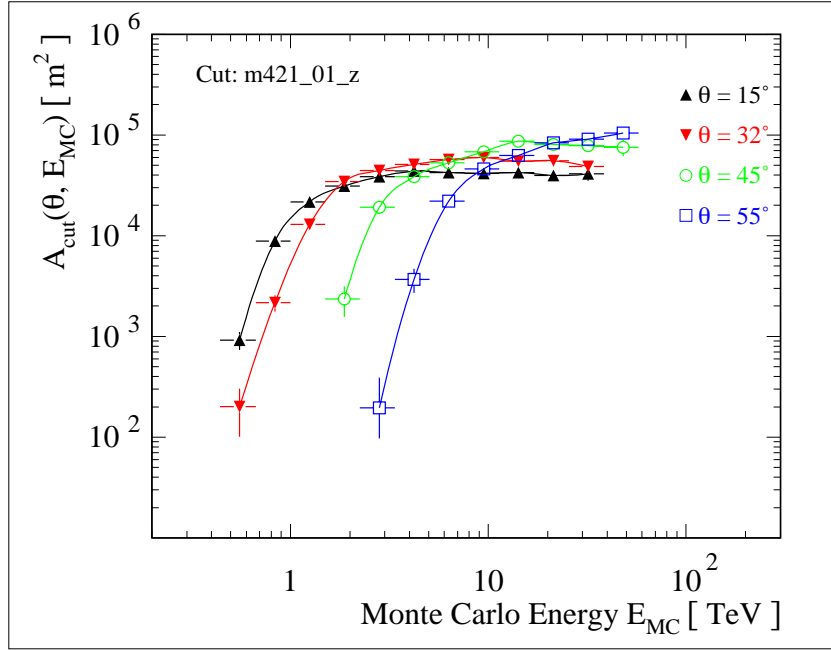


Figure 7.13: Effective cut areas  $A_{cut}(\theta, E_{MC})$  as a function of the simulated energy for the cut  $m421_01_z$  for selected simulated zenith angles. Similar to the case of the trigger areas, the shape of the  $\gamma$ -efficiencies is mirrored in the shape of the respective cut area. Source: Monte Carlo simulation for CT1

The values of  $\kappa(\Delta\theta, \Delta E)$  are determined separately for each selected differential spectral index, as the overspill of events from a given energy bin into another energy bin varies for different spectral indices. The values of  $\kappa(\Delta\theta, \Delta E)$  are calculated for each bin identified by zenith angle, energy and for a set of spectral indices. The dependence of  $\kappa$  on the latter is omitted here for the purpose of clarity, but is used for the (iterative) determination of energy spectra and fluxes, as is described below.

Multiplying the correction factors  $\kappa(\Delta\theta, \Delta E)$  and the effective areas  $A_{cut}(\Delta\theta, \Delta E_{MC})$  yields the effective cut areas for the estimated energy scale:

$$A_{cut}(\Delta\theta, \Delta E_{Est}) = A_{cut}(\Delta\theta, \Delta E_{MC}) \cdot \kappa(\Delta\theta, \Delta E) \quad . \quad (7.17)$$

## 7.8 Formalism for spectrum and flux determination in this analysis

The analysis of TeV energy spectra and fluxes yields the differential flux  $\frac{dF_\gamma(E, t)}{dE}$  of photons, which is defined as:

$$\frac{dF_\gamma(E, t)}{dE} = \frac{dN_\gamma(E, t)}{dt \cdot dA \cdot dE} \quad , \quad (7.18)$$

where the differentials

$dN_\gamma$ ,  $dt$ ,  $dA$  and  $dE$  denote increments of the number of  $\gamma$ -rays  $N_\gamma$ , of the observation time  $t$ , the collection area  $A$ , and the energy  $E$  respectively.

The term ‘energy spectrum’, used in the following, refers to this differential photon flux.

Reordering gives the increment of  $\gamma$ -rays  $dN_\gamma$  as

$$dN_\gamma(E, t) = \frac{dF_\gamma(E, t)}{dE} \cdot dt \cdot dA \cdot dE \quad . \quad (7.19)$$

The number  $\Delta N_\gamma$  of  $\gamma$ -rays arriving in a collection area element  $\Delta A$  and in an energy interval  $\Delta E$  during a finite time interval  $\Delta t$  is equal to

$$\Delta N_\gamma(E, t) = \frac{dF_\gamma(E, t)}{dE} \cdot \Delta t \cdot \Delta A \cdot \Delta E \quad . \quad (7.20)$$

$\Delta A$  in this equation may be identified with the effective cut area as defined in Section 7.7. The number of excess  $\gamma$ -events  $\Delta N_\gamma^{coll}$  is then determined from the observation time, the collection area and the flux emitted by the source:

$$\Delta N_\gamma^{coll}(E, t, \theta) = \frac{dF_\gamma(E, t)}{dE} \cdot \Delta t(\theta) \cdot A_{cut}(E, \theta) \cdot \Delta E \quad . \quad (7.21)$$

Here the dependence of the individual quantities on the initial energy  $E$  and the zenith angle  $\theta$  has been added — it had been omitted above for the purpose of clarity.

The goal of this analysis is to use the observed (excess)  $\gamma$ -rate as a basis for calculating a time-averaged differential photon flux and an energy-integrated flux as a function of time.

In summary the **differential energy spectrum**  $\frac{dF_\gamma(E, t)}{dE}$  is determined as

$$\frac{dF_\gamma(E, t)}{dE} = \frac{dN_\gamma(E, t)}{dt \cdot dA \cdot dE} \quad , \quad (7.22)$$

and the **flux**  $\mathcal{F}_\gamma(t)$  above a certain energy threshold  $E_{thr}$  is determined as

$$\mathcal{F}_\gamma(t) = \int_{E_{thr}}^{\infty} \frac{dF_\gamma(E, t)}{dE} dE \quad . \quad (7.23)$$

### 7.8.1 Determination of energy spectra from CT1 data

Using the effective areas after cut  $A_{cut}(\Delta\theta, \Delta E_{Est})$  as determined from the Monte Carlo simulation and a Crab-like input spectrum, the estimated excess rate after cuts for this spectrum can be expressed in a way similar to the simulated trigger rates for a Crab-like source that are shown in Figure 7.11. Figure 7.14 shows the expected excess  $\gamma$ -rate as a function of the energy for four selected zenith angles. The peak of the differential rate is highest for the smallest zenith angle and decreases with increasing zenith angles, as mainly high-energy events are collected at larger zenith angles.

In order to calculate energy spectra and fluxes of TeV  $\gamma$ -rays from CT1 data, the excess rate  $\Delta R / \Delta E_{Est}$  per bin of estimated energy  $\Delta E_{Est}$  is estimated according to the specifications given in Section 6.3 and (Kranich, 2001). As mentioned above, this rate is known only as a function of the estimated energy  $E_{Est}$ , while the effective cut area was initially calculated for the simulated energy  $E_{MC}$ . This difference is resolved by the use of correction parameters  $\kappa(\Delta\theta, \Delta E)$  (c.f. Section 7.7). The excess rate divided by the effective cut area  $A_{cut}(\Delta\theta, \Delta E_{Est})$  for the zenith angle of the observation and for the energy bin in question, yields the TeV flux density  $\Delta F / \Delta E$

as estimator for the energy spectrum as

$$\frac{\Delta F(\Delta\theta)}{\Delta E} = \frac{\Delta R(\Delta\theta)}{\Delta E_{Est}} \cdot \frac{1}{A_{cut}(\Delta\theta, \Delta E_{Est})} . \quad (7.24)$$

### 7.8.2 Determination of powerlaw index and cutoff energy

The two most simple hypotheses concerning the shape of a TeV energy spectrum (differential photon flux) are

- a powerlaw spectrum of the form

$$\frac{dN_\gamma}{dt \cdot dA_{cut} \cdot dE_{Est}} = f_0 \cdot (E_{Est}/\text{TeV})^{-\alpha} \quad (7.25)$$

and

- a cutoff spectrum of the form

$$\frac{dN_\gamma}{dt \cdot dA_{cut} \cdot dE_{Est}} = f_0 \cdot (E_{Est}/\text{TeV})^{-\alpha} \cdot e^{-E_{Est}/E_0} , \quad (7.26)$$

where

$f_0$  is the flux normalisation constant at 1 TeV ,

$\alpha$  is called the spectral powerlaw index, a dimensionless number,

$E_{Est}$  is the estimated energy of an individual event and

$E_0$  is the cutoff energy.

As the number of data points is limited, it does not make sense to try and fit more complicated parametrisations with higher numbers of description parameters if the  $\chi^2$  is already acceptable for fewer parameters.

Fits of the actual distributions to spectrum models are carried out in an iterative process. As a starting point the  $\kappa$ -parameters for  $\alpha = 2.7$  are used to fit the powerlaw index with a  $\chi^2$ -minimisation routine (MINUIT, (CN/ASD Group, 1994)). The resulting spectral index  $\alpha$  serves to interpolate between the tabulated sets of parameter values  $\kappa$  used in the following iteration step. This procedure is continued until the resulting spectral index from the previous iteration step and the spectral index estimated in the present iteration step are in agreement within 1%. When fitting a cutoff spectrum to the data, the estimation of the most likely shape is made in an equivalent manner, except that the 1% criterion is not applied to abort the iteration when the resulting values of the cutoff energy lie above 15 TeV. In such cases a powerlaw spectrum can usually not be distinguished from the cutoff spectrum because the cutoff energy lies above an energy where the possible rate is too low for all known sources.

More details about this routine can be found in (Kranich, 2001).

### 7.8.3 Flux determination for CT1

The procedure to calculate fluxes in the CT1 analysis was adopted from (Petry, 1997; Kranich, 2001). For a given spectral index, determined from a powerlaw fit to the data, a set of effective

Bin Number	1	2	3	4
$\cos(\theta)$	0.966	0.927	0.875	0.848
$A_{flux}^{>1\text{TeV}} [\text{m}^2]$	$48088.8 \pm 2486.0$	$47115.4 \pm 2625.5$	$47736.8 \pm 2638.7$	$44343.7 \pm 2952.6$
Bin Number	5	6	7	8
$\cos(\theta)$	0.777	0.707	0.573	0.423
$A_{flux}^{>1\text{TeV}} [\text{m}^2]$	$36657.3 \pm 2768.0$	$20007.7 \pm 3658.3$	$5960.8 \pm 1948.3$	$181.3 \pm 327.4$

Table 7.5: Effective meta-areas  $A_{flux}^{>1\text{TeV}}(\Delta\theta, \alpha = 2.9)$  (c.f. Equation (7.17)) for the flux calculation and their estimated uncertainties, as derived for the Mkn 421 data from the 1999-2000 period using the cut  $m421_01_z$ . The zenith angle bin numbers correspond to those of Table 7.4 on page 98. The  $\cos(\theta)$  values given here are calculated from the actually simulated zenith angles.

meta areas is calculated for each zenith angle bin, connecting the observed excess rate to the integral flux above a threshold of 1 TeV. The meta-areas  $A_{flux}$  are calculated according to:

$$A_{flux}^{>1\text{TeV}}(\Delta\theta, \alpha) = \frac{\sum_{\Delta E} \left( A_{cut}(\Delta E, \Delta\theta, \alpha) \cdot \int_{E_i}^{E_{i+1}} (E [\text{TeV}])^{-\alpha} dE \right)}{\int_{E_{Thr}}^{\infty} (E [\text{TeV}])^{-\alpha} dE} \quad (7.27)$$

which, with  $E_{Thr} = 1 \text{ TeV}$ , simplifies to

$$A_{flux}^{>1\text{TeV}}(\Delta\theta, \alpha) = \sum_{\Delta E} \left( A_{cut}(\Delta E, \Delta\theta, \alpha) \cdot \left( (E_i [\text{TeV}])^{-\alpha+1} - (E_{i+1} [\text{TeV}])^{-\alpha+1} \right) \right) \quad (7.28)$$

$\Delta E$  denotes an energy bin with lower bin border  $E_i$  and upper bin border  $E_{i+1}$ .

The summation over the energy bins  $\Delta E$  is carried out within the simulated range of energies. As can be seen from the simulation statistics in Appendix 16.6, the simulated range covers the smallest energies; for the highest energies the observations run out of statistics, hence it is justifiable to neglect energy values above those simulated.

The meta-areas  $A_{flux}^{>1\text{TeV}}(\Delta\theta, \alpha)$  relate the total number of  $\gamma$ -rays observed from a source to the number of  $\gamma$ -rays above a certain, preselected energy. They are sometimes also called ‘magic numbers’. The usual reference energy in TeV astronomy above which the fluxes are quoted is 1 TeV<sup>45</sup>. The meta areas (magic numbers) for the  $m421_01_z$  cut and Mkn 421 data from the period 1999-2000 are given in Table 7.5 for the specified zenith angle bins for a value of  $\alpha = 2.9$ .

---

<sup>45</sup>It is also important to note that one of the energy-bin limits is 1 TeV, as can be seen in Table 7.3 on page 95. This is a prerequisite for unbiased flux estimates when using the calculation scheme of equation (7.28).

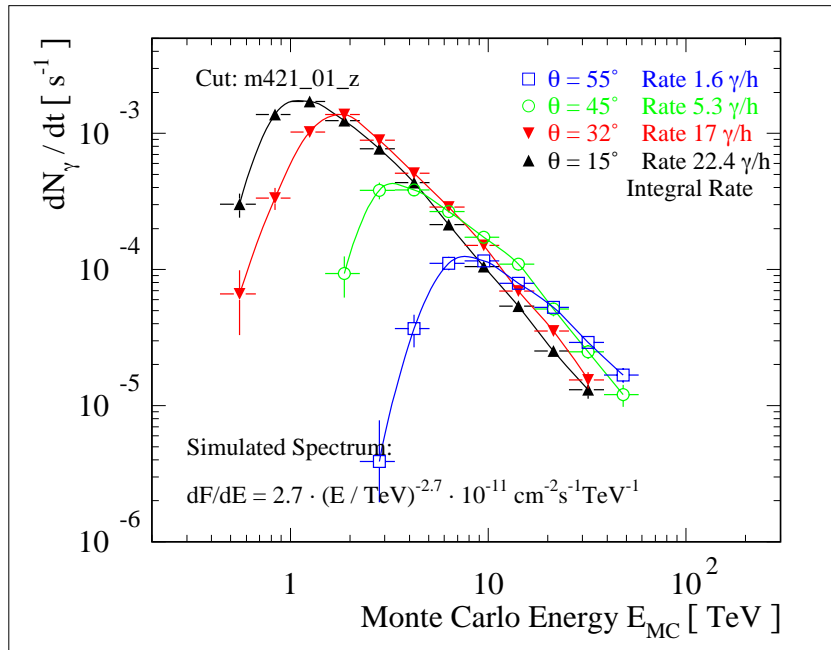


Figure 7.14: The estimated rate of  $\gamma$ -candidate events as a function of the simulated energy is drawn for an incoming stream of  $\gamma$ s which follow the energy spectrum quoted in the figure. For different zenith angles the result is different: at smaller zenith angles the peaks of the distributions are located at smaller energies. This is a reflection of the shape of the trigger and cut efficiencies, which rule this behaviour.

Source: Monte Carlo simulation for CT1



## 8 Mkn 421 light curve and spectrum in 1999-2000

Mkn 421 was quite active in the observation season 1999-2000. Several big flares were recorded, which allow one to calculate the time averaged energy spectrum of Mkn 421 during this time period.

The following observing season, 2000-2001, awarded the observers around the world with the strongest persistent TeV flares from Mkn 421 since its discovery. The long duration flaring activity (also at other wavelength bands) was recorded not only by CT1 but also by a large number of other instruments, operating at all wavelengths. This new and exciting data is currently being processed and the analysis is still in its final steps — therefore it is not possible to present more than some preliminary results in this thesis.

---

In this chapter the analysis methods described in the previous chapters are at first tested on Crab, the TeV standard candle. TeV data from the two periods 1999-2000 and 2000-2001 are examined.

Next, the time and zenith angle coverage of the Mkn 421 data recorded in 1999-2000 is presented, along with its time-averaged TeV spectrum. Usually the statistical significance of data collected in TeV astronomy is so low that only the two most simple forms of spectral shapes can be tested against each other using this data: a pure powerlaw shape and a powerlaw shape that in addition exhibits a cutoff. The TeV spectrum is examined as to whether or not the collected statistics allows one to distinguish between these two options, and if so, the value of the cutoff energy is estimated.

The flux levels of Mkn 421 were determined according to the spectral powerlaw index found in the time-averaged spectrum. They are displayed for the period 1999-2000 and in the long term lightcurve of Mkn 421, in the concluding section of this chapter.

### 8.1 Verification of the analysis methods using Crab data

Energy spectra and flux values were obtained by performing the following treatment on the raw data:

- The pedestal level and RMS of each camera pixel were determined.
- The relative calibration of pixel signals was carried out using calibration information collected in 20-minute intervals.
- The appropriate conversion factor  $\chi$  from ADC counts to photoelectrons was applied, leading to raw photoelectron images.
- Image cleaning was performed and the median values of the *Width* and *Length* distributions were determined. Thereafter the corresponding *Zonk* correction shifts were determined and applied on a run-by-run basis, i.e. for 20 minute intervals.

Conversion Factor $\chi$ [ ph. el./ADC ct. ]	0.46	0.61	0.76
Flux Constant $f_0$ [ $10^{-11} \text{ cm}^{-2} \text{ s}^{-1} \text{ TeV}^{-1}$ ]	$1.51 \pm 0.14$	$2.08 \pm 0.18$	$2.15 \pm 0.21$
Powerlaw Index $\alpha$	$2.69 \pm 0.15$	$2.63 \pm 0.12$	$2.37 \pm 0.11$
Fit Quality $\chi^2/dof.$	0.66/(8 - 2)	2.43/(9 - 2)	5.03/(9 - 2)
$\Delta f_0^{syst}$ [ $10^{-11} \text{ cm}^{-2} \text{ s}^{-1} \text{ TeV}^{-1}$ ]	0.32		
$\Delta \alpha^{syst}$	0.16		

Table 8.1: Analysis results for Crab data from 1999-2000 obtained using different values of the conversion factor  $\chi$  between ADC counts and photoelectrons. The table gives the flux constant  $f_0$  and the differential spectral index  $\alpha$  from a powerlaw fit to the data points and the resulting  $\chi^2$  value of the fit.

These results are used as estimators for the systematic uncertainties in the flux constant  $f_0$  and the powerlaw index  $\alpha$ .

Source: CT1 Crab data 1999-2000

Monte Carlo events were adjusted to the properties of this particular data set by performing the following steps:

- The night sky noise levels of the real-data set served to adjust the noise levels in the simulation to yield a dedicated Monte Carlo data set.
- The energy reconstruction algorithm was adjusted to the properties of this particular data set and the effective areas were calculated, correcting at the same time for the difference between simulated and reconstructed energy scales.

Finally, combining the Monte Carlo input and real data,

- the energy spectrum

and

- the flux

were calculated.

### 8.1.1 Spectral analysis of Crab data from 1999-2000 and from 2000-2001

A short systematic investigation concerning the influence of the conversion factor on the results of the analysis of the energy spectrum of Crab has been carried out using Crab data from the period 1999-2000. The conversion factor is the most uncertain factor in the analysis and dominates by far the systematic error. Three different conversion factors were used to determine energy estimation parameters and effective areas. These three values of the conversion factor  $\chi$  were obtained using the mean value (0.61), the mean value reduced (0.46) and the mean value increased (0.76) by the RMS of the distribution of the estimated values of  $\chi$  as shown in Figure 5.10 on page 55. The results of the analysis of Crab data from 1999-2000 using the corresponding sets of parameters are summarised in Table 8.1. The results in Table 8.1 are used to derive an estimator for the systematic uncertainty in the flux constant  $f_0$  and in the

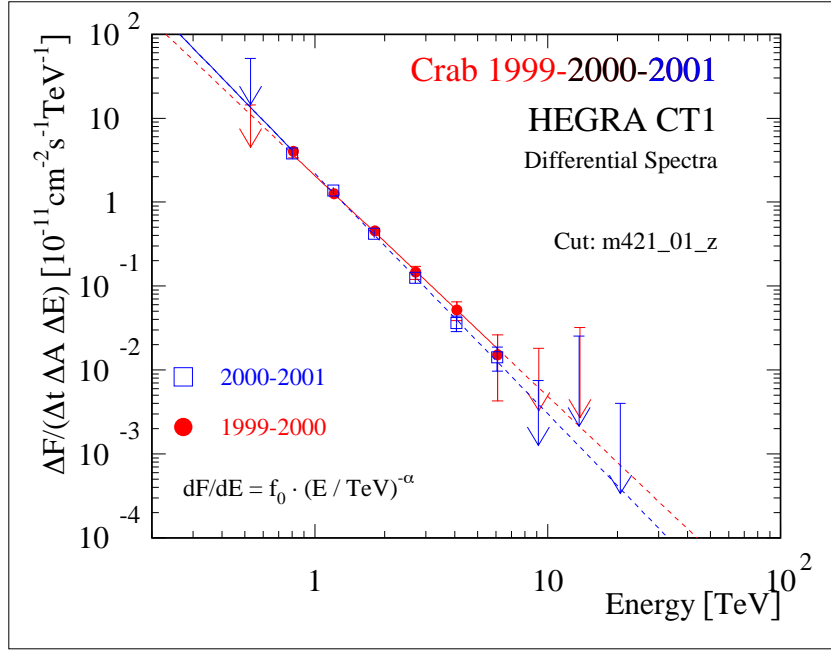


Figure 8.1: Energy spectra of Crab from the periods 1999-2000 (red, filled circles) and 2000-2001 (blue, open squares). The fit parameters for the two data sets are given in Table 8.2. Source: CT1 Crab observations 1999-2000 and 2000-2001

powerlaw index  $\alpha$  by halving the spanned range of their values from the largest to the smallest value of  $\chi$ . The systematic uncertainty in the flux constant  $f_0$  is thus estimated as

$$\Delta f_0^{syst} = \pm 0.32 \cdot 10^{-11} \text{ cm}^{-2} \text{ s}^{-1} \text{ TeV}^{-1} ,$$

and takes a value of

$$\Delta \alpha^{syst} = \pm 0.16$$

for the power-law index  $\alpha$ .

Using the mean conversion factors  $\chi_{99-00} = 0.61 \text{ ph.el./ADC ct.}$  for the period 1999-2000 and  $\chi_{00-01} = 0.55 \text{ ph.el./ADC ct.}$  for 2000-2001, the energy spectra for Crab data recorded in 1999-2000 and in 2000-2001 have been derived. The results are shown overlaid in Figure 8.1. All data points with their respective errors have been included in the fit. When the error of the data point is larger than the value, this data point is not indicated as a symbol with associated error bars but as an arrow that points to the value with a length corresponding to two times the error.

In order to allow a comparison of this result with the measurements of other TeV observatories, Table 8.2 has been compiled summarising results from Crab observations from a set of TeV instruments and observation periods. The results from both campaigns 1999-2000 and 2000-2001 obtained in this analysis agree within errors with those obtained from different instruments, periods and analysis techniques, thus giving confidence to the analysis methods applied in this thesis.

<b>Instrument</b>	<b>Cangaroo</b>	<b>Whipple</b>
Data years	1992 to 1996	1995 to 1998
Energy range [TeV]	7 to 50	0.5 to 5
Power-law index $\alpha$	$2.53 \pm 0.18$	$2.49 \pm 0.06 \pm 0.04$
$f_0$	$2.8^{+1.9}_{-1.2}$	$3.20 \pm 0.17 \pm 0.6$
Reference	(Tanimori et al., 1998)	(Hillas et al., 1998)
<b>Instrument</b>	<b>Cat</b>	<b>Hegra CT System</b>
Data years	1996 to 2000	1997 to 2000
Energy range [TeV]	0.3 to 20	0.5 to 20
Power-law index $\alpha$	$2.80 \pm 0.03 \pm 0.08$	$2.59 \pm 0.03 \pm 0.05$
$f_0$	$2.20 \pm 0.05 \pm 0.60$	$2.79 \pm 0.02 \pm 0.5$
Reference	(Masterson et al., 2001)	(Aharonian et al., 2000)
<b>Instrument</b>	<b>Hegra CT1</b>	<b>Hegra CT1</b>
Data years	1999 to 2000	2000 to 2001
Energy range [TeV]	0.8 to 6.1	0.8 to 6.1
Power-law index $\alpha$	$2.63 \pm 0.12 \pm 0.16$	$2.86 \pm 0.09$
$f_0$	$2.08 \pm 0.18 \pm 0.32$	$2.19 \pm 0.14$
Reference	(This work)	(This work)

Table 8.2: Analysis results for Crab data from several TeV instruments. Given are the observation campaigns, the energy range for which the study is valid and a reference to the publication where the values have been taken from. The last two entries contain the results as shown in Figure 8.1. The systematic uncertainties have only been derived for the 1999-2000 data of HEGRA CT1.

### 8.1.2 Crab flux as a function of the zenith angle

The TeV  $\gamma$ -ray flux from Crab has been measured by many instruments and has been found to be stable within measurement accuracy. Therefore it is interesting to look at the Crab flux measured by CT1 as a function of the zenith angle of the observation. For a steady source the result is expected to be independent of the zenith angle. Figure 8.2 shows the Crab flux of 1999-2000 for different zenith angles. Within errors and in view of the observation time spent at a given zenith angle, the results are compatible with a zenith-angle independent flux.

## 8.2 The Hegra CT1 data set of Mkn 421 in 1999-2000

The time and zenith angle coverage of the Mkn 421 observations is summarised in Figure 8.3 on the next page. It shows the measurement times as bars, where the length of the bar indicates the duration, while the location of the bar indicates the hour angle and the zenith angle of the observation, as indicated by the different axes of the plot. The gaps between observations correspond to bad weather periods and to full moon, when observation was not possible.

### 8.3 Flux curve of Mkn 421 in 1999-2000 with Hegra CT1

Mkn 421 was monitored with HEGRA CT1 in the period from November 1999 through May 2000. The analysis steps listed at the beginning of this chapter have been performed eventually for this data set.

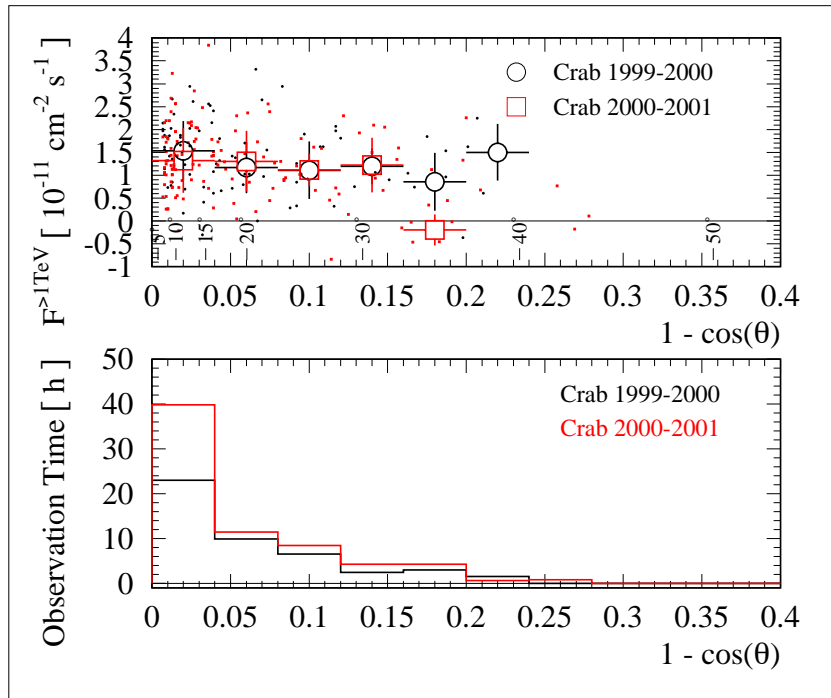


Figure 8.2: Crab flux as a function of the zenith angle of the observation (upper panel) and the corresponding cumulated observation time (lower panel). The small points in the upper plot represent flux measurements with a duration between 0.2 and 0.75 h. The error bars on these have been omitted for clarity. The large symbols represent their error-weighted average values, their spread is given as vertical error bars within the zenith angle bins indicated by the horizontal error bars.

Source: CT1 observations of Crab from 1999-2000 and from 2000-2001

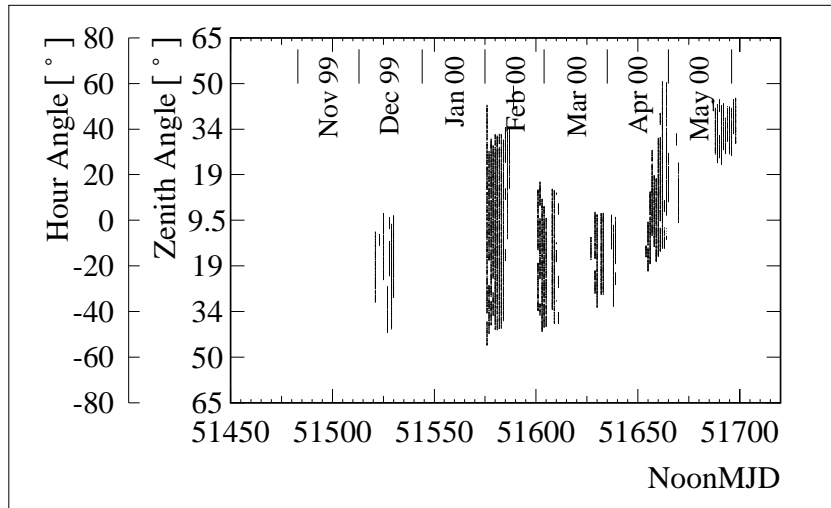


Figure 8.3: Zenith angle and hour angle coverage of the Mkn 421 data from 1999-2000.  $15^\circ$  in hour angle correspond to an observation time of one hour. Culmination of the object corresponds to an hour angle of  $0^\circ$  and to the minimum zenith angle of roughly  $9.5^\circ$ .

Source: CT1 Mkn 421 observations from 1999-2000

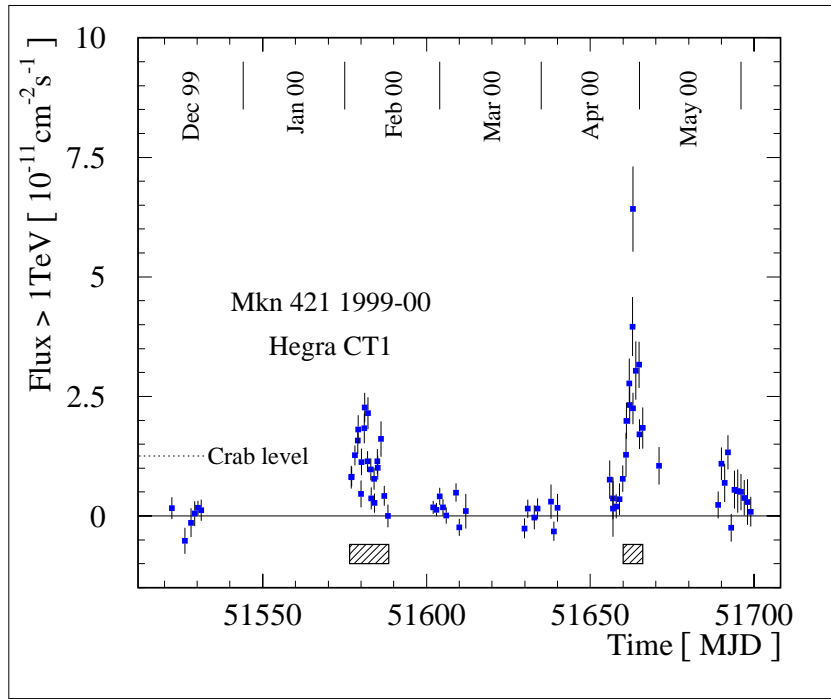


Figure 8.4: Lightcurve of Mkn 421 from the period 1999-2000. After modest activity in the first half of the season, Mkn 421 became very active in the observation time windows in April and May 2000. The hatched boxes at the bottom of the figure indicate the two time windows that are shown expanded in Figures 8.5 and 8.6.

Source: CT1 observations of Mkn 421 from 1999-2000

The overall flux curve for this period is shown in Figure 8.4. The observations in February showed modest activity of the source, reaching around two times the Crab flux level. In April/May 2000 the highest fluxes in this observation season were recorded, the peak flux being slightly higher than four times the average Crab flux level. Data around these two peak-flux windows are shown on an expanded scale in separate graphs, shown in Figures 8.5 and 8.6.

The flux levels shown in these figures have been calculated on one hour bins. It is highly interesting to compare the TeV flux measurements to contemporaneous data recorded at other wavelengths. Therefore the observations of the RXTE all sky monitor instrument (ASM) in the 2 to 12 keV energy band have been drawn in the original 90s time windows (the so-called ‘dwells’) and plotted in the bottom part of the graphs. Due to the sparseness of the data in the X-ray region, only a coarse comparison is possible during the largest flares recorded in the TeV range, because of inadequately densely sampled X-ray information. In order to provide a gross picture of the flux development of Mkn 421 over the past few years as measured with CT1, the long-term lightcurves in the TeV range (top panel) and in the keV range (RXTE/ASM, bottom panel) are shown in Figure 8.7. The outburst observed in 2001 reached flux values of up to around ten times the Crab flux level.

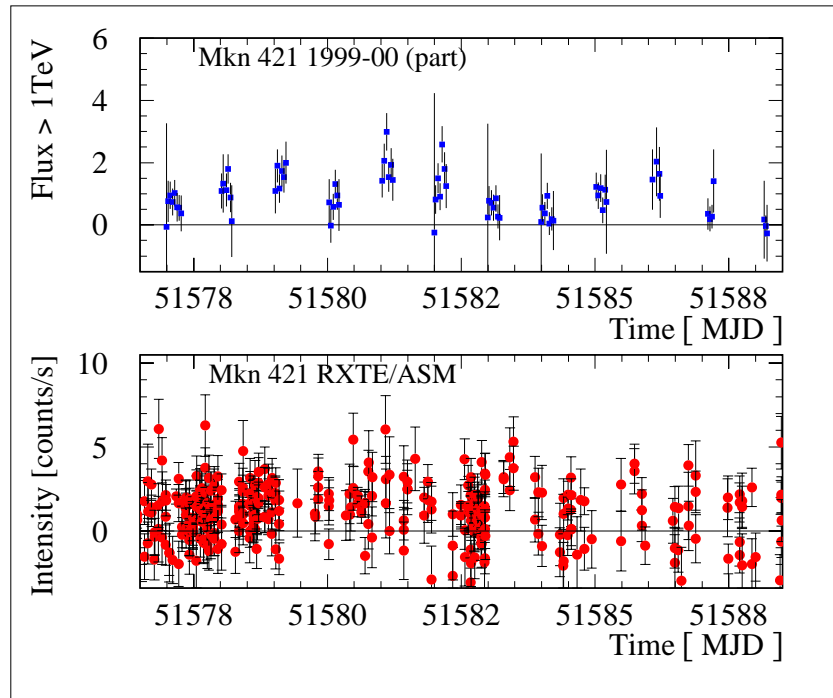


Figure 8.5: The one-hour averaged fluxes in the TeV range (the units of  $[10^{-11} \text{ cm}^{-2} \text{ s}^{-1}]$  have not been drawn for space reasons) and the contemporaneous X-ray intensity in 90 s intervals is shown for several observation nights around the highest observed peak of February 2000. The most interesting days, i.e. those with highest TeV fluxes, are only covered sparsely in the X-ray range.

Source: CT1 observations of Mkn 421 1999-2000, quick-look results provided by the RXTE/ASM team

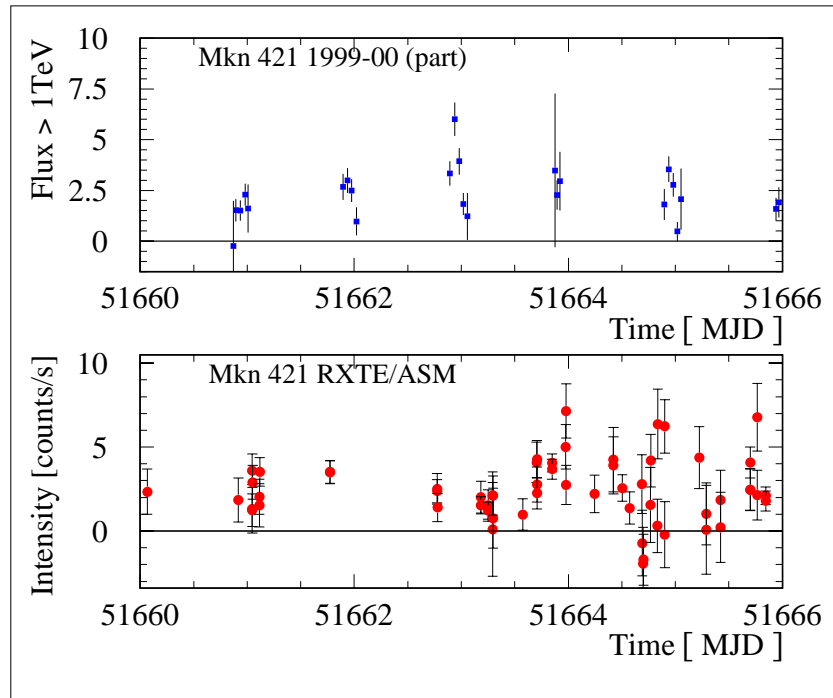


Figure 8.6: The one-hour averaged fluxes in the TeV range (the units of  $[10^{-11} \text{ cm}^{-2} \text{ s}^{-1}]$  have not been drawn for space reasons) and the contemporaneous X-ray intensity in 90 s intervals is shown for several observation nights around the highest peak observed of April 2000. Also here the most interesting days, i.e. those with highest TeV fluxes, are only covered sparsely in the X-ray range.

Source: CT1 observations of Mkn 421 1999-2000, quick-look results provided by the RXTE/ASM team

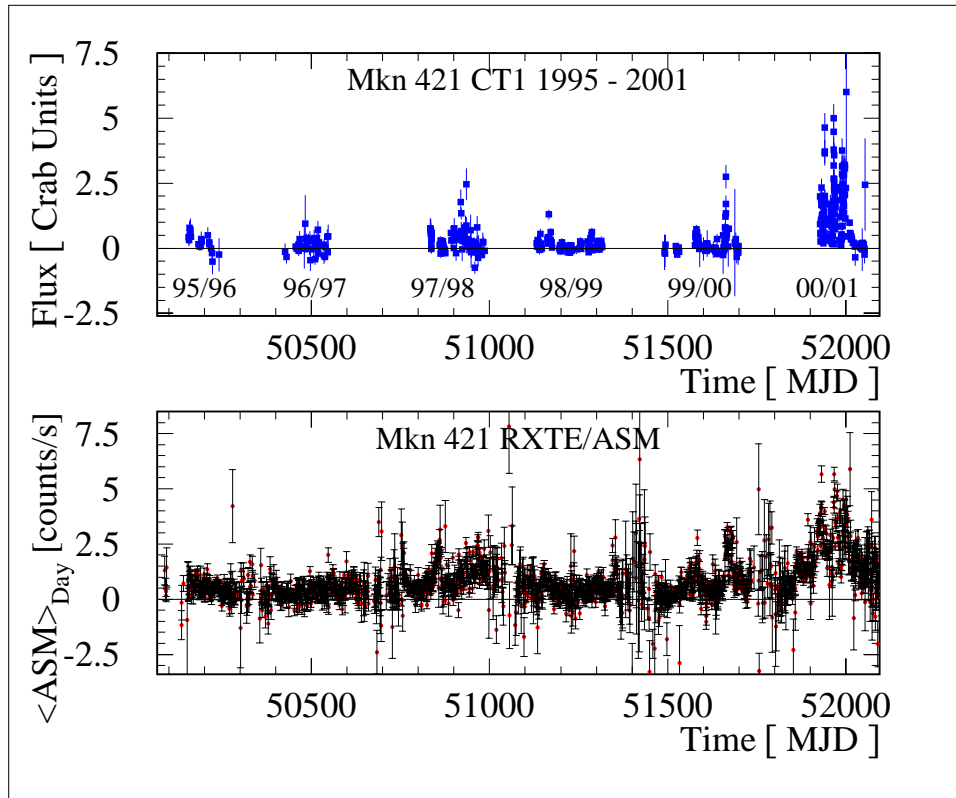


Figure 8.7: Light curve of Mkn 421 as recorded with CT1 from 1995 through 2001. In autumn 1998 the original mirror of  $5 \text{ m}^2$  area was doubled, leading finally to smaller error estimates for the flux. In the lower panel the contemporaneous X-ray activity in the band from 2 to 12 keV is shown from the RXTE all-sky monitor (ASM).

Source: CT1 observations of Mkn 421 1995 through 2001, quick-look results provided by the RXTE/ASM team

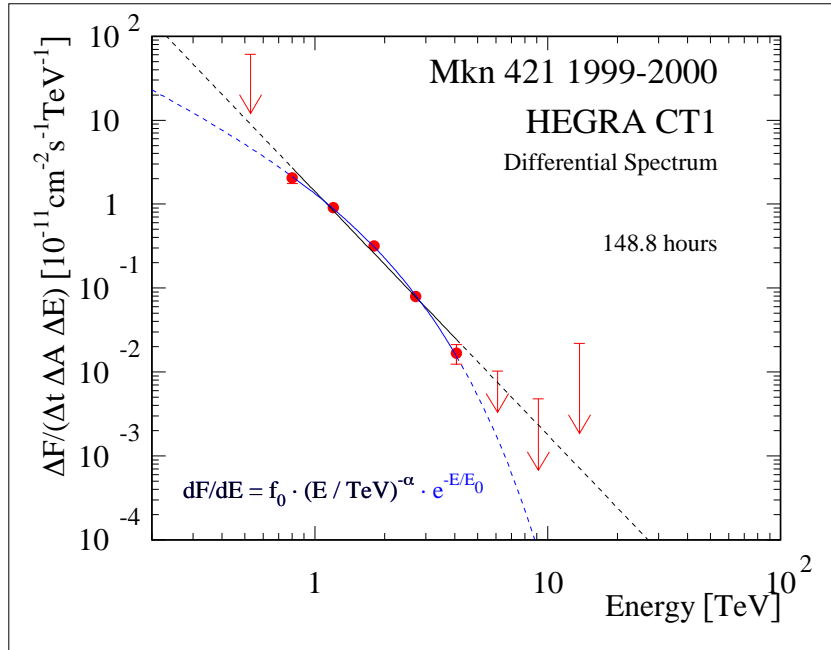


Figure 8.8: Energy spectrum of Mkn 421 data from the period 1999-2000. A pure powerlaw function (black) and a powerlaw function with an exponential cutoff (blue) have been fitted to the data points. The resulting parameters are listed in Table 8.3.  
Source: CT1 Mkn 421 observations 1999-2000

## 8.4 TeV spectrum of Mkn 421 in 1999-2000 with Hegera CT1

### 8.4.1 Time averaged energy spectrum

As the simulated zenith angle range includes the observed range, no further cut has been made on the zenith angle. The time and zenith-angle averaged TeV energy spectrum of Mkn 421 1999-2000 is shown in Figure 8.8 with a powerlaw and with a cutoff fit to the data points. All available data points have been used for the fit; in the display those data points with a value smaller than the error on this data point have been drawn as an arrow of twice the error as length, pointing to the value represented by the data point.

For the calculation of the flux a powerlaw index of  $\alpha = 2.9$  has been used (c.f. Figure 8.8, Table 8.3 together with Section 7.8.3).

### 8.4.2 Time averaged energy spectrum from 2000-2001

In order to carry out further studies with low, medium and high flux data from Mkn 421, the data set of 1999-2000 and the preliminary data set of 2000-2001 have been combined. They have been re-ordered according to their flux levels and their investigation is described below. The time and zenith-angle averaged TeV energy spectrum of Mkn 421 2000-2001 is shown in Figure 8.9 with a powerlaw fit and with a cutoff fit to the data points. As was done for the 1999-2000 data shown in Figure 8.8, all available data points have been used for the fit in Figure 8.9; in the display the data points with a value smaller than the error have been drawn in the same manner as in Figure 8.8.

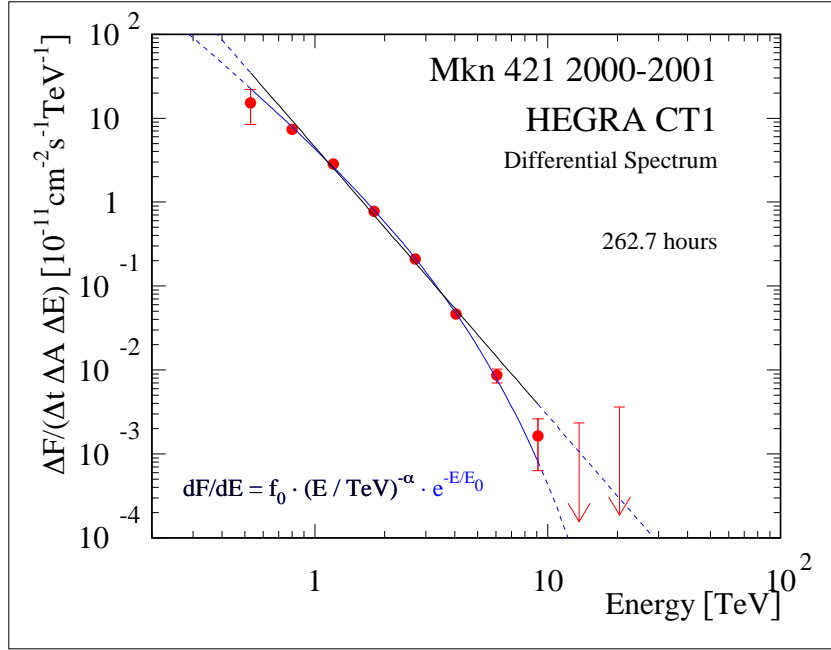


Figure 8.9: Like Figure 8.8 but for Mkn 421 data from the period 2000-2001. The fitted parameters are listed in Table 8.3.

Source: CT1 Mkn 421 observations 2000-2001

### 8.4.3 Shape investigation of the Mkn 421 spectra

Due to sparse data in the TeV region, a pure power law model shape and an exponential cutoff shape model are the only two options for the parametrisation of the energy spectrum of Mkn 421. Letting all parameters of the  $\chi^2$ -minimisation fits vary freely, the reduced  $\chi_{red}^2$  values as estimators for the quality of the fit can be calculated as:

$$\chi_{red}^2 := \frac{1}{N - N_p} \cdot \sum_{i=1}^N \left( \frac{f_i - F_i}{\Delta f_i} \right)^2, \quad (8.1)$$

where

$N$  is the number of available datapoints

counted with index  $i$ ,

$f_i$  is a measured differential flux level with

uncertainty  $\Delta f_i$  and

$F_i$  is the differential flux value calculated from the fitted parametrisation with

$N_p$  the number of free parameters in the fit:  $N_p = 2$  for the powerlaw and  $N_p = 3$  for the cutoff model spectrum.

$F_{plaw} = f_0 \cdot (E[\text{TeV}])^{-\alpha}$					
$F_{coff} = f_0 \cdot (E[\text{TeV}])^{-\alpha} \cdot e^{-E/E_0}$					
<b>1999-2000</b>					
	$f_0$ [ $10^{-11} \text{ TeV}^{-1} \text{ cm}^{-2} \text{ s}^{-1}$ ]	$\alpha$	$E_0$ [TeV]	$\chi_{red}^2$	$\mathcal{P}_\chi(\chi^2, \nu)$
$F_{plaw}$	$1.42 \pm 0.08$	$2.90 \pm 0.08$	—	$16.08/(9 - 2)$	0.02
$F_{coff}$	$3.09 \pm 1.11$	$1.35 \pm 0.68$	$1.19 \pm 0.55$	$0.90/(9 - 3)$	0.99
<b>2000-2001</b>					
	$f_0$ [ $10^{-11} \text{ TeV}^{-1} \text{ cm}^{-2} \text{ s}^{-1}$ ]	$\alpha$	$E_0$ [TeV]	$\chi_{red}^2$	$\mathcal{P}_\chi(\chi^2, \nu)$
$F_{plaw}$	$4.57 \pm 0.14$	$3.20 \pm 0.04$	—	$60.8/(11 - 2)$	$9.4 \cdot 10^{-10}$
$F_{coff}$	$6.74 \pm 0.99$	$2.27 \pm 0.34$	$2.26 \pm 0.87$	$7.35/(11 - 3)$	0.50

Table 8.3: Results from the fitting of two different model distributions to the time-averaged differential energy spectrum of Mkn 421 in 1999-2000 (upper part) and in 2000-2001 (lower part). The errors quoted in the table are statistical. The systematic errors for the flux constant and for the power law index are  $\Delta f_0^{syst.} = 0.32 \cdot 10^{-11} \text{ TeV}^{-1} \text{ cm}^{-2} \text{ s}^{-1}$  and  $\Delta \alpha^{syst.} = 0.16$  respectively. The correspondig energy spectra are shown in Figures 8.8 and 8.9 respectively. Source: CT1 Mkn 421 observations 1999-2000 and 2000-2001

The fit parameters for a pure-powerlaw-model fit and for the fit of an exponential cutoff model are given in Table 8.3 along with the values of  $\chi_{red}^2$  and the integral probabilities<sup>46</sup>  $\mathcal{P}_\chi(\chi^2, \nu)$ , defined as

$$\mathcal{P}_\chi(\chi^2, \nu) := \int_{\chi^2}^{\infty} \mathcal{P}_x(x^2, \nu) dx^2 \quad ,$$

where

$N$  is the number of data points that are included in the fit,

$\nu = N - n - 1$  is the number of degrees of freedom in the case of  $n$  coefficients and one constant term of the fit, else

$\nu = N - n$ , when there is no constant term of the fit.

When the model function is a good representation of the data points, the value of  $\chi_{red}^2$  should be close to one, or, more precisely, the integral probability should be close to the value of one half. For larger values of  $\chi_{red}^2$  the probability of obtaining such a large value from the correct model is smaller, indicating that the function used may not be the appropriate one. Large values of the integral probability  $\mathcal{P}_\chi(\chi^2, \nu)$ , on the other hand, might be indicative for too large errors entering the fit. A possible conclusion from the values of  $\chi_{red}^2$  that are obtained from the fits to the 1999-2000 data of Mkn 421 is that the power law model seems to be less favoured than the cutoff model function which, in turn, seems to be too good an option and reaches the large value of  $\mathcal{P}_\chi(\chi^2, \nu)$  due to the large errors of the data points. Therefore none of the two options is favoured clearly in this investigation which may be attributed to the sparseness of the data points.

<sup>46</sup>The probability distribution function for  $\chi^2$  with  $\nu$  degrees of freedom is given by  $\mathcal{P}_x(x^2, \nu) = \frac{(x^2)^{\frac{1}{2}(\nu-2)} \cdot e^{-\frac{x^2}{2}}}{2^{\frac{\nu}{2}} \cdot \Gamma(\frac{\nu}{2})}$ , see e.g. (Bevington, 1969) and references therein.

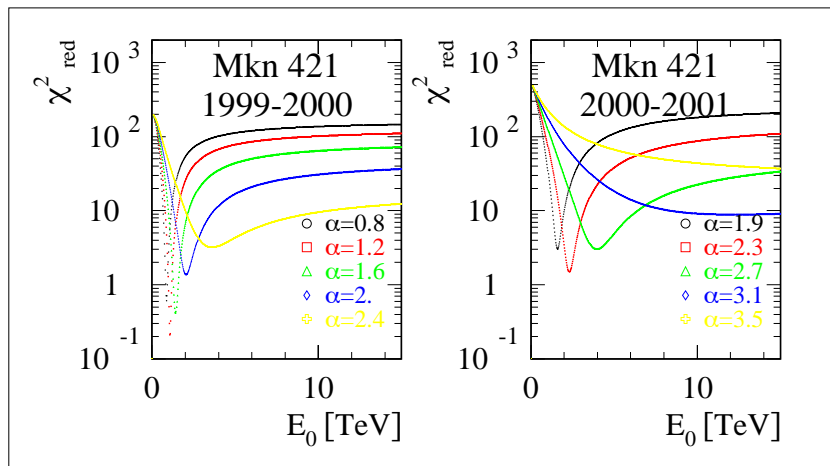


Figure 8.10: Keeping the value of the power law index  $\alpha$  fixed at a set of values, the cutoff energy  $E_0$  was varied and the resulting  $\chi^2_{red}$  calculated for the Mkn 421 data set of 1999-2000 (left-hand side) and for the Mkn 421 data set of 2000-2001.

Source: CT1 Mkn 421 observations 1999-2000 and 2000-2001

In order to demonstrate also that the powerlaw index  $\alpha$  and the cutoff energy  $E_0$  are correlated in such a fit, it has been undertaken to let  $E_0$  vary while  $\alpha$  was kept fixed at a set of values around the minimum as of the fit. The resulting values of  $\chi^2_{red}$  for these values of  $\alpha$  and for varying  $E_0$  are shown in Figure 8.10 for the case of the 1999-2000 data on the left-hand side and for the 2000-2001 data on the right-hand side.

#### 8.4.4 Flux-dependent analysis of the spectral shape

From a physics point of view the separation of data sets by the time of their recording is an arbitrary choice. Splitting up data sets according to flux levels represents a physically motivated criterion as it allows one to study spectral properties resp. their changes with flux levels. In order to have enough statistics for such a study, the combined data sets of 1999-2000 and of 2000-2001<sup>47</sup> have been split according to their flux levels: below  $1.3 \cdot 10^{-11} \text{ cm}^{-2} \text{ s}^{-1}$  (called 'Low'), into an intermediate range (called 'Medium') with fluxes of up to  $2.6 \cdot 10^{-11} \text{ cm}^{-2} \text{ s}^{-1}$  and in a high-flux range (called 'High'). The flux limits have been chosen such that the uncertainty of the flux estimates are almost equal for the three resulting data sets. By chance the flux limits roughly correspond to steps of Crab-flux equivalents. The resulting energy spectra ('Low', 'Medium' and 'High') are shown overlaid in Figure 8.11. These spectra have been fitted with a pure powerlaw model spectrum and with a spectrum that exhibits an exponential cutoff in addition. The values of the parameters are summarised in Table 8.4.

Two main conclusions can be drawn from this study:

1. Investigating the values of  $\chi^2_{red}$  respectively the values of  $\mathcal{P}_\chi(\chi^2, \nu)$  for the two functional forms, the cutoff function seems to give a more appropriate description of the underlying distribution than the pure powerlaw model for the 'medium' and for the 'high' flux

<sup>47</sup>This data set is still preliminary by the time of writing but has been added for this study in order to enhance statistics for the high flux values. Therefore the result of this study must be considered preliminary as well.

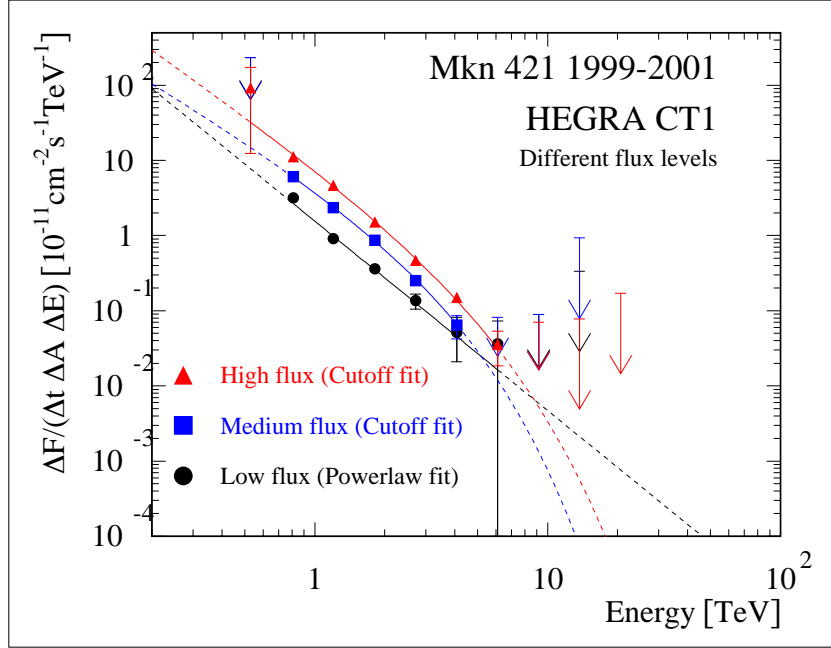


Figure 8.11: The combined data sets of Mkn 421 1999-2000 and 2000-2001 were split according to their one-day averaged flux levels. For each of the resulting data sets a differential energy spectrum was determined and is shown here overlaid. A cutoff spectrum model was fitted to the data points except for the low-flux spectrum, where only the powerlaw fit converged.

Source: CT1 Mkn 421 observations 1999-2000 and 2000-2001

$F_{plaw} = f_0 \cdot (E[\text{TeV}])^{-\alpha}$					
$F_{coff} = f_0 \cdot (E[\text{TeV}])^{-\alpha} \cdot e^{-E/E_0}$					
<b>low</b>					
	$f_0$ [ $10^{-11} \text{ TeV}^{-1} \text{ cm}^{-2} \text{ s}^{-1}$ ]	$\alpha$	$E_0$ [TeV]	$\chi_{red}^2$	$\mathcal{P}_\chi(\chi^2, \nu)$
$F_{plaw}$	$1.56 \pm 0.14$	$2.49 \pm 0.14$	—	$2.93/(9 - 2)$	0.89
$F_{coff}$	—	—	—	—	—
<b>medium</b>					
	$f_0$ [ $10^{-11} \text{ TeV}^{-1} \text{ cm}^{-2} \text{ s}^{-1}$ ]	$\alpha$	$E_0$ [TeV]	$\chi_{red}^2$	$\mathcal{P}_\chi(\chi^2, \nu)$
$F_{plaw}$	$3.77 \pm 0.17$	$2.63 \pm 0.08$	—	$5.97/(10 - 3)$	0.54
$F_{coff}$	$5.89 \pm 1.76$	$1.84 \pm 0.52$	$2.12 \pm 1.42$	$1.46/(10 - 3)$	0.98
<b>high</b>					
	$f_0$ [ $10^{-11} \text{ TeV}^{-1} \text{ cm}^{-2} \text{ s}^{-1}$ ]	$\alpha$	$E_0$ [TeV]	$\chi_{red}^2$	$\mathcal{P}_\chi(\chi^2, \nu)$
$F_{plaw}$	$7.18 \pm 0.18$	$2.68 \pm 0.04$	—	$14.0/(10 - 3)$	0.05
$F_{coff}$	$9.53 \pm 1.42$	$2.16 \pm 0.26$	$3.36 \pm 1.76$	$5.28/(10 - 3)$	0.63

Table 8.4: The energy spectra ('low', 'medium' and 'high') shown in Figure 8.11 have been fitted with a pure powerlaw model ( $F_{plaw}$ ) and with a cutoff fit ( $F_{coff}$ ). Dashes instead of entries indicate that the corresponding fit has not converged. The errors quoted in this table are statistical.

Source: combined CT1 Mkn 421 observations of 1999-2000 and 2000-2001

spectrum.

2. There is a weak indication that the cutoff energy and the powerlaw index rise with flux.

It must be noted at this place, that investigations like the ones carried out upon the measured energy spectra are not indicative of physical processes inside the sources to a high degree. Therefore the tracks outlined in Section 2.2 are followed in order to achieve a picture of processes inside Mkn 421 by investigating its source-intrinsic spectrum.

#### 8.4.5 Unfolding to source-intrinsic spectra at different flux levels

As was discussed in Section 2.2, the TeV spectra as emitted by their sources undergo a change as they interact with the cosmological background of infrared photons on their path towards the Earth. The lower the redshift, the less severe the distortion is going to be. Mkn 421 is one of the closest TeV blazars known today. From the set of blazars investigated for Figure 2.4 the attenuation is smallest for Mkn 421 with its redshift of  $z = 0.031$ . For this particular graph (Figure 2.4) a power law spectrum emitted by the source has been assumed. On the other hand, all assumptions of SSC models for TeV blazars arrive at the conclusion that the source-intrinsic spectra display a peak close to the energy range of current CHERENKOV telescopes, i.e. in the TeV domain. Examples can be seen in Figure 3.4 (a) and (b), showing the measurements and models for Mkn 421 and Mkn 501 over a wide range of energies. In their analysis of the X-ray behaviour of the two sources Mkn 421 and Mkn 501, (Kataoka et al., 2001) arrive at the two following main results for the two sources:

1. Mkn 421 and Mkn 501 display different dynamics concerning the contemporaneous fluxes in the X-ray range and in the TeV range: while Mkn 421 displays an almost linear correlation (exponent  $0.92 \pm 0.12$ ), the TeV flux of Mkn 501 rises almost quadratically (exponent  $1.96 \pm 0.07$ ) with the X-ray flux (c.f. (Kataoka et al., 2001) or Section 3.2).
2. The synchrotron peak in the X-ray domain shows very modest shifts of its position in the case of Mkn 421 and remains at values of around 1.2 keV, whereas Mkn 501 not only displays larger values but also a higher dynamic range of the synchrotron peak position between roughly 50 and 100 keV.

It has been tried for this work to achieve similar estimates for Mkn 421 in the TeV region like those shown in Figure 8.14 for the X-ray range. (Kataoka et al., 2001) find the relations

$$E_{p, Mkn\ 421} \propto L_{p, Mkn\ 421}^{0.4} \quad (8.2)$$

and

$$E_{p, Mkn\ 501} \propto L_{p, Mkn\ 501}^{1.6} \quad (8.3)$$

with

$E_p$  the peak position of the synchrotron peak in the  $\nu \cdot I_\nu$  representation and  $L_p$  the corresponding luminosity.

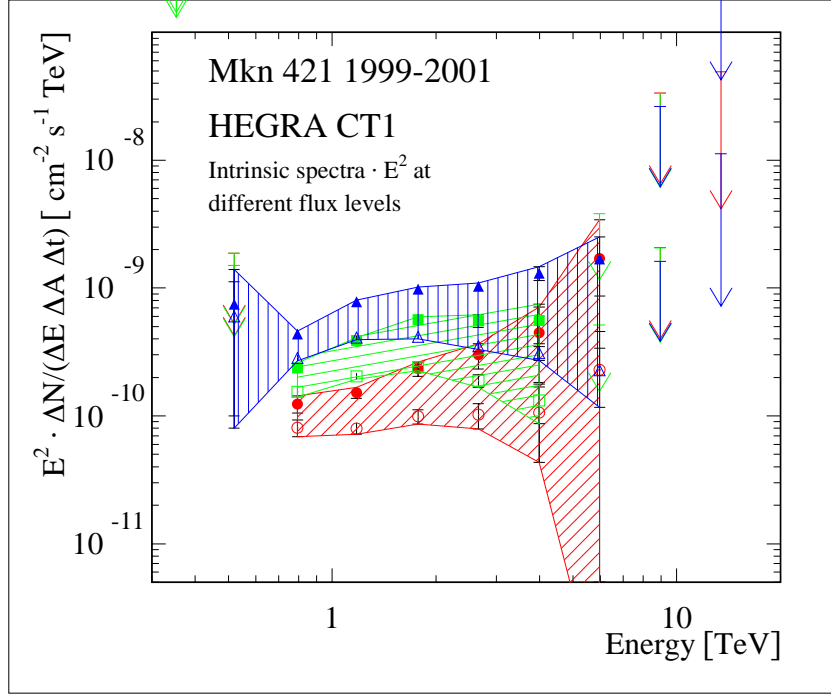


Figure 8.12: Deconvolved energy spectra multiplied with  $E^2$  at different flux levels (c.f. Figure 8.11) of Mkn 421 using the infrared background models shown in Figure 2.3. The result has been multiplied with  $E^2$  in order to be comparable to the  $\nu I_\nu$  display of Figure 3.4. The lower, open symbols represent the unfolding result using the lower estimate for the background field strength, the filled markers indicate the results of the unfolding using the upper estimate shown in Figure 2.3.

Source: Mkn 421 data from 1999-2001, unfolding kindly provided by T. Kneiske

$F_{\text{coff}}^{\text{intr.}} = f_0^{\text{intr.}} \cdot (E[\text{TeV}])^{-\alpha^{\text{intr.}}} \cdot e^{-E/E_c^{\text{intr.}}}$			
IR level	$f_0^{\text{intr.}}$ [ $10^{-10} \cdot \text{TeV}^{-1} \text{cm}^{-2} \text{s}^{-1}$ ]	$\alpha^{\text{intr.}}$ —	$E_c^{\text{intr.}}$ [TeV]
<b>high</b>			
high	$11.7 \pm 2.1$	$0.29 \pm 0.29$	$1.56 \pm 0.44$
low	$7.1 \pm 1.3$	$0.74 \pm 0.29$	$1.43 \pm 0.37$
<b>medium</b>			
high	$7.9 \pm 2.5$	$-0.13 \pm 0.50$	$1.11 \pm 0.4$
low	$4.7 \pm 1.5$	$0.34 \pm 0.51$	$1.07 \pm 0.37$
<b>low</b>			
high	$1.40 \pm 0.12$	$1.18 \pm 0.18$	$3790 \pm 19070$
low	$0.804 \pm 0.069$	$1.73 \pm 0.18$	$2605.2 \pm 1.41$

Table 8.5: The fit parameters of a cutoff fit function to the source-intrinsic energy spectra ('low', 'medium' and 'high') as shown in Figure 8.13. The fit has been carried out for two levels of the model infrared background, labeled 'low' and 'high'.  $f_0^{\text{intr.}}$  denotes the flux normalisation constant,  $\alpha^{\text{intr.}}$  the power law index,  $E_c^{\text{intr.}}$  the cutoff energy.

Source: Mkn 421 data from 1999-2001, unfolding kindly provided by T. Kneiske

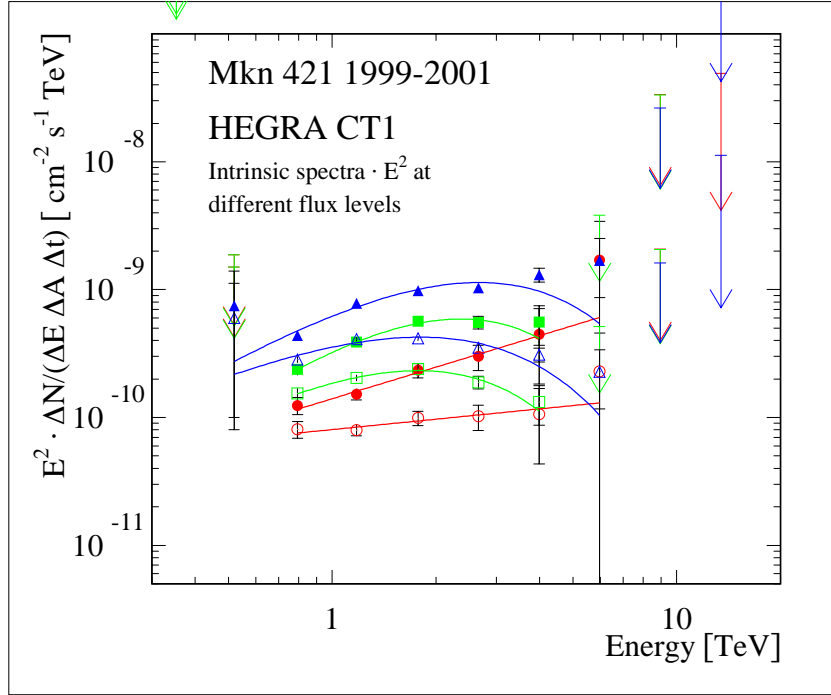


Figure 8.13: Like Figure 8.12, this time the fits of a cutoff spectrum to the unfolded spectra have been added after these fits have been multiplied with  $E^2$ . The parameters of the fits are given in Table 8.5.

Source: Mkn 421 data from 1999-2001, unfolding kindly provided by T. Kneiske

IR level	$E_p^{intr.}$ [TeV]	$f_p^{intr.}$ [ $10^{-10} \cdot \text{TeV cm}^{-2} \text{s}^{-1}$ ]	$\Gamma$ —
<b>high</b>			
high	$2.7 \pm 1.2$	$11 \pm 11$	$0.19 \pm 4.5$
low	$1.80 \pm 0.88$	$4.2 \pm 3.1$	$0.03 \pm 3.5$
mean	$2.38 \pm 1.50$	$10.5 \pm 11.4$	$0.16 \pm 5.2$
<b>medium</b>			
high	$2.4 \pm 1.4$	$5.9 \pm 9.3$	$0.19 \pm 4.5$
low	$1.77 \pm 1.16$	$2.3 \pm 3.0$	$0.03 \pm 3.5$
mean	$2.15 \pm 1.84$	$5.56 \pm 9.77$	$0.16 \pm 5.2$
<b>low</b>			
high	$3108 \pm 16320$	$450 \pm 2777$	—
low	$703 \pm 469$	$3.6 \pm 4.3$	—

Table 8.6: Parameters derived from the quantities listed in Table 8.5.  $E_p^{intr.}$  denotes the peak energy of the spectrum which has been multiplied with  $E^2$ ,  $f_p^{intr.}$  denotes the flux constant at this peak position and corresponds to the peak luminosity as shown in Figure 8.14 for the X-ray range, except that it has not been related to the distance of Mkn 421 (c.f. Appendix 11).

Source: Mkn 421 data from 1999-2001, unfolding kindly provided by T. Kneiske

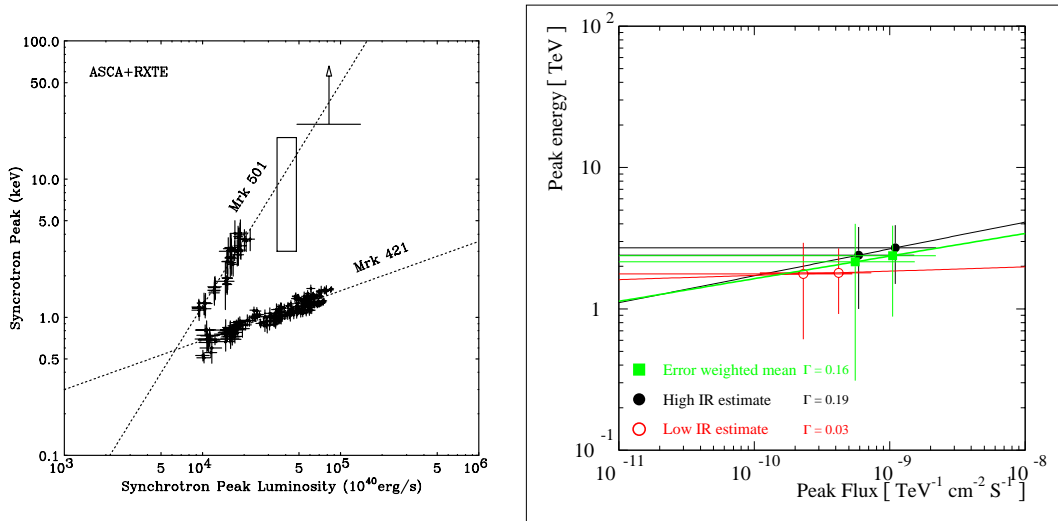


Figure 8.14: The peak energy of the synchrotron peak of Mkn 421 and Mkn 501 versus the peak luminosity in the X-ray domain, determined from pointed observations with the RXTE and ASCA satellites (left-hand side). On the right-hand side the corresponding estimates for the peak energy of the spectral peak in the TeV region versus the corresponding peak flux is shown. The red and black colour data points correspond to the lower and to the higher EBL estimate respectively, the green data points represent an error-weighted average. See text for more details.

Source: (Kataoka et al., 2001), CT1 Mkn 421 observations 1999-2000 and 2000-2001

Using the two extreme sets of infrared background models as shown in Figure 2.3, the flux-separated CT1 spectra as shown in Figure 8.11 have been unfolded to source-intrinsic spectra and multiplied with the square of the energy ( $E^2$ ). The resulting shapes — shown in Figures 8.12 and 8.13 — may be directly compared to the  $\nu I_\nu$  plot of Figure 3.4, left-hand side for Mkn 421. Such a display allows one to judge the respective energy output over a wide range of energies.

The lower infrared background used for the unfolding corresponds to lower estimates for the intrinsic flux. A cutoff fit has been performed on the unfolded spectra, the results summarised in Table 8.5. It can be seen from Figure 8.13 and from the values listed for the low-flux data that the cutoff fit has not converged for this subset. Therefore the remaining discussion concentrates on the medium and high-flux data only.

In order to compare the relation of the peak luminosity and the peak energy of the synchrotron peak (Equation (8.2)) to the behaviour in the TeV domain, a peak energy

$$E_p^{intr.} = E_c^{intr.} \cdot (2 - \alpha^{intr.}) \quad (8.4)$$

and a peak flux

$$f_p^{intr.} = (E_p^{intr.})^{2-\alpha} \cdot f_0^{intr.} \cdot e^{E_p^{intr.}/E_c^{intr.}} \quad (8.5)$$

have been calculated for the intrinsic energy spectra for the two remaining flux levels. Their values are given in Table 8.6 together with a quantity  $\Gamma$ , representing the exponent of the

relation

$$E_{p, Mkn\ 421, TeV}^{intr.} \propto (f_{p, Mkn\ 421, TeV}^{intr.})^\Gamma \quad (8.6)$$

for the TeV domain. This exponent is given in Table 8.6 in the rows of the medium and the high TeV-flux. It has been calculated using the medium and the high-flux data points for the two different sets of infrared background levels. In addition the intrinsic energy spectra for medium and for high-flux TeV data have been combined to an error-weighted mean result (label 'mean'), for which the exponent  $\Gamma$  has been calculated as well. The values of  $\Gamma$  in Table 8.6 show that

1. the range of the exponent  $\Gamma$  varies from 0.03 to 0.19 for the two extra-galactic background light levels (c.f. Figure 2.3) and that
2. the error estimates (from error propagation) are so large that it is not permissible to draw stringent conclusions from this result.

Nevertheless the trend to small variations of the peak energy as a function of the flux is visible in the TeV domain for Mkn 421, similar to the result of (Kataoka et al., 2001). It was no more possible for this thesis, to produce equivalent results for Mkn 501 in order to compare the properties of the two sources in this respect.



## 9 Summary and outlook

### 9.1 Monte Carlo simulation and analysis

As the 5 m<sup>2</sup>-area main mirror of CT1 had been doubled in size using new all-aluminium mirrors, it was necessary to carry out a new Monte Carlo simulation.

For the simulation of the CHERENKOV light production from extended air showers the CORSIKA package, the standard software package for this type of simulation, was used. Atmospheric scattering and the reflection processes of CHERENKOV light were simulated by Dorota Sobczyńska (Sobczynska and Lorenz, 2002). The simulation also included a sophisticated modeling of the trigger process, a critical ingredient both for the estimation of trigger efficiencies and for the estimation of the telescope energy threshold for the detection of TeV  $\gamma$ -rays. The zenith angle coverage was enhanced as compared to earlier data sets, as software packages for larger zenith angle simulations were now available.

The analysis of the Monte Carlo data was also reprogrammed. The analysis still, however, follows the tracks outlined in (Petry, 1997).

### 9.2 Data quality

The data collected in each observation night was examined during the following day for quality and source activity. With increasing experience it became possible to develop very powerful indicators to judge data quality. By interpreting these indicators, it was possible to get a rough idea of hardware problems, if present, and to repair the damaged parts during daytime. This scheme resulted in a very reliable data recording system.

Using this experience, it was further possible to develop sophisticated analysis routines capable of treating data affected by hardware faults. While it was sometimes impossible to correct for certain faults and such data had to be omitted, some of the minor problems could be cured, thus making a maximum amount of data available for analysis. An example of the latter is the correction for the influence of electromagnetic pickup.

Efficient monitoring was not restricted to the hardware, but was also applied to the source activity. While the policy for data recording with CT1 was to maximise the observation time of Crab and of Mkn 421 even in periods of low activity, the CT SYSTEM was alerted whenever Mkn 421 showed signs of activity. This way the higher sensitivity of the CT SYSTEM could be exploited for the search for new sources, while CT1 monitored known sources.

A further, newly developed quality cut was applied to account for changes in atmospheric transmission. Using the currents measured in the CT1 pixels, the star contribution of the currents was estimated and required to lie within a certain range. Whenever exceedingly low values of the current indicated bad atmospheric transmission, the affected data were discarded.

### 9.3 Analysis improvements

Whereas telescope tracking uncertainties were not considered important and were not corrected for while the former 5 m<sup>2</sup>-mirror was in use, the pointing correction developed for use in this

analysis is important in the case of the data presented here.

The major remaining uncertainty in this analysis is connected with the conversion factors between ADC counts and the number of photoelectrons they correspond to.

In order to quantify the influence of this uncertainty, a systematic study has been performed, based on Crab data from 1999-2000. It yields a systematic uncertainty for the powerlaw index  $\alpha$  and the flux constant  $f_0$ . Any further systematic uncertainty is unknown and can therefore not be quantified.

While the background of hadronic events is usually just considered an obstacle in the extraction of  $\gamma$ -signals, the properties of hadronic image parameter distributions have been exploited in a new method used here. As the hadronic background is uniform and non-variable in time, shape and location of the raw *Width* and *Length* distributions serve to build up a reference system: the hadronic distributions have been found to be influenced by varying nightsky background conditions brought about by the conservative image cleaning process employed in the CT1 analysis. Reverting the changes induced by the nightsky background conditions and shifting the hadronic distributions to a set of reference distributions from Crab data recorded between January and March 2001 led to a more efficient  $\gamma$ -hadron separation. Notable improvements were achieved with regard to background noise suppression, almost halving the background contribution in the signal region. For this analysis the  $\gamma$ -hadron separation cuts were optimised using half of the Mkn 421 high-flux data from 2001.

Using the more universal ratio of *Dist* / *Width* instead of *Width* and *Dist* alone for the impact parameter estimation led to a more stringent estimation of initial energies, although this estimation still bears potential for improvements.

## 9.4 Results

The improved analysis scheme has been tested on the TeV standard candle, i.e. on data from the Crab Nebula from the periods 1999-2000 and 2000-2001. The result is found stable in time, independent of the zenith angle and consistent with the measurements obtained with other CHERENKOV telescopes.

For Mkn 421 an onset of a flaring activity was found in the data from 1999-2000. Intranight flux changes can be seen very clearly.

It is difficult to clearly name the underlying spectral form of the time-averaged differential energy spectrum of Mkn 421 in 1999-2000. The quality of a cutoff fit expressed in terms of  $\chi_{red}^2$  is only modest in the case of the 1999-2000 data, whereas the (preliminary) 2000-2001 data set displays a clearly favoured value of a cutoff energy.

A clearer picture emerges, when the artificial separation according to observation periods is dropped in favour of a flux-level separation. In order to have sufficient statistics for such a test, the data sets of 1999-2000 and of 2000-2001 were combined. According to the one-day average fluxes the daily spectra were then sorted into three bins of low, intermediate and high fluxes. The low-flux data could not be fitted with an energy cutoff function, whereas the medium range and high-flux data display cutoff energies between around 2 and 3 TeV, rising with flux.

In order to address source-intrinsic properties of Mkn 421, the extragalactic background

light model of (Kneiske et al., 2002b) has been used to de-convolve the three spectra at the different flux levels to their intrinsic energy spectra. Investigating the shifts of the TeV peak as a function of the TeV flux, hints for the shift in the TeV region being smaller than that in the X-ray region were found. As the cutoff energy is close to the lower bound of the accessible energy range for the source-intrinsic energy spectra, the power-law index is only constrained by very few data points, leading to large correlations between the fitted parameters.

## 9.5 Outlook

It is beyond the scope of this thesis to give more than qualitative statements about flux dynamics and energy spectrum of Mkn 421. The observations in 2000-2001 showed a dramatic flaring activity of Mkn 421, observed at almost all wavelengths. Several multi-wavelength campaigns have been carried out during this outburst, the analysis of which is currently in progress.

The cutoff in Mkn 421's (preliminary) energy spectrum from the year 2001 is located at a slightly lower energy than that of Mkn 501 observed in the year 1997. The question about changes of intrinsic peaks in the X-ray region has been addressed earlier for the two of the sources. This thesis contains the first such analysis in the TeV region, making use of the best model of the extragalactic radiation field available today. Despite the large errors of the result obtained here, it will be interesting to compare the result obtained from Mkn 421 to that of Mkn 501.

Due to the proximity of intrinsic cutoff energies to the lower bound of the energy range accessible with CT1, the results' reliability is only weak. It shall be interesting to repeat this study in the GeV to TeV region, using data from the next generation instruments like HESS or MAGIC, maybe in combination with space borne instruments like GLAST.



## 10 Acknowledgements / Danksagung

Diese Arbeit wäre unmöglich gewesen ohne das Stipendium der Max-Planck-Gesellschaft, das ich drei Jahre lang unter Herrn Professor Schmitz in der Arbeitsgruppe von Eckart Lorenz am MPI für Physik in München genoss. Beiden gilt mein Dank für das Vertrauen, das sie in mich hatten (und haben). Ohne die unermüdliche Arbeit am Detail und die Diskussionen darüber wäre ich nicht vom Fleck gekommen.

Mein Dank dafür gilt allen Beteiligten in der Arbeitsgruppe, vor allem Daniel Kranich, meinem Partner für CT1, der in geduldigen Diskussionen die Linie finden half. Besonderer Dank geht auch an Thomas Schweizer.

Ohne Dorota Sobczynska, die die Monte Carlo Simulation schrieb und laufen liess, wäre diese Arbeit auch unmöglich gewesen. Herzlichsten Dank für die Geduld mit meinen Fragen!

Besonderer Dank geht an alle Kolleginnen und Kollegen, die im Hintergrund für ein reibungsloses Funktionieren des Computersystems — Sven Denninghoff — und aller Verwaltungs- und sonstiger unphysikalischer Dienstleistungen sorgten — besonders Ina Wacker, Katja Müller, Edeltraud Haag, Sybille Rodriguez, Peter Sawallisch und den Damen und Herren auf dem Roque de los Muchachos.

Hier ist auch der Ort um meinen Kolleginnen und Kollegen aus den anderen Instituten und Gruppen von HEGRA zu danken, die die Arbeit durch ihren Einsatz bei der Datennahme vor Ort, Analyse-, Backup- und andere Arbeiten entscheidend unterstützt haben. Vor allem möchte ich meinen weiteren Arbeitgebern — Giselher Lichti, Andreas von Kienlin und der GBM Gruppe am MPE danken, in deren Arbeitsgruppe ich mitarbeiten durfte. Ein besonderer Dank geht an Karl Mannheim: für sehr fruchtbare Diskussionen und die Bereitschaft, mich in seine Gruppen in Göttingen und Würzburg aufzunehmen, obwohl diese Arbeit noch nicht ganz fertig gestellt war.

Ein besonderes Dankeschön geht an meine Englisch-Korrektorin Karin Seeger. Ich möchte alle Komplimente, die ich für das Englisch bekommen habe, an sie weitergeben. Sie hat manche grossen und umständlichen Konstruktionen in wunderbarstes Englisch gepackt. Natürlich bin nur ich für alle Fehler verantwortlich, die noch enthalten sein könnten.

Ich möchte auch nicht versäumen, meinen Eltern, Geschwistern und vor allem meinem Grossvater selig zu danken, deren moralische und nicht zu vergessen finanzielle Unterstützung die Fertigstellung der Arbeit erst möglich gemacht haben. Ausserdem bedanke ich mich speziell bei Tantchen, meinen lieben Kusinen Ursula und Sabine und den Organisierern der letzten Ferien, wo ich mich um nichts zu kümmern brauchte.

An dieser Stelle möchte ich auch dem Arbeitsamt München und Kurt, dem Chef vom Fahrradkurier München danken.

Hier soll auch Platz sein für den Dank an meine Freunde und Bekannten im Bayerischen Wald und in München und anderswo. Spezieller Dank geht an EunAe und Stefan Donle, Roman Liebe, Jörg Fanghänel, Rainer Scheunemann, Nicole Westerkowsky, Thomas Buschky, Silke Streppelhoff, Serena Buchner, Marco Schierloh, Alex Bierstedt, Robert Schwarz, Markus Gaug, Mireia Dosil Bonmati, Elena Perez, Claudia Rossmann, Krischan Böger, Prof. Längsfeld, Verena, Gerhard, Vinzenz und Laura Riffeser, Jörg Graser, Claudia Ocaña, Kristin Bischof,

Evelyn Ringeisen, Christian Hunger und meine Freunde von der RSG Würzburg, wo man so herrlich mit dem Rad in der Gegend rumbrechen kann und an alle, die ich leider vergessen habe zu erwähnen.





## 11 Appendix: Definitions of flux and related quantities

### 11.1 Definitions of some basic physical quantities relevant to spectral analyses

In the following several quantities which appear in the literature and throughout this thesis are defined<sup>48</sup>.

#### ■ Luminosity $L$

The **luminosity**  $L$  is defined as the **total outward flow of energy**  $dE$  from a given object **per time interval**  $dt$  over all wavelengths:

$$dE = L \cdot dt \quad .$$

$L$  is the **total energy loss rate** and is identical to the **power output**.

It is an **intrinsic property** and a function of the object's temperature and size, but not a function of the distance between the observer and the object.

The **SI units** of the **luminosity** are given in  $\text{J s}^{-1}$ , which is identical to  $\text{W}$ .

#### ■ (Energy) Flux $\Phi$

The **flux**  $\Phi$  is defined as the **energy outflow** passing **through an area element**  $dA$ :

$$dE = \Phi \cdot dt dA$$

or, in other words,

$$\Phi = \frac{dE}{dt dA} \quad .$$

For isotropic emission the **relation** between the **flux** measured at a distance  $d$  from the object and the **luminosity** of this object is given by the inverse-square-law

$$\Phi = \frac{L}{4\pi \cdot d^2} \quad . \quad (11.1)$$

The **SI units** of the **flux** are given in  $\text{J s}^{-1} \text{m}^{-2}$ , which is identical to  $\text{W m}^{-2}$ .

#### ■ Flux Density $S_\nu$

The **flux density**  $S_\nu$  is defined as the **flux per unit bandwidth**, the index ' $\nu$ ' denoting that this quantity refers to a given wavelength (energy) or wavelength range:

$$dE = S_\nu \cdot dt dA d\nu$$

i.e.

$$S_\nu = \frac{dE}{dt dA d\nu} \quad .$$

The bandwidth is given as the full width half maximum (FWHM) of the accessible

---

<sup>48</sup>This section and the ordering scheme overview are based on (Rybicki and Lightman, 1979), (Longair, 1992), (Longair, 1994), (Robson, 1996) and (Kembhavi and Narlikar, 1999).

wavelength or frequency range of the observing device<sup>49</sup>.

Thus the **flux density** denotes a **flux at a given wavelength or a given wavelength interval**.

This particular definition permits the comparison of results from different instruments and different objects. Further the flux density allows one to compare the relative energy output of a given source at different energies.

The **SI units** of the **flux density** are given in  $\text{J s}^{-1} \text{m}^{-2} \text{s} \equiv \text{J m}^{-2}$ . The derived unit Jy, the 'jansky', named in honour of JANSKY, a pioneer of radio astronomy, is defined as  $1 \text{ Jy} := 10^{-26} \text{ W m}^{-2} \text{ Hz}^{-1}$ .

### ■ Specific intensity $I_\nu$

The **specific intensity** (also called **brightness**) is defined as the **flux density  $S_\nu$  per unit solid angle**<sup>50</sup>:

$$dE = I_\nu \cdot dA dt d\Omega d\nu$$

i.e.

$$I_\nu = \frac{dS_\nu}{d\Omega} \quad .$$

The **SI units** of the **intensity** are given in  $\text{J m}^{-2} \text{ s}^{-1} \text{ sr}^{-1} \text{ s} = \text{W m}^{-2} \text{ sr}^{-1}$ .

The important fact about the intensity is that it does not change with the distance to the object or with the device used for its observation, but is intrinsic to the source.

### ■ Brightness temperature $T_b$

The **brightness temperature** is usually quoted for a **pre-selected frequency** or energy and **characterises the specific intensity  $I_\nu$  at this frequency** by giving the **temperature** of a **blackbody** (see next section) that has the same specific intensity **at that particular frequency**:

$$I_\nu = B_\nu(T_b) \quad .$$

This definition is particularly useful in the RAYLEIGH-JEANS part of the spectrum ( $h\nu \ll kT$ ), where

$$I_\nu = \frac{2\nu^2}{c^2} \cdot k \cdot T_b \quad \text{or}$$

$$T_b = \frac{c^2}{2\nu^2 k} \cdot I_\nu \quad .$$

The brightness temperature is a function of the frequency ( $T_b = T_b(\nu)$ ). For blackbody

---

<sup>49</sup>As  $\nu = c/\lambda$  for electromagnetic waves of frequency  $\nu$  and wavelength  $\lambda$ , with  $c$  denoting the speed of light, the derivative is  $d\nu = -c/\lambda^2 \cdot d\lambda$ . A finite frequency interval  $\Delta\nu$  is then related to a finite wavelength interval  $\Delta\lambda$  as  $\Delta\nu = |-(c/\lambda^2) \cdot \Delta\lambda|$ .

For the human eye with a nonzero sensitivity between 400 nm and 680 nm and a FWHM range between 510 nm and 610 nm the bandwidth can be calculated to be  $9.6 \cdot 10^{13}$  Hz. For  $\lambda$  the centered value  $\langle\lambda\rangle = 560$  nm was used in this calculation.

<sup>50</sup>The relation between the total opening angle  $\theta$  of a cone and the solid angle  $\Omega$  is given by

$$\Omega = 2\pi \cdot (1 - \cos(\theta/2)) \quad ,$$

which simplifies to  $\Omega = \pi\theta^2/4$  for small angles  $\theta$ , measured in units of rad.

emitters the brightness temperature is the same for all frequencies.

### ■ Mass-to-light ratio $M/L$

The mass-to-light ratio serves to judge the luminosity  $L$  of given objects, e.g. whole galaxies or galaxy cores, in terms of the luminosity to be expected if they were made up of sun-like stars.

Usually mass-to-light ratios are given in units of the mass-to-light ratio of our sun,  $M_{\odot}/L_{\odot} = 1.989 \cdot 10^{33} \text{ g} / 3.85 \cdot 10^{33} \text{ erg s}^{-1} = 0.52 \text{ g s erg}^{-1}$ .

Here the usual astrophysical notation of  $1 \text{ erg} := 10^{-7} \text{ J}$  is used.

For stellar systems the values usually lie around 3 to  $5 \times M_{\odot}/L_{\odot}$ .

NGC 4261 is an example of a galaxy which probably has a supermassive black hole at its center, as  $M_{\text{NGC 4261}}/L_{\text{NGC 4261}} \approx 2100 \cdot M_{\odot}/L_{\odot}$  measured within a radius of 50 lightyears from its center.

### ■ Apparent Magnitude $m$

Originally dating back to the Greek astronomer HIPPARCHOS, the apparent magnitude scale divides the stars into six levels of brightness (here brightness is identified with the flux  $F$ ), that can be distinguished with the unaided eye. The eye's response to light is logarithmic. POGSON, who introduced the modern scale, deduced from his measurements that the individual thresholds in HIPPARCHOS' scale corresponds to flux values that are roughly hundredfolds of each other. POGSON adjusted the zero point of the new apparent magnitude scale to the star Vega (Lyra- $\alpha$ ). He introduced the convention that an object that appears to the observer on Earth to be fainter than Vega by a factor of 100 should be assigned an apparent magnitude of  $m = 5$ .

Therefore an apparent magnitude  $m$  of an object with a flux  $\Phi(\text{Object})$  is related to the flux of Vega  $\Phi(\text{Vega})$  as

$$m = -2.5 \cdot \log\left(\frac{\Phi(\text{Object})}{\Phi(\text{Vega})}\right) .$$

The **apparent magnitude** is ruled by the distance to the object and **does not describe an intrinsic property**.

### Absolute Magnitude $M$

The **absolute magnitude**  $M(\text{Object})$  of a given object is defined to **match** the **apparent magnitude** scale for an object **at a distance**  $d(0) := 10 \text{ pc}$ .

The definition uses the luminosity  $L(\text{Object})$  of the object:

$$M(\text{Object}) := -2.5 \cdot \log\left(\frac{L(\text{Object})}{L(0)}\right) ,$$

where

$L(0)$  is the luminosity of the reference object, corresponding to an absolute magnitude of  $M(0) = 0$ .

Using Equation (11.1) on page 137 this can be reformulated as

$$\begin{aligned}
 M &= -2.5 \cdot \log \left( \frac{\Phi \cdot 4\pi \cdot d^2}{\Phi(0) \cdot 4\pi \cdot d(0)^2} \right) \\
 &= -2.5 \cdot \log \left( \frac{\Phi}{\Phi(0)} \right) - 2.5 \cdot \log \left( \frac{d^2}{d(0)^2} \right) \\
 &= m - 2.5 \cdot \log(d^2) - 2.5 \cdot \log(d(0)^{-2}) \quad .
 \end{aligned}$$

This relation is usually expressed in the form

$$m - M = 5 \cdot \log\left(\frac{d}{[\text{pc}]}\right) - 5 \quad ,$$

and is also known as the distance modulus equation.

## 11.2 Example: flux, luminosity and intensity of the sun

The Sun's distance from the Earth is

$$d_{\odot} = 1.496 \cdot 10^8 \text{ km} \quad ,$$

and its radius is

$$r_{\odot} = 6.96 \cdot 10^5 \text{ km} \quad ,$$

which corresponds to an angular diameter of

$$\theta_{\odot} = 9.305 \cdot 10^{-3} \text{ rad} \quad .$$

The solid angle under which we see the sun is

$$\Omega_{\odot} = 6.8 \cdot 10^{-5} \text{ sr} \quad .$$

The flux  $F_{\odot}$  from the sun (also called 'solar constant') is

$$\Phi_{\odot} = 1360 \text{ W m}^{-2} \quad .$$

Assuming that this flux is emitted isotropically, and using the exact figures from (Particle Data Group, 2000), the luminosity  $L_{\odot}$  can be calculated according to Equation (11.1) as:

$$\begin{aligned}
 L_{\odot} &= \Phi_{\odot} \cdot 4\pi \cdot d_{\odot}^2 \\
 &= 3.85 \cdot 10^{26} \text{ W} \quad .
 \end{aligned}$$

Further the intensity  $I_{\odot}$  is

$$\begin{aligned} I_{\odot} &= \frac{F_{\odot}}{\Omega_{\odot}} \\ &= 2.0 \cdot 10^7 \text{ W m}^{-2} \text{ sr}^{-1} \quad . \end{aligned}$$

## 12 Appendix: Viewing effects

X-ray and TeV emission is believed to originate from regions inside the jets of AGNi. The jets of the so-called blazars approach us at relativistic speeds. Therefore observations on Earth are affected by relativistic viewing effects, which are summarised in the following.

### 12.1 Superluminal motion

The highest resolution images of jets and their origins, the AGN cores, can be obtained in the radio range<sup>51</sup>. In this energy range it is possible to identify single structural features, so-called 'blobs' in the jets as well as the cores of AGNi from which they emanate, and to follow their evolution by observing them over several years.

In the case of 3C 345 it was possible to prove the fixed position of its core with respect to other nearby radio sources (see e.g. (Bartel et al., 1986)), while several blobs in the jets were observed to move outwards from the core at apparent speeds greater than the vacuum speed of light.

The general geometry of core, jet and blobs is sketched in Figure 12.1(a): an observer sees the core of an AGN and a radio emitting feature, a blob, moving downstream along the jet with velocity  $v$ .  $\theta$  denotes the inclination angle of the jet with respect to the line of sight.

The emission duration  $dt_e^{core}$  of a given signal in the reference frame of the core is compared to the duration  $dt_o$  of the same signal when measured in the observer's restframe. Viewed along the observer's line of sight, the blob's movement along the jet during the emission duration  $dt_e^{core}$  corresponds to a movement towards the observer along a path component of length  $v \cdot dt_e^{core} \cdot \cos \theta$ , see Figure 12.1(b). Therefore the observation time  $dt_o$  is the complete emission time reduced by the time required for light to travel the length of the beforementioned component towards the observer:

$$dt_o = dt_e^{core} - \frac{1}{c} \cdot v \cdot dt_e^{core} \cdot \cos \theta = (1 - \beta \cdot \cos \theta) \cdot dt_e^{core} \quad . \quad (12.1)$$

A measured displacement in the sky then corresponds to an apparent separation speed  $v_a$  of

$$v_a = \frac{dx_{across}}{dt_o} = \frac{dt_{across}}{dt_o} \cdot c = \frac{\beta \sin \theta}{(1 - \beta \cos \theta)} \cdot c \quad , \quad (12.2)$$

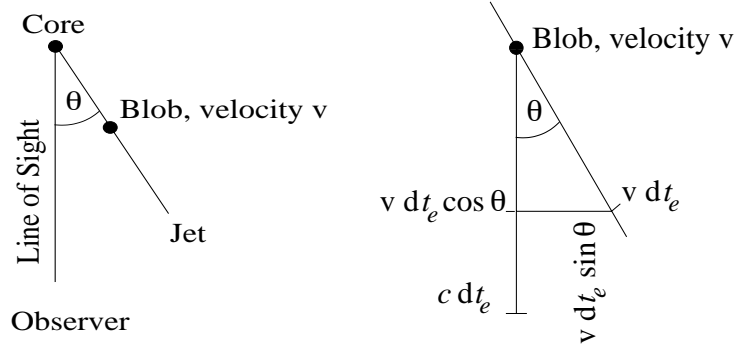
which may exceed  $c$  for combinations of sufficiently small inclination angles  $\theta$  and sufficiently large values of  $\beta = v/c$ .  $x_{across}$  and  $t_{across}$  denote the pathlength traveled perpendicular to the line of sight, and the time required for this travel respectively.

### 12.2 Relativistic bulk motion

In the following the quantity  $\gamma = 1/\sqrt{1 - v^2/c^2}$  denotes the relativistic gamma factor of an object with velocity  $v$  with respect to the core, where  $c$  denotes the vacuum speed of light.

---

<sup>51</sup>Radio receivers placed very far apart from each other are connected to form one extensive virtual dish. The method is called very long baseline interferometry (VLBI), the resolutions achievable are of the order of a few milliarcseconds.



(a) Line of sight and the direction of a radiating 'blob' moving relativistically downstream along the jet.

(b) Sketch to calculate the duration of a signal at the observer's position compared to the emission time.

Figure 12.1: Diagrams showing the superluminal motion in jets. The jet has an inclination angle  $\theta$  with respect to the line of sight. A blob moves at a speed  $v$  downstream along the jet. A signal emitted during the time period  $dt_e$  in the core's restframe arrives at the observer's position during a time period  $dt_o$ . (See text for details)

During a time  $dt_e^{blob}$  in the restframe of the blob, which dilates to  $\gamma \cdot dt_e^{blob}$  in the restframe of the core,  $N$  wave peaks are emitted. These peaks arrive at the observer's position during a time  $dt_o$

$$dt_o = \gamma \cdot dt_e^{blob} - \gamma \cdot \frac{1}{c} \cdot v \cdot dt_e^{blob} \cdot \cos \theta = \gamma \cdot (1 - \beta \cdot \cos \theta) \cdot dt_e^{blob} \quad , \quad (12.3)$$

still consisting of  $N$  wave peaks. Thus an emitted frequency  $\nu'_e$  is transformed into a frequency  $\nu_o$  at the observer's position as

$$\nu_o = \frac{N}{dt_o} = \frac{N}{\gamma(1 - \beta \cos \theta) dt_e^{blob}} = \frac{1}{\gamma(1 - \beta \cos \theta)} \cdot \nu'_e =: \mathcal{D} \cdot \nu'_e \quad , \quad (12.4)$$

defining the DOPPLER factor  $\mathcal{D}$ . Accounting for cosmological redshifts this is transformed into (Kembhavi and Narlikar, 1999, p. 57)

$$\nu_o = \frac{\mathcal{D}}{1 + z} \cdot \nu'_e \quad , \quad (12.5)$$

where  $z$  is the redshift of the source in question.

As  $I(\nu)/\nu^3$  is a Lorentz invariant, with  $I(\nu)$  being the intensity of a source emitting at a frequency  $\nu$ , the emitted intensity  $I'_e(\nu'_e)$  is transformed into an observed intensity (Kembhavi and Narlikar, 1999, p. 57) of

$$I_o(\nu_o) = \mathcal{D}^3 I'_e(\nu'_e) \quad , \quad (12.6)$$

where the indices 'e' and 'o' are again used as abbreviations for 'emitted' and 'observed' respectively.

For optically thin sources and for spherically symmetric sources the flux  $F(\nu)$  is proportional

to the intensity:  $F(\nu) \propto I(\nu)$ . For a powerlaw rest frame flux  $F'(\nu'_e) \propto \nu'_e{}^{-\alpha}$  the transformation becomes (Kembhavi and Narlikar, 1999, p. 57)

$$F(\nu_o) = \mathcal{D}^{3+\alpha} \cdot F'(\nu'_e) \quad . \quad (12.7)$$

Two identical sources, one with an inclination angle of  $\theta$  with respect to the line of sight, the second one with an inclination angle of  $\theta + \pi$ , are a simple model of two blobs in a jet moving away from the core in opposite directions. One approaches the observer and is seen with a flux  $F_{in}^\theta$ , the other one recedes from the observer and is seen with a flux  $F_{out}^{\theta+\pi}$ . According to (Kembhavi and Narlikar, 1999, p. 58) the ratio of these fluxes is

$$\frac{F_{in}^\theta}{F_{out}^{\theta+\pi}} = \left( \frac{1 - \beta \cos(\theta + \pi)}{1 - \beta \cos \theta} \right)^{3+\alpha} = \left( \frac{1 + \beta \cos \theta}{1 - \beta \cos \theta} \right)^{3+\alpha} \quad . \quad (12.8)$$

Therefore sources with intrinsically symmetric jets may appear asymmetric to a remote observer. A famous example is M 87, whose jet structure appears to be only single sided, see for instance (Keel, 2001).

## 13 Appendix: Relevant radiation processes

Observations of AGNi have been attributed to a mixture of different emission processes. The following section gives a brief description of the most important emission mechanisms and high energy interaction processes which appear in the discussion of AGNi properties.

### 13.1 Thermal processes

**Blackbody radiation is the most abundant form of radiation in the universe.**

In a blackbody, which by definition is a perfect absorber and emitter of radiation in thermal equilibrium with its surroundings, the velocities  $v$  of the atoms follow a MAXWELLIAN distribution

$$N(v)dv \propto v^2 e^{-\frac{mv^2}{2kT}} dv \quad ,$$

where

$N(v)$  is the number of atoms with velocity  $v$  in the interval  $[v; v + dv]$ ,

$k = 1.381 \times 10^{-23} \text{ JK}^{-1} = 8.617 \times 10^{-5} \text{ eVK}^{-1}$  is the BOLTZMANN constant and

$T$  is the absolute temperature characterising the blackbody.

On passing each other closely, the atoms as a whole alter their speed, emitting a photon with a wavelength corresponding to the energy difference. The result is a continuous spectrum, as the atoms act as a whole and no distinct energy levels are involved.

Blackbody radiation is emitted isotropically and unpolarised. The spectrum is described by PLANCK's radiation equation (Rybicki and Lightman, 1979)

$$\frac{dE}{d\Omega dA dt d\nu} = B_\nu(T) = \frac{2h\nu^3}{c^2(e^{h\nu/kT} - 1)} \quad ,$$

where

$B_\nu$  is the emitted intensity of radiation per unit frequency interval at a frequency

$\nu$ ,

$h = 6.626 \cdot 10^{-34} \text{ Js}$  is the PLANCK constant,

$c = 2.998 \cdot 10^8 \text{ m/s}$  the vacuum speed of light, and

$T$  the absolute temperature characterising the blackbody.

The luminosity  $L$  (radiated energy per unit time) emitted by a blackbody is given by

$$L = 4\pi r^2 \sigma T^4 \quad ,$$

where

$r$  is the radius of the source

of absolute temperature  $T$  and

$\sigma = \pi^2 k^4 / (60 \hbar^3 c^2) = 5.670 \cdot 10^{-8} \text{ W m}^{-2} \text{ K}^{-4}$  is the STEFAN-BOLTZMANN constant (Particle Data Group, 2000).

WIEN's displacement law relates the wavelength  $\lambda_{max}$  of maximum emission to the absolute temperature  $T$  as

$$\lambda_{max} T = 2.897 \times 10^{-3} \text{ m K} \approx 3 \text{ mm K}$$

(Particle Data Group, 2000).

Usually stars are treated as blackbodies.

### **Dust obscured stars are modeled as grey bodies.**

The PLANCK spectra  $B_\nu(T)$  of stars or other hot objects like AGN cores may be distorted by surrounding layers of dust. Empirically the intensity  $I(\nu)$  is found to follow distributions like (Robson, 1996, p. 119f)

$$I(\nu) = \left( \frac{\nu}{[\text{Hz}]} \right)^\beta \cdot B_\nu(T)$$

with emissivity indices  $\beta$  of around 2.

Consequently one finds  $I(\nu) \propto \nu^4$  in the RAYLEIGH-JEANS part of the spectrum ( $h\nu \ll kT$ ) instead of  $I(\nu) \propto \nu^2$  like in the pure blackbody case.

### **Any hot, ionised gas emits Bremsstrahlung.**

Bremsstrahlung is also called free-free emission. In an astronomical context it is found for example as radio emission from compact regions of ionised hydrogen, called HII regions, at temperatures  $T$  of around  $10^4 \text{ K}$ , as X-ray emission of binary X-ray sources with  $T \approx 10^7 \text{ K}$  or as diffuse X-ray emission from hot intergalactic gas in clusters of galaxies, the temperature reaching up to values of  $T \approx 10^8 \text{ K}$ .

Accelerated charged particles - in an astronomical context mostly accelerated electrons - emit most Bremsstrahlung when they are accelerated perpendicularly to their initial direction of motion. The dipole emission is polarised with the electrical field vector lying in the direction of the acceleration vector projected onto a sphere at a large distance. The maximum emitted energy corresponds to the particle's initial kinetic energy.

Bremsstrahlung is partly self-absorbed in the emitting medium. In the optically thick part of the wavelength range the intensity  $I(\nu)$  scales with  $\nu^2$ , where  $\nu$  denotes the frequency of the radiation (Robson, 1996, p. 118), whereas  $I(\nu)$  is almost constant for higher energies. Such spectra are characteristic of compact HII regions close to star-forming regions.

## 13.2 High energy processes

**Synchrotron radiation is emitted by charged particles of high or very high energy gyrating in a magnetic field.**

An electron, whose direction of flight forms a pitch angle  $\theta$  with an ambient magnetic field of strength  $B$ , has an energy loss rate  $-dE(\theta)/dt$  of (Longair, 1994, p. 231)

$$\begin{aligned} -\frac{dE(\theta)}{dt} &= 2 \left( \frac{e^4}{6\pi\epsilon_0^2 c^4 m_e^2} \right) \left( \frac{v}{c} \right)^2 c \frac{B^2}{2\mu_0} \gamma^2 \sin^2 \theta \\ &= 2\sigma_T c U_{mag} \left( \frac{v}{c} \right)^2 \gamma^2 \sin^2 \theta \quad , \end{aligned}$$

where

$$\sigma_T = \frac{e^4}{6\pi\epsilon_0^2 c^4 m_e^2} = \frac{8\pi r_0^2}{3} = 6.65 \cdot 10^{-25} \text{ cm}^2 \quad (13.1)$$

denotes the THOMSON cross section, where

$r_0 = e^2/4\pi\epsilon_0 m_e c^2$  is the classical electron radius,

$m_e$  is the electron restmass.

$U_{mag} = B^2/2\mu_0$  is the energy density of a magnetic field of strength  $B$ ,

$\gamma = 1/\sqrt{1 - (v/c)^2}$  where

$v$  is the velocity of the particle and

$c$  the vacuum speed of light.

$\epsilon_0 = 8.854 \times 10^{-12} \text{ Fm}^{-1}$  is the permittivity of free space (Particle Data Group, 2000) and

$\mu_0 = 4\pi \times 10^{-7} \text{ NA}^{-2}$  is the permeability of free space (Particle Data Group, 2000) with  $\epsilon_0 \cdot \mu_0 = 1/c^2$ .

In the ultrarelativistic limit  $v \rightarrow c$  the energy loss rate becomes (Longair, 1994, p. 232):

$$-\frac{dE(\theta)}{dt} = 2\sigma_T c U_{mag} \gamma^2 \sin^2 \theta \quad .$$

As any one particle probably undergoes many consecutive scatters that change the pitch angle  $\theta$  and as an ensemble of electrons will, at any given time, cover all pitch angles uniformly, an integration over  $\theta$  is carried out, yielding an average energy loss rate per electron of (Longair, 1994, p. 232)

$$-\frac{dE}{dt} = \frac{4}{3} \sigma_T c U_{mag} \left( \frac{v}{c} \right)^2 \gamma^2 \quad .$$

For the case of relativistic particles most of the energy is found to be emitted around a critical frequency  $\nu_c \approx \gamma^2 \nu_g$ , where  $\nu_g = ZeB/2\pi\gamma m_0$  is the gyro frequency of a particle of restmass  $m_0$  and charge  $Z$ .

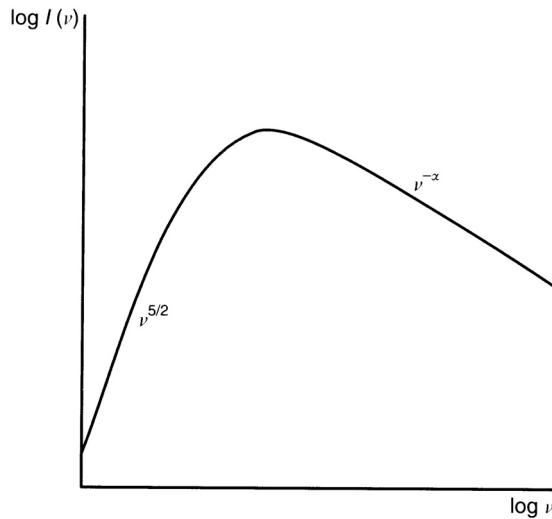


Figure 13.1: Schematic intensity spectrum for a source showing synchrotron selfabsorption. Below a certain frequency the index, defined as the negative exponent in  $E^{-\alpha}$ , changes from an observed value of  $\alpha = (p - 1)/2$  to  $-5/2$  (see text). Such curves are measured in the low energy to X-ray region of blazar (see Section 2.1 for the definition) spectra. Reproduced from (Longair, 1994)

For an electron the gyro frequency at a magnetic field strength  $B$ , expressed in units of TESLA, is

$$\frac{\nu_{g, electron}}{B/1 \text{ T}} = 28 \text{ GHz/T} \quad .$$

The intensity spectrum of a powerlaw distribution of electron energies with index  $p$  is given by (Longair, 1994, p. 252) as<sup>52</sup>

$$I(\nu)d\nu \propto B^{\frac{p+1}{2}} \cdot \nu^{-\frac{p-1}{2}} \quad .$$

**In the low energy range synchrotron radiation is selfabsorbed.**

This leads to a characteristic shape of the intensity spectrum; independently of the energy distribution of the electron population a spectral index of  $-5/2$  is observed below a certain break frequency, while above this turning point (see Figure 13.1) the intensity  $I_\nu$  scales with  $\nu^{-(p-1)/2}$ , see e.g. (Rybicki and Lightman, 1979, p. 190). The low energy slope index of  $-5/2$  is distinctly different from the RAYLEIGH-JEANS value of  $-2$ , the latter being indicative of thermal emission.

Examples for this behaviour are found at radio, centimeter and millimeter wavelengths when observing emission from AGN cores and quasars.

Synchrotron radiation in the X-ray domain is emitted from AGNi from electron populations with energies of around  $10^{12}$  eV in the presence of a magnetic field with a strength of around  $10^{-4}$  T in the AGNi.

---

<sup>52</sup>Here the distinction between units of energy and units of LORENTZ factors, which is made in the original formula, expressed by a proportionality constant named  $\kappa$ , is neglected.

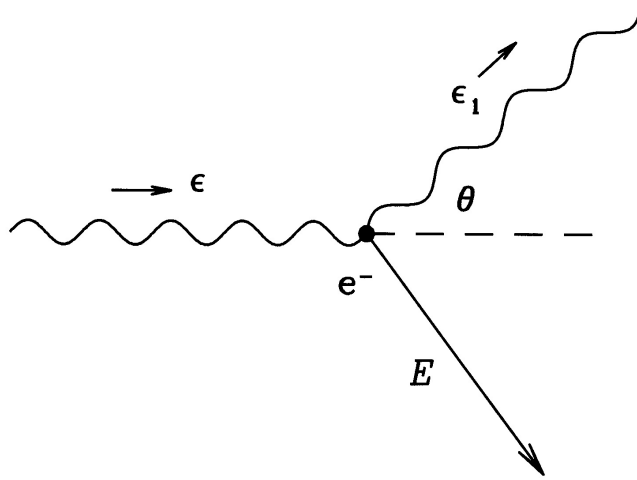


Figure 13.2: Principle sketch of COMPTON scattering: an incident photon with energy  $\epsilon$  is scattered to an energy  $\epsilon_1$  by an electron (marked  $e^-$ ) and alters its direction by an angle  $\theta$ . The electron was previously at rest and acquired an energy  $E$  through the scatter. In astronomic contexts the inverse COMPTON effect is much more important. Reproduced from (Kembhavi and Narlikar, 1999)

### Photons and electrons scatter in Compton and inverse Compton processes.

In the classical calculation ( $h\nu \ll m_e c^2$ ) the photon energy remains unchanged after scattering on an electron.

For the classical calculation it is assumed that the electron absorbs the photon and re-emits it according to LARMOR's formula. This emission is isotropic and leaves the wavelength unchanged, corresponding to elastic scattering. Integration over all possible polarisations gives the total THOMSON cross section  $\sigma_T$  (see Equation (13.1) on page 147).

The connection between initial photon energy  $\epsilon$ , the final energy  $\epsilon_1$  and the photon emission angle  $\theta$  (see also Figure 13.2) is given by (Rybicki and Lightman, 1979) as

$$\epsilon_1 = \frac{\epsilon}{1 + \frac{\epsilon}{m_e c^2} \cdot (1 - \cos \theta)} \quad .$$

The differential cross section for the COMPTON process is given by the KLEIN-NISHINA formula (Rybicki and Lightman, 1979):

$$\frac{d\sigma_{KN}}{d\Omega} = \frac{r_0^2}{2} \cdot \left(\frac{\epsilon_1}{\epsilon}\right)^2 \cdot \left(\frac{\epsilon}{\epsilon_1} + \frac{\epsilon_1}{\epsilon} - \sin^2 \theta\right) \quad ,$$

where

$\Omega$  is the solid angle subtended by the observing device.

Integrated over  $\Omega$  the total KLEIN-NISHINA cross section is given by (c.f. (Rybicki and Lightman, 1979))

$$\sigma_{KN} = \frac{3\sigma_T}{4} \cdot \left( \frac{1+x}{x^3} \cdot \left[ \frac{2x(1+x)}{1+2x} - \ln(1+2x) \right] + \frac{\ln(1+2x)}{2x} - \frac{1+3x}{(1+2x)^2} \right) ,$$

where

$$x = \epsilon/mc^2 \text{ is the ratio of the incident photon energy } \epsilon \text{ to the electron energy } mc^2.$$

In the limit of very small photon energies the *limites*  $\sigma_{KN} \xrightarrow{x \ll 1} \sigma_T$  and  $\epsilon_1 \xrightarrow{x \ll 1} \epsilon$  can be attained. For  $x \ll 1$  and  $x \gg 1$  the scattering is said to take place in the THOMSON regime and in the KLEIN-NISHINA regime respectively.

**In astrophysics, the inverse Compton effect, i.e. the scattering of electrons on photons, is more important than the Compton process.**

In an inverse COMPTON process the particle transfers energy to a photon. In order to calculate the energy transfers inside a relativistically moving jet of particles, mostly electrons, the kinematics of the scattering is evaluated in the restframe of the electrons.

For photon energies  $\epsilon' \ll m_e c^2$  viewed in the restframe of the electron, the photon boosted to the observer's frame has an energy  $\epsilon_1 \simeq \gamma^2 \epsilon$ , which can be very large for a highly relativistic electron (Kembhavi and Narlikar, 1999, p. 68).

The electron loses a fraction  $\gamma^2 \epsilon / \gamma m_e c^2 \ll 1$  of its energy in such a scatter. Energy conservation sets the limit to the energy gain  $\Delta\epsilon$  of the photon to  $\Delta\epsilon < \gamma m_e c^2$ , i.e. the photon cannot gain more than the kinetic energy of the electron.

This limit may be attained in cases where the scattering in the electron's restframe is not THOMSONIAN. In such cases the photon energy after the scatter may reach up to  $\epsilon_1 \simeq \gamma m_e c^2$ , i.e.  $\Delta\epsilon / \gamma m_e c^2 \simeq 1$  (Kembhavi and Narlikar, 1999, p. 68). An electron can, in such instances, lose its entire kinetic energy in the course of a few scatters.

**Pair Production occurs in regions of very high  $\gamma$ -ray photon energy density in the sources, leading to flux decreases. Further the pathlength integrated density of infrared photons also affects the observed TeV spectra.**

In pair production processes a very high energy photon interacts with another photon or with the field of a nucleus and converts into an electron-positron pair. Subsequently to  $e^+e^-$  production, the particles annihilate with their antiparticles, but mostly not their creation partners. The production of two photons has the highest branching ratio.

A low energy photon, e.g. an X-ray photon with energy  $E_X$ , can create an electron-positron pair with a high energy photon of energy  $E_\gamma$  if the inequality (Herterich, 1974)

$$E_X \geq 2 \cdot (m_e c^2)^2 / (1 - \cos(\alpha)) \cdot E_\gamma \quad (13.2)$$

holds. Here

$\alpha$  is the angle between the directions of motion of the two photons.

The cross section rises steeply from the threshold energy given by Equation (13.2). The maximum of the cross section is reached at twice the threshold energy; at still higher energies the cross section drops like  $E_X^{-2}$ .

The energy condition can be also written in the practical form 2000-

$$E_{max}[\text{keV}] \gtrsim 500 \cdot (E_\gamma[\text{MeV}])^{-1}$$

or

$$E_{max}[\text{eV}] \gtrsim 0.5 \cdot (E_\gamma[\text{TeV}])^{-1} \tag{13.3}$$

where

$E_{max}$  is the energy value of the low energy photon that corresponds to the maximum of the pair production cross section.

## 14 Appendix: Ordering schemes for AGN related objects

This section presents a brief overview of some object classes related to AGNi, based on the definitions in (Kembhavi and Narlikar, 1999).

A cautionary note seems in order at this point: the definitions of source types and classes differ somewhat depending on the author. This adds an unquantifiable personal set of preferences of the respective author to the observational bias which may already be inherent in certain search methods. The cataloguing may obscure the underlying physics; a generalised approach to overcome this difficulty is presented in Section 2.1.

### Seyfert Galaxies

SEYFERT Galaxies display bright, star-like nuclei and so-called ‘peculiar’ morphology, as well as strong and broad emission lines. They have been found in redshift surveys and as optical counterparts of strong X-ray and infrared sources.

SEYFERT galaxies are divided into classes I and II, with intermediate states.

**Type I Seyfert galaxies** show bright star-like nuclei with a strong continuum ranging from the far infrared to the X-ray band. Strong emission lines are present, their width ranging from  $\mathcal{O}(100 \text{ km s}^{-1})$  to  $\mathcal{O}(1000 \text{ km s}^{-1})$ .

**Type II Seyfert galaxies** display a weak continuum and only strong, narrow emission lines.

### Radio galaxies

These galaxies are identified with radio catalogue objects. Many of them appeared elliptical in the first place, which raised the question why strong radio emission seems to be correlated with ellipticals. High dynamic range observations later revealed a generally complex and disturbed morphology of radio galaxies.

Some radio galaxies contain an optical nucleus with strong continuum radiation and line emission. Broad line radio galaxies and narrow line radio galaxies resemble SEYFERT Type I and SEYFERT Type II galaxies, except for the energy range in which these properties are displayed.

### Quasars

Quasars are starlike objects that have been identified with strong radio sources.

They show strong emission lines with high redshifts  $z$  of  $z \gtrsim 0.1$ . For  $z \lesssim 1$  high dynamic range optical imaging sometimes reveals a faint fuzz around them.

Low luminosity quasars are similar to luminous SEYFERT galaxies. Therefore quasars are often required to be brighter than a certain minimal magnitude.

The **Q**uasi **S**tellar **O**bjects (QSOs) have the same optical properties but do not necessarily show strong radio emission.

### Markarian galaxies

MARKARIAN galaxies are objects with a blue excess and strong ultraviolet continuum. Roughly 1500 such galaxies were found in MARKARIAN's survey using slitless, low dispersion objective-prisms. MARKARIAN galaxies do not form a unique class of their own but are believed to be a mix of objects that share the blue to UV excess characteristics that were exploited in the search for them. Roughly 10% of them are SEYFERT galaxies. Mkn 421 is a member of the BL Lac fraction of the Blazar class (see below).

### **BL Lac objects**

BL Lac objects typically show strong continuum emission in the radio range, high polarisation and rapid variability. Line emission is weak or absent, therefore it is sometimes difficult to determine their redshifts. Many of them have been found as optical counterparts at X-ray source positions. Sometimes they are found to be the nuclei of elliptical galaxies.

- They usually have flat (powerlaw index  $< 0.5$ ) or inverted radio spectra.
- Their spectra steepen in the infrared or the optical region, showing little or no UV excess.
- They show rapid and large amplitude variation at radio, optical and X-ray energies.
- The radio and optical emission shows large and variable polarisation.
- Their continuum is smooth and featureless and emission lines are weak or absent.

### **Blazars**

The class of blazars is a combination of BL Lac objects and **O**ptically **V**iolently **V**ariable quasars or OVVs. The continuum emission is dominated by non-thermal emission, relativistically beamed due to the bulk motion of the emitting regions.

- They display a smooth continuum emission ranging from infrared to ultraviolet.
- Their optical polarisation is high, reaching up to 3%.
- They are optically rapidly variable with timescales of  $\lesssim 1$  day.
- They display a strong and variable radio continuum.

If the emission lines are weak compared to radio quiet quasars the blazars are called BL Lacs, if the emission lines are stronger, they are called OVVs.

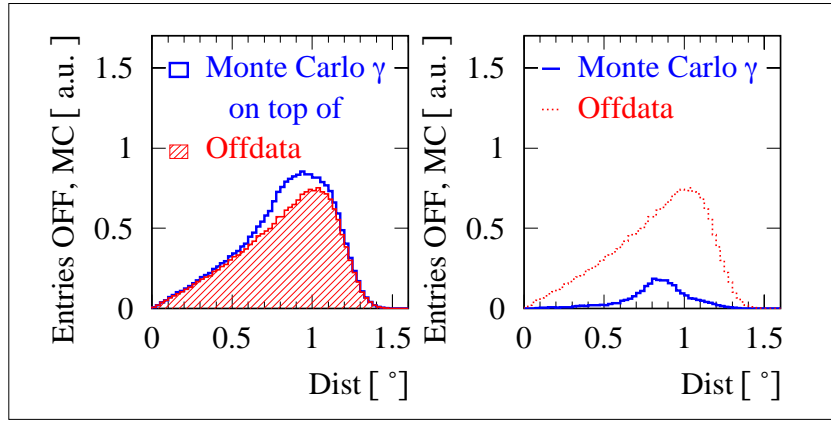


Figure 15.1: Distribution of the  $Dist$  parameter for off-data, i.e. hadrons, in the shaded histogram on the left, with the corresponding distribution for Monte Carlo generated  $\gamma$ -images superimposed as the unshaded histogram.

On the right-hand side the same off-data is shown, this time the distribution for Monte Carlo  $\gamma$ s is superimposed as the red histogram with highly exaggerated statistics.

Source: CT1 offdata and Monte Carlo simulations after noise filter, zenith angle between  $10^\circ$  and  $30^\circ$ .

## 15 Appendix: Image parameter distributions

The Monte Carlo  $\gamma$ -events that were used for the display here were simulated with a powerlaw spectral index of 1.5 and weighted in such a way that they represent a powerlaw distribution with an index of 2.7, i.e. close to that of the Crab. In a plot of the distribution of the unweighted data with the simulated spectral index, the high energy events would dominate the picture and give a distorted impression. The simulated  $\gamma$ -distributions were generated with a NSB corresponding to that of the off source region<sup>53</sup> and are superimposed on hadronic distributions as unshaded histograms. The ZA was limited to a range of  $10^\circ$  to  $30^\circ$  for both off-data and Monte Carlo data.

In the figures shown here some typical distributions of the image parameters are shown for hadronic data from off source observations (shaded histograms) and for Monte Carlo  $\gamma$ -images.

<sup>53</sup>For details of the simulation of NSB noise c.f. Section 16.5.1.

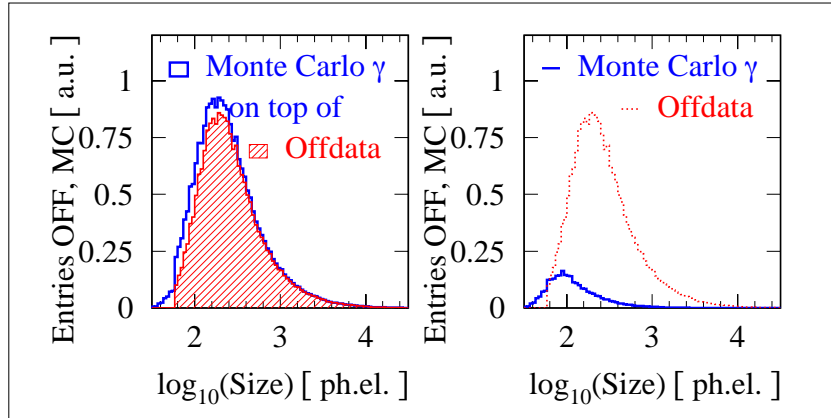


Figure 15.2: Distribution of the *Size* parameter in logarithmic scale for off-data, i.e. hadrons, in the shaded histogram, with the corresponding distribution for Monte Carlo generated  $\gamma$ -images superimposed as a blank histogram (left-hand plot). On the right-hand side the same off-data is shown, here with the distribution for the Monte Carlo  $\gamma$ s superimposed as the red histogram with highly exaggerated statistics.

Source: CT1 offdata and Monte Carlo simulations after noise filter, zenith angle between  $10^\circ$  and  $30^\circ$ .

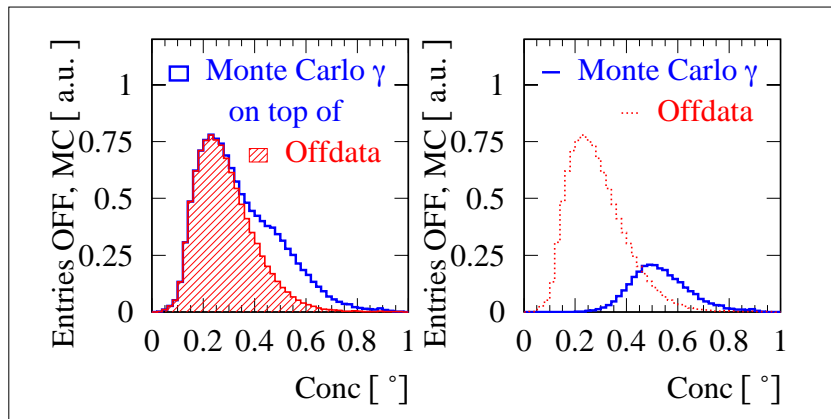


Figure 15.3: Distribution of the *Conc* parameter for off-data, i.e. hadrons, in the shaded histogram on the left, with the corresponding distribution for Monte Carlo generated  $\gamma$ -images superimposed in a blank histogram.

On the right-hand side the same off-data is shown, here with the distribution for the Monte Carlo  $\gamma$ s superimposed as the red histogram with highly exaggerated statistics.

Source: CT1 offdata and Monte Carlo simulations after noise filter, zenith angle between  $10^\circ$  and  $30^\circ$ .

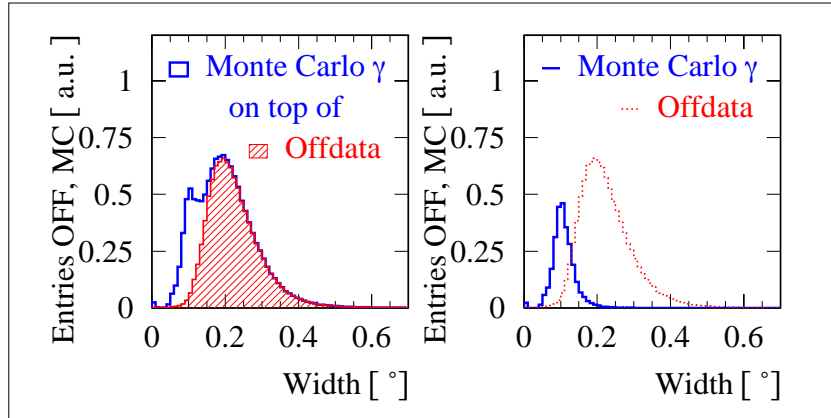


Figure 15.4: Distribution of the *Width* parameter for off-data, i.e. hadrons, in the shaded histogram on the left, with the corresponding distribution for Monte Carlo generated  $\gamma$ -images superimposed as the blank histogram.

On the right-hand side the same off-data is shown, here with the distribution for the Monte Carlo  $\gamma$ s superimposed as the red histogram with highly exaggerated statistics.

Source: CT1 offdata and Monte Carlo simulations after noise filter, zenith angle between  $10^\circ$  and  $30^\circ$ .

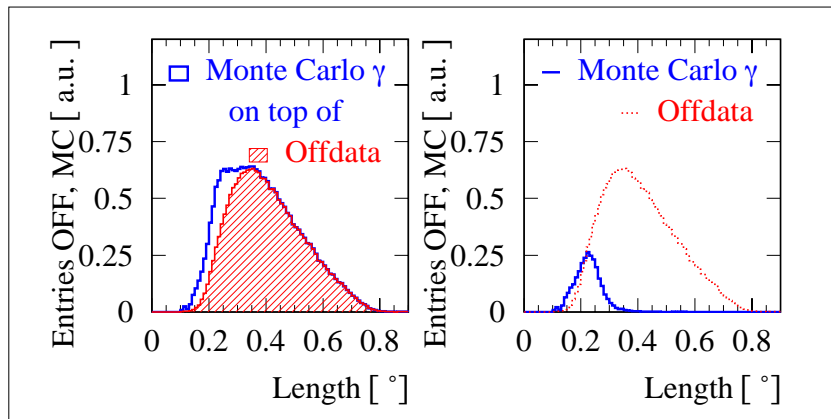


Figure 15.5: Distribution of the *Length* parameter for off-data, i.e. hadrons, in the shaded histogram on the left, with the corresponding distribution for Monte Carlo generated  $\gamma$ -images superimposed as the blank histogram.

On the right-hand side the same off-data is shown, here with the distribution for the Monte Carlo  $\gamma$ s superimposed as the red histogram with highly exaggerated statistics.

Source: CT1 offdata and Monte Carlo simulations after noise filter, zenith angle between  $10^\circ$  and  $30^\circ$ .

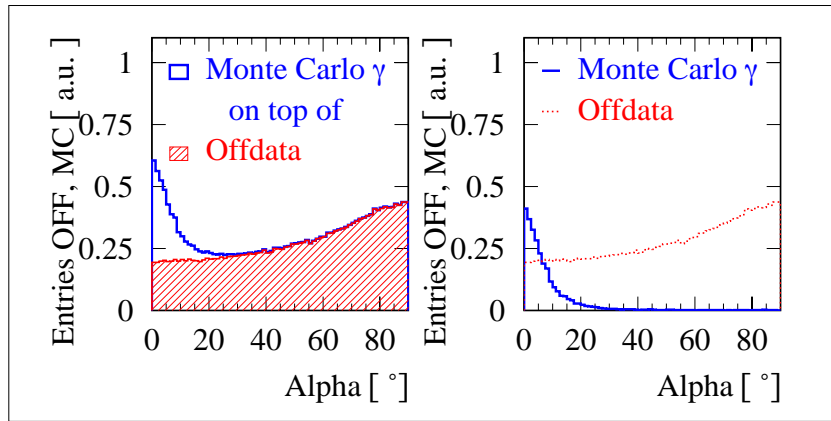


Figure 15.6: Distribution of the  $Alpha$  parameter for off-data, i.e. hadrons, (shaded histogram), with the corresponding distribution for Monte Carlo generated  $\gamma$ -images superimposed as the blank histogram.

On the right-hand side the same off-data is shown, here with the distribution for the Monte Carlo  $\gamma$ s superimposed as the red histogram with highly exaggerated statistics.

Source: CT1 offdata and Monte Carlo simulations after noise filter, zenith angle between  $10^\circ$  and  $30^\circ$ .

## 16 Appendix: Monte Carlo simulation of CT1 hardware and trigger

The development of extensive air showers induced by high energy particles and  $\gamma$ -rays impinging on the top layer of the atmosphere has been understood very early (see e.g. (Simpson et al., 1953)). Figure 16.1 shows the principal components of a shower of secondary and tertiary particles, initiated by the impact of a high energy hadronic particle or photon on the top layer of the atmosphere. The interpretation of such complex processes and the degree to which they can be exploited for purposes of experimental physics depend heavily on the availability of suitable Monte Carlo simulations, i.e. both on the software and on sufficient computing power.

A very successful effort to develop software capable of simulating the shower development for a broad variety of primary particles was undertaken by the KASCADE collaboration. The CORSIKA software package (obtainable from (Heck and Knapp, 2001)) was used to simulate the Monte Carlo events for the experiment described in this thesis<sup>54</sup>.

### 16.1 Simulation of the shower development in the atmosphere

Four sets of input parameters are required for the simulation of extended air showers in the atmosphere:

1. Primary particle type, initial energy and flight direction.
2. Atmospheric properties, i.e. density, refractive index and spectral transmission, and a

<sup>54</sup>The actual simulation was carried out by D. Sobczyńska. Further details of the simulation can be found in (Sobczynska and Lorenz, 2002).



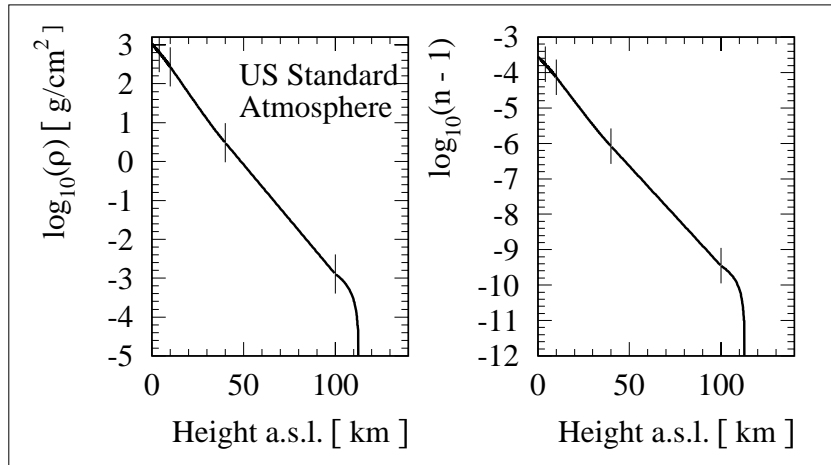


Figure 16.2: Atmospheric slant depth  $\rho$  (left-hand side) as a function of the height above sea level as it is parametrised in the 'Standard U.S. Atmosphere'. The refractive index  $n$  is calculated therefrom (right-hand side), using Equation (16.3). The short vertical bars indicate the limits between several parametrization subranges (0 to 4, 4 to 10, 10 to 40, 40 to 100, 100 + km).

C.f. (Heck et al., 1998)

model for MIE and RAYLEIGH scattering losses as a function of the height above sea level.

3. Cross sections and decay parameters for all possible particles.
4. The local strength and direction of the Earth's magnetic field.

This simulation uses the 'U.S. standard atmosphere' (Heck et al., 1998) for lack of a detailed model of the atmosphere of the Canary Islands or other comparable islands. A graphical representation of the density profile and the refractive index of this model atmosphere is shown in Figure 16.2. Above a height of about 100 to 120 km the density is almost zero.

The high energy interactions leading to the development of showers of secondary particles are simulated according to the cross section parametrisations from CORSIKA.

CORSIKA version 5.62 was used for zenith angles below  $40^\circ$ , version 5.945 for a zenith angle value of  $45^\circ$ , and version 6.003 for even larger zenith angles (see (Heck and Knapp, 2001) and links therein).

Electromagnetic interactions were simulated with the EGS4 generator. Hadronic interactions were simulated using the GHEISHA generator (*op. cit.*) for laboratory momenta below 80 GeV and the VENUS generator (*op. cit.*) for higher momenta.

Whereas a large number of muons are produced in proton showers, they are practically absent in  $\gamma$ -showers. Figure 16.3 shows a plot of the average secondary particle abundance as a function of the atmospheric depth (top-down on the  $y$ -axis, according to a side-view of the shower) is drawn for samples of several hundreds of 1 TeV  $\gamma$ -showers and for 1 and 3 TeV proton shower samples. Proton showers with initial energies 2.5 to 3 times higher than those of  $\gamma$ -showers show similar numbers of secondary high energy particles and secondary  $\gamma$ -rays (with

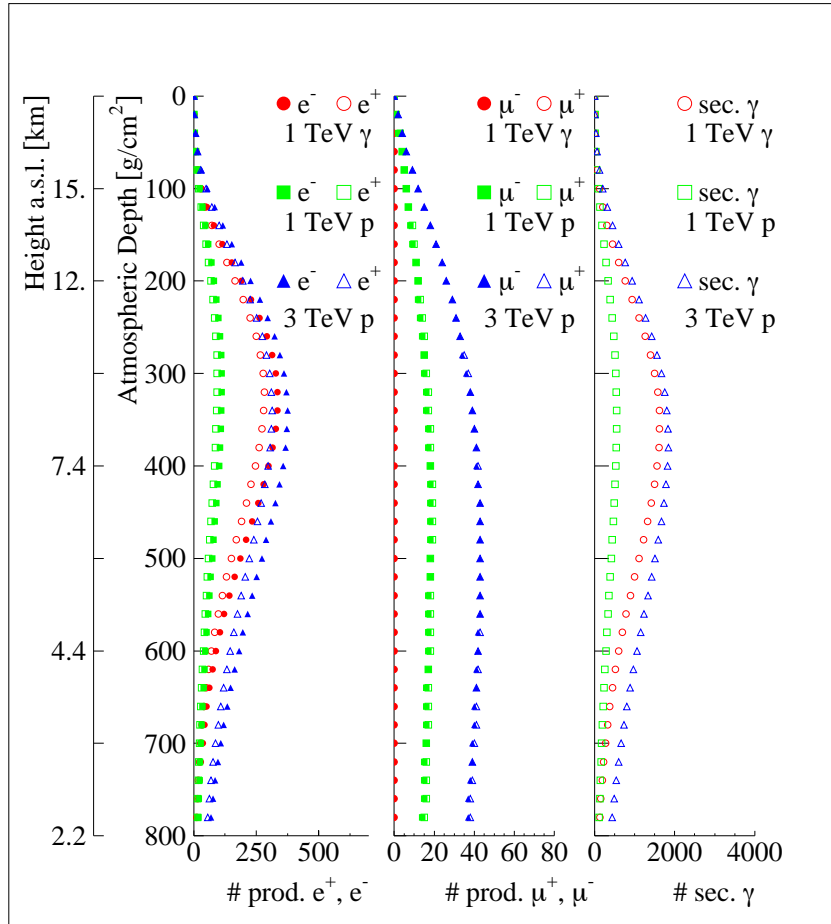


Figure 16.3: Average number of secondary particles ( $e^\pm$ ,  $\mu^\pm$ ) and high energy secondary  $\gamma$ s (HE  $\gamma$ ) produces by 500  $\gamma$ -showers with an energy of 1 TeV and 500 proton showers of energies 1 TeV and 3 TeV respectively, plotted as a function of the atmospheric depth. The figures resemble a side-view of the showers. It can be seen that 3 TeV proton showers resemble 1 TeV  $\gamma$ -showers except for the missing muon component in the  $\gamma$ -showers.

Source: Monte Carlo Simulation CT1.

energies above a few MeV). In principle the missing or extremely small muon component in  $\gamma$ -showers may be used to distinguish these from hadronic showers. This requires an independent large area muon detector, which is not available for CT1.

Any charged particle radiates CHERENKOV light if its velocity is higher than the local phase velocity of light. CHERENKOV light is emitted in a cone with a half angle  $\theta_C$  around the path of the particle with

$$\theta_C = \arccos\left(\frac{1}{n(\omega) \cdot \beta}\right) \quad , \quad (16.1)$$

where

$n(\omega)$  is the index of refraction, which is a function of the frequency  $\omega$  of the radiation,

$\beta = v/c$  is the particle's velocity  $v$  expressed in fractions of  $c$ , the vacuum speed of light.

The threshold value of  $\beta_t$  above which CHERENKOV light is emitted is a function of the index of refraction and coincides with the condition for the CHERENKOV angle to be real, i.e.

$$\beta_t > \frac{1}{n(\omega)} \quad . \quad (16.2)$$

The radiated energy per unit path length was calculated for a dense medium by FRANK and TAMM, who received the NOBEL prize for the explanation of this radiation. In honour of CHERENKOV, who had published this discovery in 1934 and who shared the NOBEL prize with FRANK and TAMM, this radiation is called CHERENKOV light.

The refractive index  $n$  of the atmosphere as a function of the atmospheric depth is approximated in CORSIKA by

$$n = 1 + 0.000283 \frac{\rho(h)}{\rho(0)} \quad , \quad (16.3)$$

where the wavelength dependence of  $n(\omega)$  is neglected and

$\rho(h)$  is the density of air calculated from the parametrisation shown in Figure 16.2 for a

height  $h$  above sea level.

$\rho(0)$  is the nominal slant depth at sea level, i.e.  $1036.14 \text{ g/cm}^2$  according to the parametrisation of the U.S. standard atmosphere, as illustrated in Figure 16.2.

The number of CHERENKOV photons emitted per path length interval  $dN_C/ds$  used in CORSIKA is (Heck et al., 1998; Particle Data Group, 2000)<sup>55</sup>

$$\begin{aligned} \frac{dN_C(\lambda_1, \lambda_2)}{ds} &= 2\pi\alpha \cdot \int_{\lambda_1}^{\lambda_2} \frac{\sin^2(\theta_C)}{\lambda^2} d\lambda \\ &= 2\pi\alpha \cdot \int_{\lambda_1}^{\lambda_2} \frac{1}{\lambda^2} \cdot \frac{1}{\beta^2 \cdot n^2(\lambda)} d\lambda \quad , \end{aligned} \quad (16.4)$$

---

<sup>55</sup>The number of CHERENKOV photons emitted is derived from the radiated energy as given originally by FRANK and TAMM.

where

$\alpha = e^2/(4\pi\epsilon_0\hbar c)$  is the fine structure constant,

$\theta_C = \arccos(1/(\beta n))$  is the angle under which the CHERENKOV light is emitted, measured with respect to the direction of flight of the charged particle in question and

$\lambda_1 \leq \lambda \leq \lambda_2$  is the wavelength range of the CHERENKOV light.

The wavelength of the simulated CHERENKOV photons was limited to the range  $300 \text{ nm} < \lambda < 600 \text{ nm}$ , corresponding to the sensitivity range of the photo-multipliers used.

## 16.2 Tracking Cherenkov light through the atmosphere to the telescope and the photomultiplier windows

In the previous simulation steps the CHERENKOV photons were simulated and their production heights, production time, emission directions and wavelengths were stored. In the next simulation step these photons are tracked on their way through the atmosphere.

MIE and RAYLEIGH scattering processes reduce the initial number of CHERENKOV photons, so that only a fraction of these arrives at the telescope's main reflector. Following the attenuation formulae in (Sokolsky, 1989), transmission probabilities<sup>56</sup>  $T_{Rayl}$  and  $T_{Mie}$  are calculated for each of the photons traveling between atmospheric heights  $X_1$  and  $X_2$  and heights  $h_1$  and  $h_2$ , respectively.  $T_{Rayl}$  refers to RAYLEIGH scattering,  $T_{Mie}$  refers to MIE scattering.

$$T_{Rayl} = \exp\left(\frac{-(X_1 - X_2)}{X_R} \cdot \left(\frac{400 \text{ nm}}{\lambda}\right)^4\right) \quad (16.5)$$

and

$$T_{Mie} = \exp\left(\frac{h_M}{l_M \cdot \cos(\theta)} \cdot \left(\exp\left(-\frac{h_1}{h_M}\right) - \exp\left(-\frac{h_2}{h_M}\right)\right)\right) \quad , \quad (16.6)$$

where

$X_R = 2970 \text{ g/cm}^2$  is the mean free path through the air for a photon of 400 nm wavelength,

$\lambda$  is the wavelength of the CHERENKOV photon,

$l_M = 4.8 \text{ km}$  is the mean free path for a photon of 400 nm wavelength for standard temperature (20° C) and pressure (1013 hPa),

$\theta$  the scattering angle by which the path is altered,

$h_M = 1.2 \text{ km}$  the reference aerosol scale height.

---

<sup>56</sup>In the case of MIE scattering the result is an approximation as its wavelength dependence is replaced using an approximate average wavelength of 400 nm.

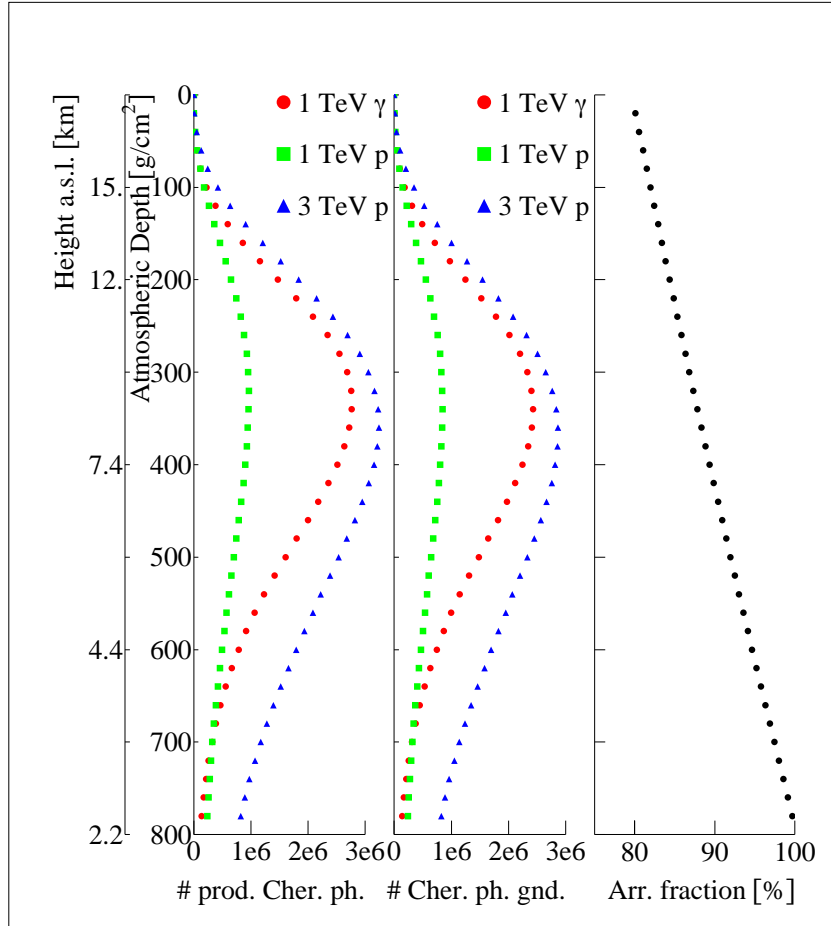


Figure 16.4: Average number of produced CHERENKOV photons from a set of 500  $\gamma$ -showers with an energy of 1 TeV and 500 proton showers of energies 1 TeV and 3 TeV respectively, plotted as a function of the atmospheric depth. The figures resemble a sideview of the showers. The plots show the number of CHERENKOV photons produced per bin in atmospheric depth (left-hand side) and the number of CHERENKOV photons that reached the ground from this particular atmospheric depth (center). It is evident that a proton shower with an energy of 2 to 3 TeV would produce roughly the same amount of CHERENKOV light as a 1 TeV  $\gamma$ -shower. Around 85% of the light produced at the shower maximum will reach the ground, whereas basically all CHERENKOV photons generated in the shower tail reach the telescope, as is shown in the right-hand side plot.

Source: Monte Carlo simulation CT1.

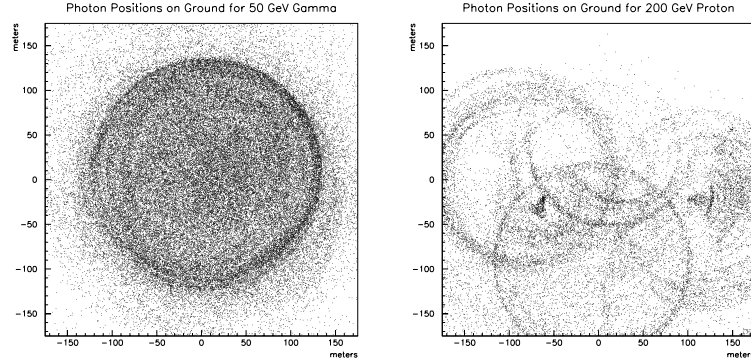


Figure 16.5: Impact of CHERENKOV photons on the ground, from a 50 GeV  $\gamma$ -induced air shower (left-hand side) and from a 200 GeV proton induced air shower (right-hand side). The figure on the right illustrates how the inhomogeneous shower development of hadronic showers proceeds, as sporadic subshowers shine their CHERENKOV rings onto the ground. Source: (Hillas, 1985)

The result of the simulation of the attenuation through MIE and RAYLEIGH scattering is illustrated in Figure 16.4. The figures resemble a sideview of the showers. The plots show the number of CHERENKOV photons (left-hand side) and the number of CHERENKOV photons that reached the ground (central plot) for the same set of showers as in Figure 16.3. On average the first interaction takes place at atmospheric depths of 3 to 10 g/cm<sup>2</sup>, while the maximum of the CHERENKOV light production is at around 300 to 400 g/cm<sup>2</sup>, corresponding to a height of 8 to 10 km above sea level. This is also the distance the main reflector is focussed to (c.f. Chapter 4).

It is evident that a proton shower with an energy of 2 to 3 TeV produces roughly the same amount of light as a 1 TeV  $\gamma$ -shower. For the purpose of this illustration an average wavelength of 415.89 nm was used for the calculation of the reduction, which is the average wavelength of a  $1/\lambda^2$  spectrum in the wavelength interval from 300 to 600 nm. The simulation for the CT1 analysis on the other hand, used the actual wavelengths.

The image in the camera plane is calculated using the flight direction of the CHERENKOV photons that reached the ground. The main reflector is made up of 33 single units. The reflectivity was simulated to vary around 80% according to a GAUSSIAN with a  $\sigma$  of 3%. It was randomised once for the whole CT1 mirror and then left constant for the entire simulation.

To simulate the imperfections of the mirror curvature, the values of the curvature that were used to calculate the impact points of CHERENKOV photons in the camera plane were varied around their ideal value from mirror to mirror by 10% for each subset of 1000 events. Further the adjustment was simulated to match the measured point spread function of the CT1 main reflector. This was achieved by a randomised misplacement of the focal distance by up to 5 mm in two directions. This randomisation was repeated for each subset of 1000 events. In addition 5% of the photons were assumed to be reflected with a further misplacement of the focal distance randomised in a range of up to 30 mm, separately for each of the two dimensions.

Depending on their impact point in the camera plane, most CHERENKOV photons need to

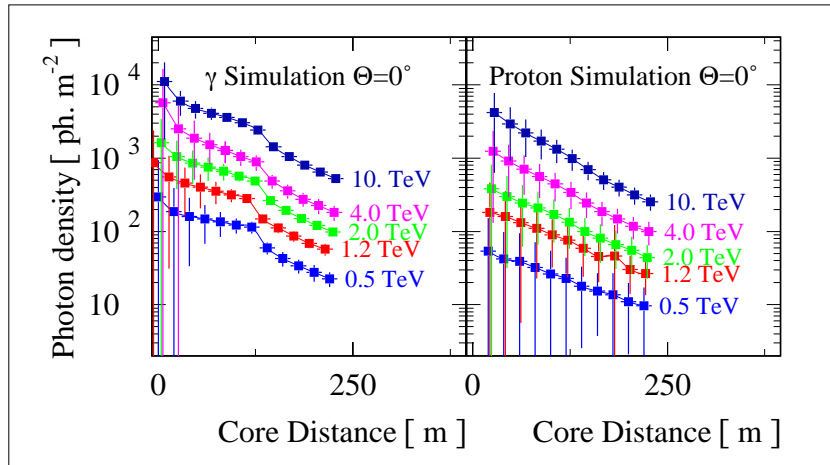


Figure 16.6: Averaged CHERENKOV photon density at 2200 m height above sea level for several hundred primary  $\gamma$ s and primary protons of different initial energies. The errorbars represent the fluctuations from shower to shower. The points were connected with a simple spline interpolation curve. In conjunction with Figure 16.5 it can be seen that the light pool on the ground is different for  $\gamma$ s and hadrons: while it is more or less flat for the  $\gamma$ s apart from the so-called 'hump' located at around 125 m, the proton showers fluctuate much more and produce a different pattern on the ground, which gives, on average, this smoothly falling set of curves. Source: CT1 Monte Carlo simulation

be guided to photo-multiplier windows by WINSTON cones. Even in the most dense package of the photomultipliers in the camera plane, the fraction of active area is slightly less than 70%. This number has to be further reduced by the spacing used by the mu-metal shielding and inefficiency of the cathodes at the tube wall ( $\emptyset_{eff} \approx 16$  mm for the photomultipliers with a diameter of  $\emptyset = 19$  mm). In order to achieve a collection efficiency of close to 100%, so-called WINSTON cone light collectors are used. A grid of WINSTON cones made from aluminised mylar foil is mounted in front of the photo-multiplier matrix of the CT1 camera. A photograph of this setup is shown in Figure 4.4(a) on page 29. In the simulation it is assumed that 75% of the CHERENKOV photons, that otherwise would be lost in the space between the round photo-multiplier tubes, are collected with the help of this grid.

The arrival times of individual CHERENKOV photons have been tracked very accurately. The simulation software accounts for the fact that only a fraction of the photons that reach the photocathodes finally release photoelectrons. Each photoelectron that is released from the photocathode creates an output pulse of variable height and shape.

### 16.3 Simulation of the electrical pulse production of photomultipliers

The conversion efficiency from photons to photoelectrons at the photocathode is presently the main limiting factor in the operation of CHERENKOV telescopes. The nominal quantum efficiency of the photo-multiplier tubes EMI-9083A used for HEGRA CT1 can be seen in Figure 16.7. For the simulation the quantum efficiency was varied around the tabulated value by 10% for each CHERENKOV photon in order to account for manufacturing spreads.

The quantum efficiency (QE) decreases from the center of a photomultiplier towards the

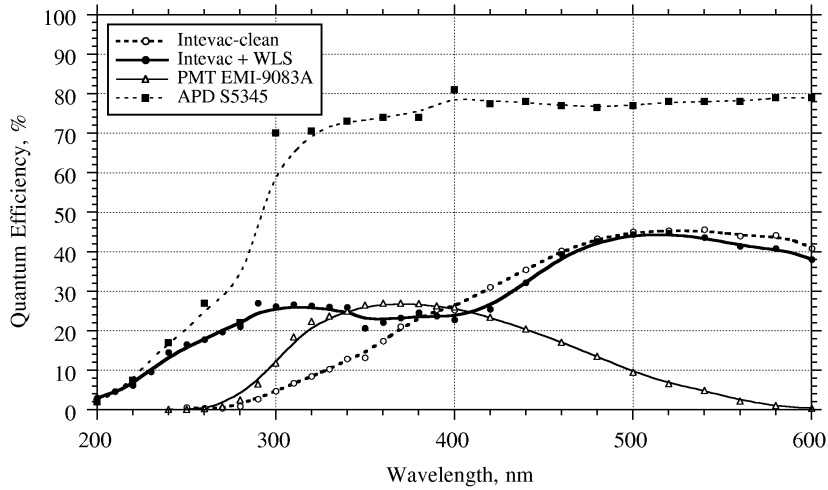


Figure 16.7: Quantum efficiencies for several types of light sensing devices. The photomultiplier tubes used on CT1 are EMI-9083A. The simulation used the parametrisation given here and once per 1000 events varied the efficiency with a GAUSSIAN  $\sigma$  of 10% around the tabulated value for each photo-multiplier tube.

Source: (Barrio et al., 1998)

border. A parametrisation of the dependence of the QE on the radial impact point is shown in Figure 16.8. It is simulated to follow a radial dependence where the maximum value of  $\phi = \arccos(\sqrt{0.8}) \cdot (r/8 \text{ mm})$  corresponds to a value of  $\cos^2(\phi) = 0.8$  at a radius  $r$  of 8 mm, which is the maximum possible impact radius given by the WINSTON cone. Integrating this function over the active area of the photomultiplier entrance windows yields the result that overall 89.9% of the nominal QE is attained for each photo-multiplier tube.

To account for this geometrical effect the nominal QE of each photo-multiplier was reduced by this factor.

photomultiplier signals vary from pulse to pulse. photomultiplier pulses from single photoelectrons have been measured and the averaged pulse shape as a function of time has been parametrised (Mirzoyan et al., 1995). The average pulse shape is shown in Figure 16.9. The pulse height is a function of the high voltage that is applied to the tubes and varies due to the stochastic nature of the multiplication processes in the tubes. The pulse height variation has also been measured and is shown in Figure 16.10.

In the simulation the pulse shape and the pulse height are randomised separately for each photoelectron according to the pulse shape parametrisation (Figure 16.9) and the pulse height distribution (Figure 16.10).

Up to this point of the simulation, the CHERENKOV photons from showers have been simulated, tracked through the atmosphere and reflected into the photo-multipliers. The photo-multipliers convert only a certain fraction of photons to photoelectrons and finally to electric pulses.

A fraction of the CHERENKOV photons that hit the cathode area of a tube are converted into electrical pulses which are then superimposed according to the photon arrival times. This is assumed to be the best possible representation of the real processes in photo-multiplier tubes

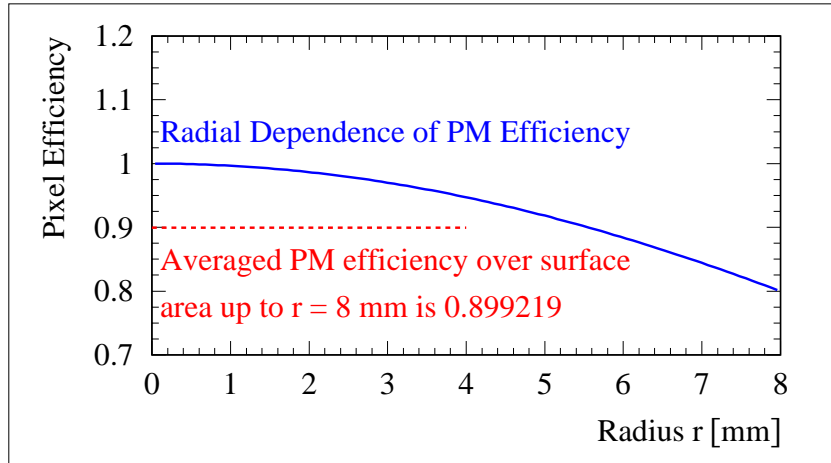


Figure 16.8: In the simulation it was assumed that the radial efficiency of a typical photo-multiplier tube decreases from its central value by 20% at the limiting opening radius  $r$  of  $r = 8$  mm, following a  $\cos^2(\arccos(\sqrt{0.8}) \cdot (r/8 \text{ mm}))$  dependence. To simplify the calculations the average value of 0.899 was used.

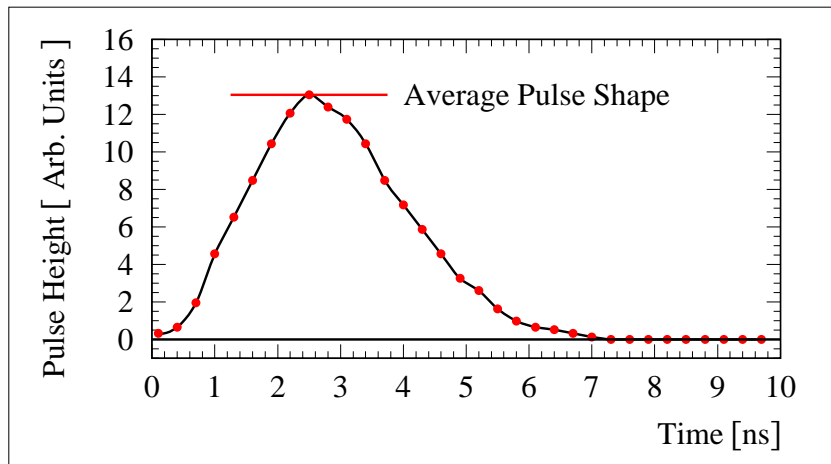


Figure 16.9: Observed pulse shape in response to a single photoelectron as observed after a preamplifier and 10 m of RG 58U coaxial cable. The pulse height is given in arbitrary units. C.f. (Mirzoyan et al., 1995)

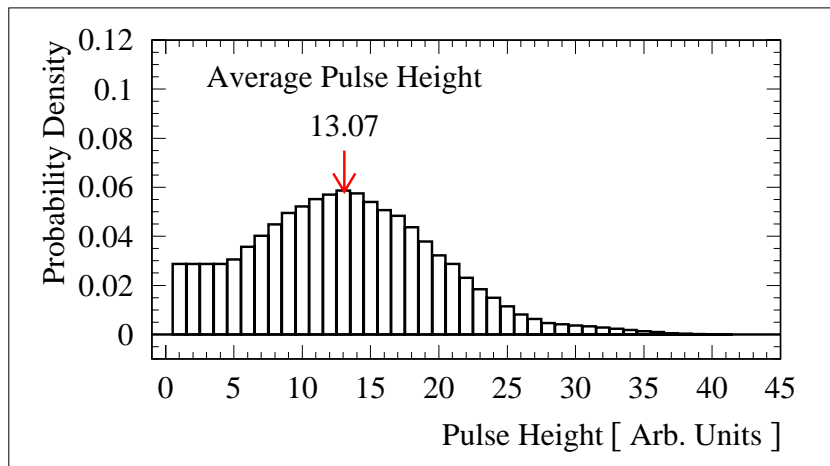


Figure 16.10: Pulse height spectrum of individual photoelectrons. C.f.(Mirzoyan et al., 1995)

when the CHERENKOV light flash from a shower is recorded.

#### 16.4 Simulation of the trigger decision

The new, time resolved pulse superposition gives a different result compared to the previous trigger simulation which used simple photoelectron counting. In preceding Monte Carlo simulations for CT1 (see e.g. (Konopelko et al., 1996)) the simulation of the trigger decision was kept quite simple: when the sum of standardised photoelectrons counted in a certain pixel exceeded 15 photoelectrons, this pixel was generating a trigger flag. Whenever two next neighbours out of the 127 available pixels showed this flag within a coincidence time of 8 ns, the event was considered to trigger telescope readout.

As a next step the number of photoelectrons from a shower was stored for each pixel, making up the Monte Carlo shower image.

**In the new simulation the time spread and the pulse-amplitude spread are taken into account.**

**The improved trigger simulation proceeds along three steps:**

1. Randomised pulse heights are simulated and superimposed according to the CHERENKOV photons' arrival times, separately for each photoelectron in each photo-multiplier tube.
2. The trigger decision is based on the resulting signal height maximum: if the threshold value is exceeded, the trigger flag is set for the respective pixel. The discriminator threshold value used here corresponds to the superposition of 13 times the average pulse height (whose value is indicated in Figure 16.10).
3. The event is stored if two neighbouring pixels out of the available 127 pixels show the trigger flag within a time window of 6 ns (8 ns – 2 ns minimum required overlap time).

**Differences between the two trigger simulation methods become evident for events with a significant time dispersion and fewer than around 50 photoelectrons, e.g. for low energy events close to the threshold energy and to hadronic events because of their larger time spread.**

$\gamma$ -showers with an impact parameter below around 100 m have typical time spreads of 1 to 3 ns (FWHM) with some late photons. Larger time dispersions occur for events with high impact parameters above around 130 m as well as in hadronic showers. With the trigger simulation that uses simple photoelectron counting the number of triggers is overestimated, leading to an overestimation of the effective areas which in turn leads to an underestimation of the flux.

## 16.5 Simulation of the influence of NSB light and of the *Zonk* correction

The NSB conditions and their influence on Monte Carlo images should be modeled as accurately as possible. In this analysis the simulation of the NSB influence on images is made separately for each source and observation period. In a second step the *Zonk* correction is modeled, again separately for each source. Here (Section 16.5) the simulation of these two steps is described.

### 16.5.1 Modeling the NSB level for a given observation

To simulate the NSB conditions around an object, the following procedure was used:

- The noise level was read from real data, individually for each pixel in the camera. For the simulation the median of the noise level was used, and, when a certain pixel had hardware problems and no reasonable noise level was available, a neighbour's value was used instead.

For the trigger decision the trigger flag of a dataset simulated without any noise was used.

Using this procedure one is able to model bright stars — like Tauri- $\zeta$  close to Crab — and their influence on the analysis of CT1 data. In an interpretation of the result, one must take into consideration that the following assumptions have been made:

- The pedestal RMS<sup>57</sup> in an individual pixel is mainly a measure of the NSB noise in this pixel.
- When the NSB light is of POISSONIAN nature, the square of the pedestal RMS represents an estimator for the parameter  $\lambda$  of the POISSONIAN probability density function
$$p(X = k) = \frac{\lambda^k \cdot e^{-\lambda}}{k!} \quad ; \quad k = 0, 1, 2, \dots \quad ; \quad 0 < \lambda < \infty \quad ,$$
giving the probability that a random variable  $X$  takes the (integer) value  $k$ , where  $\lambda$  is the mean value of the underlying probability distribution, i.e. in our case the mean number of photoelectrons from the NSB falling inside the 30 ns ADC gate.
- In order to estimate the most likely guess value for the POISSON mean  $\lambda$ , the square of the median of the distribution of pedestal RMS values is used.

---

<sup>57</sup>See Section 5.4 for more details on the pedestal RMS determination.

The NSB noise is simulated by adding a random number of photoelectrons (following a POISSONIAN distribution with mean  $\lambda$ ) to the CHERENKOV signal in each pixel before finally subtracting the value  $\lambda$ .

- The trigger simulation was made assuming zero noise in the pixels. The 'smallest' events, critical as to whether or not they will trigger the telescope with their low number of photoelectrons (small event *Size*), are those with small energies and those which arrive with high impact parameters. In order to exclude this critical fraction of the images from the Monte Carlo data sample, a lower cut of 60 photoelectrons is applied on the event *Size* and in addition four *core pixels*<sup>58</sup> are required. For events with larger values of *Size* the trigger simulation is not critical.

### 16.5.2 Deriving the *Zonk* correction to be used for Monte Carlo events from real data

The Monte Carlo  $\gamma$ -were simulated at fixed zenith angles. The aim is, therefore, to determine the best, most representative correction shift applied to data recorded in the same zenith angle bin. The same dataset that was used to extract the pedestal RMS values is used for the derivation of the *Zonk* shift parameters.

The following scheme was implemented to determine the necessary shifts:

1. The correction shifts that were applied to real data were entered into histograms sorted by the zenith angle bins of the Monte Carlo simulation.
2. To avoid undue influence of the outliers in these histograms, the medians of these distributions were used as estimators of the correction shifts. These shifts were then applied to the Monte Carlo  $\gamma$ -events of the respective zenith angle bins.

## 16.6 Number of simulated Monte Carlo events

This section contains a selection of plots showing the number of events simulated and the fraction of triggering events for both the  $\gamma$ - and the proton simulation. The simulation was carried out in such a way that the simulated impact parameter range exceeded the limit below which no single event is classed as a 'trigger event'. This is necessary in order to make sure that the effective areas are not underestimated<sup>59</sup>.

While the  $\gamma$ -events were simulated and used only once, the proton simulation events were 'recycled'. More precisely, the CHERENKOV photons from the proton simulation were reused four times, varying the 'source' point of the proton (see below) with respect to the camera field of view so as to cover an area with a radius of 5 degrees around the center of the camera.

---

<sup>58</sup>See Section 5.7 for the definition of *core pixels* and their role in the filter cut.

<sup>59</sup>C.f. Section 7.5 for the definition and the extraction procedure of effective areas.

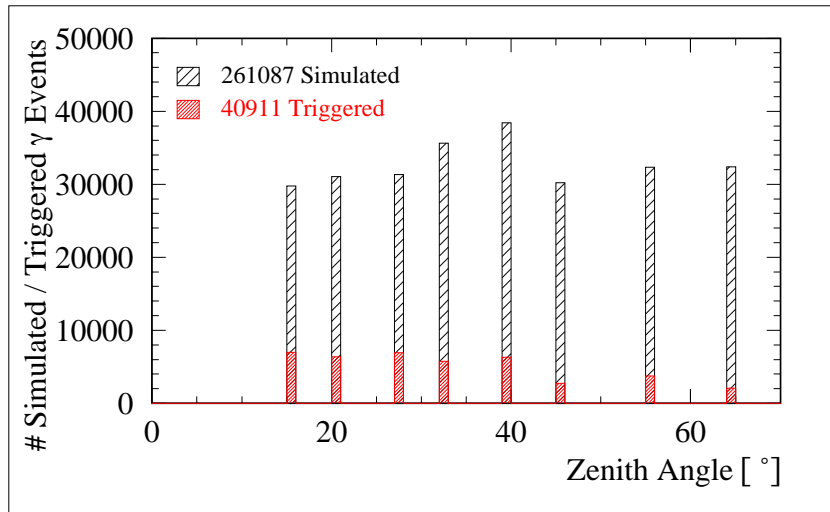


Figure 16.11: The statistics of the simulated  $\gamma$ -events for a range of zenith angles. The  $\gamma$ -simulation was carried out at a set of discrete zenith angles.  
Source: Monte Carlo simulation for CT1

### 16.6.1 Simulation statistics of Monte Carlo $\gamma$ -events

The Monte Carlo simulation was carried out at fixed zenith angles of 15, 22, 32, 39, 45, and 55 degrees. The bar chart in Figure 16.11 shows the number of  $\gamma$ -events simulated as well as the fraction passing the trigger criterion as a function of the zenith angle.

Figure 16.12 shows the simulated impact parameter range for a subset of the simulated zenith angles. For zenith angles of 15°, 27°, 39° and 55° the simulated range and the fraction of triggered events are indicated. It is apparent that for larger zenith angles the triggering events stem from a larger area around the telescope.

Finally Figure 16.13 shows the energy distribution for the simulation, again for the same set of zenith angles as displayed in Figure 16.12. Below a certain energy the light yield is so small that the events do not even trigger readout<sup>60</sup>. With increasing energy the triggering fraction grows rapidly.

### 16.6.2 Simulation statistics of Monte Carlo proton events

The proton simulation was carried out in two steps:

1. First, the proton events were simulated as if they stemmed from a single, fixed position, which can be thought of as a proton 'source' point. This proton 'source' point is located at a zenith angle of 15° and a fixed value of the azimuth angle. The CHERENKOV photons were tracked through the atmosphere and their parameters like wavelength, direction of flight, impact point etc. were stored.
2. In a second step, the main reflector and the camera of CT1 were simulated to point to a set of positions (called 'focus points') around the simulated, fixed proton 'source' point.

<sup>60</sup>C.f. Section 4.4 for a description of the trigger electronics.

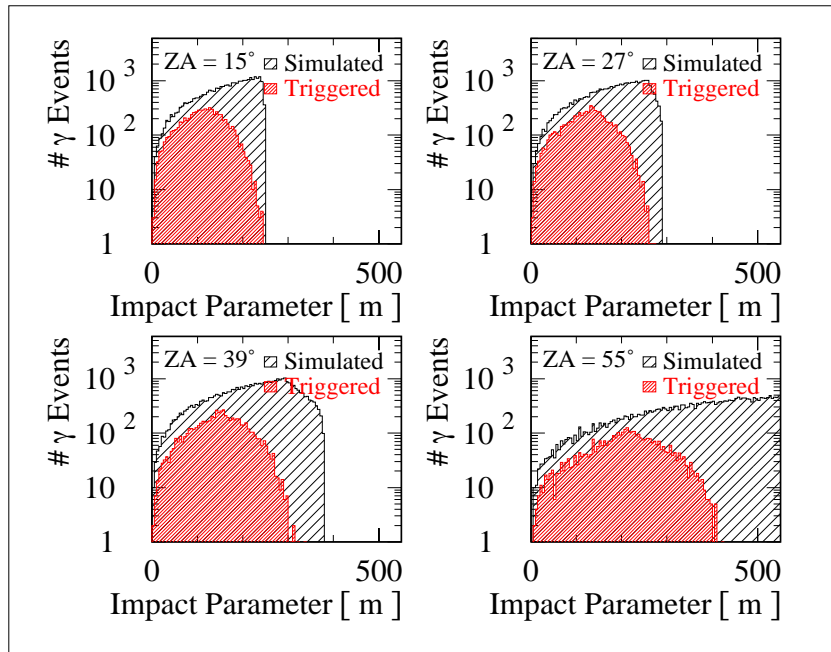


Figure 16.12: For each of the simulated zenith angles — here only a selection is shown — the impact parameter was simulated as shown here. It is clearly visible that the triggering fraction is located well within the simulated range of impact parameters.  
Source: Monte Carlo simulation for CT1

This yielded a result as if the single proton events had been simulated to originate from the 'focus points' that were mirrored in the camera with respect to the (fixed) 'source' point. The simulation of the main reflector, the trigger decision and all following processes were then carried out as usual.

The simulation of the processes in step 2 was repeated four times, each time re-randomising the source position.

The proton simulation followed a flat distribution in the cosine of the zenith angle with the distance of the 'focus points' to the 'source' point limited to  $5^\circ$ . The results of the four simulations were combined and the result is shown in Figure 16.14. This shows the distribution of the effective zenith angles to the left and the distribution of the 'focus points' to the right. The plot on the right-hand side uses elements of the box plot: the size of the boxes represents the relative number of entries in the rectangular bin. The boxes have maximum size for the highest populated bins, and are smaller or invisible for less populated or empty bins. The distribution of the arriving protons is flat, as is indicated by the minute fluctuations of the size of the boxes within the egg-shaped, simulated area<sup>61</sup>. Some small points, one for each triggering event, are superimposed on the plot, a few of them originating from outside the actual field of view of the CT1 camera, which is superimposed as the red hexagon. In order to derive reliable distributions from the simulation, it is necessary that the simulated parameter

<sup>61</sup>The projection of a circular area located on the surface of a sphere (a three-dimensional object) onto (two-dimensional) paper distorts the shape of this area in a way similar to the manner in which geographic maps of regions close the Earth's poles appear distorted.

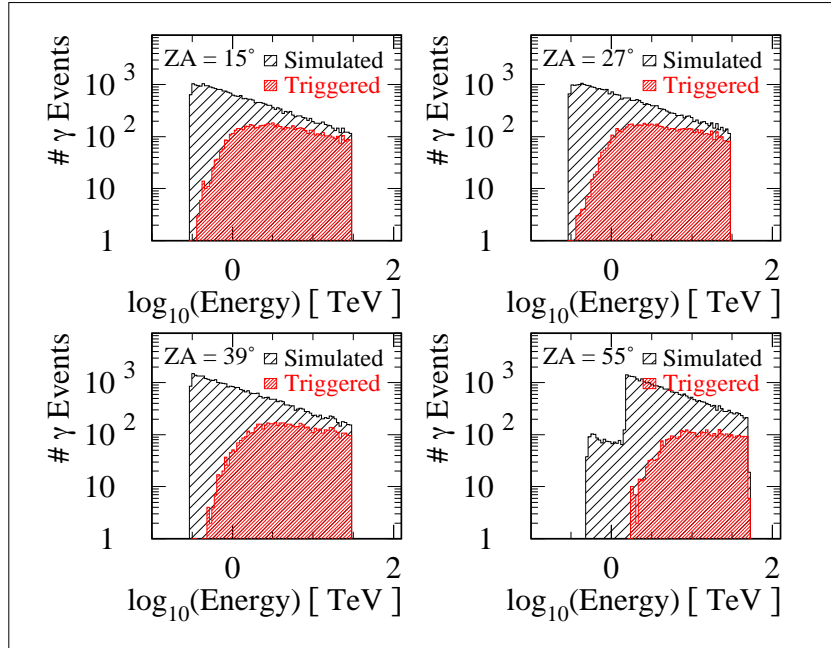


Figure 16.13: For each of the simulated zenith angles the energy was simulated with a differential powerlaw index of  $-2.5$ . In certain instances, like for a zenith angle of  $55^\circ$ , it was found that a simulation of very low energies (i.e. below 1 TeV) did not lead to triggering events. Therefore the energy range was changed in the course of the simulation, resulting in the structure displayed in the last plot. For the highest zenith angle the upper energy limit of the simulation was chosen to be 50 TeV, while for all other zenith angles the limit was 30 TeV except for the zenith angle of  $15^\circ$ , for which events with energies of up to 80 TeV were simulated.

Source: Monte Carlo simulation for CT1

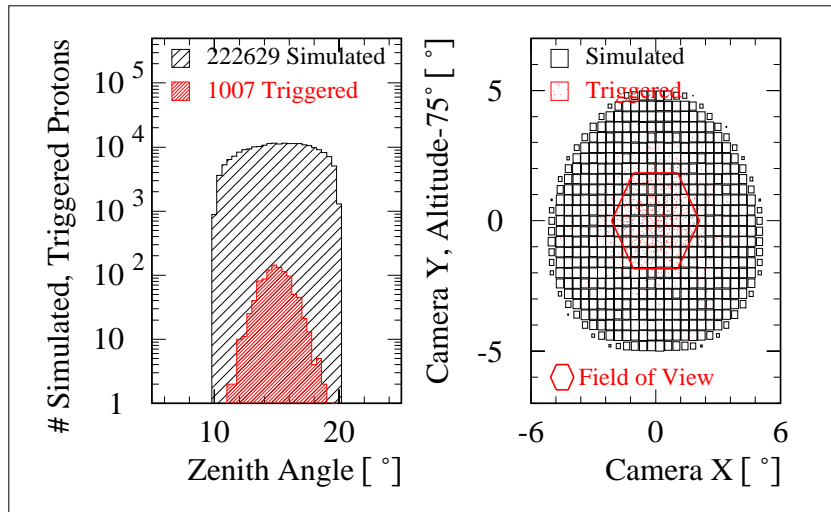


Figure 16.14: For the proton simulation the zenith angle was kept fixed at  $15^\circ$ . The camera was turned artificially such that a circular area with a radius of  $5^\circ$  around the center of the camera was covered. The source points for the simulated and the triggering events are shown in the plot to the right, the axes given as camera  $x$ -coordinate and as camera  $y$ -coordinate, which coincides with the altitude scale except for a fixed offset of  $75^\circ$ . It is worth noting that a significant number of trigger events stem from areas well outside the actual field of view of the CT1 camera.

Source: Monte Carlo simulation for CT1

ranges exceed the actually accessible parameter ranges. From Figure 16.14 it is evident that the number of simulated proton events is very low, too low to extract reliable predictions (c.f. Figures 5.19 through 5.22). Therefore in this analysis hadronic properties are estimated from real data.

## 17 Appendix: Supplemental information for data quality requirements

### 17.1 High voltage adjustments for CT1

Date / MJD	HV1	HV2	Comment
before 30 Apr 1998	855	1056	—
30 Apr 1998 / 50933	907	1120	regular increase
17 Aug 1998 / 51042	921	1137	regular increase
22 Feb 1999 / 51231	939	1160	regular increase
28 Nov 1999 / 51510	944	1164	regular increase
19 Jun 1999 / 51714	982	1211	regular increase
18 Jan 2000 / 51927	977	1204	camera repaired

Table 17.1: Values for the high voltage settings for CT1 for the two power supplies. The table gives the values adjusted, the dates of high voltage changes and a short comment about the reason for the change.

## 17.2 Quality cuts regarding the starlight contribution

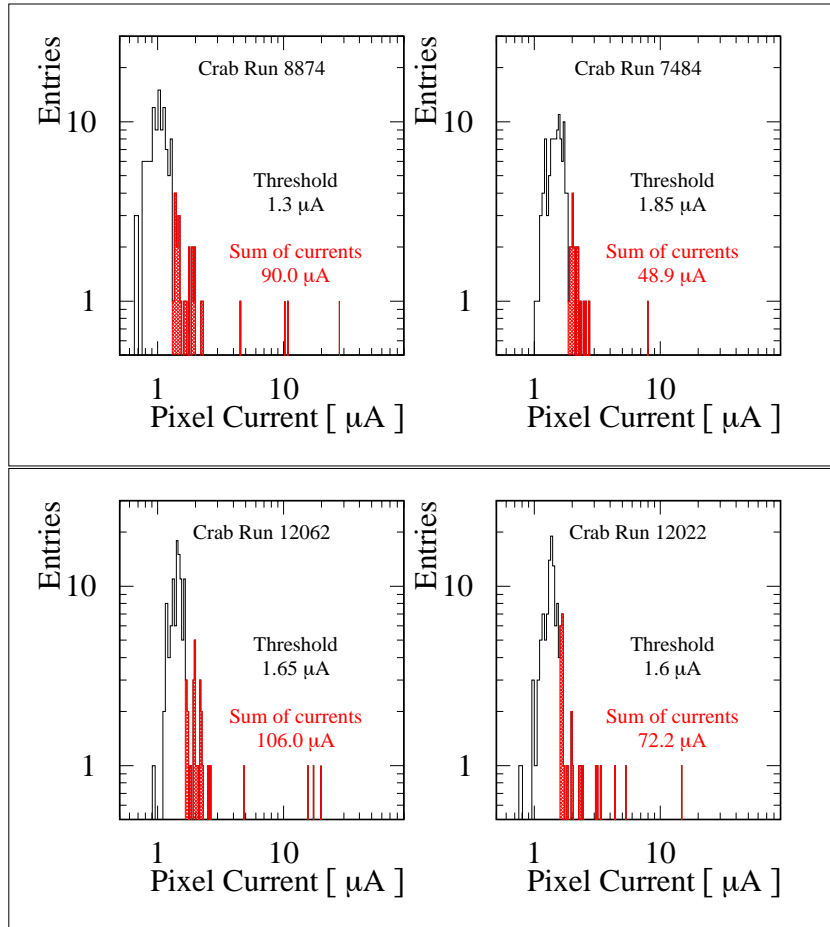


Figure 17.1: Current distributions for all pixels for two data runs on Crab from 1999-2000 (top panel) and Oct/Nov 2000 (bottom panel). The left-hand side shows data runs displaying average current values, whereas the data runs displayed on the right-hand side are characterised by currents which are too low, leading to the exclusion of the respective data runs from the analysis.

Source: Crab observations CT1 1999-2000 and 2000-2001 before the current limit quality cut

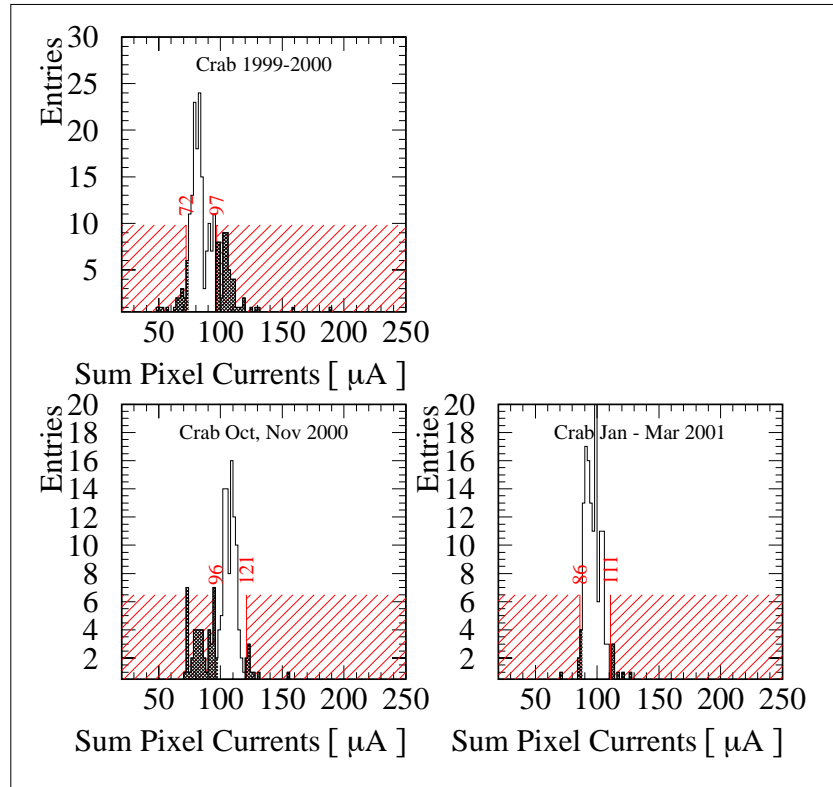


Figure 17.2: Current values from pixels into which star light is reflected for all data runs on Crab from 1999-2000 (top panel) and 2000-2001 (bottom panel). Although the high voltage was increased on November 28 1999, the data set is not split, as the statistics collected before that day is very low and cannot be used to select thresholds like the ones shown here. After the camera was repaired on 18 January 2001 the high voltage was slightly decreased, leading to two subsets of current distributions that are distinctly different. Data runs below the hatched areas were excluded from the analysis.

Source: Crab observations CT1 1999-2000 and 2000-2001 before the current limit quality cut

## References

- Aharonian, F. A., Akhperjanian, A. G. et al. 'The Energy Spectrum of TEV Gamma Rays from the Crab Nebula as Measured by the HEGRA System of Imaging Air Cerenkov Telescopes' *ApJ* Aug. 2000 **539**:317–324
- Barrau, A., Bazer-Bachi, E. et al. 'The CAT imaging telescope for very-high-energy gamma-ray astronomy' *NIMA* 1998 **416**:278–292
- Barrio, J. A. et al. 'The Magic Telescope' Tech. Rep. MPI-PhE/98-5 Max-Planck-Institut für Physik (Werner-Heisenberg-Institut) Föhringer Ring 6, 80805 München Mar. 1998
- Bartel, N., Herring, T. A. et al. 'VLBI limits on the proper motion of the 'core' of the superluminal quasar 3C345' *Nature* Feb. 1986 **319**:733–738
- Bevington, P. R. *Data reduction and error analysis for the physical sciences* McGraw-Hill, Inc. 1969
- Biller, S. D., Akerlof, C. W. et al. 'an upper limit to the infrared background from observations of TeV gamma rays' *ApJ* May 1995 **445**:227–230
- Boella, G., Butler, R. C. et al. 'BeppoSAX, the wide band mission for X-ray astronomy' *A&AS* Apr. 1997 **122**:299–307
- Bond, J. R., Carr, B. J. et al. 'Spectrum and anisotropy of the cosmic infrared background' *ApJ* Jul. 1986 **306**:428–450
- Bradbury, S. M., Deckers, T. et al. 'Detection of  $\gamma$ -rays above 1.5TeV from MKN 501.' *A&A* Apr. 1997 **320**:L5–L8
- Bromage, G. E., Boksenberg, A. et al. 'Results from the NGC 4151 ultraviolet laboratory' in *Third European IUE Conference* 1982 pages 533–536
- Buckley, J. H. 'Observations of blazars with the Whipple Observatory gamma-ray telescope' *Astroparticle Physics* Jun. 1999 **11**:119–129
- Catanese, M., Akerlof, C. W. et al. 'Discovery of Gamma-Ray Emission above 350 GeV from the BL Lacertae Object 1ES 2344+514' *ApJ* Jul. 1998 **501**:616+
- Cawley, M. F., Fegan, D. J. et al. 'A high resolution imaging detector for TeV gamma-ray astronomy' *Experimental Astronomy* 1990 **1**:173–193
- CN/ASD Group *Minuit users guide, Program Library D506* CERN 1994
- Collmar, W., Bennett, K. et al. 'COMPTEL MeV Observations of the TeV Sources Markarian 421 and Markarian 501' in *Proc. 26th ICRC (Salt Lake City), vol 3* 1999 page 374
- Cooke, B. A., Ricketts, M. J. et al. 'The Ariel V /SSI/ catalogue of high galactic latitude /absolute value of B greater than 10 deg/ X-ray sources' *MNRAS* Feb. 1978 **182**:489–515
- Coppi, P. S. and Aharonian, F. A. 'Constraints on the Very High Energy Emissivity of the Universe from the Diffuse GeV Gamma-Ray Background' *ApJ* Sep. 1997 **487**:L9+
- Cortina, J. et al. 'The New Data Acquisition System of the First Telescope in HEGRA' in et al., B. D. (editor), *Gev-TeV Gamma Ray Astrophysics Workshop (Snowbird)* 1999 pages 368–371
- Daum, A., Hermann, G. et al. 'First results on the performance of the HEGRA IACT array' *Astroparticle Physics* Dec. 1997 **8**:1–2
- de Jager, O. C., Stecker, F. W. et al. 'Estimate of the Intergalactic Infrared Radiation Field from

- Gamma-Ray Observations of the Galaxy MARKARIAN:421' *Nature* May 1994 **369**:294–+
- Deckers, T. *Messung von hochenergetischer  $\gamma$ -Strahlung aus der Richtung des Krebsnebels und der aktiven Galaxie Markarian 501 mit einem Cherenkov-Teleskop* Ph.D. thesis Christian-Albrechts-Universität Kiel 1997
- Dwek, E. and Slavin, J. 'On the determination of the cosmic infrared background radiation from the high-energy spectrum of extragalactic gamma-ray sources' *ApJ* Dec. 1994 **436**:696–704
- ESA 'TUE Home Page <http://www.vilspa.esa.es/iue/iue.html>' 2001
- Fan, X., White, R. L. et al. 'The Discovery of a Luminous  $Z=5.80$  Quasar from the Sloan Digital Sky Survey' *AJ* Sep. 2000 **120**:1167–1174
- Funk, B., Magnussen, N. et al. 'An upper limit on the infrared background density from HEGRA data on MKN 501' *Astroparticle Physics* Jun. 1998 **9**:97–103
- Gaidos, J. A., Akerlof, C. W. et al. 'Very Rapid and Energetic Bursts of TeV Photons from the Active Galaxy Markarian 421.' *Nature* 1996 **383**:319+
- George, I. M., Warwick, R. S. et al. 'X-ray and ultraviolet observations of Markarian 421' *MNRAS* Jun. 1988 **232**:793–808
- Gorham, P. W., van Zee, L. et al. 'Markarian 421'S Unusual Satellite Galaxy' *AJ* Apr. 2000 **119**:1677–1686
- Hall, R., Ricketts, M. J. et al. 'Ariel-6 medium energy spectral observations of active galaxies' *Space Science Reviews* 1981 **30**:47–54
- Harwit, M. *Astrophysical Concepts* vol. 1 Springer third edn. 1998
- Hauser, M. G. and Dwek, E. 'The Cosmic Infrared Background: Measurements and Implications' *ARA&A* 2001 **39**:249–307
- Heck, D. and Knapp, J. 'CORSIKA Homepage' 2001
- Heck, D., J., K. et al. 'CORSIKA: A Monte Carlo Code to Simulate Extensive Air Showers' 1998
- Herterich, K. 'absorption of gamma rays in intense X-ray sources' *Nature* Jul. 1974 **250**:311+
- Hillas, A. 'd' in *Proc. 19th ICRC (La Jolla), Vol 3* 1985 page 445
- Hillas, A. M. 'Cerenkov light images of EAS produced by primary gamma' *NASA. Goddard Space Flight Center 19th Intern. Cosmic Ray Conf., Vol. 3 p 445-448 (SEE N85-34862 23-93)* Aug. 1985 **3**:445–448
- Hillas, A. M., Akerlof, C. W. et al. 'The Spectrum of TeV Gamma Rays from the Crab Nebula' *ApJ* Aug. 1998 **503**:744–+
- Kataoka, J., Mattox, J. R. et al. 'Multiwavelength observations of the TeV blazar MRK 501 in March 1996. The first report of the detection by EGRET' *Astroparticle Physics* Jun. 1999 **11**:149–151
- Kataoka, J., Takahashi, T. et al. 'Five-year Monitorings of TeV Blazars with ASCA and RXTE' *astro-ph/0105029* 2001 in preparation
- Keel, B. 'Mkn 421 Broadband Spectrum, <http://www.astr.ua.edu/~keel/agn/>' 2001
- Kellermann, K. I. and Pauliny-Toth, I. I. K. 'Variable Radio Sources' *ARA&A* 1968 **6**:417+
- Kembhavi, A. K. and Narlikar, J. V. *Quasars and Active Galactic Nuclei* vol. 1 Cambridge University Press first edn. 1999

- Kneiske, T., Mannheim, K. et al. ‘Blazar observations with MAGIC’ in *Blazar Observations with BeppoSAX and other Observatories (Frascati, Italy)* 2001
- Kneiske, T. M., Bretz, T. et al. ‘Upper limit for the dust-enshrouded star formation rate in the Universe’ *A&A* 2002a submitted
- Kneiske, T. M., Mannheim, K. et al. ‘Implications of cosmological gamma-ray absorption. I. Evolution of the metagalactic radiation field’ *A&A* Apr. 2002b **386**:1–11
- Königl, A. ‘Relativistic jets as X-ray and gamma-ray sources’ *ApJ* Feb. 1981 **243**:700–709
- Konopelko, A., Aharonian, F. et al. ‘Detection of gamma rays above 1 TeV from the Crab Nebula by the second HEGRA imaging atmospheric Cherenkov telescope at La Palma’ *Astroparticle Physics* Feb. 1996 **4**:199–215
- Kranich, D. *Verbesserung der Gamma/Hadron-Trennung in der Hochenergie Gamma-Astronomie mit Cherenkov Teleskopen* Master’s thesis Technische Universität München Apr. 1997 MPI-PhE/97-11
- Kranich, D. *Temporal and spectral characteristics of the active galactic nucleus Mkn 501 during a phase of high activity in the TeV range* Ph.D. thesis Technische Universität München Jul. 2001
- Laurent-Muehleisen, S. A., Kollgaard, R. I. et al. ‘The RGB Sample of Intermediate BL Lacertae Objects’ *ApJ* Nov. 1999 **525**:127–143
- Le Bohec, S., Degrange, B. et al. ‘A new analysis method for very high definition Imaging Atmospheric Cherenkov Telescopes as applied to the CAT telescope’ *NIMA* 1998 **416**:425–437
- Lin, Y. C., Bertsch, D. L. et al. ‘Detection of high-energy gamma-ray emission from the BL Lacertae object Markarian 421 by the EGRET telescope on the Compton Observatory’ *ApJ* Dec. 1992 **401**:L61–L64
- Liu, F. K., Liu, B. F. et al. ‘The long-term optical behavior of MKN 421’ *A&AS* Jun. 1997 **123**:569–574
- Longair, M. S. *High Energy Astrophysics* vol. 1 Cambridge University Press second edn. 1992
- Longair, M. S. *High Energy Astrophysics* vol. 2 Cambridge University Press second edn. 1994
- Mannheim, K. ‘Possible Production of High-Energy Gamma Rays from Proton Acceleration in the Extragalactic Radio Source Markarian 501’ *Science* Jan. 1998 **279**:684–+
- Maraschi, L., Fossati, G. et al. ‘Correlated variability of MKN 421 at X-ray and TeV wavelengths on time scales of hours’ *Astroparticle Physics* Jun. 1999 **11**:189–192
- Marscher, A. P. ‘Relativistic jets and the continuum emission in QSOs’ *ApJ* Jan. 1980 **235**:386–391
- Masterson, C. and The CAT Collaboration ‘Observations of the Crab Nebula with the CAT Imaging Atmospheric Čerenkov Telescope’ in *High Energy Gamma-Ray Astronomy* 2001 pages 753–+
- Mather, J. C., Fixsen, D. J. et al. ‘Calibrator Design for the COBE Far-Infrared Absolute Spectrophotometer (FIRAS)’ *ApJ* Feb. 1999 **512**:511–520
- Mirzoyan, R. and Lorenz, E. ‘On the Calibration Accuracy of Light Sensors in Atmospheric Cherenkov, Fluorescence and Neutrino Experiments’ in *25th International Cosmic Ray Con-*

- ference (Durban)* vol. 7 1998 pages 265+
- Mirzoyan, R., Kankanian, R. et al. ‘The first telescope of the HEGRA air Cherenkov imaging telescope array’ *NIMA* 1994 **351**:513–526
- Mirzoyan, R., Fernandez, J. et al. ‘A direct method of measuring the single photoelectron to ADC counts conversion factor for Cherenkov Telescopes and determination of the Telescope trigger threshold’ in Cresti, C. (editor), *Towards a Major Atmospheric Cherenkov Detector IV (Padua)* 1995
- Mushotzky, R. F., Boldt, E. A. et al. ‘X-ray observations of BL Lacertae objects’ *ApJ* Dec. 1978 **226**:L65–L67
- Mushotzky, R. F., Boldt, E. A. et al. ‘A change in the X-ray spectrum of Markarian 421’ *ApJ* Aug. 1979 **232**:L17–L19
- NASA ‘NASA EXOSAT overview page <http://heasarc.gsfc.nasa.gov/docs/exosat/exosat.html>’ 2001
- Nishiyama, T., Chamoto, N. et al. ‘Detection of a new TeV gamma-ray source of BL Lac object 1ES 1959+650’ in *Proc. 26th ICRC (Salt Lake City), vol 3* 1999 page 370
- Particle Data Group ‘Review of Particle Physics’ *Eur. Phys. J. C* 2000 **15**
- Penzias, A. A. and Wilson, R. W. ‘A Measurement of Excess Antenna Temperature at 4080 Mc/s.’ *ApJ* Jul. 1965 **142**:419+
- Perola, G. C., Boksenberg, A. et al. ‘Detailed observations of NGC 4151 with IUE. II - Variability of the continuum from 1978 February to 1980 May, including X-ray and optical observations’ *MNRAS* Jul. 1982 **200**:293–312
- Petry, D. *Beobachtung hochenergetischer  $\gamma$ -Strahlung ( $E > 1$  TeV) aus Richtung der aktiven Galaxien Mkn 421 und Mkn 501* Ph.D. thesis Technische Universität München / Sep. 1997 MPI-PhE/97-27
- Piner, B. G., Unwin, S. C. et al. ‘VSOP and Ground-based VLBI Imaging of the TEV Blazar Markarian 421 at Multiple Epochs’ *ApJ* Nov. 1999 **525**:176–190
- Piron, F., Djannati-Atai, A. et al. ‘Temporal and spectral gamma-ray properties of Mkn 421 above 250 GeV from CAT observations between 1996 and 2000’ *A&A* Aug. 2001 **374**:895–906
- Protheroe, J., Bhat, C. L. et al. ‘Very High Energy Gamma Rays from Markarian 501’ in *25th International Cosmic Ray Conference* vol. 25 1998 pages 317+
- Punch, M., Akerlof, C. W. et al. ‘Detection of TeV photons from the active galaxy Markarian 421’ *Nature* Aug. 1992a **358**:477+
- Punch, M., Akerlof, C. W. et al. ‘Detection of TeV photons from the active galaxy Markarian 421’ *Nature* Aug. 1992b **358**:477+
- Purton, C. R., Kojoian, G. et al. ‘Markarian 421: A Lacertid’ *PASP* Apr. 1977 **89**:119+
- Quinn, J., Akerlof, C. W. et al. ‘Detection of Gamma Rays with E > 300 GeV from Markarian 501’ *ApJ* Jan. 1996 **456**:L83–+
- Quinn, J., Bond, I. H. et al. ‘The Flux Variability of Markarian 501 in Very High Energy Gamma Rays’ *ApJ* Jun. 1999 **518**:693–698
- Ricketts, M. J., Cooke, B. A. et al. ‘X-ray transient source at high galactic latitude and sug-

- gested extragalactic identification' *Nature* Feb. 1976 **259**:546+
- Robson, I. *Active Galactic Nuclei* vol. 1 John Wiley & Sons Ltd first edn. 1996
- Rybicki, G. B. and Lightman, A. P. *Radiative Processes in Astrophysics* vol. 1 John Wiley & Sons Ltd first edn. 1979
- Schweizer, T. *Analysis of the large gamma ray flares of Mkn 421 observed with HEGRA CT1 and the calibration of the MAGIC Cherenkov Telescope on La Palma* Ph.D. thesis IFAE, Universitat Autònoma de Barcelona 2002
- Shlosman, I., Begelman, M. C. et al. 'The fuelling of active galactic nuclei' *Nature* Jun. 1990 **345**:679–686
- Simpson, J. A., Fonger, W. et al. 'Cosmic Radiation Intensity-Time Variations and Their Origin. I. Neutron Intensity Variation Method and Meteorological Factors' *Phys. Rev.* Jun. 1953 **90**:934–950
- Sobczynska, D. and Lorenz, E. 'Influence of peak sensitive discriminator on the collection area and flux calculations for air Cherenkov telescopes in  $\gamma$  astronomy' *A&A* 2002 in preparation
- Sokolsky, P. *Introduction to Ultrahigh Energy Cosmic Ray Physics* Addison Wesley 1989
- Space Telescope Science Institute 'Digital Sky Survey, <http://archive.stsci.edu/dss/>' 2001
- Stanev, T. and Franceschini, A. 'Constraints on the Extragalactic Infrared Background from Gamma-Ray Observations of MRK 501' *ApJ* Feb. 1998 **494**:L159–+
- Stecker, F. W. and de Jager, O. C. 'New Upper Limits on Intergalactic Infrared Radiation from High-Energy Astrophysics' *ApJ* Oct. 1993 **415**:L71–+
- Tanimori, T., Sakurazawa, K. et al. 'Detection of Gamma Rays of up to 50 TeV from the Crab Nebula' *ApJ* Jan. 1998 **492**:L33–+
- Ulrich, M. ., Kinman, T. D. et al. 'Nonthermal continuum radiation in three elliptical galaxies' *ApJ* Jun. 1975 **198**:261–266
- Ulrich, M.-H. 'Spectra of the Stellar Population in Three Objects Related to BL Lacertae' *ApJ* May 1978 **222**:L3–L6
- Ulrich, M. H. and Boisson, C. 'The ultraviolet spectrum of the Seyfert galaxies NGC 3516 and NGC 5548' *ApJ* Apr. 1983 **267**:515–527
- Urry, C. M. and Padovani, P. 'Unified Schemes for Radio-Loud Active Galactic Nuclei' *PASP* Sep. 1995 **107**:803+
- Walker, I. R., Mihos, J. C. et al. 'Mergers to Bars to Boxy Bulges: A Galaxy Evolution Story' in *ASP Conf. Ser. 91: IAU Colloq. 157: Barred Galaxies* 1996 pages 486+
- Weekes, T. C., Cawley, M. F. et al. 'Observation of TeV gamma rays from the Crab nebula using the atmospheric Cerenkov imaging technique' *ApJ* Jul. 1989 **342**:379–395
- Zhang, F. J. and Baath, L. B. 'The radio fine structure of the BL Lacertae object MK 421' *A&A* Sep. 1990 **236**:47–52
- Zweerink, J. A., Akerlof, C. W. et al. 'The TeV Gamma-Ray Spectrum of Markarian 421 during an Intense Flare' *ApJ* Dec. 1997 **490**:L141–+